TECHNISCHE UNIVERSITÄT MÜNCHEN
Fakultät für Luftfahrt, Raumfahrt und Geodäsie
Lehrstuhl für Luftfahrtsysteme

Conceptual Sizing Methods for Propulsive Fuselage Aircraft Concepts

Julian Raphael Bijewitz

Vollständiger Abdruck der von der Fakultät für Luftfahrt, Raumfahrt und Geodäsie der Technischen Universität München zur Erlangung des akademischen Grades eines

Doktor-Ingenieurs (Dr.-Ing.)

genehmigten Dissertation.

Vorsitzender:	Prof. Dr.-Ing. Volker Gümmer
Prüfer der Dissertation:	1. Prof. Dr.-Ing. Mirko Hornung
	2. Prof. Dr.-Ing. Jens Friedrichs

Die Dissertation wurde am 19.11.2019 bei der Technischen Universität München eingereicht und durch die Fakultät für Luftfahrt, Raumfahrt und Geodäsie am 10.11.2020 angenommen.

Vorwort

Die vorliegende Arbeit entstand größtenteils während meiner Tätigkeit als wissenschaftlicher Mitarbeiter am Bauhaus Luftfahrt e.V. Mein größter Dank gilt meinem Doktorvater, Herrn Prof. Dr.-Ing. Mirko Hornung, der mir während dieser Zeit mit vielen wertvollen Hinweisen und Ratschlägen unterstützend zur Seite stand.

Herrn Prof. Dr.-Ing. Jens Friedrichs möchte ich für das Interesse an meiner Arbeit und die freundliche Übernahme des Koreferats danken. Darüber hinaus danke ich Herrn Prof. Dr.-Ing. Volker Gümmer für die Übernahme des Prüfungsvorsitzes.

Besonders bedanken möchte ich mich bei Herrn Dr.-Ing. Arne Seitz, dessen fundierten Rat ich oft suchte und der mich mit zahlreichen Anregungen und Hinweisen zu meiner wissenschaftlichen Arbeit unterstützt hat. Herrn Dr. Askin T. Isikveren danke ich für viele Ratschläge während der anfänglichen thematischen Definition dieser Arbeit sowie für seine Beteiligung als Co-Autor wissenschaftlicher Publikationen im Kontext dieser Arbeit. Herrn Richard Grenon und Herrn Jean-Luc Godard danke ich für die Bereitstellung numerischer Daten im Zusammenhang mit dem DisPURSAL-Projekt. Herrn Dr.-Ing. Reinhold Schaber danke ich für viele fachliche Hinweise im Bereich der Triebwerksauslegung sowie Herrn Dr.-Ing. Sascha Kaiser für die Unterstützung in Fragen der Triebwerksleistungsrechnung. Allen Mitarbeiterinnen und Mitarbeitern des Bauhaus Luftfahrt danke ich für das stets angenehme Arbeitsklima.

Besonderer Dank gilt meinen Eltern, die mit ihrer fortwährenden Unterstützung die Grundlage zum erfolgreichen Abschluss dieser Arbeit gelegt haben. Zu guter Letzt möchte ich mich bei meiner Freundin Katjana für ihre Geduld und den bedingungslosen Rückhalt über die Jahre bedanken.

München, im Februar 2021

Julian Bijewitz

Abstract

The aviation industry increasingly faces challenges from ever more stringent environmental regulations and continuously strong traffic growth. While in the past significant improvements in air transportation fuel efficiency have been achieved, disruptive technology solutions in propulsion system and aircraft design will be required. Beyond the evolutionary improvement of contemporary systems, new propulsion system integration options are considered an enabler for future environmentally friendly aircraft. A particularly promising approach towards mitigating the installation penalties connected to high propulsive efficiency levels intrinsically suffered under conventional engine installation paradigms is associated with a more synergistic way of propulsion system integration. In particular, the notion of ingesting large fractions of the airframe boundary layer into the propulsive device and filling the airframe wake is considered a promising approach in recent research activities.

In this thesis, a methodological framework for the sizing and assessment of a novel configurational approach for synergistic propulsion system integration is presented suitable for the early phases of conceptual design. Key feature of the investigated Propulsive Fuselage Concept is a propulsive device centrally installed in the aft fuselage affording localized ingestion and re-energization of the fuselage boundary layer. In this work, gas turbine based power transmission is considered. The presented approach targets sizing and analysis capability with respect to the primary physical effects associated with highly integrated propulsion systems and is equally applicable to conventionally installed power plants. In view of the increased level of aero-propulsive interaction, emphasis is placed on the integrated analysis of propulsion system and aircraft design and performance characteristics. A primary focus is set on introducing a methodological formulation allowing for multidisciplinary, parametric design studies leading to the identification of optimal design settings at the vehicular level.

Appropriate methods for the mapping of aero-propulsive interaction effects are introduced based on high-fidelity numerical data. An efficient process for the data incorporation in gas turbine performance calculation is presented utilizing a series of derived regression functions. Coherent bookkeeping schemes, common design standards as well as sizing and performance laws are introduced to ensure consistency between the alternative engine integration strategies. Beyond general predesign methods for propulsion system synthesis, several specialized methods covering cycle and flow path design, component sizing, performance evaluation and weight estimation are proposed dedicated to the modeling of fuselage-installed boundary layer ingesting propulsion systems. Upon individual validation, the methods are integrated in a conceptual aircraft design framework allowing for appropriate propagation of the individual power plant characteristics to the overall system level. The basic plausibility of the overall methodology is verified through comparison of recalculated key performance figures with published conceptual studies.

The implemented methodology is demonstrated for a medium-to-long range application scenario. Beyond comparative design studies on the features and characteristics of the fuselage-installed power plant in relation to those of conventionally installed engines, the focus is on the discussion of parametric studies at aircraft level. For a given design Mach number and advanced technology settings, the analyses conducted in the present work indicate design mission block fuel reductions ranging between 5.4% and 7.8% compared to an equally advanced conventional aircraft equipped with underwing-podded engines. It has been established that the identified fuel burn benefit strongly depends on the selection of key design parameters and power plant sizing strategies. The diminished fuel saving potential relative to previous studies is attributed to the enhanced level of detail in system modeling and the consideration of additional sizing constraints thus far not entirely accounted for, thereby emphasizing the relevance of an integrated analysis at the overall system level.

Contents

List of Figures

List of Tables

Nomenclature

Acronyms

AC	Aircraft
ACARE	Advisory Council for Aviation Research and Innovation in Europe
AGARD	Advisory Group for Aerospace Research and Development
AIP	Aerodynamic Interface Plane
ANN	Artificial Neural Network
APSS	Aircraft Propulsion System Simulation
ATAG	Air Transport Action Group
B	Burner
BL	Boundary Layer
BLI	Boundary Layer Ingestion
BPR	Bypass Ratio
BWB	Blended Wing Body
CAS	Calibrated Air Speed
CCS	Common Core Strategy
CEA	Chemical Equilibrium and Applications
CENTRELINE	ConcEpt validatioN sTudy foR fusElage wakefilLIng propulsioN intEgration
CFD	Computational Fluid Dynamics
CFRP	Carbon Fiber Reinforced Polymer
CO_2	Carbon Dioxide
CV	Control Volume
D	Design Sample
DEAP	Distributed Electrical Aerospace Propulsion
DisPURSAL	Distributed Propulsion and Ultra-high bypass Rotor Study at Aircraft Level
DoE	Design of Experiments
DP	Distributed Propulsion
EC	European Commission
EIS	Entry Into Service
ETOPS	Extended Twin Operations
FDGS	Fan Drive Gear System
FF	Fuselage Fan
FL	Flight Level
FNN	Feedforward Neural Network
FPR	Fan Pressure Ratio
GasTurb	Gas Turbine performance software – GasTurb® is a registered trademark of GasTurb GmbH
GE	General Electric Company
GTF	Geared Turbofan
H2020	Horizon 2020
HP	High-Pressure
HPC	High-Pressure Compressor
HPT	High-Pressure Turbine
HT	Horizontal Tail
IAE	International Aero Engines

IATA	International Air Transport Association
ICAO	International Civil Aviation Organization
IP	Intermediate-Pressure
IPC	Intermediate-Pressure Compressor
IPT	Intermediate-Pressure Turbine
ISA	International Standard Atmosphere
KCAS	Knots Calibrated Air Speed
LDMF	Long Duct Mixed Flow
LFL	Landing Field Length
LHS	Latin Hypercube Sampling
LP	Low-Pressure
LPT	Low-Pressure Turbine
LTH	Luftfahrttechnisches Handbuch
LTO	Landing and Takeoff
M	Mach number[1]
Matlab	Matrix Laboratory – Matlab® is a registered trademark of The Mathworks, Inc.
MCL	Maximum Climb
MDO	Multidisciplinary Design Optimization
MIT	Massachusetts Institute of Technology
MTO	Maximum Takeoff
MTOW	Maximum Takeoff Weight
N3CC	N+3 Conventional Configuration
NASA	National Aeronautics and Space Administration
NATO	North Atlantic Treaty Organization
NOVA	Nextgen Onera Versatile Aircraft
NO_x	Nitrogen Oxides
OEI	One Engine Inoperative
OPR	Overall Pressure Ratio
OWE	Operating Weight Empty
PAX	Passengers
PBM	Power Balance Method
PFC	Propulsive Fuselage Concept
PLA	Power Lever Angle
PPS	Propulsion System
PR	Pressure Ratio
PSC	Power Saving Coefficient
RANS	Reynolds-Averaged Navier Stokes
REF	Reference aircraft
RMS	Root Mean Square
RTO	Research and Technology Organization
SAI	Silent Aircraft Initiative
SAR	Specific Air Range
SDSF	Short Duct Separate Flow
SL	Sea Level
SLS	Sea Level Static
SM	Surge Margin
SPI	Synergistic Propulsion System Integration
SRIA	Strategic Research and Innovation Agenda
STARC-ABL	Single-aisle Turboelectric AiRCraft with an Aft Boundary Layer propulsor

[1] For convenience, the notation typically used in aerospace of flight Mach numbers being expressed as "Mx.y" will be adopted.

SUGAR	Subsonic Ultra Green Aircraft Research
TaW	Tube and Wing
TF	Turbofan
TLARs	Top-Level Aircraft Requirements
ToC	Top-of-Climb
TOFL	Takeoff Field Length
TRL	Technology Readiness Level
TSFC	Thrust-Specific Fuel Consumption
UHBR	Ultra-High Bypass Ratio
UK	United Kingdom
UP	Underwing-Podded
VGV	Variable Guide Vanes
VT	Vertical Tail
VTOL	Vertical Takeoff and Landing
WATE	Weight Analysis of Turbine Engines
WF	Wake Filling

Latin Symbols

Symbol	Unit	Description
A	m^2	Area
AN^2	m^2/s^2	Structural loading metric
c	-	Constant
c	m	Chord length
c_m	m/s	Axial velocity component
c_D	-	Nozzle discharge coefficient
c_{FG}	-	Nozzle gross thrust coefficient
c_L	-	Aircraft lift coefficient
$c_{N,MCL}$	-	Engine thrust scaling factor
D	N	Drag
D	m	Diameter
DC_θ	-	Distortion coefficient
ΔF_X	N	Integration impact metric
E	N/m^2	Young's modulus
F	N	Force
f	-	Design regression function
f	-	Factor
F_N	N	Net thrust
F_N/w_2	m/s	Specific thrust
g	-	Operational regression function
H_0	m	Altitude
h	m	Duct height
h	J/kg	Total mass-specific enthalpy
i	-	Gear ratio
L	N	Lift
L	m	Length
l	m	Length
M	-	Mach number
m	-	Model constant
M_B	Nm	Bending moment

M_x	Nm	Torsional moment
$\dot{m}$	kg/s	Mass flow
N	1/min	Rotational speed
n	-	Model constant
P	W	Power
p	Pa	Total pressure
R	m	Range
R	-	Ratio of applied to permissible stress
R	m	Curvature radius
r	m	Radius
Re	-	Reynold number
s	m	Arc length
s	m	Spacing
S_{Ref}	m^2	Reference area
S_{wet}	m^2	Wetted area
T	-	Total temperature
t	m	Thickness
U	m/s	Circumferential velocity
u	m/s	Flow velocity
V	m/s	Flow velocity
V_0	m/s	Flight velocity
W	kg	Mass
X	-	Independent variable
$\vec{X}$	-	Vector of design variables
x	m	Longitudinal coordinate
Y	-	Dependent variable
$\vec{Y}$	-	Model response vector
y	m	Radial coordinate
z	m	Spanwise coordinate

Greek Symbols

α	°	Incidence angle
β	-	Ingested drag ratio
β	-	Auxiliary map variable
γ	-	Ratio of specific heat capacities
γ	-	Empirical buckling coefficient
δ	m	Boundary layer thickness
δ_R	°	Rudder deflection
ϵ	-	Efficiency metric
ε	-	Sensitivity index
ζ	-	Pressure loss coefficient
η	-	Efficiency
ϑ	-	Thrust split ratio
Θ	-	Power split ratio
θ	°	Angle
Λ	-	Blade aspect ratio
λ_D	-	Duct flow coefficient
μ	-	Poisson's ratio
ν	-	Hub/tip ratio

π	-	Pressure ratio
π_{int}	-	Intake total freestream recovery ratio
ρ	kg/m^3	Density
σ	-	Blade solidity
σ_b	N/m^2	Bending stress
σ_B	N/m^2	Material resistance to buckling
τ	-	Blade taper ratio
τ	N/m^2	Shear stress
φ	-	Flow coefficient
φ	°	Arc angle
ψ	-	Aerodynamic loading parameter
ω	rad/s	Angular velocity

Subscripts

a	aerodynamic
aft	aft-body
ax	axial
b	bending
BP	bypass duct
C	cooling air
C	casing
c	related to cooling
CI	core intake
CL	centerline
co	core
$corr$	corrected
cr	cruise
$crit$	critical
ds	design
E	elevator
F	fuselage-installed
F	fuel
fr	free
Fus	fuselage
G	gas
GB	gearbox
hl	highlight
HT	horizontal tail
i	inlet
i	inner
id	ideal
ing	ingested
Int	intake
$interf$	interference
is	isentropic
it	iteration required
M	material
m	area-averaged radius
MP	multi-point related
N	nacelle
Nac	nacelle
o	outlet
od	off-design
ov	overall
p	pressure
pd	propulsive device
pol	polytropic
pr	propulsive
R	rudder
Re	Reynolds number effects related
ref	reference condition
rel	relative to design point
Res	residual
s	static condition
s	shear
std	standard day
SP	single-point related
t	torsional
t	tip
TC	turbo components
$tech$	technological
th	throat
TO	takeoff
tot	total
tr	transmission
VT	vertical tail
v	viscous
W	wing-installed
w	weight
X	in axial direction

Superscripts

$\tilde{}$	alternative accounting scheme
$\hat{}$	CFD-related property
$\bar{}$	mass-averaged property
$'$	without accounting for BLI/WF effects
$'$	baseline efficiency value

Thermodynamic Stations

0	Ambient
1	Aircraft/engine interface
2	Fan inlet
21	Inner stream fan exit
13	Outer stream fan exit
16	Bypass exit
18	Bypass nozzle throat
22	Intermediate-pressure compressor inlet
24	Intermediate-pressure compressor exit
25	High-pressure compressor inlet
3	High-pressure compressor exit
4	Burner exit
41	High-pressure turbine rotor inlet
45	Low-pressure turbine inlet
5	Low-pressure turbine exit
8	Core nozzle throat

1 Introduction

Great advancements in aircraft fuel efficiency have been made since the first commercially successful jet airliner, the Boeing 707, entered service in 1958. A major share of this enhancement can be attributed to the propulsion system, and it is expected that the power plant system will continue to constitute a main contributor to significant system-level enhancements. Over the decades, gas turbine-based aero propulsion has proven to remain the unrivaled choice of aircraft motive power for commercial transports. Enabled through enormous investments in research and development, remarkable improvements in several key areas have been made since the beginning of the jet age. As an example, average propulsion system specific fuel consumption at cruise has improved by almost 50% between 1958 and 2000 while noise levels could be reduced by 75% [1]. In addition, reliability expressed as inflight shutdown rates improved by a factor of 200 over the last 50 years and maintainability measured as time between overhauls by a factor of 15 to 18 [2]. As a result, gas turbine engine design has culminated in a complex technical system combining considerable fuel efficiency with established maturity, versatility to a wide range of customer requirements and excellent reliability. Together with substantial advancements in airframe efficiency, fuel consumption per seat-kilometer of gas turbine powered commercial aircraft has been reduced by 70% since the 1950s [3].

Continuously strong growth rates of worldwide air traffic, the threatening scarcity of fossil resources and increasing awareness of the general public with regards to pollution and global warming pose major challenges to aviation as a whole. As a consequence, progressively more stringent environmental regulations have been put forward. In 2011, ambitious targets for the future of air traffic were formulated by the European Commission (EC) in the Flightpath 2050 vision [4]. These targets were substantiated by the Advisory Council for Aviation Research and Innovation in Europe (ACARE) and expressed through the Strategic Research and Innovation Agenda (SRIA). Apart from addressing socioeconomic, safety and security related aspects, the SRIA stipulates dramatic environmental targets by year 2050 including a 75% reduction in carbon dioxide (CO_2) emissions per passenger kilometer, a 90% reduction in nitrogen oxides (NO_x) emissions, and 65% reduced perceived noise relative to the capabilities of a typical aircraft of year 2000 standard [5]. With regards to CO_2 emissions, these targets were further broken down into main contributing areas involving airframe, propulsion system, air traffic management and airline operations. The SRIA also declared targets at a sequence of temporal waypoints including year 2035, which suggest reductions of 60% CO_2, 84% NO_x and 53% external noise relative to the year 2000 standard [5]. Similarly challenging targets for emissions, noise, fuel and energy consumption were declared by the National Aeronautics and Space Administration (NASA) in the Fundamental Aeronautics Subsonic Fixed Wing Project through the N+1, N+2 and N+3 goals, each representing a new generation of aircraft achieving a Technology Readiness Level (TRL) of 4 to 6 by years 2015, 2020 and 2025, respectively [6]. Additional environmental targets were published by international organizations including the International Air Transport Association (IATA) [7] and the Air Transport Action Group (ATAG) [8]. In addition to the environmental challenges, it becomes an increasingly demanding effort for airline operators to maintain acceptable levels of operating cost in the context of generally anticipated rising fuel prices. Although aircraft fuel efficiency has substantially improved, the rate of progress is not matching the described ambitious long-term targets. Therefore, beyond the evolutionary improvement of the already highly optimized existing systems, fundamental changes in power plant and aircraft design need to be considered.

1.1 Challenges and Motivation

In order to tackle these challenging environmental targets, a multitude of worldwide research and technological development projects has been conducted in the recent past. With regards to advancing aero propulsion technologies, in the European context extensive research has been executed within the European Union's Framework Programmes focusing on advanced turbofan low-pressure systems [9], unducted propulsors [10], radical core engine technologies and thermodynamic cycles [11]–[13] as well as groundbreaking engine components and subsystems [14]. Long-term propulsion research initiatives focus on the exploration of novel energy sources, i.e. (hybrid)-electric power supply and transmission options, cf. e.g. References [15]–[17]. With emphasis placed on the demonstration and validation of advanced technological solutions, the public-private partnership between the EC and the aviation industry, the Clean Sky and Clean Sky 2 Joint Technology Initiative [18], [19] investigate new technologies to reduce environmental pollution and noise levels of next generation aircraft.

Despite considerable advances, the enhancement of propulsion system and airframe on the isolated disciplinary level is expected to fall short of the required efficiency improvements [20]. Taking Joule/Brayton cycle based propulsion, the improvement of thermal efficiency becomes increasingly challenging due to physical limitations of the associated components, while engine installation issues related to decreasing specific thrust levels restrict feasible propulsive efficiency gains when retaining conventional propulsion system integration. Therefore, the consideration of novel propulsion system integration options constitutes a key factor for future environmentally friendly air transport systems. Especially the perspective of introducing a more synergistic integration to the airframe is expected to significantly contribute to reaching these goal settings. A particularly promising approach towards eluding the weight and drag penalties connected to high propulsive efficiency levels intrinsically suffered under conventional systems integration paradigms is associated with the notion of distributing the propulsive thrust along main components of the airframe, thereby capitalizing on beneficial aero-propulsive interaction effects. Advancements in computational and experimental tools capable of resolving mutual aero-propulsion interaction effects along with remarkable progression in propulsion system technology, material sciences and aircraft control have enabled new avenues towards making more tightly-coupled engine-airframe integration practically feasible [21]. As predicted in numerous studies, one of the key benefits of such more closely integrated arrangements is associated with the localized ingestion and re-energization of the viscosity-induced low momentum wake flow of the wetted body via Boundary Layer Ingestion (BLI), which is also referred to as wake filling propulsion system integration. A comprehensive literature review on synergistic propulsion system integration and related configurational solutions will be provided in the second chapter of this thesis.

Apart from potentially beneficial aero-propulsive interaction effects affording a reduction in aircraft motive power demand, an array of technical challenges is connected to more closely integrated propulsion systems. Different from contemporary civil transports featuring freestream propulsion system installation, synergistic propulsion integration is often associated with fundamentally different inflow conditions of the propulsive device. The implications typically include impaired intake total pressure recovery, flow distortion and propulsor efficiency penalties. Apart from propulsion system related changes, the novel installation layout affects aircraft geometric arrangement, weight and balance characteristics, aerodynamics and integrated performance, thus rendering synergistic propulsion system integration a truly multidisciplinary effort. From a modeling and simulation perspective, the consistent assessment of such systems tends to become more complex resulting from the stronger interaction between the traditionally separate disciplines of airframe and propulsion system. The subsequent section presents methodological aspects derived as research objectives for the present work.

1.2 Formulation of Research Objectives

The more closely coupled integration of the propulsion system to the airframe is connected to a series of changes required for the sizing and performance assessment of the associated systems. The mutual interaction of airframe and propulsion system requires the consistent treatment of conventionally installed and highly integrated systems. As will be elaborated in more detail, traditional handbook methods are insufficient to capture the strong interaction effects of airframe and engine, thus motivating the utilization of numerical calculation methods. As a consequence of the unconventional engine installation, a series of implications related to additional loss effects need to be taken into account. As an intuitive prerequisite, the assessment needs to be conducted at the integrated aircraft level.

Although a multitude of conceptual studies in this field has been performed, a lack in the assessment capability of synergistic propulsion integration has been recognized. In particular, previous studies have primarily focused on the analysis of single-point vehicle solutions, thereby inhibiting the derivation of trends and identification of optimal settings. The strong impact of non-uniform inflow on propulsion system design and operation has been handled incompletely. As a consequence, the following methodological aspects have been recognized as research focal points of the present work:

- Introduction of propulsion system synthesis models coherently applicable to conventionally installed and highly integrated, boundary layer ingesting power plant architectures, which allow for appropriate mapping of aero-propulsive interaction effects at the vehicular level.
- Application of consistent interfacing standards and aero-propulsive bookkeeping schemes facilitating efficient incorporation of parameterized, high-fidelity aerodynamic data within conceptual aircraft and propulsion system sizing.
- Consistent propagation of the impact emanating from fuselage BLI/wake filling propulsion integration to engine and eventually aircraft-integrated characteristics including geometric implications, effects from aircraft weight and balance and aero-propulsive characteristics.
- Declaration of key influential design parameters associated with propulsion system and airframe as free variables, thereby enabling the execution of parametric trade studies at the vehicular level and allowing for the identification of the overall efficiency potential.

The presented methodology comprises a series of methods for design synthesis and performance prediction of conventionally installed and advanced propulsion system integration strategies employing BLI propulsion systems. Aero-propulsive interaction effects are captured based on numerical data. As part of the work, a process for the efficient incorporation of numerical aerodynamic data in typical gas turbine performance calculation will be proposed. Coherent bookkeeping schemes, common design standards as well as sizing and performance laws will be introduced to ensure consistency between the alternative engine integration strategies. The propagation of propulsion system characteristics to the aircraft level and the repercussive information exchange is handled via surrogate modeling techniques. The inherently fast responding model evaluation supports the exploration of large variations within the design space.

Building on previous work in the field of advanced engine integration, the methodological framework developed in this work will be applied to a novel approach for synergistic propulsion system integration, the “Propulsive Fuselage Concept” (PFC). This configuration constitutes a promising candidate for the practical implementation of more closely coupled propulsion airframe integration. As will be elaborated in more detail, this configuration adhering to the general “tube-and-wing” aircraft

layout employing gas turbine-based power trains is selected over more unconventional airframe morphologies due to the possibility to separate BLI effects from the implications emanating from the airframe topology itself, thus minimizing uncertainty in models and results.

The proposed methodological approach is demonstrated at both system and aircraft level. Engine related studies focus on the implications of ingesting boundary layer flow on turbofan characteristics, while integrated analyses target the identification of important design drivers at the vehicular level. Sensitivity studies are utilized to gauge the impact of critical assumptions and potential uncertainties.

1.3 Organization of Thesis

Starting from a broad overview of environmental targets stipulated for aviation and the required efficiency improvement of future air transport systems, the notion of synergistic propulsion system integration was introduced in the present chapter as a potential contributor to reaching these goals. In **Chapter 2**, a comprehensive summary of the current state of research in synergistic propulsion integration is provided. As part of this elaboration, the characteristics of tightly-coupled propulsion-airframe arrangements are presented and recent research on BLI propulsion integration is outlined. As a result of the literature survey, existing methodological approaches for the modeling and assessment of highly integrated propulsion architectures are described and key areas of research needs identified. **Chapter 3** deals with the general principles of BLI and Wake Filling (WF). As part of a theoretical discussion, important metrics for system description and the integrated assessment of BLI configurations are derived. Based on a simplified analytical pre-study, the basic efficiency potential of the selected configuration is established compared to alternative morphologies and the detailed system analysis and integration studies presented in this work are motivated. Following an overview of the aero-numerical data available, in **Chapter 4** the thrust and drag bookkeeping approach employed in this work is defined and analytically applied to the studied configurational setup. A model matching procedure for the efficient incorporation of numerical aerodynamic airframe data into propulsion system design and performance is proposed. Based on this, a series of regression functions are presented useful for the parametric mapping of the integration of BLI power plants at design and off-design conditions. **Chapter 5** handles the methodological approach towards propulsion system integration. A set of general conceptual methods for propulsion system synthesis is introduced and validated. With focus on the advanced, highly integrated propulsion integration, a series of specialized methods are thereafter presented dedicated to the modeling of fuselage-installed BLI propulsion systems and the framework employed for aircraft-integrated studies is characterized. In **Chapter 6**, the implemented methods are demonstrated. Upon the description of the considered application case, propulsion system studies are presented aiming at the characterization of the boundary layer ingesting propulsion system relative to the trends of a conventionally installed turbofan. Thereafter, a series of insightful aircraft-integrated parametric studies of the PFC are discussed demonstrating the developed capability for identifying optimum propulsion system design settings at aircraft level. Moreover, the basic plausibility of the overall methodology is verified. To round off, in **Chapter 7** important results and findings are summarized and perspectives for further research in this field are outlined.

Elements of the literature review, the basic methodological approach connected to the present thesis and its application have been published in six conference contributions and two journal articles. Reference [22] provides a review of novel aircraft configurations with synergistic propulsion integration. In References [23] and [24], basic propulsion system modeling aspects are elaborated and demonstrated in the context of alternative power plant architecture studies. References [25] and [26] deal with the methodological approach of PFC propulsion system integration, while References [27]–[29] focus on the discussion of trade studies.

2 State-of-the-Art in Synergistic Propulsion System Integration

In the present chapter, previous work connected to advanced propulsion system integration is presented starting from expounding elements of the current practice in propulsion system integration. The subsequent section is devoted to outlining recent challenges of contemporary propulsion system integration. Thereafter, advanced propulsion system integration strategies associated with more synergistically arranged engine-airframe integration are discussed, and the characteristics concerning expected benefits and challenges are outlined. Furthermore, a brief historical overview of strongly integrated propulsion is provided and selected case studies are highlighted. Upon the introduction of the aircraft configuration investigated as part of the present thesis and the review of relevant previous work, essential research needs in the associated fields are itemized.

2.1 Introduction to Propulsion System Integration

The integration of propulsion system and airframe is a highly complex task involving multiple disciplines. Apart from the aircraft and aero-engine manufacturers, also the airline as a customer is involved in the process. Additional stakeholders include airworthiness authorities governing e.g. safety requirements and compliance with environmental standards as well as airports as regulators of local emissions and operations [30]. In the past, the development of airframe and propulsion system used to be a relatively separate effort in commercial aircraft design leading to a situation where various propulsion system options offered by different engine manufacturers or joint ventures were available to the customer to be installed on a certain aircraft. This paradigm ensured low development cost while supporting high market shares for engine manufacturers [30].

In the recent past, a multitude of factors including increasingly strict requirements for environmental protection (see Chapter 1) have led to a departure from the traditional practice of selecting the best available engine for a given aircraft. Recognizing the efficiency potential available from an integrated engineering design optimization, engine manufacturers tend to become more involved already during the early product development phases of new aircraft programs, thereby making the conceptual design phase a truly interactive and iterative effort [31]. Consequently, a stronger customization of modern flight propulsion systems to the specific needs of the aircraft is entailed.[2] As outlined in Reference [32], during the initial phase of an aircraft design process the Top Level Aircraft Requirements (TLARs) mirroring customer, environmental and airworthiness expectations such as payload, range, emissions and the targeted Entry-Into-Service (EIS) date result in an initial sizing of the aircraft concept. Based on key performance specifications engine architectural options and key properties of the thermodynamic cycle are evaluated by the engine manufacturer. Trade-off studies are conducted to determine the impact of engine efficiency, weight and dimensions on typical objectives including fuel consumption, noise emissions and cost. The typical propulsion system conceptual design process is described e.g. by Stricker [33] and Schaber [34]. A parameter typically subject to aircraft-level optimization refers to the propulsor diameter. Typical multidisciplinary trade-offs emanating from propulsion system installation with impact on the designer's choice for engine longitudinal, lateral, vertical, and angular positioning include evaluation of aircraft stability and engine-out control aspects,

[2] Consider e.g. Boeing 777-X, Airbus A350 and A220 programs.

aerodynamic interference, structural considerations, maintenance aspects, cabin noise characteristics, foreign object ingestion hazards, subsystem location, and flight safety aspects [35]. Assessment of these factors in conjunction with further aircraft configuration parameters such as landing gear height subsequently feed into an aircraft resizing under consideration of the updated TLARs. An overview of further aspects to be evaluated when deciding on the propulsion system installation option was provided by Sadraey [35].

2.2 Overview of Contemporary Propulsion System Integration

Over the past decades, a major contribution to the remarkable improvements in propulsion system fuel efficiency can be attributed to the increase in propulsive efficiency, which statistically has improved by 0.3% per year in average [3]. This parameter is typically improved by reducing engine specific thrust (i.e. net thrust per unit engine mass flow). Assuming constant net thrust requirements, lower specific thrust can be facilitated by larger propulsor sizes. Considering traditional propulsion system integration standards, the installation of larger power plants, however, normally generates a series of complex integration issues. As the propulsor and nacelle in case of ducted propulsive devices constitute a major share of the total propulsion system weight, growing engine radial dimensions are typically accompanied by increased weight penalties. Beyond, the presence of the nacelle adversely influences the localized wing flow field and hence the aerodynamic efficiency of the lifting surfaces, and, moreover, limits the space available for the installation of leading edge high-lift devices [36]. In addition, the wetted area of the nacelle has a significant impact on the parasitic drag of the nacelle and thus the aerodynamic performance of the aircraft. From a geometric perspective, a minimum ground clearance of the underwing-podded nacelles must not be violated, thereby additionally constraining the maximum practicable propulsor diameter or requiring an increased landing gear length. Further aspects placing constraints on feasible propulsor sizes include the evaluation of nose gear collapse scenarios, aircraft roll angle considerations, ramp safety aspects and maintenance accessibility [30]. Consequently, optimum Bypass Ratios (BPRs) of state-of-the-art commercial turbofan engines are currently found in the range of 10 to 12 and may require a geared architecture to reduce the aerodynamic mismatch of fan, booster and Low-Pressure Turbine (LPT). For more advanced technological settings, BPRs in the range of approximately 12 to 21 have been reported as optimal within the frame of conceptual studies depending on the application, thrust class and optimization objectives [9], [23], [37]–[42]. Even lower specific thrust levels may, apart from fan drive gear systems, necessitate adaptive propulsor elements such as a variable area fan nozzle or variable pitch fan [43] to ensure sufficient stability margins. While aircraft powered by unducted propulsion systems, i.e. turboprops, feature very high propulsive efficiencies, current applications are limited to moderate flight speeds.

Pursuing the exploitation of additional system and aircraft-level efficiency potentials, the introduction of a more synergistically coupled propulsion airframe integration approach beyond the traditional podded engine installation is currently being considered by several engine and airframe manufacturers as a possible candidate for future advanced concepts. This includes e.g. the companies Rolls-Royce [44], GE Aviation [45], Pratt & Whitney [46], Safran [47], Airbus [48], The Boeing Company [49], Northrop Grumman [50], Lockheed Martin [51] and GKN [52].

2.3 Advanced Propulsion System Integration Strategies

In contemporary, highly optimized propulsion system integration, the arrangement of propulsion system and airframe is tailored to yield minimum undesirable aerodynamic interaction between the

engine and airframe. Detrimental effects include interference drag between pylon-mounted engines and the wing. For fuselage-buried engines of classic transport aircraft with s-duct intakes,[3] care has been taken to position the inlet outside the low-momentum fuselage boundary layer (BL). In military, especially supersonic applications with more closely integrated engines, BL diverter or bleed systems are often utilized. For propeller driven aircraft, the propeller-induced velocities in the slipstream typically have an adverse effect on the aerodynamic characteristics of the airframe components immersed in the propeller wash. Different from the separated primary functions of engine and airframe prevailing in most current commercial aircraft, a beneficial superposition of thrust and lift forces is afforded by powered lift systems aiming at improving aircraft low-speed performance.

In order to exploit the benefits of further reduced specific thrust levels, or, "Ultra-High Bypass Ratio" (UHBR) engines, various research projects focus on the investigation of innovative nacelle configurations aiming at mitigating the weight and drag penalties caused by larger propulsor dimensions [53]. Emphasis has been placed on realizing shorter and thinner inlets and exhaust ducts. Besides anticipated benefits in weight and drag characteristics, challenges include reduced internal diffusion capability and potentially exacerbated inlet flow distortion effects, fan efficiency penalties and aero-mechanical issues including thrust reverser integration. Moreover, the reduced area available for applying acoustic liners to attenuate noise is in conflict with the lower frequencies caused by decreasing fan pressure ratios and thus fan tip speeds [3]. Furthermore, active shape adaptation of nacelle elements such as the intake lip characteristics may facilitate additional beneficial effects [54]. Beyond "tube-and-wing" (TaW) layouts, morphological airframe options being considered to accommodate larger propulsors include blended wing bodies, high-wing designs [55] and even more exotic configurations. Examples are provided in References [50], [56]. Motivated by intrinsically superior propulsive efficiency levels, the concept of unducted propulsion systems, i.e. propfan ("open rotor") configurations with single or counter rotating propeller configurations has been under investigation for several decades. After early demonstration testing in the 1980's, the concept has been subject to renewed investigations [57], [58].

Now, in order to address the discussed challenges of conventional propulsion system integration while intending to tackle the dramatic energy efficiency improvements needed, even more disruptive approaches are required calling for a fundamental change in propulsion system integration paradigm. As indicated in several studies, a departure from the above-described classic separation between airframe and propulsion, in particular the strategic arrangement of the thrust producing devices may facilitate a series of synergy effects resulting from the fully integrated design of engine and airframe. The benefits potentially attainable from a stronger coupling are diverse and cover various disciplines including aerodynamics, propulsion, structural design and flight controls. Frequently, the term "Distributed Propulsion" (DP) has been used to subsume novel aircraft morphologies incorporating a distribution of thrust production [21], [59]–[62]. Since this terminology infers a limitation to arrangements with multiple propulsor, in the present context the more generalized term "synergistic propulsion integration" (SPI) shall be used. This designation covers all concepts, which in general seek to capitalize on benefits attainable from a more tightly coupled engine installation. As indicated in Reference [22], the majority of such propulsion integration concepts is associated with propulsor unit counts comparable to in-service commercial transports. The following section provides an overview and categorization of integration solutions.

[3] Examples include Boeing 727, Hawker Siddeley HS-121 and Lockheed L-1011

2.3.1 Overview and Classification of Synergistic Propulsion System Integration

Campbell [59], Sehra and Whitlow [60] as well as Kim [21] proposed a classification scheme of DP according to the propulsion system integration approach, which is briefly reviewed in the following.[4] Generally, DP may be grouped into three main categories involving multiple distributed engines, multiple propulsors driven by a small number of core engines and distributed exhaust. It is noticeable that this classification is incomplete in a sense that several concepts of SPI are incompatible with the scheme. Therefore, aspects focusing especially on synergistic aft fuselage-installed propulsion integration will be discussed in Section 2.3.2.

2.3.1.1 Multiple discrete engines

An arrangement employing multiple discrete engines distributed along lifting surfaces has been considered as a means to benefit from reduced life cycle costs [61] due to the exploitation of economies of scale. Reference [63] suggests that replacing the currently dominating small number of engines by a larger count could stimulate the application of different manufacturing techniques suitable for mass production, thus allowing for significantly decreased production cost and the possibility to substitute the current maintenance practice by a simpler replacement strategy upon engine failure. However, a number of unfavorable effects were identified gaining dominance as the number of propulsors is increased including degrading gas turbine efficiency, smaller sized engines becoming heavier in relative terms, manufacturing issues as well as increasing drag. As a positive effect, the spanwise distribution of engines was found to improve wing bending relief, thereby promoting a lighter wing design. Beneficial indirect effects were expected from increased aircraft robustness against engine-out cases and possibly reduced control surfaces by using thrust vectoring as a means of aircraft directional control. Yet, the degraded engine efficiency was found to prevent any technical and economic viability. Another investigation [64] explored the potential of integrating 30 gas turbine engines within the wing of a military transport applying rigorous use of upper surface blowing with intent to significantly increase high-lift performance to reduce the required field length. While this target could be met, a 25% reduction in payload and a 2.5-fold increase in gross weight relative to a conventionally designed transport were found.

2.3.1.2 Multiple propulsors powered by a small number of core engines

This refers to an arrangement where a number of decentralized ducted or unducted propulsive devices are powered by a small number of power generators. In the most straightforward way, these are constituted by gas turbine based power plants, while also combinations with voltaic energy sources have been investigated. The proposed power transmission concepts include mechanical, pneumatic or electric options. An example for a gear-driven multiple-fan distribution concept is the SAX-40 Blended Wing Body (BWB) concept featuring three semi-buried nacelles, each housing a package of three fans driven by a single core. While shaft and gear system transmission is in principle well-established technology, challenges exist in ensuring high gear system efficiencies and controlling complexity related to cooling and lubrication [65]. Pneumatic power distribution refers to propulsors being driven by high-pressure gas extracted from core engines. As an example, the ADAM III fighter concept investigated in the 1960's by the Vought Aeronautics Division used a duct layout to route gas generator exhaust flow to wing-installed turbines connected to fan assemblies [66]. Although some of the concepts were experimentally studied, a successful application has not been realized, possibly due to difficulties encountered by ducting hot gas through the wing structure and inefficiencies related to duct pressure losses [21]. In the recent past, power trains based on electric transmission from a centralized energy and power source to remotely placed electric propulsors have gained increasing attention. One of the power train layouts commonly investigated refers to the serial hybrid electric drive,[5] where

[4] Additional classification approaches were proposed by Gohardani *et al.* [62], Gohardani [329] and Laskaridis [165].
[5] For a classification of different (hybrid-) electric power train arrangements, see e.g. References [17], [330].

power is extracted from a limited number of power plants using generators and is distributed via a Power Management and Distribution system including an optional storage of electric energy.[6] Electric motors ultimately drive the propulsive devices. As a result, an enhanced aircraft configurational flexibility is reported, in principle motivating a multitude of decentralized propulsors to be powered by a small number of core engines. One of the main challenges is to realize power train designs with sufficiently high gravimetric and volumetric power and/or energy densities as well as efficiencies of the associated components. Exemplary integration studies of transport aircraft include the NASA N3X BWB concept [67], the split-wing designs proposed by Empirical Systems Aerospace [68] and the concepts investigated within the Subsonic Ultra Green Aircraft Research (SUGAR) study undertaken by Boeing [55].

2.3.1.3 Distributed exhaust

This category comprises integration strategies where exhaust gas from gas generating engines is expelled out of the wing trailing edge. Possible benefits enabled by the technology include application of wake filling (see Section 2.3.2), thrust vectoring and increase in high-lift. Downward deflected ejection of a sheet of gas out of the wing's trailing edge has been investigated in the past as a means of realizing Short Takeoff and Landing through a jet flap arrangement. An example for a historical demonstrator is the Hunting H.126 experimental aircraft [21]. More recently, the notion of using gas expelled out of a slot at the trailing edge for thrust production ("jet-wing" propulsion) has received renewed attention in the context of BWB concepts. Other forms of distributing the exhaust is constituted by the cross-flow fan, a two-dimensional propulsor integrated within a wing structure with the primary objective of yielding very high maximum lift coefficients [69]. Although experimentally demonstrated, issues pertaining to poor efficiency due to inherent loss mechanisms, limited cruise speed and mechanical complexity have prevented the commercial application [70].

2.3.2 Characteristics of Tightly-Coupled Propulsion-Airframe Integration

The close coupling of propulsion-airframe integration allows fundamentally different effects to be utilized at the vehicular level. One of the main benefits enabled by a more integrated propulsion-airframe installation is rooted in the notion of ingesting the low-momentum BL developing on wetted surfaces of the airframe into the propulsor and using the propulsive jet to directly compensate the viscosity-induced momentum deficit in the wake field behind the airframe. This principle of BLI and WF propulsion integration has been known for a long time in the field of marine propulsion, where often submersible, streamlined bodies such as torpedoes and submarines are configured with a single wake-ingesting propeller on the central axis. As discussed in References [71]–[74] dealing with naval applications, this tends to maximize propulsive efficiency. As will be outlined, for commercial airborne applications this engine integration strategy has not been realized yet.

In classic aircraft propulsion system installation the airframe momentum deficit is balanced by a locally introduced excess amount in momentum provided by the propulsive jet of the power plants. The kinetic energy excess in the jet represents a source of mixing losses. As described in Section 2.2, the common strategy to reduce these losses and thereby improve propulsive efficiency has been over the past decades to reduce the engine specific thrust via growing values of BPR. While the associated increased mass flow through the propulsor allows for lower nozzle exit velocities, the previously described integration issues increasingly complicate further significant improvements. Now, in a more closely coupled airframe propulsion arrangement, the airframe momentum deficit may be compensated directly using the jet of a specially installed propulsor ingesting and reenergizing a fraction of the airframe BL, thereby giving scope to significantly reducing flow dissipation [75]. As a net effect,

[6] In case electric energy storage is disregarded, this power train option is referred to as a (partial) turbo electric drive [330].

ideally a reduction in propulsive power is achieved. Due to the large share of wetted surface area, the fuselage of transport aircraft is most attractive for the application of WF by means of BLI. In Section 2.4, an overview of configurations considered for BLI is given, while in Chapter 3 a theoretical discussion of the effects will be provided.

In addition to the aero-propulsion related advantages offered by BLI and WF, a number of beneficial effects are expected from realizing an increased engine-airframe coupling. One of the benefits rooted in the distribution of power onto several propulsors refers to the feasibility of realizing very low specific thrust configuration while yielding acceptable propulsor diameters and retaining the efficiency level of large core engines. Besides inherently lower jet velocities due to low specific thrust propulsors, these configurations may support additional reduction of external noise through embedding the engines or using the airframe to shield and divert the noise emission. In case of hybrid-electric power train concepts the decoupling of the energy-to-power and power-to-thrust conversion process allows for increased freedom to synergistically arrange the power and thrust producing devices, thus contributing to making novel morphological options practically feasible. The strategic positioning of propulsors and operation in terms of vectored or differential thrust may give scope to novel options for decreasing or even eliminating control surface areas intrinsic to current configurations [59]. Beyond that, structural weight and wetted area savings are often connected to integration solutions facilitating partial or full omission of elements of classic propulsion installation such as pylons and nacelles. An example refers to semi-embedded engines in BWB layouts [76].

Apart from the outlined favorable effect, a number of challenges arise from highly integrated propulsion airframe configurations. A primary challenge of BLI propulsion is associated with the BL-induced spatial non-uniformity in the flow properties entering the propulsor. The distorted flow field may have a pronounced effect on fan efficiency and stability with regards to its susceptibility to compressor stall [77], and on the fan's aero-mechanical characteristics [78]. In particular, semi-embedded engine arrangements often require dedicated passive or active flow control measures to counteract adverse secondary flow phenomena and to maintain acceptable fan stability margins [79]–[81]. As a result of the ingestion of the low-momentum BL flow, the propulsor inlet condition is characterized by reduced momentum flux compared to freestream stagnation conditions [82] and therefore freestream total pressure recovery ratio is typically impaired [83], [84], thus requiring careful aerodynamic shaping of the associated structures. System architectures with remotely placed propulsors incur losses along the transmission chain that need to be balanced against any improvements. Challenges may arise in the positioning of multiple laterally arranged propulsors in order to ensure sufficient redundancy in case of uncontained engine failures. Appropriate thermal management, control of vibratory excitations and suppression of noise are exemplary challenges connected with embedded engines.

In Figure 2.1, the key airframe-propulsion interactions are compared and contrasted between conventional and more integrated systems using a schematic representation. In the traditional setup (left part of Figure 2.1), propulsion system performance, weights and external (i.e. airframe) aerodynamics affect the airframe performance and are fed back as net thrust requirements. In more integrated designs,[7] external aerodynamics and net thrust are directly influenced by each other (symbolized by the double arrow in the right part of Figure 2.1), since flow entering the propulsion system has been interacting with the upstream airframe surfaces. As important aspects, the aerodynamic characteristics of the body are modified due to the presence of the WF propulsor, the low-momentum inflow induces a non-uniform flow pattern and intake pressure recovery is penalized. From a performance prediction point of view, an important characteristic of highly integrated propulsion is linked to the aerodynamic and propulsive forces no longer being clearly separated as in conventional

[7] The propulsor and the airframe may be subsumed under the term "propulsion-airframe integration".

propulsion system integration. Therefore, a methodological adaptation of the assessment framework is required to account for these circumstances (see Chapter 3).

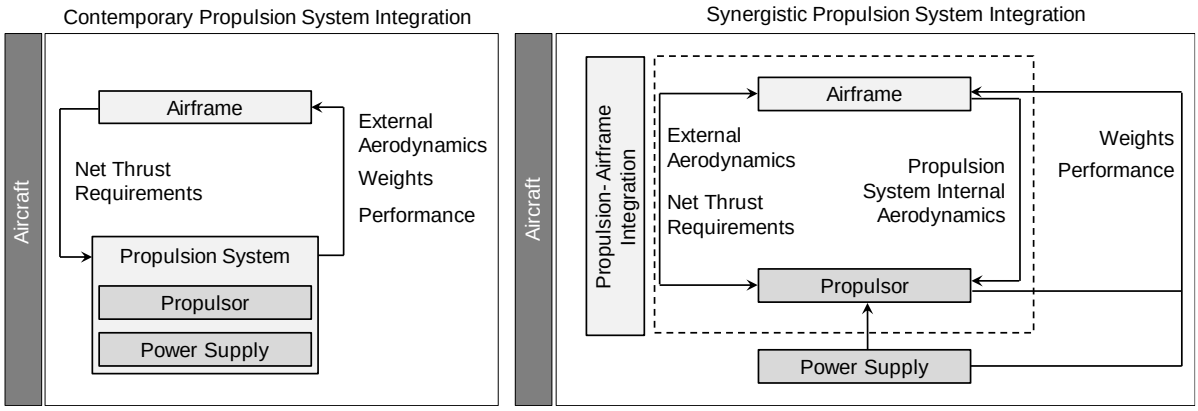

Figure 2.1: Schematic representation of the propulsion-airframe interfaces in contemporary (left) and highly integrated propulsion system integration (right)

The following section provides a brief historical overview of previous research on tightly-coupled propulsion airframe integration with special emphasis placed on the prospects of using BL air for propulsion.

2.4 Research on Boundary Layer Ingesting Propulsion System Integration

The exploration of the beneficial effects of BLI and WF propulsion dates back to the first half of the 20th century. Over the years, a multitude of theoretical, experimental and numerical studies have been conducted with varying levels of fidelity covering a broad range of applications, aircraft morphologies, propulsion system installation options and system architectures. While the majority of early investigations were elementary studies exploring the feasibility of adapting the beneficial phenomena known from marine propulsion to airborne systems, studies of the recent past have acknowledged the potential of BLI and WF to significantly improve aircraft vehicular efficiency.

Perhaps the first theoretical treatise considering the utilization of BL air for aircraft motive power was conducted by Heppner in 1944 [85] as part of a study conducted at the former aero-engine company Armstrong Siddeley Motors Ltd.[8] Here, the theoretical potential of airframe BL suction and WF was derived analytically. As a key result, it was stated that an energetic benefit exists in using sucked in BL air to reduce the excess velocity needed for compensating the drag-induced momentum deficit in the wake, rather than to balance the drag by expelling air from a freestream-installed propulsion system. A further aircraft-integrated analysis was conducted by Smith and Roberts in 1947 [86]. Different from Heppner, the intention of sucking in BL air through slots placed at different positions along the airframe was to delay the transition of the laminar BL and thus to reduce skin friction drag. As a main result, it was established that the fuselage is most beneficial for sucking due to the extremely low-energy BL profile on the aft portion, thus motivating arrangement of suction slots here. Lynch [87] conducted an analytical wake momentum balance on a generic body-propulsion arrangement, where a turbojet engine ingested parts of the fuselage BL flow, cf. also Reference [88]. For an existing turbojet, a minor efficiency improvement was determined. Similarly early analytical studies on WF propulsion were published by Küchemann and Weber [89], Betz [90] and Douglass [91].

[8] A patent with reference to fuselage wake filling propulsion system integration was filed by Heppner in 1941 [331].

A novel arrangement for fuselage BL control and propulsion was proposed by Goldschmied [92]. Starting in the 1950's, a series of analytical and experimental studies of axisymmetric bodies featuring a circular BL suction slot in the aft section were conducted including airship [93] and naval applications [94]. While initially tested configurations were unpropelled, later versions were more adapted to a realistic vehicle design and also included an internal compressor sucking in the BL air and expelling it out at the rear of the body[9] [95], thereby benefitting in addition to a pressure drag reduction from the WF effect. In some of the studies, also an empennage and wing were added to represent a General Aviation layout. The reported benefits ranged from 40% to 60% total aircraft power reduction compared to existing General Aviation aircraft [95]. However, recently conducted numerical [96], [97] and experimental [98] studies were unable to fully reproduce the significant benefits claimed in the original publications of Goldschmied.

Inspired by the work of naval architects, theoretical discussions about adopting this technology also for airborne applications were conducted by Smith [99]. He applied an actuator disk model suitably extended to account for radially varying flow properties to model a wake ingesting axisymmetric unducted propulsor assuming incompressible flow and ambient static pressure at the inlet. The theoretical power saving potential between the propulsive power without and with wake ingestion was derived as a function of wake shape parameters and quantified using the initially introduced Power Saving Coefficient (PSC). Similar to experience with marine propulsion, it was noted that in the wake ingesting case, based on the employed bookkeeping scheme where the control volume encompasses just the propulsor with the wake flow at the inlet, a propulsive efficiency of greater than unity was achieved, motivating the use of a "propulsive coefficient" instead. It was followed that for realizing maximum power savings the propulsor should be sized to ingest as much of the wake fluid as possible and should be installed at a position where it can entrain the fluid before the wake has flattened due to dissipation. In addition, greatest power savings were calculated to occur if the wake velocity is restored to uniform free stream value.

Recently, experimental proof of the basic power saving potential of WF propulsion system integration was established for generic bodies of revolution by means of wind tunnel test campaigns. In these experiments, the propulsor was arranged in close proximity to the aft end of the investigated bodies. The French research agency ONERA conducted low-speed wind tunnel test campaigns to determine the effect of ingesting the wake of a generic body of revolution into a ducted fan [100], [101]. The propulsor position was axially and laterally adjustable in order to measure the effects of ingesting different fractions of the BL flow. As an important result, at a free stream Mach number of 0.20, a power saving of up to approximately 25% was determined at an equilibrium condition relative to the power required in a case of no wake ingestion. Similarly, at Delft University of Technology an axisymmetric body was tested in the wind tunnel. It was observed that placing the propeller coaxially downstream of the body at the minimum feasible distance afforded a shaft power reduction of 18% at axial force equilibrium [102].

As a recapitulation, different strategies have been pursued for BLI and WF regarding the aircraft morphology ranging from conventional TaW designs to BWBs. While for BWBs the installation of semi-buried engines on the upper body surface was found to be most commonly pursued, for TaW layouts the BLI/WF propulsors can be conceived at different locations. Morphological solutions for application of fuselage BLI to a TaW design will be discussed in detail in the subsequent sections. A comprehensive compilation of additional, more exotic SPI concepts was presented by Yaros *et al.* [103].

[9] This configuration is commonly referred to as a „Goldschmied propulsor".

2.4.1 Synopsis of Selected Case Studies

In the following, a selection of existing studies focusing on BLI and WF and, more specifically, with application to the fuselage are reviewed, which were judged as relevant for the context of the present work. The studies cover different morphological solutions of the general TaW layout.

2.4.1.1 MIT D8 platform

A recent illustration of examining the potential of fuselage BLI and WF constitutes the D8 platform investigated by Massachusetts Institute of Technology (MIT)[10] in the frame of the NASA N+3 program. The concept features a wide dual-lobe fuselage cross section in conjunction with a twin "pi-tail" and is sized for a typical narrowbody mission (180 passengers and 3,000 nm design range [104]). Two parallel turbofan engines are flush-mounted in the aft end of the upper fuselage surface entraining a fraction of the fuselage BL. For reasons of evading the risk of fratricidal engine damage, the core engines are installed in a tilted and reversed arrangement requiring significant ducting effort [46]. The concept has been subject to a series of multidisciplinary investigations. During the first phase of the investigation, a fuel burn reduction of 36% compared to the Boeing 737-800 was predicted for the D8.2 design incorporating state-of-the-art technology [105].[11] Within the series of subsequently performed development steps, the largest contributor to the announced fuel saving potential was associated with the engine installation enabling the ingestion of approximately 40% of the fuselage BL. As a further major contributor, slower en route speed schedules (reduced to M0.72) were adopted allowing for reduced wing sweep and hence lighter structures. Subsequently conducted high-fidelity numerical analyses [106] and subscale wind tunnel test campaigns [107] were performed demonstrating an 8.6% saving in mechanical flow power directly attributable to the BLI/WF effect relative to a morphologically and technologically similar configuration with fuselage-podded engines. Later revisions of the design retained typical cruise Mach numbers (M0.78) and contemporary airport compatibility constraints [108].

2.4.1.2 ONERA NOVA and ONERA/Airbus Nautilius

A similar configuration as the D8 platform has been subject to an ongoing investigation performed by ONERA as part of a design exploration study entitled NOVA ("Nextgen Onera Versatile Aircraft") [109]. One of the concepts sized for a single-aisle, medium-range mission (180 PAX, 3,000 nm design range) with a cruise Mach number of 0.82 features two UHBR turbofans installed in a semi-embedded way laterally at the rear fuselage ingesting approximately 40% of the fuselage BL at cruise. The configuration draws advantage from a reduced wetted area due to the removal of the pylon. As a main result from an initial aero-propulsive investigation, it was found that a power saving of 5% could be achieved at cruise condition relative to a similar, podded configuration. With intent to increase the share of the ingested BL, a derivative of the NOVA configuration has recently been studied by ONERA in collaboration with Airbus featuring a setup where two parallel installed propulsors encircle the very aft portion of a split fuselage [110]. The front part of the fuselage and wing was retained while initially the empennage was neglected. For this "Nautilius" concept, an uninstalled power saving of 12.5% to 14% has been reported.

2.4.1.3 Airbus Group Innovations E-Thrust

In 2012, Airbus Group Innovations, Rolls-Royce and other partners formed a consortium to conjointly conduct research within the Distributed Electrical Aerospace Propulsion (DEAP) project [111]. As an initial configuration, the "E-Thrust" platform was presented aiming at the regional segment [112]. As a key characteristic of the investigated system architecture featuring superconducting components, six

[10] in cooperation with Aurora Flight Sciences, Aerodyne Research and Pratt & Whitney, a United Technologies Company

[11] Upon application of a set of radical technological assumptions expected to occur in the 2035-2040 timeframe, a fuel burn reduction of 71% was predicted compared to the 737-800 aircraft [104] and exemplified by the D8.6 design [105].

electrically driven fans are distributed in two arrays along each wing. A turboshaft engine is foreseen to provide the electrical power absorbed by the propulsors and recharges the energy storage. With intent to reduce the momentum losses in the aircraft wake, the fans ingest parts of the fuselage and wing BL. As part of the research, the fan design is specifically optimized to cater for the non-uniform inflow conditions experienced in the BLI arrangement.

As an additional configurational approach to fuselage WF propulsion integration for transport aircraft, the Propulsive Fuselage Concept will be introduced in the next section including a review of previous research specifically related to this field.

2.4.2 The Propulsive Fuselage Concept

A promising configurational arrangement for synergistic propulsion-airframe integration constitutes a configuration exhibiting a propulsor encircling the aft of a cylindrical fuselage. Initially proposed by Steiner *et al.* [113] in the context of transport category aircraft, such a Propulsive Fuselage Concept (PFC) has been subject to a number of investigations in the past. It will be derived later in Section 3.2 that this integration option particularly benefits from the coupling of aerodynamics and propulsion system performance. This is connected to the large share of wetted area associated with the fuselage that is available to BLI and WF. Different from arrangements with discrete engines installed in a circumferential or semi-embedded way, for such a configuration the full annular wake-filling potential can be utilized using a single propulsor. Apart from an inherently large BLI potential, an additional benefit is rooted in the shape of the BL-induced inflow distortion. For cruise, distortion can be expected to be widely limited to a non-uniformity in radial direction, while the previously discussed configurational solutions are characterized by distortion patterns exhibiting strongly coupled non-uniformities in radial and angular direction. Different from spanwise distributed propulsors, the PFC does not require a separate performance analysis of the flow conditions of multiple BLI propulsors.

General morphological options in principle include non-conventional fuselage shapes such as “double-bubble” or twin-fuselage arrangements [114]. However, a conventional fuselage and cantilever wing layout is considered most appropriate for evaluating the basic principles of WF propulsion integration, thereby dispensing with the need to separate the effects attained from WF and the ones resulting from the airframe morphology itself. Most studies consider a T-tail design as the most suitable way of integrating the empennage. Similarly, regarding the BLI propulsor, different architectures are generally conceivable including ducted and unducted devices [115]–[117]. As outlined in Reference [118], a ducted, single-rotating fan is deemed most appropriate due to the significantly reduced mechanical complexity for structurally integrating the propulsive device. A ducted propulsor is favored over an open rotor layout for reasons of noise shielding and robustness against tail strike events. While in principle power train options featuring elements of electrification (e.g. partial turbo-electric[12] architectures) can be envisaged (cf. References [49], [119]–[123]), as an initial step towards the basic characterization of the PFC a gas turbine powered fuselage propulsor is considered in the present thesis. The utilization of well-established turbo component technology is considered to reduce the level of uncertainty emanating from the necessity to impose several assumptions for the technological advancement of electric power train components.

Regarding the overall propulsion configuration, different layouts have been proposed. While in References [113], [119], [124] a fuselage propulsor was used as the sole propulsive device, most studies retain contemporary redundancy requirements of transport category aircraft and therefore consider arrangements with a fuselage propulsor in conjunction with conventionally installed power

[12] The term “partial turbo-electric” refers to a setup of turbo engines supplying electric power while also providing net thrust [330].

plants. In the investigated configuration, the fuselage propulsor is powered by the LPT of a Geared Turbofan (GTF) engine via a reduction gear system. Air supply to the core engine may be realized using an eccentrical s-duct intake integrated in the bypass duct. A schematic view of a possible arrangement of the aft-fuselage section is given in Figure 2.2. The longitudinal arrangement of the engine systems needs to be tailored to ensure adequate disk burst corridors with respect to critical functions of the tail and the fuselage pressure vessel. Initial guidelines can be found in previous publications, cf. References [114], [118].

In the following, a short chronological overview of previous research connected to the PFC is presented, exemplified by selected case studies.

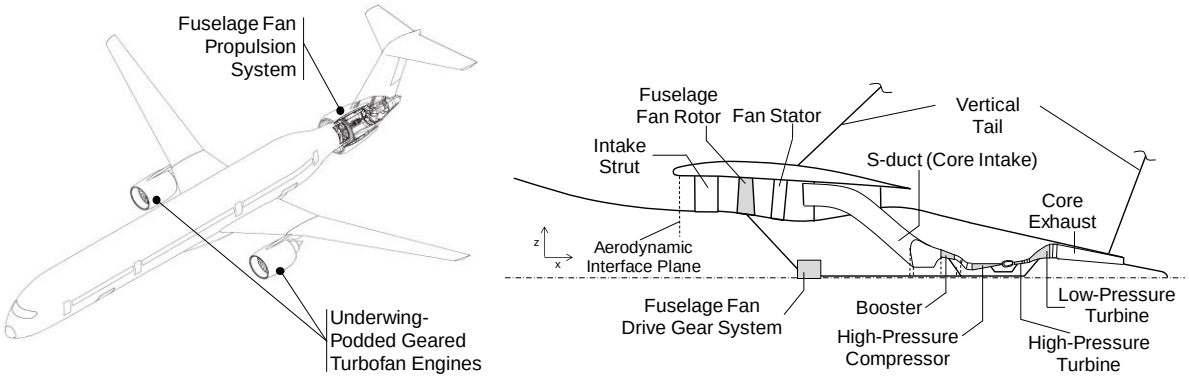

Figure 2.2: Principal arrangement of a typical mechanically powered Propulsive Fuselage Concept (left, adapted from Reference [118]) and schematic view of fuselage fan propulsion system (right, adapted from Reference [27])

2.4.2.1 Steiner et al. (2012)

Steiner *et al.* [113] performed a design space exploration and systematic down-selection exercise of various BLI propulsion integration options. Based on a comprehensive qualitative down-selection process, the general PFC configuration featuring a single Fuselage Fan (FF) device was identified as particularly advantageous. The BLI potential was estimated based on simplified geometric relations and wetted area considerations. While the considered PFC candidate design exhibited shortcomings with regards to a number of operational attributes, a significant potential for efficiency improvements was recognized emanating from the large BLI/WF potential. When applied to a short-range passenger transport with 900 nm design range and cruise at M0.75 employing a universally electric system architecture and targeting EIS of 2035, an increase in energy specific air range of up to 9.4% compared to an advanced reference aircraft was identified.

2.4.2.2 Airbus Group Innovations VoltAir (2012)

Stückl *et al.* [119] performed a design space exploration and sizing study of an electrically powered regional aircraft with a single aft-fuselage BLI propulsor and high-temperature superconducting system architecture. Upon assumption of a gain in propulsive efficiency of 5% due to BLI and incorporation of a set of advanced annexed technologies, a 25% potential improvement in energy efficiency was obtained relative to a fully electrically powered concept utilizing conventional propulsion system installation.

2.4.2.3 Boeing SUGAR Freeze (2012)

As part of the SUGAR project conducted by Boeing under NASA contract in collaboration with GE Aviation and Georgia Institute of Technology, the aircraft-level impact of a series of advanced technologies was investigated [49]. In Phase II of the project, a potential EIS scenario in the 2040 to 2050 timeframe was addressed.[13] The configurations investigated comprised high-aspect ratio, strut-

[13] "N+4" timeframe in NASA terminology

braced wing designs with payload-range requirements similar to a Boeing 737 class aircraft (3,500 nm at 154 passengers), however, with a cruise Mach number of 0.70. In the variant "SUGAR Freeze Hybrid BLI", an aft fuselage-installed ducted fan is driven by an electric motor in conjunction with two underwing-podded direct drive turbofans. Electrical power is produced through a gas turbine topping cycle featuring a solid oxide fuel cell running on liquefied natural gas. For a 900 nm mission, a reduction in block fuel of 8.5% relative to the baseline "SUGAR Freeze" was found.

2.4.2.4 Seitz and Gologan (2013)

Based on semi-empirical methods, Seitz and Gologan [124] presented unified bookkeeping standards for BLI and conventional propulsion integration. For the design investigation of a configuration exhibiting a single FF device, an air transport task typical for a widebody application, specifically 4,800 nm design range at 300 passenger design payload, was selected. Initial parametric design studies regarding the isolated FF performance and at the vehicular level were conducted assuming ideal WF and the entire fuselage momentum deficit to be utilized for WF purposes. A peak improvement of approximately 12% in Energy Specific Air Range was found relative to the reference aircraft equipped with conventionally installed podded turbofans.

2.4.2.5 European Commission FP7 DisPURSAL (2013-2015)

Within the frame of an EC funded research project "Distributed Propulsion and Ultra-high bypass Rotor Study at Aircraft Level" (DisPURSAL) [114], an initial multidisciplinary low-TRL design study for fuselage WF propulsion integration for transport aircraft was conducted. As a result of a down-selection process, a widebody, medium-to-long range, TaW design featuring an aft fuselage-installed fan driven by a turbo core engine in conjunction with two underwing-podded GTFs was selected, where the fuselage-installed power plant was primarily intended to serve the purpose of WF, while the podded engines delivered residual thrust. Upon incorporation of numerically computed aerodynamic data, as a key result, a nominal 9% reduction in block fuel was identified for the design mission compared to an evolutionary improved conventional reference aircraft targeting an identical potential EIS of year 2035.

2.4.2.6 NASA STARC-ABL (2016)

In 2016, a study of a narrowbody aircraft featuring a turbo-electrically driven aft-fuselage propulsor was published by NASA [121] assuming an EIS in the 2035 timeframe. In the investigated arrangement dubbed "Single-aisle Turboelectric AiRCraft with an Aft Boundary Layer propulsor" (STARC-ABL), the partial turbo electric propulsion system architecture consists of generators attached to two underwing turbofans to extract power from the low-pressure spool used to power the aft-fuselage fan. The BLI aerodynamics were estimated based on previous CFD-simulated BL profiles from a bare fuselage geometry taken from the SUGAR studies, which were averaged for processing in power plant performance calculation. In a design revision "Rev. B2.0", a block fuel reduction of 3.4% was calculated on the 3,500 nm design mission and a 2.7% reduction was predicted on a 900 nm stage length [125].

2.4.2.7 European Commission H2020 CENTRELINE (2017)

With intent to provide an experimental proof of concept of the PFC, the EC-funded research project CENTRELINE commenced in 2017. As an application, a wide body long-range scenario characterized by a 6,500 nm design range and a cabin capacity of 340 passengers was selected. Based on preliminary methods, a block fuel reduction of 11.3% on the design mission has been initially predicted [123] compared to an equally advanced reference aircraft with a potential EIS year 2035.

Further configurational suggestions for integrating fuselage-encircling propulsors can be found in the literature, cf. References [117], [126]–[128].[14]

2.4.3 Existing Methodological Approaches

As can be observed from the literature review discussed in the previous sections, various studies have been conducted aiming at the investigation of BLI for transport category aircraft. The effects of BLI have been considered based on different methodological approaches and varying levels of fidelity. Accordingly, the current state of research may be clustered into several categories depending on the methodological approach and expended computational effort, which is presented in the following sections sorted in ascending order of required numerical simulation demand.[15]

2.4.3.1 Analytical/semi-empirical methods

Several studies have been identified were the impact of BLI/WF was estimated by directly applying constant increments to sizing parameters based on initial assumptions or values from the literature, cf. e.g. References [61], [117], [119], [129]–[131]. For first order assessments, a representation of the BL profile is frequently assumed based on empirical BL correlations such as done in References [132]–[135]. Frequently, power-based profiles are employed. Based on averaging, mean inlet conditions of BL ingesting propulsors are obtained as inputs for propulsion performance models. It is recognized that many of the studies based on lower-fidelity or analytical aerodynamic methods tend to suffer from simplifying assumptions. This is observed independently from the accounting scheme used. Commonly encountered assumptions include e.g. BL representation using simple empirical correlations such as flat plate approximation (e.g. [132]–[139]), thereby neglecting the streamwise pressure gradient imposed on the BL flow along the body. As noted by Thurston and Evenbar [73] in the context of naval propulsion, the implicitly made assumption of non-intrusive behavior of airframe and propulsor is problematic in a sense that the presence of the propulsor will in fact influence the flow field of the body whose BL is ingested. In addition to changing the body's pressure field and thus pressure drag, the propulsor suction effect will alter the BL velocity gradient at the wall and hence the localized skin friction drag. Since this effect is dependent on the flight conditions and thrust setting, a strong coupling of propulsor performance and fuselage aerodynamics can be expected throughout the flight envelope. The often-encountered assumption of incompressible flow lacks applicability to the transonic regime of transport aircraft applications, thereby limiting the substantiation of conclusions with regards to the aircraft-level potential.

Quasi-analytical aerodynamic methods constitute an intermediate step between analytical or semi-empirical and higher order numerical methods. Pelz *et al.* [136] applied potential theory and the integral BL equations to analyze the impact of BL properties on an unducted propulsor immersed in the BL flow. The fuselage was approximated as a flat plate assuming incompressible flow. Kaiser *et al.* [115] presented a set of quasi-analytical aerodynamic methods for the calculation of the characteristics of an axisymmetric body of revolution with an unducted BL ingesting propulsor working in compressible flow. The BL properties were computed using different empirical models, while the propulsor was simulated using a superposition of a compressible actuator disk model and a blade element momentum theory based propeller code. Similarly, during the initial sizing activities of MIT's D8 configuration, a combination of potential flow calculations and axisymmetric formulation of the integral BL equations was used to describe BL properties [84]. It is recognized that quasi-analytical methods applicable to

[14] For completeness sake, examples of existing aircraft featuring coaxial aft-fuselage propulsion integration, which, however, not primarily focus on exploiting BLI/WF, comprise the Curtiss XP-55 prototype (1942), the Douglas XB-42 (1944), the RFB Fantrainer (1978) as well as the business aircraft LearAvia LearFan 2100 (1981) and Grob GF200 (1991).

[15] Additional categorizations of modeling approaches limited to aerodynamic aspects can be found in References [161], [164].

the targeted application have thus far been restricted to unducted propulsors, simple geometries and strictly subsonic flight Mach numbers.

2.4.3.2 Investigation of uninstalled aero-propulsive coupling effects

Utilizing higher-order numerical methods for the calculation of the aerodynamics of external surfaces has been the subject of a multitude of investigations. Here, typically Reynolds Averaged Navier Stokes (RANS) methods are utilized. The full-annulus aerodynamic performance of the propulsor is typically not fully resolved in the CFD calculation. Instead, the problem is decomposed and the sub-domains are separately processed using different fidelity levels. As such, within the numerical simulation, fan performance has been represented using different approaches including basic thermodynamic cycle analysis working on averaged inlet properties as well as different actuator disk or body-force formulations. As an example, studies connected to ONERA's NOVA and "Nautilius" concepts used three-dimensional RANS methods and evaluated the applicability of different actuator disk and body-force formulations [109], [110]. Gray *et al.* conducted aerodynamic shape optimization studies of a PFC layout similar to the STARC-ABL concept, where a 2D [140], [141] and 3D [142] RANS solver was coupled to a fan cycle model in an optimization environment. The fan model processed averaged values of the inflow properties. Apart from ducted BLI fans, also unducted propulsors have been considered [116], [143]. Several numerical studies were found limited to investigating the aero-propulsion characteristics without considering important power plant installation effects and repercussive implications regarding the impact on aircraft dimensions, external drag, propulsion system characteristics, component weights and aircraft balancing, as well as flight performance, cf. e.g. References [83], [109], [110], [116], [140]–[150]. This inhibits parametric variations of the integrated characteristics, thus possibly impeding a proper identification of optimality at the vehicular level and making it difficult to evaluate the performance from a true block energy perspective.

2.4.3.3 Aero-numerical simulations for a fixed aircraft design case

Significant effort has been expended in numerical studies employing CFD methods for the examination of airframe and propulsor characteristics under presence of BLI. As a result of the computational effort, it is observed that with growing levels of numerical fidelity the practical feasibility of conducting integrated studies at aircraft level becomes increasingly impaired. As such, many studies were identified, where only for a fixed design setup CFD simulations were conducted, see References [49], [129], [151], [152]. As an example, in Reference [108] related to the latest design iteration of the D8 configuration, from a CFD simulation the fraction of momentum deficit ingested into the propulsive device was obtained and kept constant during integrated studies. Marien *et al.* [153] derived a representative ingested BL fraction as well as intake momentum deficit from a separately conducted CFD study described in Reference [154] and retained that value. A similar assumption was made in Reference [155] dealing with a configuration similar to STARC-ABL. In some instances, possibly due to unavailability of corresponding data, a disconnection has been observed between the geometry investigated in the numerical setup and the configurational properties aircraft sizing is based on. Specifically, frequently CFD data has been employed from previous or other projects, where similar yet in detail different configurations were investigated (cf. e.g. References [49], [118], [121], [124], [129]), thereby disregarding the aero-propulsive interaction effects between the propulsor and the flow field ingested and inhibiting the geometric optimization of the associated contour shapes.

2.4.3.4 Detailed analysis of propulsor aerodynamic and aero-mechanical characteristics

Great advances in design, optimization and performance prediction of propulsors in presence of non-uniform inflow conditions using high-fidelity numerical methods have been identified, primarily for arrangements with intrinsically high levels of distortion. As a result of the large computational effort of full-annulus calculations, these are typically conducted "off-line", i.e. as specialized studies and not as part of the overall aircraft sizing process and have targeted the minimization of the detrimental impact of distortion on fan efficiency and the implications on the operational behavior, especially fan

stability. Designing a distortion-tolerant fan has been the subject of a variety of recent investigations. Details are described e.g. in References [156], [157].

2.4.4 Characterization of Research Needs

From the literature survey on the research status on BLI/WF propulsion system integration it is recognized that thus far conducted airframe integration studies utilizing high-fidelity and integrated representation of BL characteristics including resolution of mutual interaction effects have been widely limited to unconventional aircraft configurations such as BWB layouts [81], [158], [159]. This makes it difficult to assess the true effect of WF propulsion system integration for a contemporary aircraft layout. In contrast to unconventional airframe morphologies, the PFC allows for direct comparison with conventional technology and does not require several comparative cases. With regards to the PFC layout, it has been established that for the mapping of the aero-propulsive effects often strongly simplified assumptions or non-conformal aero-numerical data has been applied. Conversely, the use of high-fidelity aero-numerical analysis has been used for aerodynamic shape optimization without considering aircraft-integrated characteristics. In this respect, the highly automated and simultaneous optimization of a multitude of shaping parameters associated with fuselage and nacelle contouring on an isolated aero-propulsive level is considered to limit the knowledge gain on the overall system level, thus preventing the identification of truly optimal vehicle solutions.

These findings are graphically summarized in Figure 2.3. The abscissa is correlated to the extent aero-propulsive analyses have been conducted, which is clustered into seven categories, while the extent aircraft-integrated analyses have been performed is categorized in four groups shown on the ordinate. As an initial indication of the frequency of certain combinations, the marker size correlates with the number of publications identified for each specific value pair. Hyperbolic contours indicate the overall

	Extent of Aero-Propulsive Analysis	Extent of Aircraft-Integrated Analysis
0	Assuming BLI fractions; applying increments to account for BLI/WF	Isolated power plant study
1	Analytical representation of BLI via wake shape; semi-empirical BL representation including scaling of profile	Scaling aircraft characteristics from existing data; use of trade factors
2	Scaling of existing CFD data to considered problem; assuming applicability of CFD data irrespective of differences in configuration	Consideration of single-point aircraft design
3	De-coupled airframe and PPS CFD analysis	Aircraft-integrated parametric studies
4	Coupled airframe-PPS analysis, 2D	
5	Coupled airframe-PPS analysis, 3D	
6	3D fan aerodynamic and/or aero-mechanical analysis	

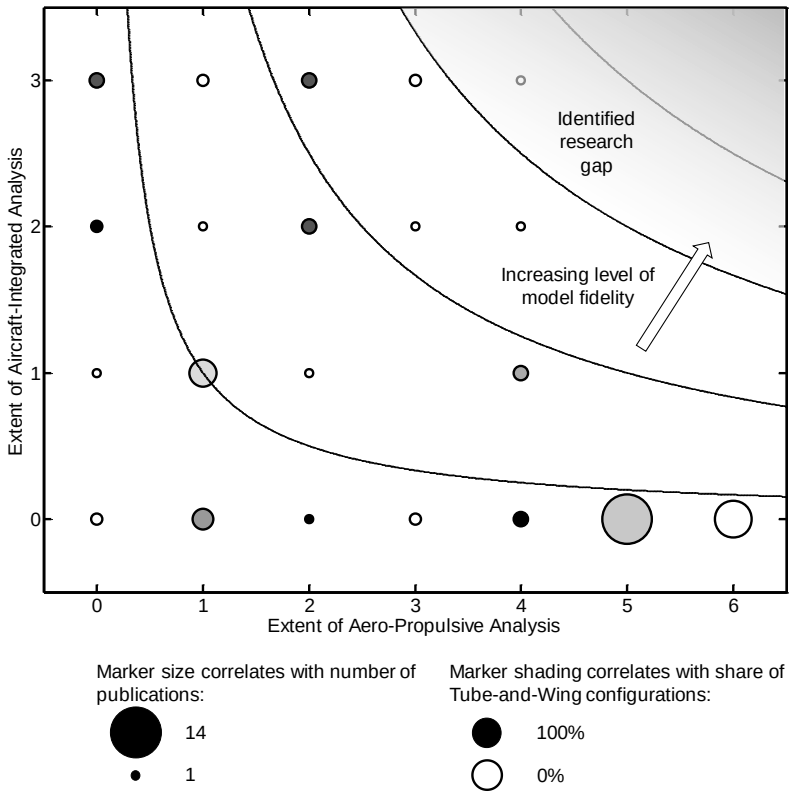

Figure 2.3: Visualization of current research state in BLI/WF propulsion system integration

fidelity levels of the methodology. The marker shading denotes the relative share of TaW concepts per value pair.

Based on the literature survey, the need for the development of a consistent set of methods for the conceptual design and analysis of synergistic wake-filling propulsion system integration via BLI has been identified. Moreover, it has been recognized that the highly integrated nature of the considered application necessitates an assessment at aircraft level. The decision regarding the way the propulsion-airframe interaction is resolved has to be balanced between expending adequate computational effort and thus sufficient flexibility with regards to parameter variations, and the assurance of appropriate accuracy levels. Judging from the literature scanned, the general practicality of using higher order numerical, i.e. CFD-based aerodynamic methods in combination with an actuator disk theory-based propulsor simulation to model the aero-propulsion impact has been acknowledged. In this respect, for the considered PFC application featuring a widely axisymmetric fuselage layout, axisymmetric RANS methods based on a two-dimensional geometry representation are considered a suitable trade-off between accuracy and fast result generation within the frame of low-TRL conceptual studies. Yet, no computational concept has been detected allowing for the efficient incorporation and consistency assurance of parameterized aero-numerical data within conceptual aircraft and propulsion system sizing, and the coherent representation of design and off-design characteristics in the context of BLI propulsion. Taking gas turbine based applications, no studies have been identified where the impact of fuselage wake filling propulsion system integration on engine performance and eventually on the aircraft-integrated characteristics is propagated in a consistent manner. However, in case of BLI, the significant deviation from the clean inflow will trigger changes on power plant key characteristics and accordingly cycle optimality settings. Appropriate interfacing and bookkeeping strategies need to be applied to ensure consistent incorporation of aero-numerical data into a superordinate conceptual propulsion system and aircraft framework.[16] In this respect, compatibility with conventional practices for sizing and performance as well as typical figures of merit should be pursued to ensure comparability to a suitable reference configuration, thus allowing for identifying the integrated potential of BLI/WF. In order to determine optimum parameter settings during the integrated aircraft sizing process and to quantify the aircraft-level characteristics in terms of typical figures of merit such as mission block fuel or emissions, the methodological framework needs to capture the implications with respect to system and aircraft-level aerodynamics, weights, propulsion system design and performance including the respective cascading effects. Here, the ability for the parametric mapping of aero-propulsive interaction effects at design and off-design conditions has been found a critical prerequisite to enable – beyond the calculation of point performances – trade studies, sensitivities and mission properties, thereby allowing for identification of optimality at aircraft level. This research gap is illustrated by the shaded region in Figure 2.3. Fast-responding model behavior should be pursued to ensure enhanced design space exploration capability and correspondingly quick knowledge gain. Since installation effects from highly integrated propulsion systems are dependent on the specific engine integration approach, these are typically not *a priori* included in system simulation programs. Therefore, a computational framework is required featuring sufficient flexibility for adaptation to unconventional engine installation paradigms and offering the possibility to integrate custom tailored methods.

To summarize, a deficiency in the integrated assessment of propulsion system and airframe has been identified with regards to fuselage-BLI propulsion system integration in aircraft conceptual design. In the following chapters, a methodology for the aircraft-integrated sizing and optimization of fuselage BLI/WF propulsion system integration for transport category aircraft will be proposed and demonstrated.

[16] Reviews of state-of-the-art conceptual design tools for propulsion system and aircraft synthesis can be found in References [309], [332].

3 Principles of Boundary Layer Ingestion and Wake Filling

The purpose of this chapter is to provide a general introduction to the principles of Boundary Layer Ingestion and Wake Filling (BLI/WF). As part of this theoretical discussion, suitable thrust and drag bookkeeping strategies will be discussed and important metrics for system description and the integrated assessment of BLI configurations will be derived. Based on these, a formulation illustrating analytically the impact of multiple propulsion system types on the overall vehicular performance is presented. An initial pre-study utilizing these constructs will serve the purpose of motivating the detailed system analysis and integration studies presented in this work. Moreover, based on a simplified, generic estimation, the relative potential of the targeted PFC configuration compared to alternative advanced propulsion system integration configurations with BLI is estimated.

3.1 Theoretical Foundation and Bookkeeping Standards

For a body immersed in a flow, a mass and momentum balance shows that viscous and form drag manifest as a momentum defect in the wake downstream the body [160, p. 135]. Taking contemporary propulsion system installation, the airframe momentum deficit is balanced by a separately introduced localized excess amount in momentum provided by the propulsive jet of the engine. As in order to obtain positive net thrust a velocity increment between the exhaust jet and the incoming free stream inlet air, V_0, is required, an over-velocity needs to be induced to the propulsive jet (see Figure 3.1, case A). This excess kinetic energy in both the jet and the wake represents a source of loss due to flow mixing. With respect to the propulsive jet, this is reflected in the propulsive efficiency metric measuring the quality of the conversion of jet power to thrust power.

Now, installing the propulsion system in close proximity to the airframe such that a part of the airframe BL is ingested by the propulsor and re-energized affords the following effects [75], [82]: it reduces the kinetic energy expended in the propulsive jet due to smaller over-velocities, and enables direct compensation of the wake-induced momentum defect by filling the deficit using the jet of the propulsor. As a result, less energy is wasted in the combined wake and jet flow, ultimately leading to a reduction in propulsive power demand required for a given streamwise net force, cf. e.g. References [107], [154]. Apart from the conventional propulsion system installation, Figure 3.1 indicates different schematic cases of WF propulsion system integration. For a hypothetical case of ideal WF and no sources of residual airframe drag (not shown), the momentum required to balance the drag corresponds to accelerating the wake flow to freesteam condition yielding a vehicular propulsive efficiency of unity. In a realistic configuration, residual drag emanating from other airframe components as well as lift-induced drag needs to be overcome, which is indicated in Figure 3.1 by an additional increment in momentum beyond the amount solely required for ideal fuselage wake compensation. Therefore, case B shows a configuration, where a portion of the fuselage BL is ingested and re-accelerated, allowing for partial wake cancellation. Comparing the reduced momentum deficit in the wake and jet field to case A elucidates the benefit in vehicular propulsive efficiency over case A. Finally, the generic PFC arrangement indicated in case C ideally allows for 360° ingestion of the fuselage BL and the filling of the entire fuselage wake. As can be seen, a higher recovery of the momentum deficit may theoretically be achieved by this configuration. As described in Reference [124], intermediate solutions

between case A and C constitute an interesting configurational arrangement for a practical application scenario, where the fuselage propulsor serves the purpose of fuselage WF, while conventionally installed propulsors generate residual thrust.

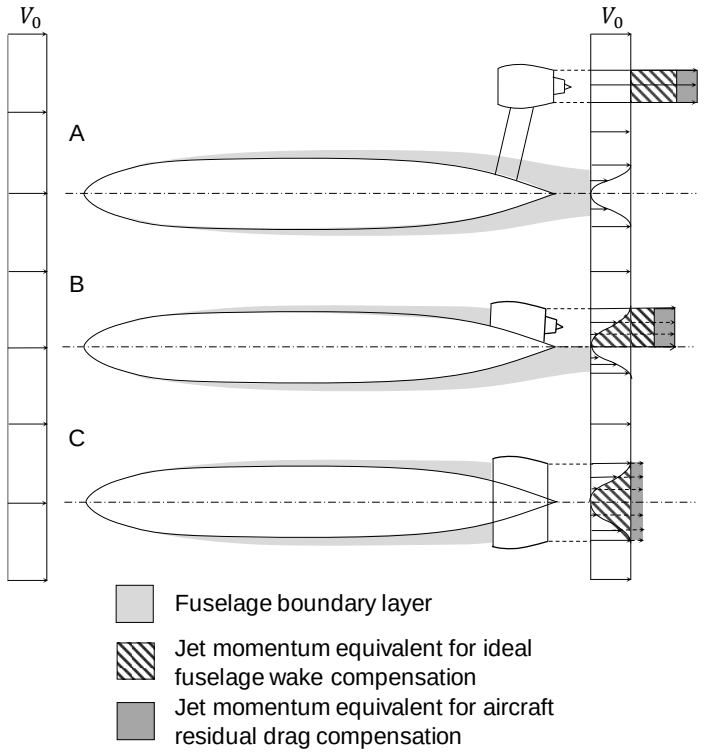

Figure 3.1: Scheme indicating different cases to compensate for the momentum deficit in the aircraft wake, modified from Reference [124]

3.1.1 Overview of Bookkeeping Options

The consistent analysis of highly integrated and conventionally installed power plants requires adherence to a set of common standards and definitions. In particular, thrust and drag bookkeeping tends to become more complicated once airframe and propulsion system are more closely coupled [75], since a portion of the fluid entering and exiting the propulsor has interacted with parts of the airframe. In the past, a variety of approaches has been proposed utilizing different physical accounting principles including momentum, power and exergy [161].

In case of the traditionally experienced weak interaction between airframe and propulsion system, momentum-based bookkeeping has typically been used which allows for the separate evaluation of engine net thrust and airframe drag characteristics. In general, farfield and nearfield approaches can be distinguished for the definition of control volumes [161]. A momentum-based approach was initially applied to WF propulsion system integration by Smith [99], followed by Plas *et al.* [151] for BWB concepts. Further examples can be found in References [61], [81], [83], [109], [133], [162], [163]. For the assessment of a PFC application, Seitz and Gologan [124] proposed a unified bookkeeping standard for conventionally installed and BLI power plants. Specifically targeting the aerodynamic analysis of the STARC-ABL configuration, a momentum-based accounting method was applied in Reference [140] to evaluate the performance of the integrated system.

The Power Balance Method (PBM) recently introduced by Drela [75] is based on the conservation of flow mechanical energy, i.e. the balance of flow dissipation terms and mechanical flow power added by the propulsor. The PBM was applied for several numerical and experimental investigations to

evaluate the benefit of different BLI configurations [147], [158], [159] with primary focus set on fundamental analyses of the flow physics associated with BLI. It can be observed from the literature that utilization of the PBM-based accounting for the analysis of integrated characteristics using CFD data of the entire configuration requires a series of assumptions [161]. The most important one intrinsically stipulated includes that the surface dissipation is unaffected by the presence of the BLI propulsor and that the nacelle surface dissipation is negligible. Moreover, the method has only been found applied to problems where the fan face is located at the trailing edge of the fuselage [161]. In particular, the last assumption is considered problematic for many PFC configurations, where the propulsor intake position is typically in the range of 80 to 95% of the fuselage length. As will be demonstrated in Chapter 4, the nozzle aft-body contributes to the overall fuselage net force. Moreover, direct applicability of the PBM in typical aircraft sizing suites has been found inhibited by the lack of compatibility between the traditional force-based accounting schemes and the power-based terms gained from the PBM. In an effort to address this, adaptations to the original formulation of the PBM were introduced in References [108], [153] in order to translate the power-based methodology to the conventional thrust and drag terminology. As an extension of the PBM, an exergy-based methodology was proposed by Arntz *et al.* [146].

As a recapitulation, it is observed that in case detailed analysis of the loss phenomena (i.e. dissipation effects) within the BL, jet and wake flow is the study focus, methods based on power or exergy balance are useful. Moreover, a recent evaluation of Hendricks [164] recommends to employ power-based schemes in cases where the analysis setup is "uncoupled" or only "weakly coupled", and points out that the necessary input quantities are typically difficult to determine, thus rendering the PBM primarily suitable for investigations where interaction effects cannot be captured in the simulation setup. In contrast to that, for conceptual aircraft studies and aircraft-integrated propulsion system analysis, momentum-based accounting schemes are considered more practical. This eases the handling of BLI installation cases within typical engine and aircraft sizing environments and allows for direct comparative assessment in terms of typical gas turbine performance metrics.

Taking the momentum-based accounting paradigm, the bookkeeping of forces in a BLI/WF arrangement depends on the choice of the control volumes. While the overall aircraft performance is not affected by accounting conventions, the interpretation of the effects on airframe and propulsion system are different and depend on the definition of the control volume boundaries [83], [134]. Two main approaches have been applied in the past and their specific characteristics are e.g. outlined in References [49], [61], [83], [134], [165]. The key difference is rooted in the definition of the airframe and power plant interface. In Figure 3.2, a scheme for control volume (CV) definitions is presented showing on the lower half section a podded turbofan and on the upper half section a turbofan installed on a propulsive fuselage arrangement.

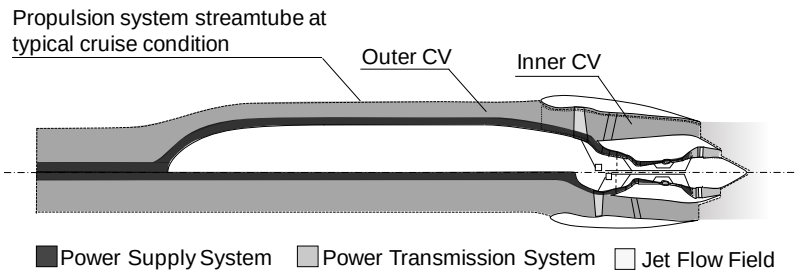

Figure 3.2: Control volume definitions applicable to conventionally installed and propulsive fuselage power plants, modified from Reference [124]

In case of the **inner control volume** convention indicated in Figure 3.2, the boundary between airframe and power plant is located at a plane close to the intake highlight. Thereby, the inflow condition of the

power plant is characterized through a flow of reduced momentum compared to free stream conditions. Consequently, engine ram drag is reduced by an amount equivalent to the fuselage momentum deficit exhibited at this particular interface plane. Different from a conventional installation, at the inlet boundary of the CV the static pressure is not the ambient one but altered due to the pressure field of the body, which has to be considered in the accounting scheme. For the handling of this scheme within gas turbine simulation software, it was proposed in early studies to apply a reduced equivalent free-stream Mach number [83], which, however appears problematic considering consistency in efficiency definitions. When defining propulsive efficiency as the ratio of thrust power to change in kinetic flow energy between the CV inlet and exhaust planes, it can be easily established that values numerically exceeding unity can be obtained utilizing this accounting scheme. This makes it difficult to quantify losses and appears to contradict basic conservation principles. The drag of the upstream body is treated as ideally unaffected. It should be noted that ambiguities may arise when defining the longitudinal position of the interface between the upstream body and the propulsion system, i.e. the plane where the inlet conditions for the propulsion system are defined. This option has been widely used in the literature, cf. e.g. References [61], [81], [99], [133], [149], [163], [166].

In case of an **outer control volume** approach, the CV reaches from free stream conditions far upstream up to the nozzle exit (see dashed boundaries in Figure 3.2). This scheme is consistent with the one typically adopted for turbofan engines [134]. Consequently, the free stream velocity is applied as a boundary condition at the CV inlet. Application of this convention to a BLI configuration reveals that depending on the investigated configuration the propulsor inflow has interacted with parts of the airframe. The momentum deficit developing inside the streamtube due to the BL flow translates into a loss in total pressure, hence yielding reduced intake total pressure recovery ratios [124]. As a key characteristic of this bookkeeping convention, all flow effects occurring inside the streamtube belong to the power plant sizing and performance analysis.[17] In case of conventional (podded) turbofan installation, this refers to ram drag, drag due to intake total pressure loss and scrubbing drag on the nozzle aft-body and cone. Aerodynamic forces occurring outside the streamtube such as inlet additive drag, nacelle lip suction and nacelle form drag are bookkept as part of airframe characteristics and thus impact the engine net thrust requirement [124]. Examination of the BLI arrangement shown in the upper half section of Figure 3.2 reveals that as a consequence of the bookkeeping scheme, viscous wake and BL effects emanating from skin friction along the fuselage surface belong to the power plant internal bookkeeping. Therefore, as already recognized by Küchemann and Weber [89], the drag shares of the body which act inside the streamtube need to be removed from the aircraft bookkeeping scheme translating into reduced effective net thrust requirements [61], [124], [134]. Accordingly, the apparent lift-to-drag ratio of the aircraft is synthetically increased over a conventional layout, while engine performance in terms of Thrust Specific Fuel Consumption (TSFC) is degraded due to increased intake total pressure losses yielding penalized transmission efficiency.[18] For the practical application of this scheme, the drag of the body whose BL is ingested needs to be identified, and the share of momentum deficit corresponding to the portion of BL inside and outside the streamtube has to be quantified. This has been conducted in the past via semi-empirical aerodynamic methods or using CFD. One distinct drawback connected to this approach is rooted in the fact that the consideration of physical effects is incomplete in a sense that the change of pressure forces due to the coupling of airframe and propulsor is difficult to apply to this scheme. Note that also intermediate definitions of inner and outer CV schemes are possible, where the interface plane is located at an arbitrary longitudinal position upstream the intake [137].

As a consequence, instead of locally evaluating separate forces acting on the body and the propulsor, an approach based on a metric describing the global longitudinal net force of the combined

[17] Consider the analogy of an extended turbofan spinner equivalent to parts of the airframe.
[18] Additional loss effects encountered in BLI arrangements typically include fan efficiency and duct losses.

airframe/propulsion arrangement is selected as a basis of the bookkeeping scheme adopted in the present work. This is a typical approach employed in the frame of numerical aerodynamic simulation of aircraft configurations with conventional propulsion system integration [167]. For BLI/WF configurations, similar approaches have been applied. In Reference [137], the net propulsive force defined in Reference [168] was employed to balance propulsor net force with drag constituents and was applied to the N3-X platform. In References [140], [141], a "total force coefficient" acting on the entire configuration was computed by means of CFD incorporating the aggregated drag of all simulated airframe components as well as the body-force of the propulsor. An adaptation for the consistent application of this scheme to the PFC layout and an approach for the matching of aero-numerical data with standard gas turbine performance software will be proposed in Chapter 4.

3.1.2 Propulsion System Efficiency Definitions

Apart from airframe/propulsion interfacing definitions, Figure 3.2 also indicates the typical control volumes for the power supply system, power transmission system and jet flow field. These domains are characterized by the energy conversion efficiency, η_{co}, transmission efficiency, η_{tr}, and propulsive efficiency, η_{pr} [169]:

$$\eta_{co} = \frac{P_{useful}}{P_{supply}}, \qquad \eta_{tr} = \frac{P_{jet}}{P_{useful}}, \qquad \eta_{pr} = \frac{P_{thrust}}{P_{jet}}, \qquad \eta_{ov} = \frac{P_{thrust}}{P_{supply}} \tag{3.1}$$

The product $\eta_{co}\eta_{tr}\eta_{pr}$ determines the overall efficiency of the engine, η_{ov}. In equation (3.1), P_{thrust} describes the effective propulsive power $F_N V_0$ and P_{supply} denotes the power extracted from the energy source, which is equal to the product of fuel heating value and fuel mass flow. The energy conversion efficiency, η_{co}, measures the quality of the conversion of the energy carrier on the vehicle to the useful power, P_{useful}. For gas turbine engines, this metric is equivalent to the core efficiency and encompasses the high-pressure system including the upstream occurring polytropic compression in the inner fan and the optional booster, as well as effects in the inner streamtube and the associated ducting. The useful power represents the ideal core excess power, i.e. the power available after all power requirements of the core stream compression have been satisfied [170]. The transmission efficiency describes the conversion from the useful power to the power in the propulsive jet, P_{jet}. For turbofan engines, η_{tr} includes the LPT, the core nozzle, the Low-Pressure (LP) shaft, an optional gear system, the fan as well all internal losses connected to the propulsive device (i.e. outer streamtube, intake, bypass duct and nozzle losses) [169]. Finally, for ducted propulsive devices the propulsive efficiency relates P_{thrust} to the power in the jet. The term P_{jet} is equal to the kinetic energy expended in the core (index 8) and bypass (index 18) jets and reads for a turbofan arrangement with the outer CV definition applied:

$$P_{jet} = \frac{1}{2}\dot{m}_8 v_8^2 + \frac{1}{2}\dot{m}_{18} v_{18}^2 - \frac{1}{2}\dot{m}_0 v_0^2 \tag{3.2}$$

In equation (3.2), $\dot{m}$ denotes the mass flow and v the flow velocity. The product of propulsive and transmission efficiency constitutes the propulsive device efficiency, η_{pd} [169].

3.1.3 Ingested Drag Ratio

The "ingested drag ratio" was originally introduced by Smith [99] to quantify the amount of airframe wake entrained by the propulsive device. Now, taking an outer CV accounting approach, the effective net thrust requirement of the aircraft with BLI/WF propulsion integration is reduced by the amount of aircraft momentum deficit ingested by the propulsor, D_{ing}, according to Reference [124]:

$$F_N = F_N' - D_{ing} \tag{3.3}$$

The ingested drag ratio quantifies D_{ing} relative to the total aircraft net thrust without accounting for any BLI/WF effects, $F_N{}'$:

$$\beta = \frac{D_{ing}}{F_N{}'} = \frac{D_{ing}}{F_N + D_{ing}} \tag{3.4}$$

In the above-described bookkeeping scheme employing global force accounting it is more appropriate to consider the change in net forward force acting on the configuration relative to a configuration without BLI/WF effects while still retaining the basic concept of the β metric. As will be derived in Section 4.2, the total required net thrust is reduced in the BLI/WF case by an amount ΔF_X, and – during cruise – aircraft drag D equals F_N', hence yielding:

$$F_N = F_N' - \Delta F_X = D - \Delta F_X \tag{3.5}$$

The adapted formulation of β then is suggested as:

$$\tilde{\beta} = \frac{\Delta F_X}{F_N{}'} = \frac{\Delta F_X}{D} \tag{3.6}$$

3.1.4 Thrust Split Ratio and Power Split Ratio

For purposes of system description in presence of multiple power plant types with individual characteristics, the thrust split ratio, ϑ, is introduced [29], [118]. This metric relates the net thrust produced by the Fuselage Fan (FF) power plant, $F_{N,F}$, to the overall net thrust installed on the aircraft. For the tri-engine arrangement studied in the present context, this refers to the sum of $F_{N,F}$ and the net thrust of the wing-installed power plants, $F_{N,W}$, i.e.

$$\vartheta = \frac{F_{N,F}}{F_{N,F} + F_{N,W}} \tag{3.7}$$

Similarly, the power split may be defined as the ratio of fuselage-installed propulsion power to the total power:

$$\Theta = \frac{P_F}{P_F + P_W} \tag{3.8}$$

In equation (3.8), the definition of P_F and P_W may be chosen according to the scope of the investigation. If thrust power is selected, the trivial result $\Theta = \vartheta$ is obtained, while for a more practical use P should either refer to useful power or supply power, yielding upon recalling equations (3.1) and (3.7):

$$\Theta = \frac{\vartheta}{\vartheta + (1-\vartheta)\dfrac{\eta_{ov,F}}{\eta_{ov,W}}} \tag{3.9}$$

3.1.5 Metrics for Performance Assessment in Presence of BLI

As noted by various researches (e.g. Reference [151]), for performance benchmarking of BLI applications the classic TSFC metric can be problematic due to the highly coupled aero-propulsive characteristics causing both changes in fuel flow and net thrust, which may lead to ambiguity in the TSFC definition and therefore requires a precise definition. The power saving coefficient, PSC, initially proposed by Smith [99] is a useful metric since it is only correlated to the relative difference of propulsive powers without, P', and with BLI, P, required for a given flight condition:

$$PSC = \frac{P' - P}{P'} \tag{3.10}$$

Hence, positive values of PSC indicate a net benefit of the BLI configuration. Since no general definition for the type of power employed in equation (3.10) exists [164], PSC may be based on various

power definitions including jet flow power, shaft power or supplied power. Furthermore, the metric may be applied to compare system or aircraft-level aspects. For highly integrated arrangements, PSC should be based on the installed characteristics and hence the power in equation (3.10) needs to incorporate sizing effects at the vehicular level, e.g. due to geometry and weight changes. As a convenient feature of this metric, PSC then incorporates all losses in the integrated system.

In particular for the comparative assessment of integrated vehicular efficiency, the Specific Air Range (SAR) measuring the instantaneous distance R covered per unit fuel consumed, W_F, may be employed [171]. Generally, in steady, level flight and for a given true air speed V_0, SAR is dependent on the lift-to-drag ratio, L/D, TSFC and the instantaneous gross weight, $W_{IGW} \cdot g$:

$$SAR = \frac{dR}{dW_F} = \frac{V_0}{\dot{m}_F} = \frac{V_0}{TSFC \cdot F_N} = \frac{V_0 \cdot L/D}{TSFC \cdot W_{IGW} \cdot g} \tag{3.11}$$

It will be demonstrated in Section 6.4 that different yet consistent accounting schemes for TSFC, L/D and net thrust result in coherent values of SAR.

3.1.6 Derivation of Analytical Constructs

For aircraft-level studies, the influence of the individual power plants on the overall propulsion system efficiency of the aircraft, η_{ov}, is of importance. As discussed above, in general, η_{ov} is defined as the ratio of effective thrust power, P_{thrust}, to the power extracted from the energy source, P_{supply}. Now, taking aircraft applications employing multiple propulsion system types, algebraic manipulation may be used to express η_{ov} as a function of the individual overall efficiencies of power plants, $\eta_{ov,i}$, each constituting a relative net thrust share ϑ_i:

$$\eta_{ov} = \frac{1}{\frac{\vartheta_1}{\eta_{ov,1}} + \frac{\vartheta_2}{\eta_{ov,2}} + \cdots + \frac{\vartheta_i}{\eta_{ov,i}}} \tag{3.12}$$

As derived by Bijewitz *et al.* [29], for a PFC layout with two power plant types installed, equation (3.12) becomes using $\vartheta_1 = \vartheta$ and $\vartheta_2 = 1 - \vartheta$:

$$\eta_{ov} = \frac{1}{\vartheta \frac{1}{\eta_{ov,F}} + (1 - \vartheta) \frac{1}{\eta_{ov,W}}} \tag{3.13}$$

Expressing equation (3.13) in relation to the efficiency of the conventionally installed power plant, $\eta_{ov}{}'$, and assuming that the efficiency of the wing-installed power plants is similar to this reference efficiency, i.e. $\eta_{ov,W} = \eta_{ov}{}'$, yields

$$\frac{\eta_{ov}}{\eta_{ov}{}'} = \frac{1}{1 + \vartheta \cdot \left(\frac{1}{\eta_{ov,F}/\eta_{ov}{}'} - 1 \right)} \tag{3.14}$$

If the power split ratio is considered as a study variable, this normalized efficiency is conveniently given by

$$\frac{\eta_{ov}}{\eta_{ov}{}'} = \Theta \cdot \left(\frac{\eta_{ov,F}}{\eta_{ov}{}'} - 1 \right) + 1 \tag{3.15}$$

Assuming that PSC is based on P_{supply}, thus incorporating the entire propulsion system efficiency chain, this metric can be expressed as

$$PSC = 1 - \frac{P_{supply}}{P_{supply}{}'} = 1 - \frac{F_N}{F_N{}'} \cdot \left(\frac{\eta_{ov}{}'}{\eta_{ov,W}} (1 - \vartheta) + \frac{\eta_{ov}{}'}{\eta_{ov,F}} \vartheta \right) \tag{3.16}$$

Using equations (3.5) and (3.6) and assuming again $\eta_{ov,W} = \eta_{ov}{}'$ produces

$$PSC = 1 - \left(1 - \tilde{\beta}\right) \cdot \left(1 + \vartheta \cdot \left(\frac{1}{\eta_{ov,F}/\eta_{ov}{}'} - 1\right)\right) \tag{3.17}$$

or similarly, expressed as a function of power split:

$$PSC = 1 - \left(1 - \tilde{\beta}\right) \cdot \frac{1}{1 + \Theta \cdot \left(\eta_{ov,F}/\eta_{ov}{}' - 1\right)} \tag{3.18}$$

It can be seen that for the reference case, i.e. $\tilde{\beta} = 0$ and $\vartheta = 0$ or $\Theta = 0$, a PSC of zero is obtained.

It is worthwhile to briefly discuss the theoretical impact of varying FF power plant efficiency levels on the overall propulsion system level. The left part of Figure 3.3 presents an evaluation of equation (3.14). The contour parameter indicates varying levels of relative degradations of the FF propulsion system overall efficiency caused by the non-uniform inflow effects including reduced ram pressure recovery and fan efficiency penalties, i.e. $\eta_{ov,F}/\eta_{ov}{}'$. Also shown are contours of the power split ratio Θ given in equation (3.9). As can be seen, the impact of degraded FF propulsion system efficiencies diminishes for small values of ϑ. Moreover, for a given power split ratio, the fraction of fuselage-installed thrust increases as the efficiency of the FF propulsion system improves. The right part shows the characteristics of PSC (cf. equation (3.17)) for a prescribed level of $\tilde{\beta}$ = 0.2. The ratio $\eta_{ov,F}/\eta_{ov}{}'$ is again treated as a study parameter. It is visible from this considerably simplified analysis that for a given power split, degrading efficiencies of the fuselage-installed power plant translate into reducing thrust splits at diminishing power saving levels. Note that in the PSC equations (3.17) and (3.18), $\tilde{\beta}$ as well as ϑ or Θ, respectively, appear as independent variables, which means that this analytical relation neither provides insight about the correlation between fuselage-installed net thrust and the relative integration force, nor regarding the impact of BLI on propulsion system efficiency. This, again, highlights the necessity for an integrated assessment capable of resolving the interplay between the relative power share of the BLI propulsor, the impact on the overall net force attainable from integration of the BLI power plant, and the penalty the FF power plant incurs relative to the power plant installed in free stream.

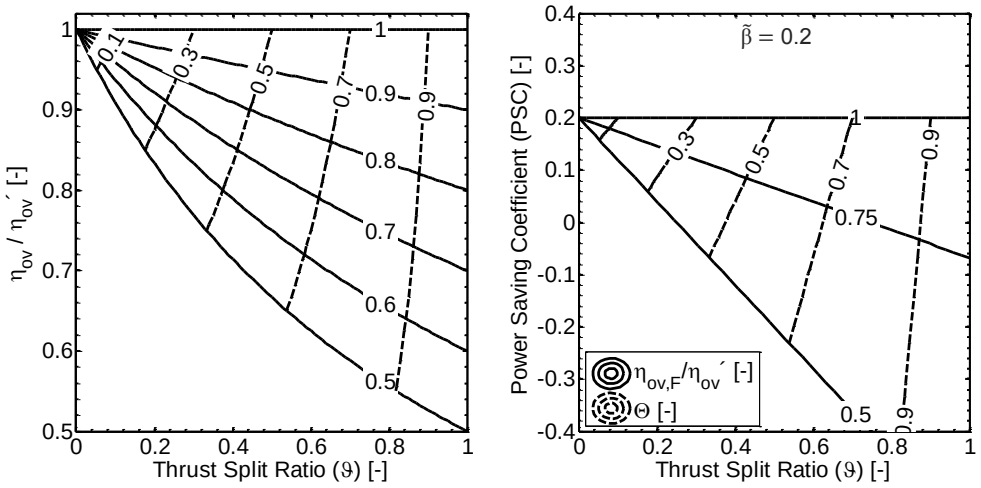

Figure 3.3: Theoretical impact of thrust split ratio and power split ratio on normalized propulsion system overall efficiency (left, adapted from Reference [29]) and on Power Saving Coefficient (right)

3.2 Estimating the Potential of Generic Airframe Configurations

As a simplified pre-study, the theoretical relative merits available from a selection of generic airframe configurations are estimated. For rapid estimation within the frame of this study, the assessment is

based on the notion of the "ingested drag ratio", where the ingested airframe momentum deficit at a representative cruise condition for each configuration is separately approximated. The topological characteristics of the configurations are captured using simplified two-dimensional geometric relations. Acknowledging that the ingested drag ratio is closely correlated to the power saving potential, the ideal PSC, i.e. the saving attainable from aerodynamics only without including any integration effects, was taken as a figure of merit for the purpose of this study. Owing to the simplified nature of this pre-study, the ingestible momentum deficit is approximated as the viscous drag developing within the propulsion system streamtube(s) ahead the air intake system(s). All other drag sources including lift-induced drag are assumed to be unaffected by BLI. The streamtube is assumed to encompass the airframe portion upstream and perpendicular to the propulsion system inlet area and taken to be equal to the inlet width and height. Crossflow and streamtube contraction effects are neglected, in the first instance. In the radial dimension, only the drag inside the streamtube, i.e. the momentum deficit developing up to the inlet height is included. At the control volume boundaries the static pressure is assumed constant. The captured viscous drag is modeled by directly integrating the momentum deficit due to skin friction on the wetted surface in radial (y) and spanwise (z) direction for each streamtube:

$$D_{ing} = \int_0^{z_{inl}} \int_0^{h_{inl}} \rho u(y,z)\,(V_0 - u(y,z))\mathrm{d}y\mathrm{d}z \tag{3.19}$$

where u is the velocity, ρ the density, V_0 the freestream velocity and h_{inl} and z_{inl} the representative inlet height and width. The local BL thickness at the inlet axial and spanwise position, $\delta_x(z)$, is computed as a function of the local longitudinal position $x(z)$ using a classic flat plate correlation for turbulent boundary layers [172, p. 328], thereby neglecting the pressure gradient along the body contour:

$$\delta_x(z) = 0.37x(z) \cdot \mathrm{Re}_x^{-0.2} \tag{3.20}$$

where Re_x denotes the local Reynolds number based on the axial position. The velocity profile is estimated using a power law distribution [172, p. 328], $u/V_0 = (y/\delta)^{1/7}$, and assumed to be fully attached. The total ingested momentum deficit is computed as the sum of the viscous drag constituents ingested in each streamtube and the ingested drag ratio results from equation (3.4), where an equal total net thrust requirement (without accounting for BLI/WF effects) is computed from a basic force equilibrium at steady, level flight. The instantaneous gross weight is correlated to a given, constant maximum takeoff weight. The PSC is estimated based on equation (3.18).

The configurations considered in this study are schematically depicted in Figure 3.5. In order to ensure comparability of all considered configurations, similarity in the air transport task, specifically in the fuselage capacity is assumed. Key assumptions of the generic widebody application scenario are given in Figure 3.4. Commencing with a reference TaW widebody layout, for BWB configurations the body span and length is scaled according to empirical factors given by Liebeck *et al.* [173]. Corresponding factors for non-circular ("double bubble") fuselage layouts have been derived from Reference [104]. All other configurations are considered to have equal fuselage dimensions as the reference case. The longitudinal position of the inlet measured at the fuselage centerline is assumed to be at 85% relative fuselage length, if not otherwise specified. Moreover, the total intake area is assumed identical within all configurations. In Figure 3.4, the results of the ideal PSC are displayed. The spread in results symbolized through the vertical bars refers to a variation in input values: anticipating potential degradations in fan efficiency due to BLI, this parameter $\Delta\eta_{Fan}$ has been varied between a hypothetically negligible impact and a 5% relative degradation consistently applied to all

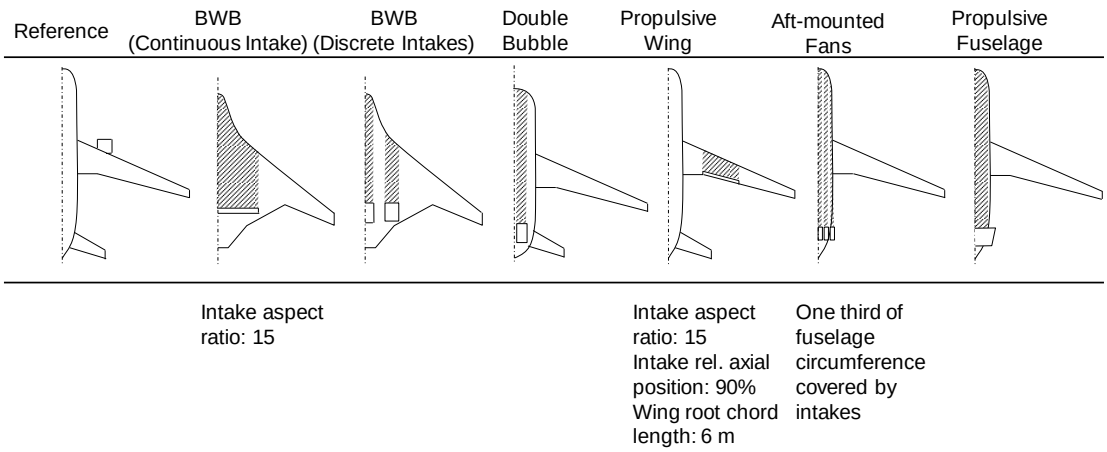

Figure 3.5: Overview of generic airframe morphologies considered: Shaded areas correspond to airframe portions available for BLI

configurations.[19] While the method does capture the changing impact of $\Delta\eta_{Fan}$ on the spread in PSC with varying levels of β, within the range of β and $\Delta\eta_{Fan}$ considered in Figure 3.4 the implications can be characterized as minor, which, however, may be attributed to the idealized analytical formulation. With regards to the predicted drag ingestion potential, the simplified approach appears to estimate the airframe drag captured within the propulsion system streamtube satisfactorily. Three test cases are considered: Comparison of the estimated value of β (10.3%) of the BWB morphology featuring a continuous intake with numerical data for a similar configuration [162, Fig. 6] evaluated at the identical relative longitudinal position yields a deviation of -1.5 percentage points. For the generic

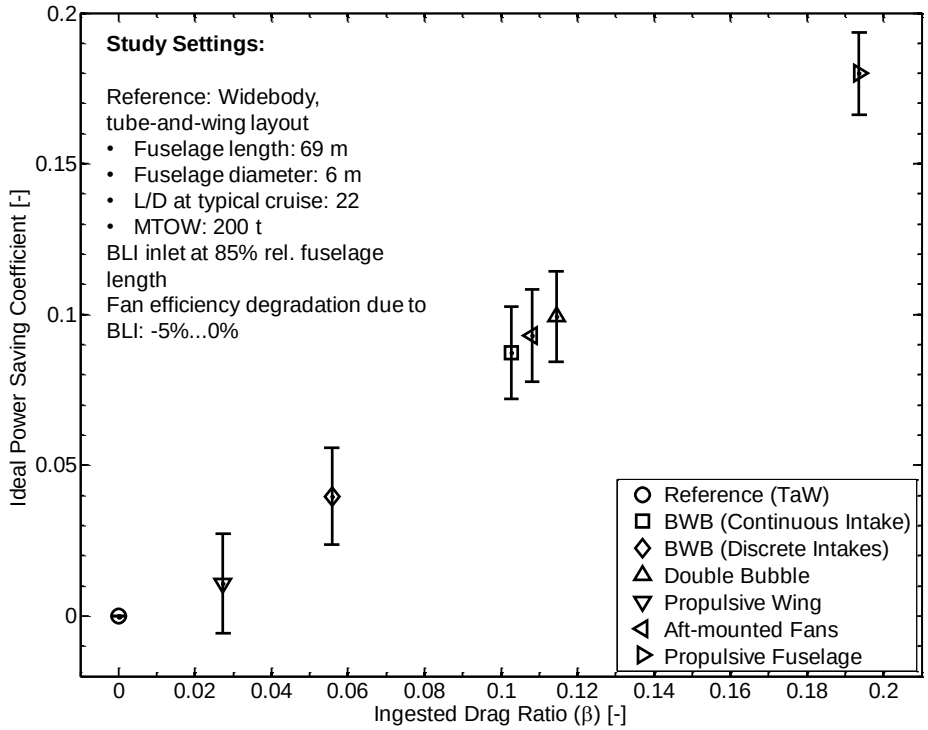

Figure 3.4: Simplified comparative assessment of ideal power saving coefficient attainable from general configurational options

[19] Configurations exhibiting strongly coupled azimuthal and radial variation in flow properties may suffer from higher efficiency penalties than arrangements with distortion intrinsically limited to radial nature.

double bubble design, β is estimated as 11.5%, which compares well with the value stated in Reference [109, Fig. 3] (approximately -0.5 percentage points deviation). Finally, for the generic PFC design β = 19.4% is obtained (-1.6% compared to Reference [118, p. 470]) From a power saving perspective, the results compare favorably to a previous generic study, which was based on wetted area considerations [113]. As can be seen, for the PFC, the high airframe portions available for ingestion of momentum deficit yield particularly high values of β and accordingly a comparatively high power saving potential can be expected.

4 Modeling of Aero-Propulsive Interaction Effects

The increased level of interaction effects between airframe aerodynamics and propulsion constitutes a central challenge of highly integrated propulsion-airframe arrangements. As elaborated in Chapter 2, the identification of the integrated efficiency potential requires appropriate modeling of these effects and their implications on the overall system level.

The methodological development of this thesis is centered around enhancing the assessment capability of synergistic propulsion-airframe concepts through improved resolution of the multidisciplinary inter-dependencies between vehicle aero-propulsive effects, propulsion system characteristics and overall conceptual aircraft design. The implemented procedure encompasses a suite of existing and custom developed methods aiming at the consistent propagation of the driving physical mechanisms to the vehicular level. A key aspect of the developed methods refers to a novel approach for the efficient processing and integration of high-fidelity numerical aero-propulsive data in conceptual aircraft design. Through consistent treatment of both conventionally installed and BL ingesting configurations, the proposed methodology allows for the identification of the integrated efficiency potential of the studied advanced propulsion system integration architecture. The parametric setup facilitates fast exploration of the trending behavior at a global level and thus supports typical conceptual design task such as analyzing the impact of component-level technological advances.

The present chapter focusses on the approach towards modeling of aero-propulsive interaction effects of the PFC and their incorporation at the overall system level. As pointed out in Chapter 2, established handbook methods for the mapping of aircraft aerodynamics are insufficient to appropriately resolve the mutual interaction effects, and thus, the utilization of higher-order computational methods is required. Owing to the approximately axisymmetric layout intrinsic to the studied layout and in contrast to more unconventional morphologies, the numerical simulation of a two-dimensional representation of the fully integrated fuselage-propulsion arrangement at relevant cruise conditions in the transonic regime is considered suitable to capture the relevant physical effects for the purpose of the conceptual studies targeted in the present context. For the methods developed in this thesis, corresponding aero-numerical data is available for the investigated PFC configuration. In Section 4.1, an overview of this data is given.

Different from contemporary propulsion system integration paradigms, for the investigated configuration power plant thrust and airframe drag are no longer clearly distinguishable. In fact, mutual interaction is typical. Therefore, rigorous adherence to well-defined aero-propulsive accounting conventions and efficiency definitions is required to elude any ambiguity for system description. In Section 4.2, thrust and drag bookkeeping standards applicable to conventionally installed and highly integrated power plants are proposed and the applicability of the derived scheme is demonstrated. In order to facilitate quick exploration of the integrated characteristics, numerical simulation of aero-propulsive characteristics of the PFC directly in the aircraft and propulsion system sizing loop is considered impractical in the early conceptual design phase, since the excessive computation effort inhibits large parameter variations. Instead, separately computed, coupled aerodynamic and propulsion system characteristics are processed in the present context and subsequently incorporated within system-level calculations. While with computationally expensive numerical calculations frequently only a small dataset of design and operating variations is manageable, conceptual design typically intents exploration of a large parameter space. In order to unite these conflicting goals, a process for

the efficient incorporation of numerical data in typical gas turbine performance calculation will be presented utilizing surrogate models of the numerical data. The model matching procedure presented in Section 4.3 describes the generic approach towards integration of aero-propulsive data in propulsion system design and performance via regression analysis enabling the execution of parametric studies at aircraft level. The proposed approach is sufficiently adaptable to be employed with different aero-numerical datasets. Specifically addressing the considered PFC application and the numerical data available in the present context, Sections 4.4 to 4.9 discuss the physical effects and geometric as well as operational dependencies of the parameters derived from the model matching procedure.

4.1 Overview of Available Aero-Numerical Data

As part of the multidisciplinary project DisPURSAL (see Section 2.4.2.5) high-fidelity numerical flow simulations of the PFC were conducted by the research organization ONERA. The geometric arrangement simulated through CFD included the PFC fuselage and the FF nacelle together with the fuselage-installed propulsive device.[20] The FF propulsion system core flow was neglected. For sake of simplicity, an axisymmetric layout was analyzed and the simulation was limited to cruise condition. Moreover, no intake struts were considered. Effects not captured by the two-dimensional representation include the influence of the wing-induced wash on the flow field entering the fuselage propulsor as well as three-dimensional flow effects occurring during flight at incidence and/or sideslip angle. For the initial parametric mapping of distortion effects on the performance of the FF propulsion system, a simplified approach will be presented in Section 5.2.5. The application scenario refers to a widebody, medium-to-long range commercial transport. Key aircraft design attributes along with geometric and computational settings are given in Table 4.1 [114].

Parameter	Unit	
Application case		Medium-to-long range widebody aircraft
Air transport task		4,800 nm design range, 340 passengers
Fuselage length	m	69.0
Fuselage equivalent diameter	m	6.07
Rel. longitudinal position of FF highlight	-	0.85
Intake length	m	1.55
Typical cruise condition		M0.80, FL350, ISA
CFD setup		Axisymmetric RANS with enhanced actuator disk model

Table 4.1:Essential geometric and computational settings of considered PFC application case [114]

From a computational perspective, a proprietary flow solver developed by ONERA [174] was employed to solve the Reynolds-Averaged Navier Stokes (RANS) equations on multi-block structured meshes using the Spalart-Allmaras turbulence model. Owing to the axisymmetric nature of the analyzed problem, RANS calculations were performed based on a computational setup, where the two-dimensional geometry was rotated an angular increment around the longitudinal axis. The CFD solution was obtained upon the application of periodicity conditions on the planes of the thus created volume segment. The fan of the FF propulsion system was approximated by an actuator disk formulation with appropriate distributions of blade characteristics in radial and azimuthal directions based on Glauert theory extended to ducted fan devices, thus giving a suitable emulation of a fan rotor and stator arrangement. More details on the computational setup can be found in Reference [114]. The

[20] This arrangement will hereafter be referred to as “bare PFC”.

data gained from these analyses is considered representative for the widebody, medium-to-long range PFC application studied in this work.

As described in Reference [114], in a first step, the geometric shaping of the fuselage and FF nacelle had been refined through an iterative procedure to obtain benign flow characteristics without separation and detrimental regions of super-velocities. Then, treating this design designated as D_0 as a baseline, as part of an exploratory activity, simulations were conducted for a variety of geometric variations of the FF. Specifically, five additional design points were analyzed through CFD (D_1 to D_5). The variables included the intake duct height at a specifically defined position upstream of the fan plane denoted as Aerodynamic Interface Plane (AIP), which was set congruent with the intake throat (see Figure 5.4). In addition, the design fan pressure ratio, $FPR_{ds} = p_{13}/p_2$, was varied. The range of feasible values was restricted by the applicability of the actuator disk model employed in the CFD simulations. The fuselage shaping including the hub radii at the AIP and fan inlet was kept invariant, while nacelle contouring was adapted according to each combination of design variables. Each design was subject to a series of computations of varying fan power settings. A representation of the fuselage and nacelle contour is provided in Figure B.1 in Annex B for design D_0.

In order to ensure similarity between all sampled design points, as part of the data processing in this work, a common axial Mach number at the fan inlet is applied at the design conditions. Based on interpolation between different simulated power settings of each geometric design, a mass-averaged value of 0.56 has been identified to be consistently covering all design variations and is hence set as a common design standard. As an initial conservative approach, this value, which is approximately 20% lower than typically exhibited by advanced conventionally installed turbofans [175], has been selected in order to cater for anticipated stronger radial non-uniformities in the Mach number distribution at the fan face. For typical blade tip speeds, this results in moderated relative Mach numbers, thus mitigating the risk of excessive shock losses [176]. The sample points featuring other power settings are treated as off-design points and constitute the basis for operational analyses. In addition, characteristics of a speed sensitivity analysis are available for the baseline design covering free stream Mach numbers between 0.75 and 0.85. An itemization of the available data is given in Table 4.2. The upper part

Parameter	Unit	D_0	D_1	D_2	D_3	D_4	D_5
Design variations							
Flight condition			M0.80, FL350 (10,668 m), ISA				
Intake duct height at AIP, h_{AIP}	m	0.526	0.650	0.900	0.900	0.500	0.500
Design Fan Pressure Ratio, FPR_{ds} [a]	-	1.498	1.369	1.249	1.494	1.314	1.405
Flight condition			FL350 (10,668 m), ISA				
Flight Mach number, $M_{0,ds}$	-	0.75					
	-	0.85					
Off-design variations							
Flight condition			M0.80, FL350 (10,668 m), ISA				
Normalized Fan Pressure Ratio, FPR/FPR_{ds}	-	0.95	0.98	0.97	0.83	0.97	0.92
	-	0.97	1.00	1.00	0.85	0.99	0.95
	-	1.00	1.01	1.00	0.88	1.00	0.97
	-		1.03	1.03	0.90	1.01	0.99
	-		1.06	1.06	0.96	1.04	1.00
	-		1.09		1.00		1.01
	-				1.02		1.04

[a] based on interpolation for a common axial fan inlet Mach number of 0.56

Table 4.2:Overview of available CFD calculated simulation samples

describes the nominal design conditions for each sample design, while the lower part indicates the operating conditions with respect to fan power setting analyzed for the respective designs cases.

The available result data from CFD comprises mass-averaged values of total pressure, p, axial Mach number, M_{ax}, as well as mass flow, $\dot{m}$, at various stations along the FF duct including AIP, fan inlet, fan outlet and nozzle exit. In addition, the isentropic fan power (determined as the product of mass flow and the change in total flow enthalpy across the fan) and the total force acting on the entire bare PFC arrangement is available, which will be discussed in Section 4.2 in more detail.

4.2 Thrust and Drag Bookkeeping Standards

A key requirement for a consistent bookkeeping scheme is to avoid ambiguity in the classification of power plant and airframe related properties [168]. While an effort to resolve the nature of all forces acting on wetted surfaces may yield high transparency, it also greatly increases the computational complexity and the risk of improper accounting, especially if the interfaces change for varying design and/or operating conditions. From a practical perspective, the choice of the bookkeeping scheme is typically strongly influenced by the availability of data that can consistently be applied to the considered application case. In addition, bookkeeping should target appropriate applicability to standard methods for aircraft and propulsion system sizing and performance.

In the present section, standards for the thrust and drag bookkeeping are described, both applicable to conventionally installed turbofans and highly integrated power plants. Based on the available aero-numerical data, the momentum-based bookkeeping approach is focused at the overall net propulsive force of the entire bare PFC arrangement investigated in the CFD setup. A descriptor will be introduced appropriate for capturing the physical mechanisms associated with the installation of an aft-fuselage, BL ingesting propulsive device, based on which sizing and performance heuristics for subsequent parametric, aircraft-integrated exploration of the design space will be derived. As a result of a reasonably generic approach, the proposed bookkeeping scheme may be applied to arbitrary configurations of propelled bodies as long as a minimum set of parameters is known.

4.2.1 Conventionally Installed Turbofan Power Plants

For the definition of net thrust of conventionally installed turbofans, the convention typically employed in power plant simulation software is used. Accordingly, the thrust and drag bookkeeping is aligned with the propulsion system streamtube [175], [177], [178]. The control volume (CV) for net thrust calculation is indicated in Figure 4.1 and extends from freestream conditions far upstream the intake to the exit of the nozzle, which either refers to the common nozzle of mixed-flow turbofans or the individual exhausts of core and bypass nozzles in case of unmixed-flow engines. Net thrust, F_N, is computed as the difference between the sum of gross thrusts of core and bypass streams including momentum and pressure terms, and ram drag. Net thrust incorporates all effects occurring within the streamtube shown in Figure 4.1, including engine mechanical and/or customer bleed offtakes as well as any internal non-idealities such as duct pressure losses. Loss effects due to friction and pressure forces on the core nozzle aft-body and plug are captured via a streamtube correction factor (cf. e.g. Reference [175], [179]) applied to the net thrust calculation. This means, F_N refers to the "standard net thrust" defined in Reference [168], corrected for streamtube losses, which is generally accepted as a practical thrust definition [178]. Turbofan installation drag includes intake additive drag due to the pressure distribution on the capture streamtube, which is, however, for well-shaped nacelle fore-bodies widely compensated by the suction force acting at the nacelle lip [175], [180]. Therefore, intake spillage drag, i.e. the imbalance between additive drag and lip suction force, is small in the absence of

flow separation and neglected in the present context. The remaining pressure force acting on the nacelle external surface as well as viscous cowl losses are captured by the semi-empirical nacelle drag prediction of Raymer [181] (see Section 5.5) and are bookkept as part of the airframe drag breakdown. Further aerodynamic interaction effects with airframe components are neglected, in the first instance.

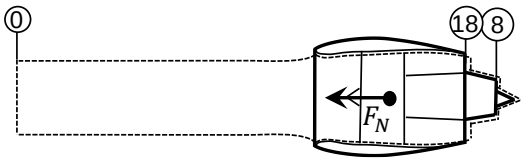

Figure 4.1: Control volume used for net thrust calculation for conventionally installed turbofans

4.2.2 Highly Integrated Propulsive Devices

For highly integrated propulsive devices such as the PFC, an important implication is linked to the integration effects caused by the interaction of the fuselage flow field and the FF propulsion system installed in the aft-fuselage section. Geometric dimensions of the FF have a major impact on the momentum deficit captured in the power plant and on the extent wake filling can be realized. In addition, the presence of the FF device alters the static pressure distribution along the fuselage and the FF nacelle, thus yielding different pressure force contributions acting on the contracting fuselage section in front of the FF, downstream on the fuselage aft-cone and on the nacelle. In addition, local skin friction coefficients are influenced by the wall-normal gradient of the velocity profile. Apart from geometric properties, these forces also depend on the power level of the FF propulsion system.

As outlined above, the computational setup of the aero-propulsive simulations, which constitute the data basis for the present work, did not facilitate a component-based analysis of the individual loss effects. Therefore, a conversion procedure for the quantification and subsequent parametric mapping of integration effects has been developed as part of the present work, which is discussed in the following. In the upper part of Figure 4.2, a schematic view of a generic bare PFC half-sectional layout as simulated in the CFD setup (hereafter referred to as "Setup A") is presented. The force contributions included in the aero-numerical analysis within the control volume CV are indicated with a hat symbol and comprise fuselage viscous and pressure drag ($\widehat{D}_{Fus,v}, \widehat{D}_{Fus,p}$), the corresponding properties occurring at the FF external nacelle surface ($\widehat{D}_{Nac,v}, \widehat{D}_{Nac,p}$), as well as drag on the fuselage aft-body downstream the propulsor ($\widehat{D}_{aft,v}, \widehat{D}_{aft,p}$). Furthermore, within the FF ducting, friction and pressure forces are included ($\widehat{D}_{duct,v}, \widehat{D}_{duct,p}$). The forward force applied by the propulsor disk model ($\widehat{F}$) is also indicated, as is the isentropic power applied to the fan, $\widehat{P}_{is}$. Properties available for further system processing refer to the ones indicated with boxes. These include as a most important characteristic the overall net force of the configuration simulated in the CFD setup measured in longitudinal direction, $\widehat{F}_X$. Expressed in the reference frame of the aero-numerical setup, this net forward force is given by the thrust force produced by the actuator disk reduced by the sum of all viscous and pressure forces integrated over all body surfaces existing in the considered setup, $\widehat{D}$:

$$\widehat{F}_X = \widehat{F} - \sum_i \left(\widehat{D}_{i,v} + \widehat{D}_{i,p}\right) = \widehat{F} - \widehat{D} \tag{4.1}$$

The characteristics of $\widehat{F}_X$ constitute an important parameter used for further system analysis.

The lower half-section of Figure 4.2 presents the computational setup ("Setup B") used for incorporation of CFD results within the power plant performance calculation discussed in Chapter 5. The setup is divided into two CVs to signify the application of a standard separate-flow turbofan cycle model. In order to emulate the CFD setup, the inflow conditions and geometric properties of the

turbofan engine shown in the figure are consistently adjusted according to the corresponding properties of Setup A. As such, an identical fan hub/tip ratio is set, the fan inlet axial Mach number is prescribed as described in Section 4.1, the fan duct height is iterated and the fan pressure ratio is set according to the respective design considered in Setup A. In addition, intake total pressure recovery ratio with respect to freestream conditions, $\pi_{int} = p_2/p_0$, is prescribed. In order to account for the inexistence of the core flow in the CFD calculation, the bypass ratio of Setup B is iterated to yield equal core and bypass nozzle exit velocities, thereby allowing to treat both nozzles as a common one and ensuring similarity in nozzle exit conditions between CFD and gas turbine-based setups. To validate the matching, important cycle properties such as fan inlet mass flow, bypass nozzle exit area and pressure ratio were compared between both computational setups exhibiting close agreement (see Table 4.3). For comparing nozzle exit areas, the property of the CFD setup is compared to the area A_{18} of Setup B corrected by the term $BPR/(1+BPR)$. As an important premise, the isentropic power absorbed by the fan, $P_{Fan,is}$, is similar.

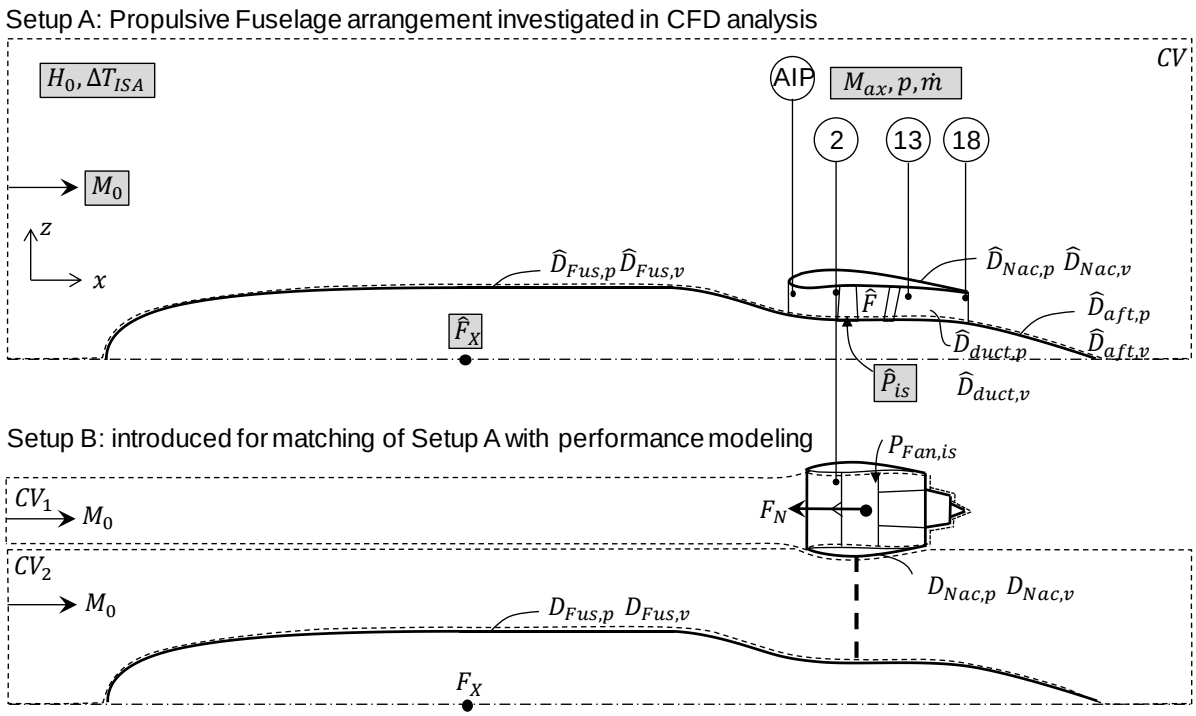

Figure 4.2: Aero-propulsive bookkeeping scheme indicating force contributions and important flow properties. Highlighted properties indicate data available from CFD results.

The approach towards the identification of integration effects is based on the comparison of the net propulsive forces exhibited in both setups. For a given power input, the net force of Setup A, $\hat{F}_X$, incorporating fuselage and nacelle drag as well as interaction effects is different from the gas turbine net thrust, F_N, obtained from CV_1 of Setup B. The latter is computed based on the CV definition for the conventionally installed power plant outlined above and hence intrinsically no integration effects are included in the calculation of net thrust. For all designs considered in the CFD experimental plan, $\hat{F}_X < F_N$ is obtained. In order to ensure comparability of the physical mechanisms reflected in the net forces of Setups A and B, a corresponding property is introduced for Setup B. Accordingly, the net forward force, F_X, denotes the balance of F_N against the drag of the bare, isolated fuselage body and the external drag of the FF nacelle:

$$F_X = F_N - D_{Fus} - D_{Nac} \tag{4.2}$$

Therefore, a second control volume, CV_2, is introduced in Setup B. Fuselage fan nacelle drag forces constitute the interface between CV_1 and CV_2 and the external thrust force induced into CV_2, i.e. F_N, is symbolized by the dashed line. As can be seen, F_X is the net forward force acting on CV_2.

For the prediction of the bare fuselage drag, D_{Fus}, the semi-empirical approach of Raymer [181] is employed capturing viscous and pressure (form) drag effects. Following Reference [182], compressibility drag expected for the transonic application is mapped using a characteristic given in Reference [183]. The semi-empirical fuselage drag prediction has been calibrated using a CFD-derived value obtained for the isolated PFC fuselage.[21] Similarly, applicability of the drag calculation of Reference [181] for the prediction of FF nacelle drag, D_{Nac}, is assumed. Reduced dynamic head due to BL flow is neglected, in the first instance. The wetted area of the fuselage and external FF nacelle directly results from area-integration of the axisymmetric contour coordinates (see Section 5.5.1), thus ensuring identical wetted areas in both setups. For given ambient conditions, the isolated fuselage drag D_{Fus} remains invariant for all designs investigated, while D_{Nac} varies with the radial dimension of the nacelle and, due to different nozzle contraction angles, also – albeit in a weaker manner – with FPR_{ds}. Based on the proposed formulation, the collective effect emanating from the integration of the FF propulsive device to the fuselage on the net forward force of the bare PFC arrangement is derived from:

$$\Delta F_X = \hat{F}_X - F_X \quad \text{at } P_{Fan,is} = \hat{P}_{is} \tag{4.3}$$

The integration impact metric, ΔF_X, serves as an auxiliary variable and is especially useful for aircraft-integrated sizing and performance assessment (see Chapter 6). Different from F_N, the parameter $\hat{F}_X$ and consequently also ΔF_X captures the integrated impact of the FF sizing and operating parameters on the physical effects related to BLI/WF integration. This includes the reduction of excess kinetic energy in the combined jet and airframe wake enabled by ingesting the fuselage BL and filling the momentum deficit in the wake, as well as the propulsive device's impact on the fuselage and aft-body pressure distribution and hence modified pressure drag. The effect on localized pressure forces will be

Parameter	Unit	Setup A[a]	Setup B[b]	Δ [%]
Geometry designation		D_0		
Flight condition		M0.80, FL350, ISA		
Fan Pressure Ratio, FPR_{ds}	-	1.498	1.498	±0.0[c]
Intake total pressure recovery ratio, π_{int}	-	0.860	0.860	±0.0[c]
Fan axial inlet Mach number	-	0.561	0.561	±0.0[c]
Duct height at fan inlet	m	0.62	0.62	±0.0[c]
Fan inlet mass flow	kg/s	424.4	427.5	+0.72
Fan nozzle exit area	m^2	3.824	3.826	+0.05
Isentropic fan power, $\hat{P}_{is}$, P_{is}	MW	12.78	12.98	+1.54
Gas turbine net thrust, F_N	kN	-[d]	31.08	-
Bare fuselage drag, D_{Fus}	kN	-[d]	23.20	-
Fuselage Fan nacelle external drag, $D_{Nac,F}$	kN	-[d]	5.08	-
Net forward force, $\hat{F}_X$, F_X	kN	23.24	2.80	-
Integration impact metric, ΔF_X	kN	20.44		-

[a] axisymmetric RANS CFD results, setup comprising integrated fuselage and FF device
[b] setup for matching of CFD results with engine and aircraft performance calculation
[c] input value
[d] value not available for CFD setup

Table 4.3: Comparison of data obtained from CFD setup and corresponding performance characteristics from power plant and aircraft sizing, exemplary shown for design D_0

[21] Calibration factor: 0.971

discussed in Sections 4.4.2 and 4.6.2. In addition, the implications of changes to the skin friction coefficient are captured in the BL representation of the computational setup. Numerical values of the discussed parameters are tabulated in Table 4.3, exemplified for design D_0. Supplementary data on the remaining design cases can be found in Table C.1 in Annex C. The observable small deviation in mass flow, exit area and power can primarily be attributed to inaccuracies in averaging the radially distributed CFD data and slightly different gas property models.

In order to elucidate the behavior of the parameters $\hat{F}_X$ and F_X, the upper part of Figure 4.3 shows an evaluation of the net forward force values of both Setups A and B against h_{AIP} at nominal design conditions. Solely positive values are obtained for $\hat{F}_X$. In contrast to that, since in the gas turbine setup the beneficial aero-propulsive interaction effects are not captured, consistently smaller values in net forward force are obtained for Setup B, which are even negative for designs D_4 and D_5. The lower part of Figure 4.3 presents the corresponding values of ΔF_X. A strong correlation between ΔF_X and h_{AIP}, which will be discussed in Section 4.4.2, can be observed.

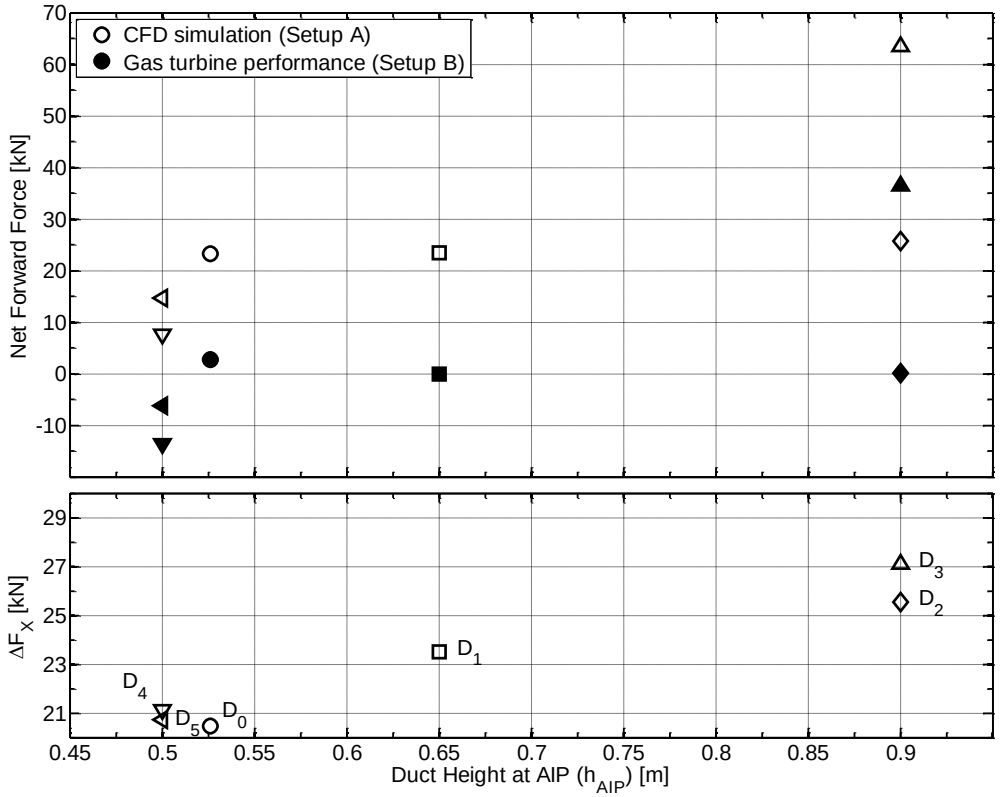

Figure 4.3: Net forward force of Setup A and B, and integration impact metric at nominal design conditions

The functional sensitivities of ΔF_X with respect to important sizing and operating parameters are derived from regression analysis conducted as part of the model matching procedure described in Section 4.3. The resulting characteristics are presented in Sections 4.4 to 4.6. An evaluation of the metrics $\hat{F}_X$ and F_X against isentropic power absorbed by the fan for all considered design settings is given in Figure 4.4. In the visualization, all design points investigated through CFD (Setup A) are plotted along with the corresponding data associated with the setup of gas turbine performance calculation. In addition, the metric representing the integration impact, ΔF_X, is annotated. Linear curve fits are included to indicate the trend for each dataset. As can be seen, the obtained trends of net force against ideal fan power are adequately represented by the linear regression. The reduced slope of the fitted samples of Setup A, i.e. the opportunity to produce a higher change in net force from the same change in power may be regarded as an indication that the aero-propulsive interaction effects associated with BLI/WF, which are captured in Setup A, translate into an improved vehicular

efficiency. It can be derived from the chart that for a given net forward force consistently less power is consumed for Setup A. Note that the power reduction, however, depends on the quality of the drag predictions for isolated fuselage and FF nacelle, and is therefore only accurately represented in Figure 4.4 if the fuselage and nacelle drag would behave similar to a conventional airframe.

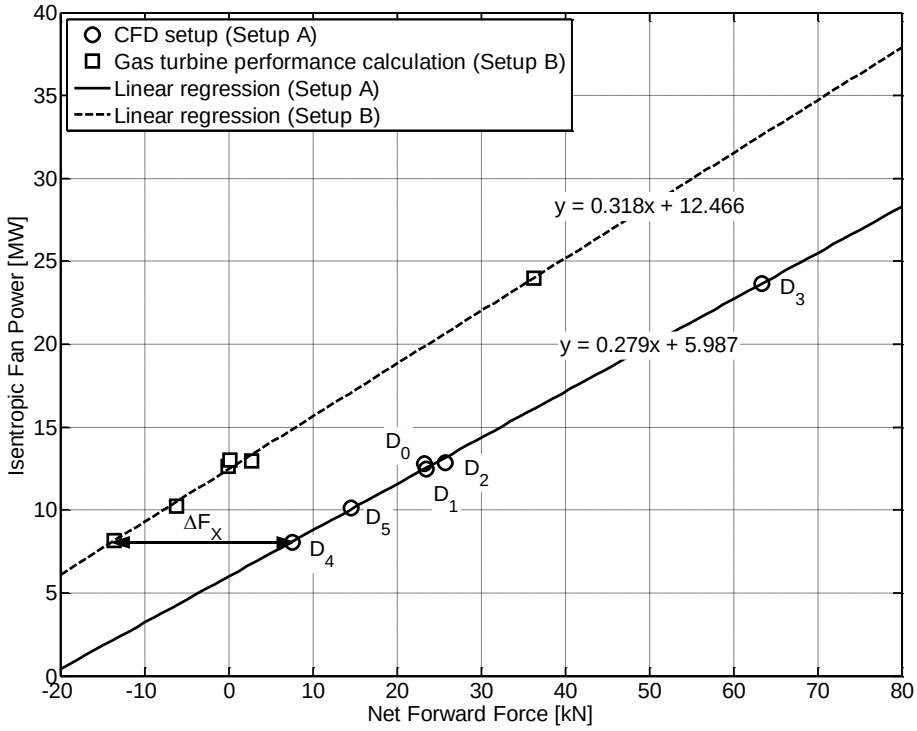

Figure 4.4: Comparative evaluation of net forward forces and absorbed fan power corresponding to aero-numerical and gas turbine based setups

From a computational perspective, it is recognized that the utilization of the ΔF_X metric eliminates the need to classify parts of the fuselage and FF nacelle aerodynamic forces as drag and thrust related forces, respectively, which may suffer from ambiguity and, as will be shown later, strongly depends on design and operating parameters. Due to strict adherence to overall force terms, the scheme does not rely on unconventional parameters such as "ingested drag". Owing to the generalized approach, the proposed bookkeeping scheme may be universally applied to airframe-propulsion arrangements, provided if their net propulsive force along with the consumed propulsive power is known, and is applicable for sizing purposes and off-design performance prediction. As will be presented in the next section, minimum adaptation demand is required for introducing the scheme to standard modeling practices for power plant calculation and aircraft sizing.

4.2.3 Application of Proposed Thrust and Drag Bookkeeping Scheme

The application of the implemented bookkeeping scheme to the aircraft and propulsion system sizing process is described in the following. Figure 4.5 shows a half-sectional top view of a generic PFC layout. The net forward force associated with the regions indicated in shaded color refers to the resulting force of the CV in the upper section of Figure 4.2, $\hat{F}_X$. Residual drag components not simulated in the CFD setup include skin friction, form and compressibility drag of the remaining airframe components, i.e. the wing, empennage, pylons and nacelles of any power plants in underwing-podded installation, as well as lift-induced drag, and are lumped together as D_{Res}. Wing-installed

power plants produce the total net thrust $F_{N,W}$. In steady level flight, the overall force balance of the arrangement shown in Figure 4.5 reads:

$$F_{A/C} = \left(\hat{F} - \hat{D}_{Fus} - \hat{D}_{Nac}\right) - D_{Res} + F_{N,W} = \hat{F}_X - D_{Res} + F_{N,W} = 0 \tag{4.4}$$

Recalling equations (4.2) and (4.3), this yields upon rearrangement:

$$F_{N,F} + \Delta F_X - D_{Fus} - D_{Nac,F} - D_{Res} + F_{N,W} = 0 \tag{4.5}$$

where $F_{N,F}$ refers to the net thrust of the fuselage-installed power plant. As can be observed from equation (4.5), the sizing net thrust requirement of the aircraft is reduced by the net force increment ΔF_X associated with BLI power plant integration. Note that for cases of conventional power plant installation, i.e. vanishing ΔF_X, equation (4.5) transforms into the usual equation for the description of thrust and drag equilibrium. It is recognized that due to the definition of F_X the application of the scheme only relies on the drag prediction of the isolated fuselage and FF nacelle, where empirical methods may be utilized (Section 4.2.2). It is assumed, in the first instance, that small changes to fuselage dimensions e.g. to accommodate varying fuselage-installed power plant dimensions are captured by the corresponding change in D_{Fus} obtained from empirical methods. The rigorous adherence to the traditional, momentum-based formulation eases integration of the BLI/WF configuration model into existing propulsion system and aircraft sizing frameworks.

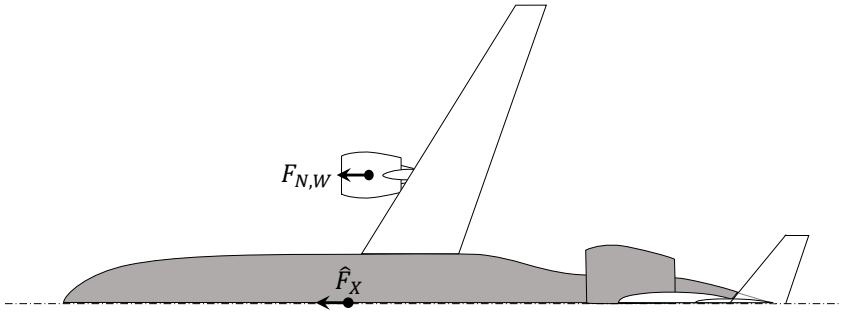

Figure 4.5: Control volumes used for the application of developed bookkeeping scheme to aircraft and propulsion system sizing process

In terms of efficiency definitions, different e.g. from the inner CV accounting approach outlined in Section 3.1.1, the conventional definitions of propulsive, transmission and core efficiency may be employed (Section 3.1.2), thereby ensuring full compatibility and consistency with conventionally installed power plants. The implications of BLI/WF propulsion system integration on the individual constituents of overall efficiency will be discussed in Chapter 6.

4.3 Description of Implemented Model Matching Procedure

In order to incorporate the aero-numerical data outlined in Section 4.1 into an aircraft-integrated propulsion system analysis process, a matching procedure has been developed as part of the present thesis. The approach is structured in four distinct steps executed subsequently. As an essential task, the proposed procedure seeks to minimize the deviation of the response of the implemented propulsion system model from the original aero-numerical data, thereby ensuring consistency between CFD setup and gas turbine design and performance results. The basic workflow – exemplified for the studied case and available data – is summarized in the following and visualized in Figure 4.6.

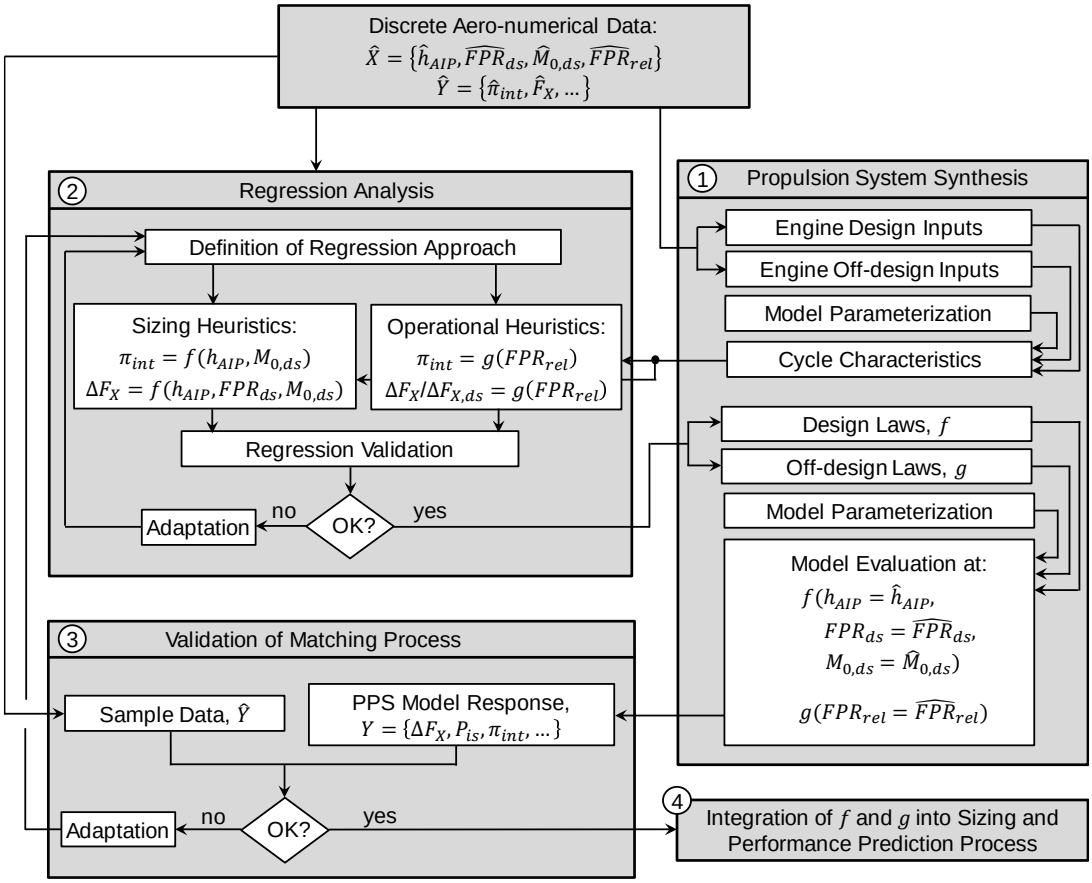

Figure 4.6: Overview of established workflow for the incorporation of aero-numerical data in propulsion system design and performance calculation

Firstly, for data generation purpose, the available numerical aero-propulsive data is directly processed in the gas turbine performance framework. In general, the relevant numerical data comprises a set of free input variables $\hat{X} = \{h_{AIP}, FPR_{ds}, M_{0,ds}, FPR_{rel}\}$, where FPR_{rel} denotes the normalized operating FPR. These are given at a series of discrete sample points denoted as $\hat{h}_{AIP}$, $\widehat{FPR}_{ds}$, $\hat{M}_{0,ds}$, and $\widehat{FPR}_{rel}$. The result space of the CFD simulation is described through the dependent result variables, $\hat{Y}$, and comprises most importantly π_{int} and $\hat{F}_X$. In this first step, the gas turbine cycle model is directly evaluated at the sample points, thereby allowing for the derivation of the characteristics of ΔF_X, which are not directly apparent in the CFD data. In addition, the applicability of the introduced bookkeeping scheme is verified by comparing the gas turbine model response at the sample points to the corresponding aero-numerical result values, $\hat{Y}$, which has yielded satisfactory agreement across all designs. An example for D_0 was shown in Table 4.3.

As a second step, heuristics allowing for integrated calculation are derived. Targeting the execution of integrated parametric studies, the creation of surrogate models continuously defined across the considered design space is required, which facilitate the approximation of the discrete data sets obtained from the aero-numerical design space exploration. For response fitting, approaches based on single and multi-dimensional linear or nonlinear regression have been selected using a least-squares algorithm [184]. Since the available sample size is small and the number of input variables is low, this method is preferred over alternative, non-parametric surrogate modeling techniques. As an intrinsic characteristic of the notion of regression analysis, transparency and reproducibility is ensured due to the possibility to directly state the regression approach, coefficients and fitting quality. Fitting is conducted in a straightforward way by using the datasets $\hat{X}$ and $\hat{Y}$ to obtain regression functions. The

implemented process is executed with respect to both design and off-design parameters yielding sizing heuristics, f, and operational characteristics, g. As a key requirement for ensuring adequate surface fitting quality, each regression is validated against the original data by comparing the model response evaluated at the sample points with the original sample result values $\hat{Y}$. In case of excessive deviation in maximum or root mean squared errors, the regression approach is adapted.

The derived regression functions are integrated in the propulsion system synthesis model as parametric design and off-design laws, respectively. As part of this step, the model parameterization is adjusted to focus at executing integrated studies. Therefore, typical study variables such as specific thrust are set as input parameters, while e.g. π_{int} now is part of the power plant internal performance prediction process and hence becomes an output parameter, thus changing the direction of information flow compared to the previously conducted regression analysis.

As a third procedural step, adequate accuracy of the matching process is verified. Therefore, the synthesis model featuring the derived design and off-design laws is evaluated at the sample points (see Figure 4.6). The model response, Y, of a compilation of sizing and performance parameters including e.g. ΔF_X, π_{int}, P_{is} as well as flow areas and mass flows is compared to the corresponding expected values within the set of aero-numerical data. The following metric for a relative deviation is employed:

$$\Delta Y = \frac{\left|Y - \hat{Y}\right|}{\hat{Y}} \tag{4.6}$$

A graphical evaluation of ΔY will be provided in Section 4.7. Upon verification of both the numerical validity and physical plausibility of the results, the derived heuristics are integrated into the superordinate sizing and performance prediction process.

4.4 Regression Results at Nominal Design Conditions

Serving the purpose of establishing the capability to execute parametric studies across the design space, regression analyses have been conducted to derive surrogate models for important parameters described in this section. The current section refers to nominal design conditions, i.e. Maximum Climb (MCL) thrust setting at Top-of-Climb (ToC) conditions. From Section 4.1, it is recalled that the domain covered by the numerical sample data is strictly defined within the intervals $\hat{h}_{AIP} \in$ [0.5m; 0.9m], $\widehat{FPR}_{ds} \in$ [1.249; 1.498] and $\hat{M}_{0,ds} \in$ [0.75; 0.85]. It is assumed that due to the smoothness of the derived regression results the extrapolation beyond these domains is valid, in the first instance.

4.4.1 Intake Total Pressure Recovery Ratio

While in conventionally installed power plants viscous losses within the streamtube ahead of the intake are typically negligible, as a consequence of the momentum deficit in front of the FF propulsion system intake caused by viscous BL flow, for PFC arrangements the total pressure at the engine interface position is reduced relative to its free stream value. Therefore, a degradation in intake total pressure recovery ratio is obtained over conventional installations. This quantity is defined in the present context as the total pressure ratio between fan face and free stream, $\pi_{int} = p_2/p_0$, thus capturing both the loss effects due to reduced ram pressure, p_1/p_0, and the traditional total pressure ratio within the intake duct described by p_2/p_1.[22] Depending on the geometric arrangement and operating conditions, the degradation may be substantial [81], [124].

[22] While in the literature different definitions for intake pressure ratio exist, a definition typically employed (e.g. by the software GasTurb) defines this property as p_2/p_1 [191].

For the nominal design conditions, the independent design variables constituting the basis for the regression analysis comprise duct height at the AIP and FPR_{ds}. The parameter π_{int} is recognized to be highly dependent on the duct height at the AIP. In contrast to that, the dependency of π_{int} on FPR_{ds} is found to be minor and thus disregarded in the present regression model. A polynomial regression approach of second degree is considered appropriate. For the considered widebody application (see Table 4.1) the identified correlation function is given as

$$\pi_{int} = 0.767 + 0.221h_{AIP} - 0.0809h_{AIP}^2, \quad h_{AIP} \text{ in [m]} \tag{4.7}$$

The sampled data along with the derived regression function is presented in Figure 4.7. A synopsis of the data fitting quality results of this regression as well as the regression models to be presented in this chapter is provided in Table C.2 in Annex C.

The resulting behavior of π_{int} appears reasonable, since for decreasing h_{AIP} the effective mass flow-averaged BL velocity reduces translating into an increasingly severe equivalent intake total pressure loss. Within the frame of aircraft-integrated studies, an additional non-dimensional pressure loss is applied to account for pressure losses due to the presence of intake struts.

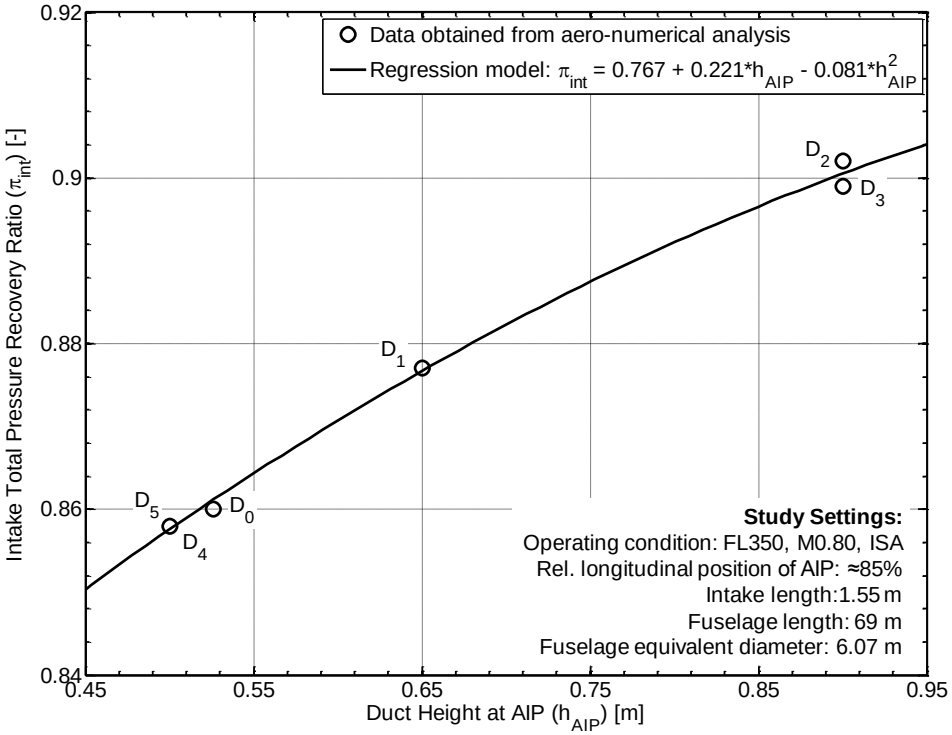

Figure 4.7: Regression model for FF power plant intake total pressure recovery ratio at nominal design conditions

4.4.2 Integration Impact Metric

Since the descriptor for the integration impact has been found sensitive to both h_{AIP} and FPR_{ds}, these parameters are chosen as inputs to the regression model. Due to the nonlinear behavior of the computed sample response data, a polynomial approach of second order in two dimensions is chosen. The resulting correlation is given as:

$$\Delta F_X = 38.75 - 23.37FPR_{ds} - 8.990h_{AIP} - 16.08h_{AIP}^2 + 33.00h_{AIP} \cdot FPR_{ds}, \quad \Delta F_X \text{ in [kN]}, h_{AIP} \text{ in [m]} \tag{4.8}$$

The regression result is visualized in Figure 4.8. The regression error at the individual sample points is correlated to the size of the cross-shaped symbols included in the figure. As expected, ΔF_X is highly dependent on the radial size of the propulsor intake. This is attributed to different physical effects captured in ΔF_X. For increasing h_{AIP}, a higher effectiveness of the wake filling mechanism is expected. A larger share of the airframe wake is compensated by the localized FF jet velocity in case of increasing h_{AIP}, thereby yielding globally lower wake and jet dissipation losses. When expressing the dependency in terms of ingested momentum deficit, increasing h_{AIP} is equivalent to a higher share of fuselage viscous momentum deficit being captured by the propulsive device and hence, less fuselage momentum deficit is spilled around the nacelle. Therefore, a higher ingested momentum deficit can be expected for growing h_{AIP}. Also included in Figure 4.8 for information purposes are contours of an efficiency metric relating the power of the net forward force experienced in the CFD setup to the isentropic power absorbed by the FF,

$$\hat{\epsilon} = \frac{\hat{F}_X V_0}{\hat{P}_{is}} \tag{4.9}$$

The magnitude of $\hat{\epsilon}$ has been computed for all designs and a two-dimensional regression has been produced. As can be seen, $\hat{\epsilon}$ favors designs characterized by large propulsive devices and high design FPRs, which may be attributed to the above discussed trends of wake filling effectiveness and intake total pressure recovery. It should be noted that $\hat{\epsilon}$ only captures the characteristics of the arrangement investigated in the CFD setup without a reference condition and no conclusions can be drawn on the relative differences to a setup comprising the isolated installation of the FF power plant to the adjacent airframe components (Setup B). The discussion in the following will therefore elucidate further significant implications captured in the ΔF_X metric.

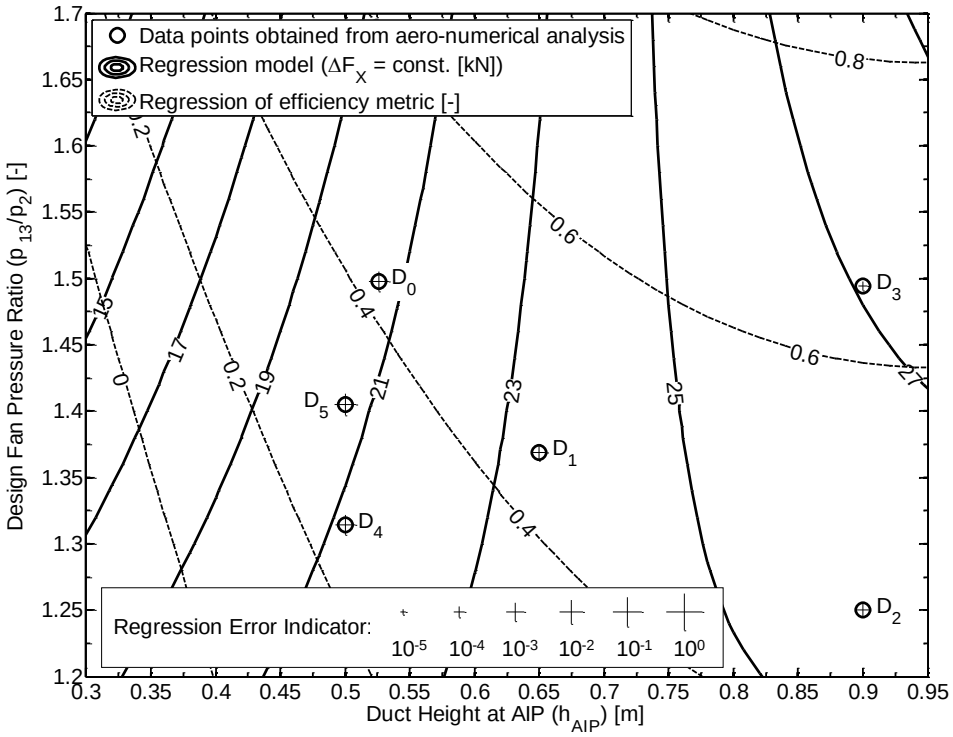

Figure 4.8: Regression model for FF propulsion system integration impact matric at nominal design conditions. For settings, see Figure 4.7

While the available aero-numerical data does not explicitly comprise a complete dataset of the distribution of static pressure along the fuselage body for the various design settings, it is nonetheless of interest to analyze the mutual interaction between propulsor design or off-design settings and the

aerodynamic characteristics of the fuselage regions upstream and downstream the FF device. Therefore, the static pressure, p_s, at the AIP position has been derived from the available values of local average total pressure and Mach number using basic relations of compressible flow and assuming invariant values of the heat capacity ratio γ. Similarly, the static pressure at the nozzle exit has been determined for all design and off-design conditions covered in the CFD investigation. It is assumed, in the first instance, that the trends at the AIP, in particular static pressure, are representative of the tendencies occurring at the diffusing section upstream the FF intake, while the characteristics at the nozzle exit are taken to be representative of the evolution along the nozzle aft-body. Figure 4.9 presents a summary of Mach number and pressure ratios $p_s/p_{s,0}$ at these locations, where $p_{s,0}$ is the ambient static pressure. As can be seen, the geometric design parameters have an impact on the Mach number at the AIP, M_{AIP}, on the corresponding static pressure ratio and hence local pressure forces. As a result of the design approach that had been followed during the sizing of the duct geometry of the design cases investigated in the CFD setup, which features a constant offset between duct heights at AIP and fan inlet, for increasing h_{AIP} an increasing area ratio A_{AIP}/A_2 is obtained. Therefore, designs with higher h_{AIP} generally exhibit increased static pressure at the diffusing fuselage section, hence giving scope to locally alleviated pressure drag. In fact, based on the presumption of the local static pressure being representative for the s-shaped fuselage section, for designs D_2 and D_3 even a positive static pressure ratio is obtained. This tendency is construed to contribute to the rising values of ΔF_X for growing h_{AIP}.

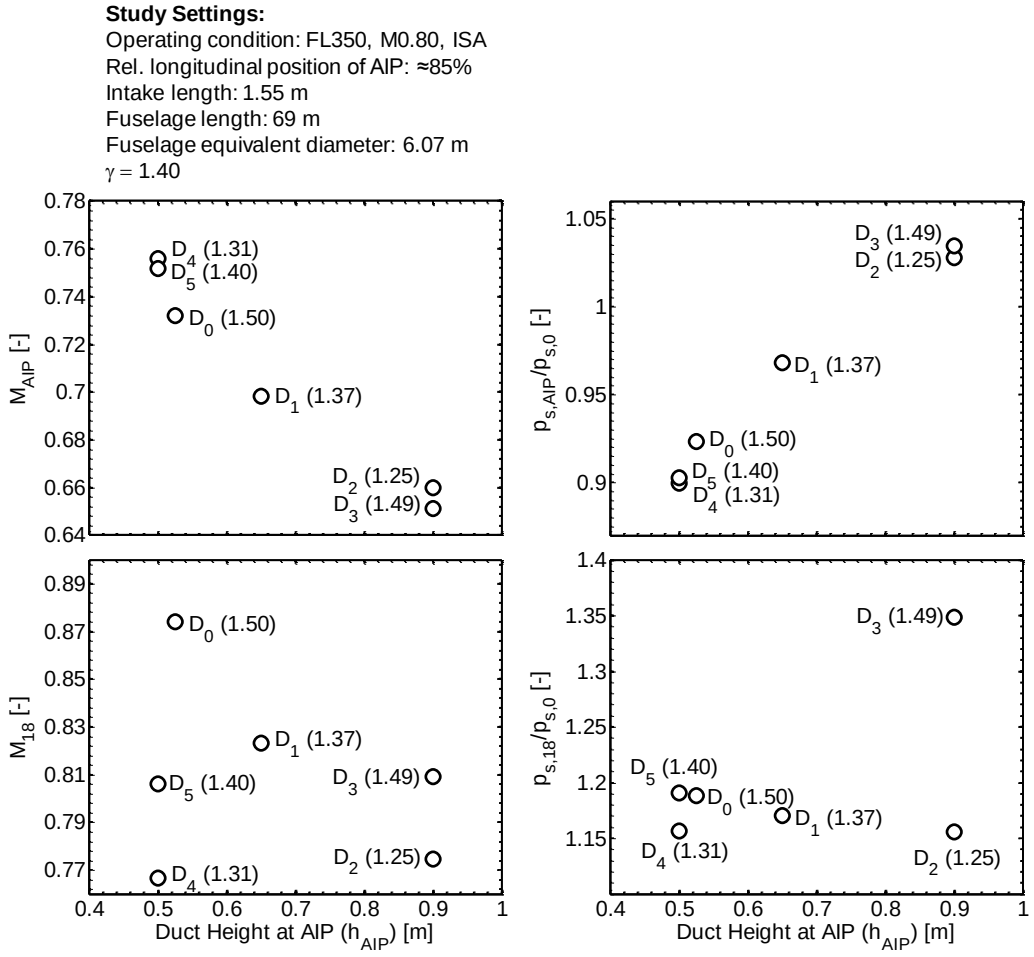

Figure 4.9: Mach numbers and normalized static pressures at AIP and nozzle exit for considered design cases. Parenthesized values denote design FPR.

It can be seen from Figure 4.8 that the dependency of ΔF_X on h_{AIP} is much stronger than on FPR_{ds}. The trend of ΔF_X against FPR_{ds} depends on the duct height. Towards smaller h_{AIP}, increasing FPR yield decreasing ΔF_X, while for h_{AIP} larger than approximately 0.7 m an opposite trend is obtained. Similar to h_{AIP}, several aspects contribute to the dependencies of ΔF_X on FPR. Beyond the effect of varying FPRs on the WF potential due to changing jet velocities, secondary effects are connected to slight variations in design mass flow. For example, inspection of two designs featuring equal duct height but different design FPRs such as D_2 and D_3 reveals a slightly smaller mass flow for D_3 due to minor differences in intake pressure ratio, thus causing M_{AIP} to reduce. Consequently, a minor increase in $p_{s,AIP}$ is obtained for D_3 over D_2. Since generally for larger h_{AIP} the levels of static pressure are elevated, the lever attainable from static pressure increase appears to be higher. An additional effect contributing to the ΔF_X characteristic refers to the impact of FPR on nozzle exit static pressure and hence the impact on local static pressure on the nozzle aft-body. Due to the contracting shape of the body, static pressure ratios greater than unity translate into a force oriented in forward flight direction. As can be observed from Figure 4.9, for increasing h_{AIP} the improving intake total pressure ratio causes absolute static pressure at the nozzle exit, $p_{s,18}$, to increase for a given design FPR (compare e.g. designs D_0 and D_3). Hence, the impact on the pressure force on the nozzle cone becomes augmented for greater h_{AIP}, which is considered an important effect associated with the inversion of the ΔF_X versus FPR characteristic as a function of h_{AIP}.

4.5 Design Speed Sensitivity

In order to allow for parametric studies of varying design cruise speeds, regression functions describing the sensitivity of π_{int} and ΔF_X with respect to the design Mach number have been derived from the CFD data. Besides the nominal design condition, the aero-numerical dataset contains sample points at two additional Mach numbers (see Table 4.2) computed for design D_0. The data has been normalized with the nominal design condition and is considered representative for other design settings. In Figure 4.10, the regression results are presented for both metrics. For the normalized π_{int}, a polynomial approach of second order is selected,

$$\frac{\pi_{int}}{\pi_{int,ref}} = -0.465M_{0,ds}^2 + 0.349M_{0,ds} + 1.019 \tag{4.10}$$

while for ΔF_X an approach based on a rational function,

$$\frac{\Delta F_X}{\Delta F_{X,ref}} = 90.4274 - 245.456M_{0,ds}^{-1} + 255.270M_{0,ds}^{-2} - 119.230M_{0,ds}^{-3} + 21.0560M_{0,ds}^{-4} \tag{4.11}$$

yields optimum fitting quality.

The effects causing π_{int} to improve towards lower Mach numbers will be discussed in Section 4.8. The right part of Figure 4.10 shows in conjunction with ΔF_X the net forward forces of CFD and gas turbine based calculations. These parameters decline towards higher Mach numbers, thus indicating a decreasing benefit of BLI at higher speeds. Analysis of the contributing terms of F_X show that stronger ram drag and penalized π_{int} causing reduced gross thrust trigger the reduction in F_X for a given fan power input. While the effects on propulsor net thrust are surmised to be similar in both setups, the speed sensitivity of the semi-empirical drag prediction apparently deviates from the trend exhibited by the CFD setup, thus causing F_X and $\hat{F}_X$ to diverge. This is reflected in the increasing characteristic of ΔF_X with rising Mach numbers.

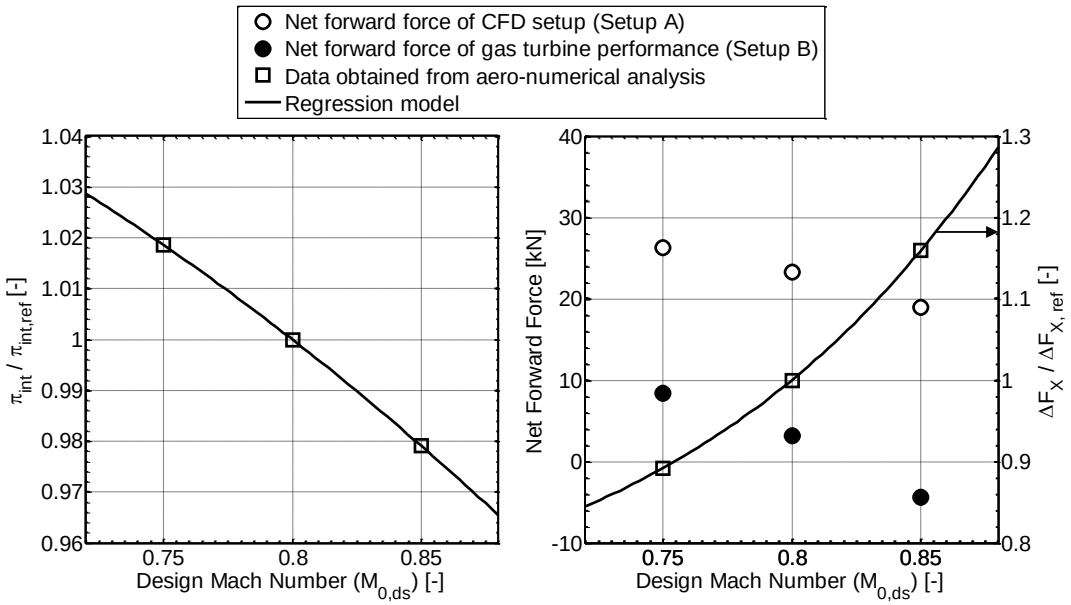

Figure 4.10: Regression models for design intake total pressure ratio (left) and design integration impact metric (right), each normalized for nominal design conditions at M0.80

4.6 Part Power Characteristics

Depending on the FF propulsion system power setting, the interaction between the incoming flow and the power plant performance is altered. In order to facilitate the parametric mapping of the resulting effects during performance evaluation, regression models have been fashioned for the operational intake total pressure ratio and the integration metric.

4.6.1 Intake Total Pressure Recovery Ratio

As a result of the changing BL profile, a variation of the average intake properties and hence of intake total pressure ratio can be expected. As can be observed from the sampled data, the sensitivity of power setting on intake pressure ratio tends to be greater for larger duct sizes, as the portion of the influenced BL becomes larger. The available data captures the impact of the propulsor power setting on the upstream effect of the fuselage flow field: for lower power settings, reduced suction effect causes the BL velocity profile to become thicker and hence for a given duct height a lower average Mach number and reduced intake pressure ratio is obtained.

In order to allow for the mapping of these effects, a multi-dimensional regression has been applied to the aero-numerical data at nominal cruise conditions featuring sensitivity with the size of the propulsor (h_{AIP}) and the power setting. The latter parameter is correlated to the FF operating FPR normalized by its design value, i.e.

$$FPR_{rel} = FPR/FPR_{ds} \tag{4.12}$$

The regression is based on a full polynomial approach of second order in both dimensions and is given as:

$$\pi_{int} = 0.593 + 0.0450h_{AIP} - 0.0631h_{AIP}^2 + 0.406FPR_{rel} - 0.223FPR_{rel}^2 \ldots \\ +0.151h_{AIP} \cdot FPR_{rel},\ h_{AIP} \text{ in [m]} \tag{4.13}$$

An evaluation of the regression model is presented in Figure 4.11 indicating contours of π_{int} against

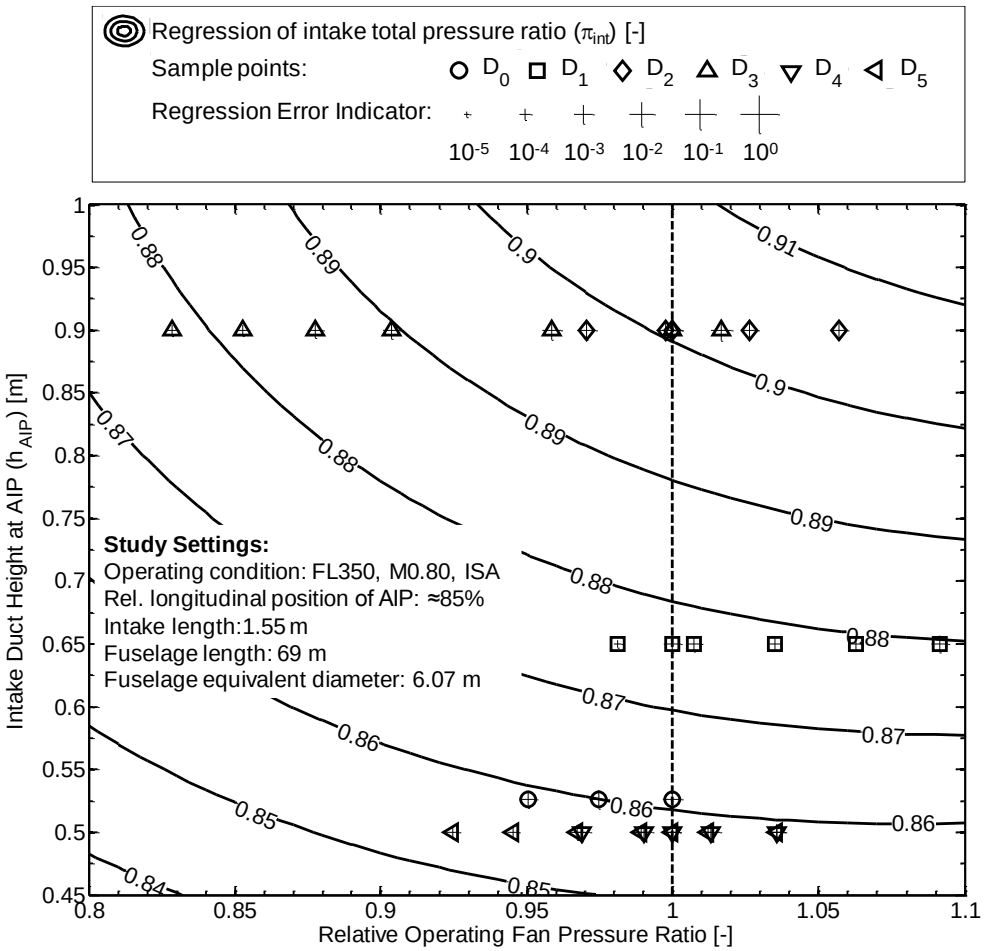

Figure 4.11: Regression of intake total pressure ratio at design speed and part power. The dashed line denotes the design condition

h_{AIP} and FPR_{rel}. As can be seen, reducing power settings yield decreasing values of π_{int}, which results from the weaker suction effect upstream of the fan, thus yielding a thicker BL profile and accordingly a reduced average total pressure. For FPR_{rel} = 1, a correlation for the design characteristic of π_{int} in dependence of h_{AIP} is obtained, which is in almost exact agreement with the characteristic described in Section 4.4.1, thus verifying the generalization of the pure design regression given in the present section. The characteristics of π_{int} have been normalized using the design values and are considered representative for other flight conditions, in the first instance.

4.6.2 Integration Impact Metric

Similarly, for the operational integration impact metric a regression analysis has been conducted. Due to only minor influence of design settings, the compilation of all normalized data points has been fitted as a function of the normalized operating FPR using a fourth-order polynomial approach:

$$\frac{\Delta F_X}{\Delta F_{X,ds}} = -4.8850 + 31.576 FPR_{rel} - 64.504 FPR_{rel}^2 + 58.919 FPR_{rel}^3 \ldots - 20.104 FPR_{rel}^4 \tag{4.14}$$

A strong dependency on power settings is observed in Figure 4.12. The impact of changing fan power settings on the static pressure distribution and hence the pressure drag exhibited by the fuselage constitutes an important contribution to the change of the net forward force as a function of FPR_{rel}.

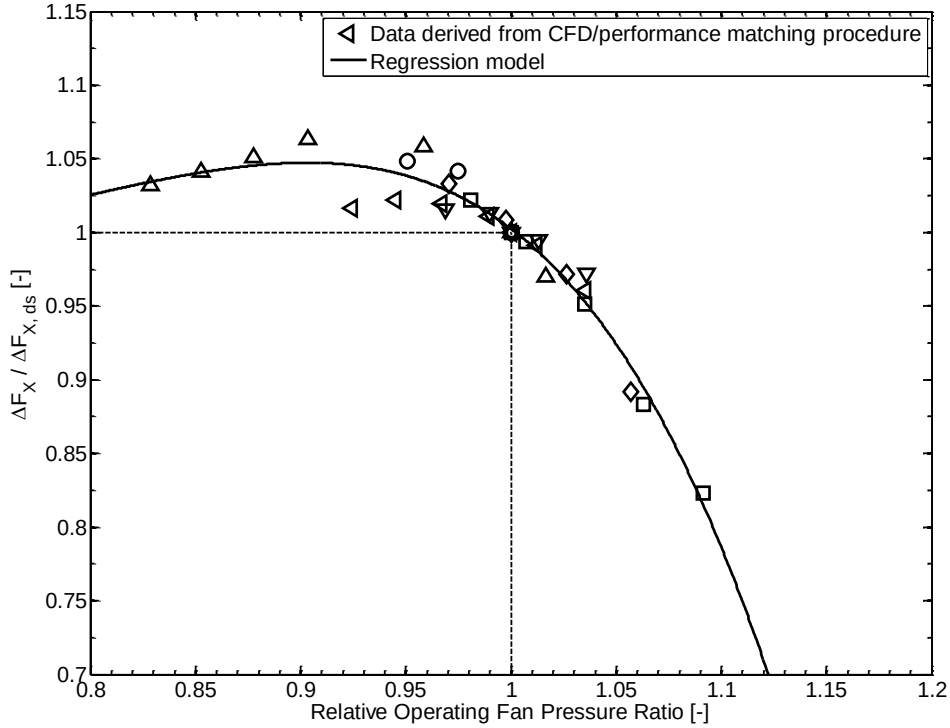

Figure 4.12: Regression of integration impact metric at part power. For marker symbols, see legend in Figure 4.11

Similar as for the analysis of design characteristics above, static pressure trends at the AIP and nozzle exit have been derived from the set of available numerical data, which are displayed in Figure 4.13. With regards to the diffusing fuselage section upstream the intake, for smaller FPRs, suction into the fan is weakened, thus yielding lower local flow Mach numbers and hence higher static pressure. Therefore, a locally reduced pressure drag or even positive pressure force is surmised to occur. As noted above, the available data does not directly allow for the quantification of fuselage drag characteristics at each power setting, however, comprises the distribution of static pressure along the fuselage for one single design sample (D_0) with and without the propulsor being active (see Figure B.1 in Annex B). The latter hypothetical condition may be regarded to represent a lower limiting case of power setting, i.e. $FPR_{rel} \rightarrow 1$ and confirms the presumption of increasing static wall pressure as the operating FPR reduces. Now, the pressure force acting on a body of revolution in axisymmetric flow can generally be derived from the static pressure distribution according to Reference [185]:

$$D_p = 2\pi \cdot \int_0^{s_L} p_s(x) \cdot y(x) \sin\theta \mathrm{d}s \tag{4.15}$$

where ds and s_L denote the incremental and total arc length of the body contour, respectively, y represents the radial contour coordinate and θ the angle between the local tangent to the contour and the body longitudinal axis. Equation (4.15) has been evaluated subsequently for the cases with active and inactive FF operation and the difference in pressure drag accumulated from the fuselage nose to the intake highlight derived. In Figure B.1 in Annex B, an evaluation of the difference in pressure force is provided. It can be seen that between the discrete cases of inactive FF and a FPR of 1.5 an approximate increase of 17.9 kN in pressure drag results with regards to the diffusing fuselage section. Hence, taking e.g. a typical cruise operating FPR of 80% of the design value and assuming a linear trend, an approximate 3.6 kN decrease in pressure drag can be expected between the part power condition and the full power operation. As a converse effect, however, reducing FPR_{rel} cause decreased wall pressure at the nozzle cone (see Figure 4.13). Similar to the aft-fuselage section, the

difference in pressure force between powered and unpowered propulsor settings has been derived (see also Figure B.2 in Annex B) indicating a decreased forward acting pressure force on the nozzle aft-body for reducing levels of FPR_{rel}. In addition, a higher curvature of the streamlines in the vicinity of the nacelle stagnation point associated with lower power settings is observed from flow pictures available for several power settings. Therefore, in similarity to conventionally installed turbofans, spillage drag is expected for reducing power settings [178], [186]. As can be seen, the superposition of these effects is reflected in the concave shape of normalized ΔF_X displayed in Figure 4.12, which exhibits a maximum at approximately FPR_{rel} = 0.91.

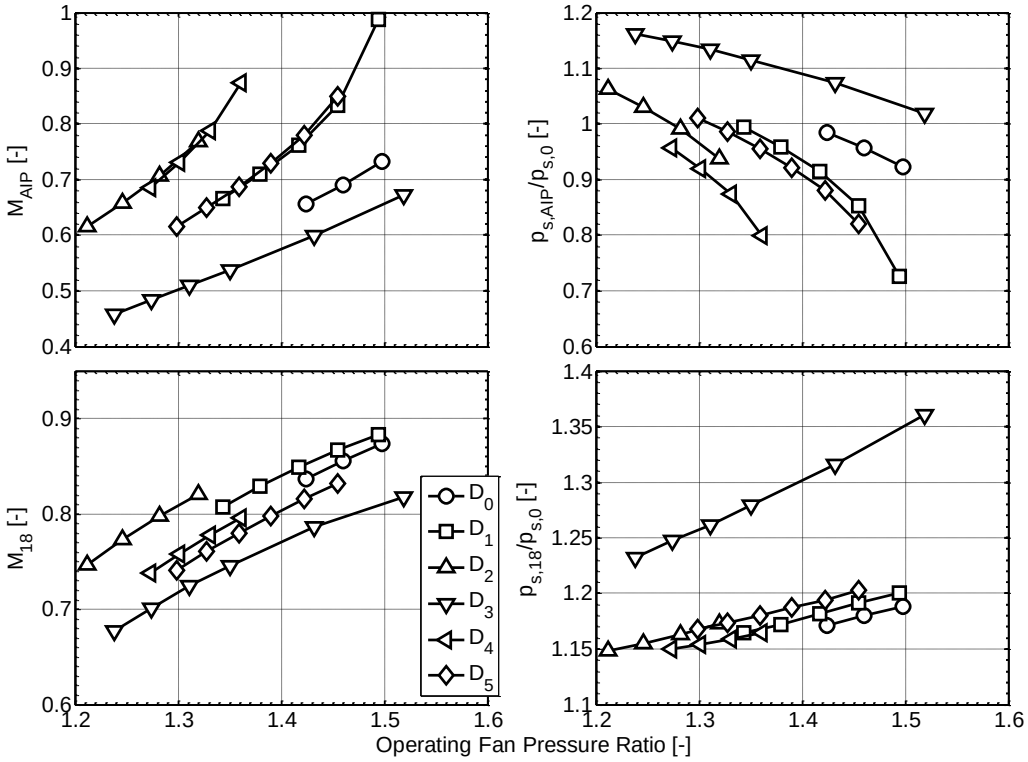

Figure 4.13: Mach numbers and relative static pressures at AIP and nozzle exit for considered design samples and power settings. For study settings, see Figure 4.9

4.7 Validation of the Matching Approach

In this section, the applicability and accuracy of the gas turbine synthesis model incorporating the derived heuristics as parametric laws and featuring the correspondingly adapted model parameterization is demonstrated. Therefore, the results of the model are compared against the original numerical data (see equation (4.6)). As outlined in Section 4.3, different from the previous steps of the matching procedure, the parameterization of the propulsion synthesis model is adjusted to the purpose of conducting integrated studies. Thus, the net forward force acting on the configuration in Setup A, $\hat{F}_X$, is declared as an input in conjunction with design specific thrust, F_N/w_2, while e.g. π_{int}, geometric properties and mass flow become result values. Based on the obtained results presented in Figure 4.14, the matching process is considered to appropriately represent the CFD computed characteristics. A root mean squared error of 1.0% is obtained. While for the sake of clarity Figure 4.14 is restricted to nominal design conditions, in Figure B.3 in Annex B, similar visualizations for several power setting are provided for each design sample. The obtained deviations are comparable in magnitude.

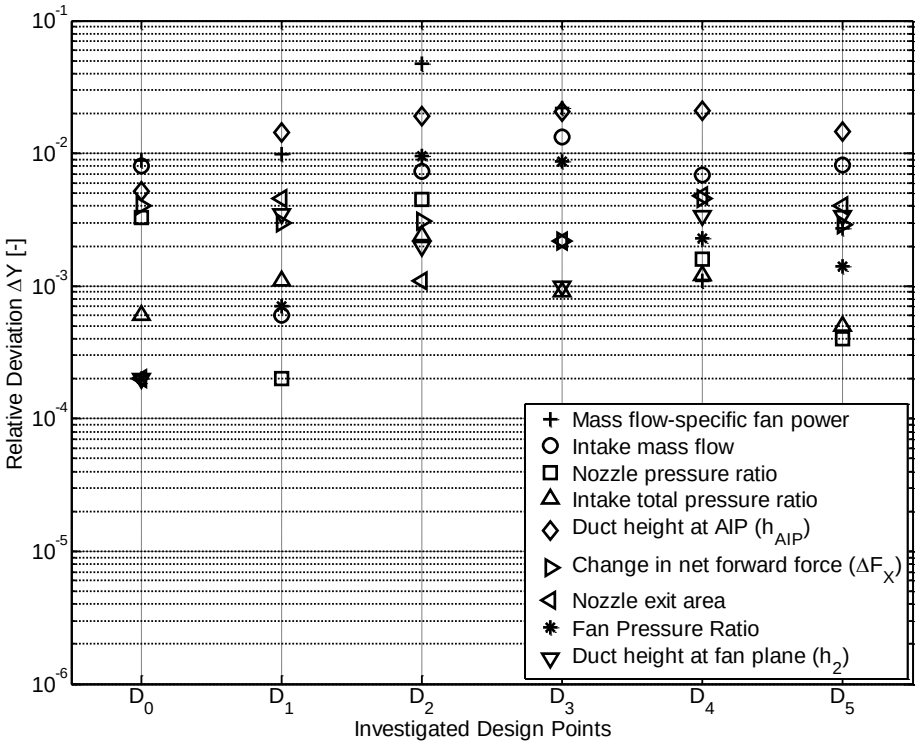

Figure 4.14: Validation results of implemented model matching procedure at nominal design conditions

4.8 Estimation of Characteristics at Off-design Flight Conditions

Since the available aero-numerical data is limited to cruise conditions, the impact of varying flight Reynolds numbers intrinsic to changes in altitude and Mach number and thus variations in BL flow characteristics along the flight mission is estimated using a simple scaling procedure. The non-dimensional fuselage BL velocity profile derived from the aforementioned CFD-based computations (see Section 4.1) is scaled using the BL thickness expected at the respective flight condition defined through altitude, Mach number and ISA temperature deviation. Here, a classic correlation for turbulent BL flow along a flat plate is employed, in the first instance [172, p. 328],

$$\delta_x = 0.37 x_{AIP} \cdot \mathrm{Re}_x^{-0.2} \tag{4.16}$$

where Re_x denotes the local Reynolds number based on the position of the AIP located at the axial position x_{AIP}. From the scaled velocity profile the mass flow averaged Mach number, $\bar{M}_1$, is calculated and subsequently employed to determine the total pressure recovery ratio p_1/p_0 from basic relations of compressible flow,

$$\pi_{0,1} = \frac{p_1}{p_0} = \left(\frac{1 + \frac{\gamma - 1}{2} \bar{M}_1^2}{1 + \frac{\gamma - 1}{2} M_0^2} \right)^{\frac{\gamma}{\gamma - 1}} \tag{4.17}$$

where p_1 indicates the total pressure at the AIP, while p_0 represents the same quantity evaluated at free stream conditions.[23] The approach has been validated against corresponding CFD computations available at two Mach numbers and an altitude of 10,668 m. Therefore, the computed values of $\pi_{0,1}$

[23] In equation (4.17), the heat capacity ratio γ is assumed identical for both considered conditions.

have been normalized with the nominal design point at M_0 = 0.80 and compared to the respective CFD samples. As can be seen from Table 4.4, the tendency obtained from the implemented method is reasonably captured.

As an initial approximation, the implemented method is considered applicable throughout the flight envelope. In Figure 4.15, an evaluation is visualized. The shown computational domain is bound by the typical operational envelope of subsonic transports featuring restrictions through minimum and maximum Calibrated Air Speeds (CAS) of 170 and 350 kts, respectively, a Maximum operating Mach number of 0.86 and a service ceiling of 12,500 m [187].

M_0 [a] [-]	$\pi_{0,1}$ [b] [-]	$\pi_{0,1}/\pi_{0,1,ds}$ [b] [-]	Error [c] [%]
0.75	0.877	1.016	–0.22
0.80 [d]	0.863	1.000	±0.00
0.85	0.849	0.983	+0.38

[a] at FL350 (10,668 m), ISA
[b] calculated with present method
[c] relative to CFD-simulated values at design D_0
[d] nominal design point

Table 4.4: Validation results of FF power plant off-design pressure recovery prediction for considered widebody aircraft layout conducted for design D_0

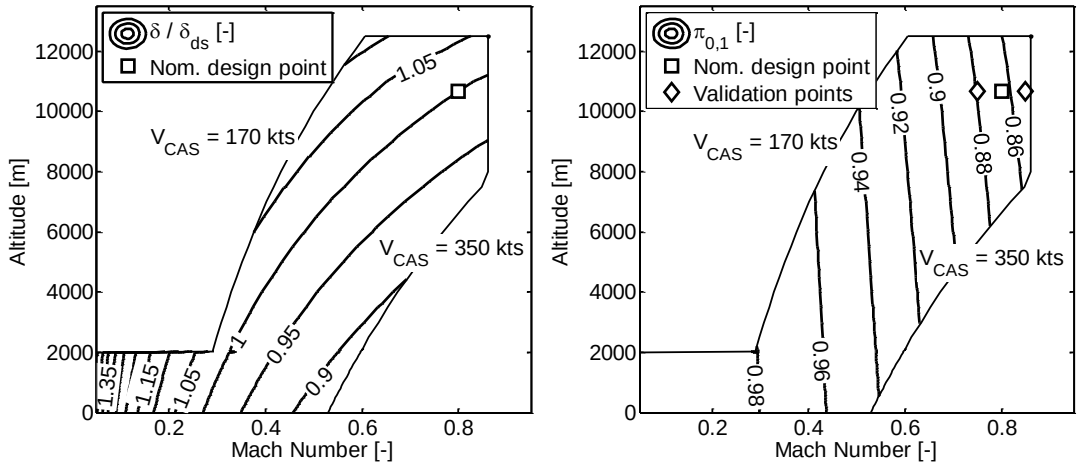

Figure 4.15: Estimation of boundary layer properties (relative fuselage boundary layer thickness at AIP, left, and total pressure recovery ratio, right) within the typical flight envelope

The left part of Figure 4.15 shows the scaled fuselage BL thickness at the AIP relative to the thickness at the declared nominal design point located at M0.80 and FL350 (10,668 m). It can be seen that along a typical climb segment featuring constant CAS[24] the variation of the relative BL thickness is small. Inspection of the right part of Figure 4.15 indicates that the pressure recovery ratio decreases for increasing Mach numbers. This is due to the fact that, although higher M_0 yield decreasing BL thicknesses and hence increasing average Mach numbers at the AIP, $\pi_{0,1}$ itself is also inversely correlated to M_0 (cf. equation (4.17)), and hence, $\pi_{0,1}$ tends to reduce. At takeoff conditions, $\pi_{0,1}$ is significantly improved compared to the typical ToC point, hence giving scope to mitigating the adverse effects of the low-momentum BL flow at low-speed operating conditions. However, as a result of three-dimensional flow effects that may be experienced during operation at large incidence angles at takeoff

[24] Typically, above 10,000 ft (3,048 m) up to the crossover point from which the climb schedule is characterized by a constant Mach number.

rotation, additional pressure losses can be expected. Due to the inexistence of corresponding empirical data for the present application, in the first instance, the impact of incidence angles on intake total pressure loss is mapped using interpolated characteristics of conventionally installed turbofans from Reference [178, Fig. 13.13] described in Section 5.1.5.1.

For the prediction of the off-design characteristics of the integration impact metric, a similar procedure has been developed. The model assumes the mass-averaged flow momentum at the intake highlight as the representative scaling variable (see Figure B.4 in Annex B). The results of the scaling law have been validated for two representative Mach numbers within the flight envelope (see Table 4.5), where the reference values have been derived from the CFD data using the matching procedure described in Section 4.3. The obtained level of agreement is considered satisfactory.

M_0 [a] [-]	$\Delta F_X/\Delta F_{x,ds}$ [b] [-]	Error [c] [%]
0.75	0.892	–1.9
0.80 [d]	1.000	±0.0
0.85	1.159	–2.2

[a] FL350 (10,668 m), ISA
[b] calculated with present method
[c] relative to CFD-simulated values
[d] nominal design point

Table 4.5: Validation results of off-design integration metric prediction conducted for design D_0

4.9 Overall Synthesis of Methods

As a result of the methodological concept proposed for the mapping of aero-propulsive interaction effects, the parameters π_{int} and ΔF_X have been recognized to be of key significance. Now, for the aircraft-integrated evaluation of the FF propulsion system, the capability for continuous mapping of these metrics throughout the design space and within the operating envelope is required. In Figure 4.16, a workflow is presented illustrating the connection of the implemented models and the corresponding information exchange used for the parametric calculation of FF intake total pressure ratio and the integration impact metric at design and off-design conditions. Exemplified for π_{int}, starting from the calculation of the design value evaluated at the power plant sizing point, i.e. ToC condition, (Section 4.4.1), $\pi_{int,ds}$, the characteristics at all other operating points along the mission, $\tilde{\pi}_{op}$, are calculated as a function of flight altitude, H_0, Mach number, M_0, and ISA temperature deviation, ΔT_{ISA} (Section 4.8) using a simple loss-based scaling approach. At the representative takeoff point, the characteristic used for the mapping of incidence effects is applied (see Section 5.1.5.1) and superimposed with the operational behavior. Finally, the normalized characteristics predicting the impact of off-design power settings, $\tilde{\pi}_{pp}$, (Section 4.6) are applied. The resulting intake pressure ratio is used as an input for the evaluation of the power plant synthesis model. A similar procedure has been implemented for the mapping of the integration impact metric.

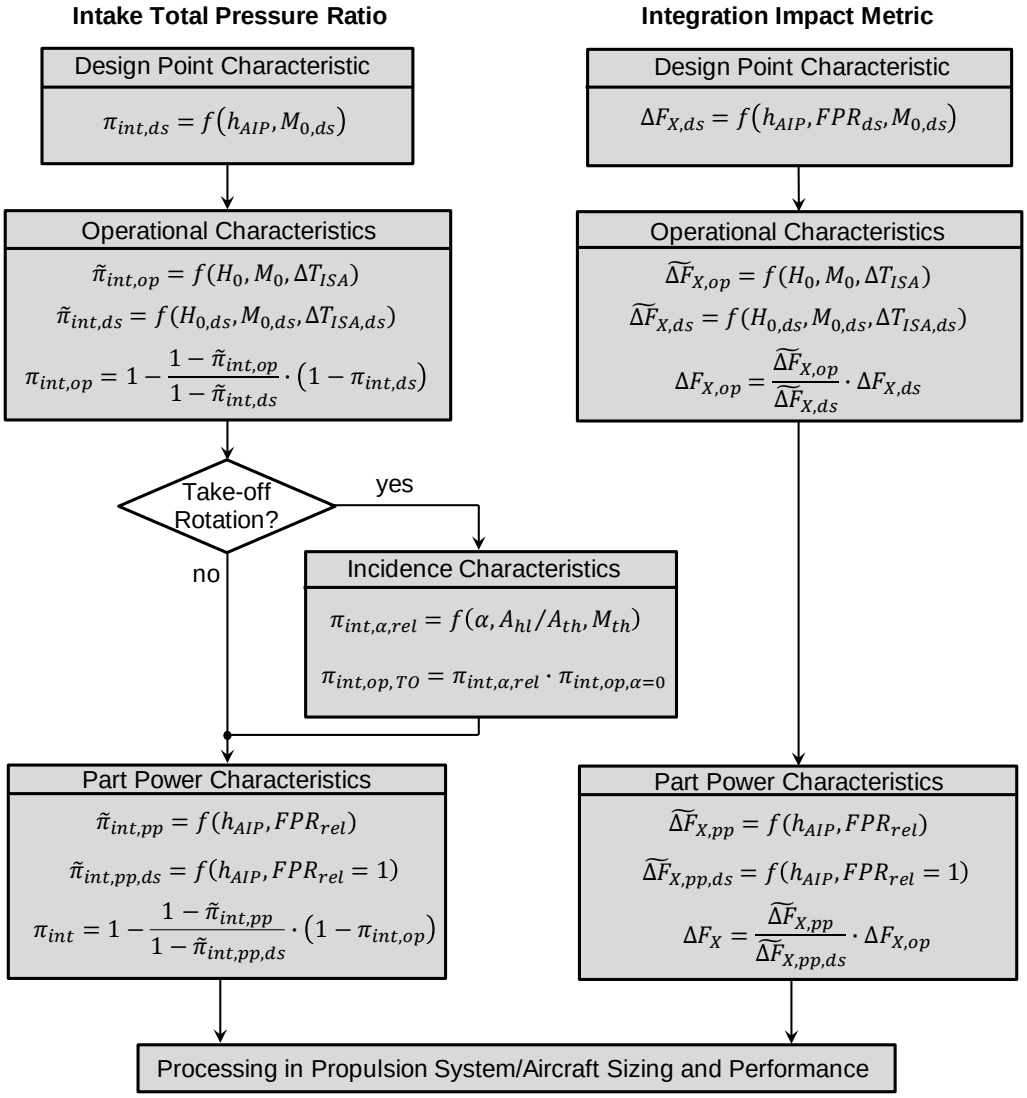

Figure 4.16: Flowchart indicating the implemented procedure for the calculation of design and off-design FF intake total pressure ratio and integration impact metric

5 Propulsion System Integration Methods

A major part of the present work is concerned with the synthesis of propulsion system design and performance and its integrated assessment at aircraft level. Emphasis is placed on the parametric mapping of key propulsion system design aspects covering thermodynamic cycle design, flow path sizing, geometric dimensioning and weight prediction. Therefore, in the present chapter, a compilation of methods for the conceptual modeling of aero-engine design and operating characteristics is presented. Beyond the development of a set of customized disciplinary models, a main focus of the present work is on establishing a calculation process facilitating the consistent propagation of the characteristics of BL ingesting power plants to the aircraft level while similarly supporting the assessment of conventionally installed power plants. The process allows for comparative system and aircraft-level trade-off analyses with respect to typical objective functions including mission fuel burn.

Starting from the description of cycle design and performance synthesis, a set of design laws and off-design heuristics is presented and validated in Section 5.1. Appropriate models are introduced for the parametric mapping of the different loss mechanisms associated with the considered propulsion system architectures. While flow path geometry is based on corrected mass flows, axial Mach numbers and hub/tip ratios, external dimensions are mapped utilizing semi-empirical heuristics. Both aspects constitute essential inputs to the power plant weight prediction elaborated in Section 5.3. In order to ensure consistency between conventionally installed and highly integrated power plants, the methodological basis for propulsion synthesis is applicable to both propulsion system architectures, while methods specifically developed in this thesis to allow for the assessment of the FF propulsion system are presented in Section 5.2. Sections 5.4 and 5.5 provide a description of the methodological framework employed for the aircraft-integrated assessment conducted as part of the present work including the description of surrogate-based incorporation of propulsion system characteristics. To round off, in Section 5.6, metrics useful for performance assessment at propulsion system and aircraft level are described.

5.1 Conceptual Propulsion System Design Methods

Conceptual cycle design studies and performance calculations are based on an Aircraft Propulsion System Simulation (APSS) framework introduced by Schmitz [188], [189] and Kaiser *et al.* [190]. Due to the implementation in the Matlab® [184] programming environment offering full accessibility and modifiability of the source code, the framework features both transparency and large flexibility for adaptation and extension of the underlying methods. In addition, it provides the possibility to assemble arbitrary and novel engine configurations and enables convenient interfacing with other programs, thus allowing for implementing user-defined pre and post-processing procedures. The use of Matlab's built-in functionality for vectorization highly increases the computational performance [189], thus being particularly suited for the generation of simulation sample data for subsequent surrogate model creation. In particular, due to the possibility for the integration of custom methods and iteration schemes into the simulation setup, in this work APSS was preferred over commercial propulsion simulation solutions. An overview of the fundamental thermodynamic performance methods featuring a fidelity level similar to the software GasTurb® [191] can be found in Reference [189].

Thermodynamic fluid properties are represented using half-ideal gas equations,[25] where the functional dependencies are computed from tabulated data derived from the NASA Chemical Equilibrium and Applications (CEA) database [192], [193]. The atmospheric properties are modeled according to the International Standard Atmosphere (ISA) model with optional application of temperature deviation. The basic functionality of APSS was validated against the software GasTurb 11® [191] and GasTurb Details 5® [194], cf. Reference [189]. Apart from user-defined listings of key engine parameters, enhanced means to verify the physical and numerical plausibility of the calculated results are offered through graphical result representation such as enthalpy-entropy diagrams of the thermodynamic cycle and simplified visualization of the geometric general arrangement of the components.

For the consistent design and performance assessment of conventionally installed and BL ingesting propulsion systems, a set of conceptual design and performance methods has been implemented capturing basic cycle synthesis, essential aspects of component design and the evaluation of operational characteristics. Emphasis has been placed on allowing for parametric evaluation of the resulting models, thus enabling the execution of system and, upon surrogate model creation, aircraft-integrated studies. In Table 5.1, an overview of the proposed methods is provided including a number of methodological aspects specifically developed for the modeling of the FF power plant.

Aspect	Method
Cycle synthesis and flow path sizing [a]	Aircraft Propulsion System Simulation (APSS) framework [b] [189], [190]
Component design	
Turbo component design efficiencies	custom (Section 5.1.4)
Bypass duct pressure ratio	custom (Section 5.1.5)
Intake pressure ratio	custom (Section 5.1.5)
Turbine cooling air [c]	according to References [195] and [182] (Section 5.1.2)
Nacelle shape, external dimensions	custom (Section 5.1.6) and according to [182]
FF intake total pressure ratio [d]	custom (Section 5.1.5)
FF core intake pressure ratio [d]	custom (Section 5.2.4)
FF integration effects [d]	custom (Sections 4.4 and 4.5)
Operational behavior	
Turbo component performance maps	GasTurb 11 standard maps [191]
Handling bleed scheduling	according to References [182] (Section 5.1.3)
Intake pressure ratio	custom (Section 5.1.5)
Nozzle characteristics	according to References [175] and [182] (Section 5.1.5)
Fan drive gear system efficiency	custom (Section 5.1.7)
Fan nozzle area scheduling	custom (Section 5.1.3)
FF integration effects [d]	custom (Sections 4.6 and 4.8)
FF intake distortion [d]	custom (Section 5.2.5)

[a] including component geometric description using custom parameterization
[b] implemented in Matlab® environment [184]
[c] including impact on design efficiency of cooled turbines
[d] only applicable to Fuselage Fan propulsion system

Table 5.1:Overview of methods used for propulsion system conceptual design and performance

A generic fuel with a Fuel Heating Value (i.e. lower caloric value) of 43.124 MJ/kg is employed, and air is assumed to be of zero humidity. The analyses are based on the assumption of steady flow, i.e. transient behavior is not considered.

[25] This means the properties of specific heat, gas constant, heat capacity ratio, enthalpy and entropy function are functions of temperature and fuel/air ratio, but not the pressure.

5.1.1 Cycle Definition, Flow Path Sizing and Performance Prediction

The power plant cycle considered in the present context is characterized through the classic Joule/Brayton thermodynamic cycle. The incorporation of advanced cycle elements offering potential for enhancing thermal efficiency such as intercooling or recuperating devices is not subject to the thesis. Owing to the targeted technology status and thus the expectation of generally reduced specific thrust levels over contemporary designs, the considered propulsion system architecture of podded and fuselage-installed power plants refers to a two-spool, geared turbofan layout with the booster driven by the LP shaft. For the expected large propulsor dimensions and high Bypass Ratios, a Short Duct Separate Flow (SDSF) nacelle design is considered more appropriate than a mixed flow configuration [175, Fig. 3.5.9]. All components are considered to be of axial flow type.

As outlined in Reference [182], different options are in general available for choosing the propulsion system design point. Since component axial Mach numbers and hence corrected mass flows are maximum at the Maximum Climb (MCL) operating point characterized through Top-of-Climb (ToC) condition and required aircraft residual climb capability, this point is decisive for the definition of the flow capacity of engine components. At hot-day[26] takeoff condition based on a given Maximum Takeoff (MTO) thrust requirement, typically maximum temperature levels and mechanical spool speeds are reached, thereby placing strong requirements on the dimensioning of the secondary air system and mechanical component layout, which, in turn, both have a direct impact on the cycle design and accordingly attainable cruise performance. In particular for long-range applications, the achievement of maximum engine efficiency levels during significant cruise conditions needs to be ensured.

In this thesis, the selected sizing strategy is based on conducting the flow path design process at ToC conditions using a temperature deviation of ISA + 10 K while incorporating important characteristics attained at representative takeoff conditions within the cycle and component design using a multi-point sizing procedure (see Section 5.1.2). Engine thrust sizing is achieved through iterative determination of the corrected intake mass flow for obtaining a specified streamtube loss corrected net thrust. Control volume conventions determining the interfacing between propulsion system and airframe were discussed in Section 4.2. As a result of the integrated treatment of aircraft and propulsion system, net thrust requirements are not given as constant input values but rather determined as part of the aircraft-integrated analysis.

Turbo component geometric design is parametrically conducted on a component-resolved basis. This constitutes in general a complex multidisciplinary design effort involving, amongst others, aerodynamic, thermo-mechanical, and economic[27] disciplines. Due to the consideration of widely similar component designs in this thesis, this process is simplified and incorporated in propulsion system sizing via a series of basic design principles. The required flow area of the engine components results from their individual corrected mass flow levels and given axial Mach numbers, M_{ax}, applied at the component's inlets and outlets. The dimensions in radial direction are governed through specification of inlet and outlet hub/tip ratios, ν. Typical values for M_{ax} and ν can be found in the literature, cf. References [34], [175], [176], [196]. Turbo component longitudinal dimensions are mapped using the approach presented in Reference [182], which is based on the summation of stage-resolved component lengths. Here, the component's rotor aspect ratios at the inlet and outlet, respectively, are treated as input parameters. While for different types of compressors and turbines typical values from Reference [175] are employed and kept constant, for the fan, a dependency on corrected mass flow is considered. Based on the data given in Reference [175, Fig. 5.2.2.14b], a

[26] typically defined as ISA+15 K [170]
[27] Consider e.g. blade/stage count and associated design, manufacturing and maintenance cost aspects.

parametric model for the mapping of fan blade aspect ratios has been derived. For the aspect ratio of the stator vanes, a constant offset is assumed, which has been graphically determined from an existing GTF design [170]. The engine spool speeds are determined through the mechanical loading of the associated components (see Section 5.1.2).

The turbo component stage configuration is defined based on the evaluation of the individual aerodynamic loading conditions. For compressors (excluding fans), the number of stages results from the total pressure ratio assuming typical mean stage pressure ratios given in References [175], [176]. The compressor work split of twin-spool turbofans results from prescribed booster pressure ratios [175, p. 554], which have been selected to yield stage counts of typical advanced high-speed booster designs [197, Fig. 7] while verifying the feasibility of uncooled LPT designs.[28] Acknowledging the observable trend of modern civil turbofans in two-spool configuration to employ a two-stage High-Pressure Turbine (HPT) design [170], [198]–[200], this layout is adopted for the HPT. The LPT stage count results from the turbine expansion ratio and a predefined mean stage pressure ratio [175] while verifying the feasibility in terms of the aerodynamic loading parameter.

In view of the noticeable tendency to employ an increasing level of electrification for aircraft subsystem power (i.e. “More-Electric” (MEA) [201] and even “All-Electric Aircraft” [202], respectively), customer bleed air extraction for cabin air conditioning is dispensed with and all power demands for engine auxiliaries and aircraft subsystems are considered to be covered by High-Pressure (HP) spool power extraction. Typical power levels required for the MEA system architecture of the Boeing 787 are provided in Reference [203, p. 4]. The values are taken to represent a mean mission value and, pursuant to References [204], [205], scaled with the aircraft takeoff gross weight, in the first instance. The employed scaling law exhibits good agreement with characteristics published in the frame of the Boeing SUGAR studies [55].

For verifying the plausibility of the obtained cycle calculation results, compliance with basic design and performance limits is necessary. Typical geometric parameters subject to examination include the High-Pressure Compressor (HPC) bore radius (see Section 5.1.3.1) and, particularly for designs with low core size, the blade height at the HPC exit. Within the calculations performed in the present work, this parameter has been found uncritical since clearly located above feasible minimum heights, which are typically in the order of 12 mm, cf. Reference [39]. Further parameters include component aerodynamic stage loadings, component circumferential velocities,[29] and, during off-design calculation, operational limits including temperature levels, mechanical and corrected spool speeds as well as compressor surge margins.

5.1.2 Multi-Point Sizing Approach

The realistic simulation of propulsion system design and performance requires consideration of power plant characteristics occurring at key engine operating points within the cycle design definition and mechanical dimensioning. In general, different computational options are available for acknowledging this circumstance. For initial estimations, the assumption of constant margins in relevant parameters such as temperatures, shaft rotational speeds or AN^2 values[30] during design point calculation may be sufficient. In a more detailed analysis, the design settings may be manually adjusted such that desired off-design conditions are met through repeatedly conducting design and off-design calculations. This is common practice in propulsion simulation programs featuring strictly separated and confined design and off-design calculation modes.[31] However, as the simulated level of detail in terms of implemented

[28] In case of three-spool layouts, the optimum compressor work split typically becomes a more complex exercise [44].
[29] Permissible area-averaged velocities at component inlet and outlet are given in Reference [175].
[30] Local flow area multiplied by rotational speed squared.
[31] Examples include the commercial software GasTurb [191].

heuristics and considered multidisciplinary aspects rises, the time consumption of this approach and susceptibility to errors may rapidly become excessive and is thus considered inappropriate for the present studies. In fact, in the present work emphasis is placed on directly processing off-design results within the cycle design definition.[32] Due to the high level of interdependencies between the geometric sizing and the prediction of off-design behavior, this requires iterative procedures. The employed propulsion system simulation setup (see Section 5.1.1) conveniently allows for the information exchange between the computational modes and thus offers means for implementing automated procedures, thereby facilitating the definition of a user-defined set of parameters to be evaluated at different operating conditions. The operating condition for evaluating the thermal and mechanical loading is considered the representative hot-day takeoff point at Sea Level (SL), M_0 = 0.25 and an ISA temperature deviation of +15 K. Incorporation of the takeoff characteristics within cycle definition is considered particularly significant with regards to the following aspects:

- The required relative turbine cooling air mass flow involves evaluation of the maximum thermal loading of the component to be cooled, and the temperature level of the cooling air (see Section 5.1.3). Both parameters are computed at takeoff rating. The determined cooling air demand is fed back to the design point calculation.
- In the local frame of the Fan Drive Gear System (FDGS), the component's efficiency at MCL constitutes an off-design condition, since gearbox sizing is executed at maximum power condition. As discussed in Section 5.1.7, MCL gear system efficiency is determined as a function of the relative power between MCL and MTO and the gearbox design point efficiency.
- The HPC design tip speed at the first rotor inlet, which is directly coupled to the HP spool speed, is determined such that a prescribed maximum value in the AN^2 metric of the HPT last rotor is attained at takeoff condition. In analogy, the LPT design outlet tip speed is iterated to yield a given takeoff mechanical loading of the last rotor of the LPT, thereby defining the design LP spool speed. Guidelines for maximum feasible AN^2 values for turbines can be found in Reference [175, Fig. 5.2.3.6, 5.2.3.23].

In Figure 5.1, the iterative computation process between design and off-design points as used for the present work is visualized as a flowchart, which is shortly discussed in the following.

Since the takeoff requirements in terms of net thrust are only known upon the aircraft-integrated assessment, an iterative procedure involving aircraft-level thrust sizing is required to accurately match engine and airframe requirements at the relevant operating conditions. Therefore, engine design parameters that are unknown from the outset and thus are to be determined through multi-point sizing, $\vec{X}_{ds,MP}$, need to be defined as free design input variables along with the design inputs that are solely relevant at the design point, $\vec{X}_{ds,SP}$. The former set of parameters refers e.g. to the turbine cooling air demand, which is strongly correlated to the temperature levels exhibited at takeoff conditions (see Section 5.1.3.1). Similarly, the FDGS design efficiency is determined through the condition of maximum power throughput, thus rendering the MCL point an operational point for the gear system. For a given flow path layout, the HPC inlet and LPT outlet design tip speeds are the parameters to determine the AN^2 values in the turbine last rotor planes exhibited at takeoff condition. The process is initiated by assuming suitable start values for the multi-point dependent sizing parameters. Once the propulsion system characteristics at takeoff are determined based on a number of free off-design variables, $\vec{X}_{od}$, the models for the calculation of the multi-point sensitive parameters are executed based on the consolidated design and off-design model response vectors, $\vec{Y}_{ds}$ and $\vec{Y}_{od}$. In addition, power

[32] cf. also discussion by Bijewitz *et al.* [29]

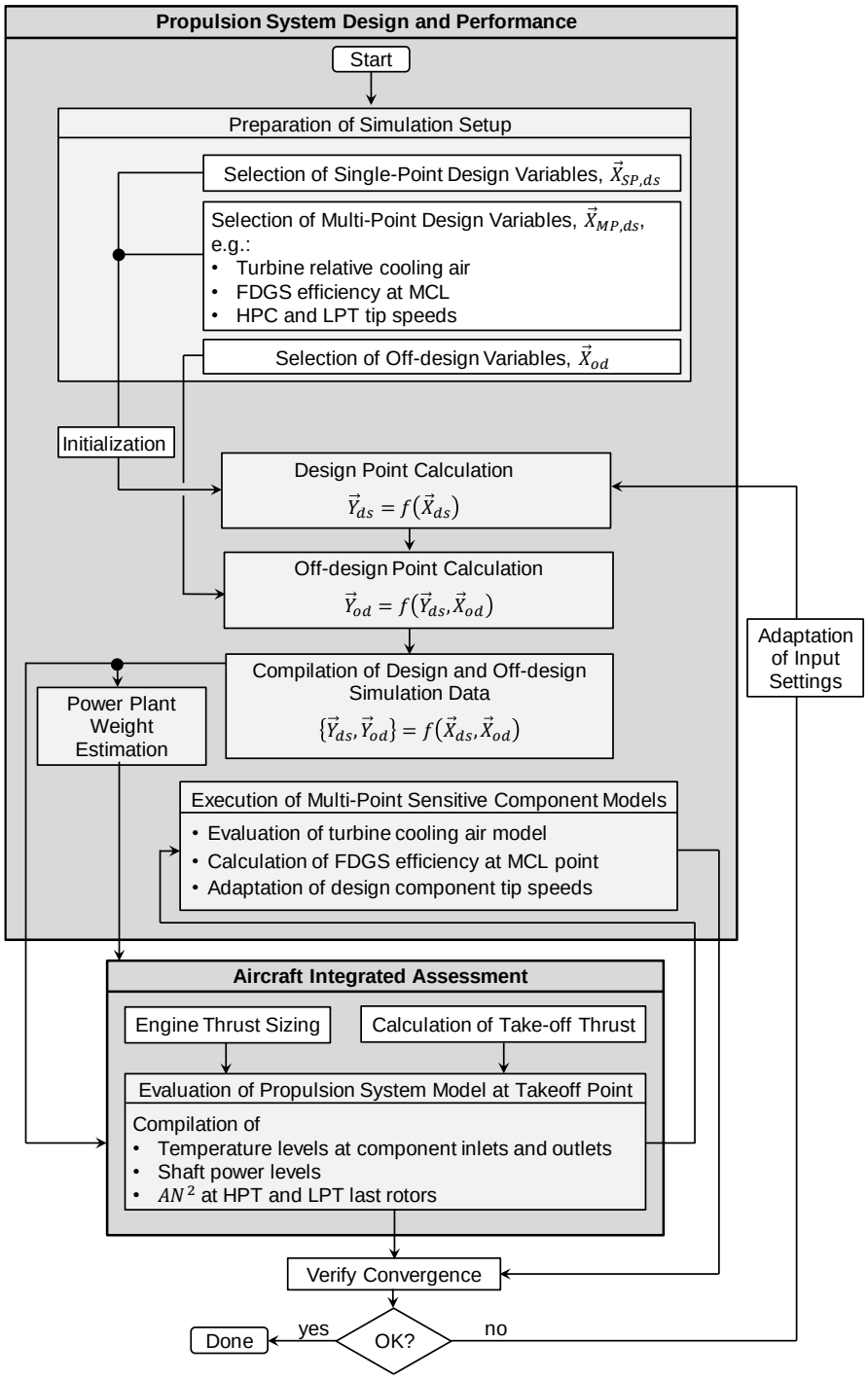

Figure 5.1: Implemented computational scheme for conducting multi-point sizing under consideration of aircraft level requirements

plant weight, which is strongly dependent on the engine takeoff conditions, is calculated (see Section 5.3). The described process is iteratively repeated until sufficient convergence is achieved. As will be described in Section 5.4, for the practical handling of this approach the power plant design and performance synthesis has been wrapped using surrogate modeling techniques. The implemented process is fully adaptable and may be custom tailored based on the scope of the considered investigation. A possible scenario for extension may involve the iteration of the design compressor work split[33] for a user-prescribed LPT inlet temperature level exhibited at takeoff condition.

[33] i.e. the logarithm of booster pressure ratio divided by the logarithm of OPR

5.1.3 Implemented Laws and Modeling Strategies

For the consistent analysis of the investigated propulsion systems, a set of parametric design laws has been implemented and a design iteration scheme accordingly set up. The applied laws include heuristics defining basic cycle characteristics and comprise design and off-design parameters. The modeling approach is primarily based on semi-empirical data and engineering guidelines provided in established textbooks such as the ones published by Grieb [175], Walsh and Fletcher [196] and Kurzke and Halliwell [170].

5.1.3.1 Design Laws

During the design of ducted propulsion systems, frequently the design BPR is used as an input variable. Now, for separate flow turbofans, propulsive efficiency is closely correlated to the ratio of nozzle exit velocities to the velocity in the free stream. Since the parameter specific thrust is proportional to the difference in equivalent nozzle exit velocity and free stream velocity, the prescription of specific thrust is preferred over specifying BPR due to the direct physical coupling to the propulsive efficiency level. Accordingly, in the proposed parameterization of the design iteration scheme, both propulsor diameter and BPR are output values.

As commonly done in propulsion system simulation programs, fan performance is separated into a cold and hot stream operating at an outer and inner Fan Pressure Ratio (FPR), respectively [175]. The inner part contributes to the core compression process, while for high-bypass turbofans the outer part provides a majority of the total net thrust. In the present implementation, outer FPR is optimized to yield the optimum ideal bypass and core nozzle exit velocity ratio, $(V_{18}/V_8)_{id}$, thereby ensuring minimum TSFC for given cycle settings. The value of the optimum $(V_{18}/V_8)_{id}$ was analytically derived by Gasparovic [206] and depends on the component efficiencies and pressure ratios along the LP power chain. For mixed-flow turbofans, outer FPR is adjusted such that total pressures of core and bypass flow in the mixer entry plane are close to unity, thereby minimizing mixing losses [43]. As proposed in Reference [182], inner FPR is determined based on the optimum ratio of specific works done in the outer and inner fan stream using data given in Reference [175, Fig. 5.2.2.12]. Fan design tip speed is mapped in dependency of the outer FPR according to Reference [175, Fig. 5.2.2.6a], while Intermediate Pressure Compressor (IPC) and HPC tip speeds are iteratively adjusted based on feasible mechanical loading levels exhibited at MTO rating (cf. Section 5.1.2). HPC pressure ratio is iterated to yield a prescribed Overall Pressure Ratio (OPR) while maintaining a given booster pressure ratio. The parametric mapping of turbo component design efficiencies refers to a custom approach discussed in Section 5.1.4 and the modeling of ducts and related losses is described in Section 5.1.5. The HPC inlet hub/tip ratio is iteratively adjusted to yield adequate inlet hub (i.e. bore) radii, thereby ensuring proper fitting of the LP spool through the core engine. Representative values for the bore radius have been derived from the literature [34] and scaled with the torque transmitted. The reduction ratio of the FDGS is determined as a function of the individual rotational speeds of the fan and LP spool.

As a consequence of the substantial thermal loads exhibited particularly by the components located downstream the combustor of a gas turbine, active cooling of structures exposed to hot gas is usually required, thereby allowing the operating temperature of the working fluid to exceed the material's melting point without affecting the structural integrity. Total cooling air flows of modern machines may amount to more than 25% of the core flow [207]. In current aero-engines, cooling air for the first nozzle guide vane of HPTs is usually taken from the HPC last stage and re-inserted within the turbine, while cooling air for downstream grids is typically extracted from HPC inter-stage offtake ports [208]. For state-of-the-art gas turbines, sophisticated cooling mechanisms have been developed, an overview of which is provided in References [177], [209]. The physical phenomena associated with the cooling process involve a highly complex interplay of different heat transfer mechanisms, and therefore the

prediction of the required cooling air amount requires correspondingly extensive calculation methods. Generally, a variety of aspects determine the required cooling air mass flow including the technology levels of the cooling mechanism and the associated materials, in particular its permissible temperature, the turbine configuration as well as the material's temporal exposure to temperature levels and the corresponding impact on thermal damage and component life requirements.[34] In the present context, a simplified method for the parametric mapping of cooling air demand is employed. According to Reference [195, p. 81], the cooling air effectiveness is defined depending on the mean inlet gas temperature, T_G, the maximum permissible bulk material temperature, T_M, and the cooling air temperature, T_C:

$$\eta_c = \frac{T_G - T_M}{T_G - T_C} \tag{5.1}$$

For T_M, eligible values depending on the material technology employed are given in Reference [210, Fig. 5.5]. Note that the application of advanced thermal barrier coatings may significantly increase the allowable gas temperature beyond T_M [175]. Following Reference [182], for T_G, the respective grid total inlet temperatures at MTO rating are taken as representative for both turbine vanes and rotors. The relative cooling mass flow relative to the HPC inlet flow is expressed as a function of a cooling air constant, c_c, and η_c [195, p. 82]:[35]

$$\dot{m}_c/\dot{m}_{25} = c_c \cdot \frac{\eta_c}{1 - \eta_c} \tag{5.2}$$

For c_c, varying values can be found in the literature reflecting different technology levels and cooling mechanisms [182], [195], [211], [212]. In analogy to commercial gas turbine performance software such as GasTurb, in the present work, an equivalent single-stage cooling air model is utilized. For the conversion of multi-stage cooled turbines to the equivalent single-stage performance, the procedure given by Seitz [182] is used. A typical distribution of work potentials within single- and multi-stage turbines provided by Kurzke and Halliwell [170, p. 670] is applied. Cooling air for HPTs is considered to be extracted at the HPC exit, while LPT secondary air is taken from an HPC inter-stage bleed port with the relative enthalpy rise of the flow tailored to match the required pressure differential. In addition to turbine cooling, secondary air extracted from the compressors is typically used for various other purposes involving sealing (including bearing chambers), thrust balancing and engine auxiliary cooling [196]. For these purposes, a temperature-independent relative HPC bleed rate is assumed, in the first instance. The cooling air constant c_c is assumed identical for both rotors and vanes and has been calibrated such that for the settings of a turbofan power plant representing typical year 2000 technology status[36] realistic HPT stator and rotor cooling air flows are obtained, where representative values have been derived from Reference [213, Figs. 2-4]. For LPT disk cooling and rim sealing, a constant relative cooling airflow is assumed [196]. Secondary air extraction for the cooling of external systems such as the core cowling or for turbine active clearance control as well as additional leakage air is neglected, in the first instance. An itemization of simulation settings is provided in Table C.11 in Annex C.

For the FF propulsion system, the specific design aspects are reflected in partially adapted model parameterization settings. Due to the aft-fuselage installation, the fan inlet hub diameter is declared as an input, while the fan inlet hub/tip ratio is accordingly iterated (see also Section 5.2.1). A series of specialized methods applicable to the FF power plant are presented in Section 5.2.

[34] Further effects affecting the required cooling air flow are described by Walsh and Fletcher [196, p. 226].
[35] A series of similar correlations can be found in Reference [211].
[36] Including component efficiencies and duct pressure losses taken from Reference [34] and a maximum allowable material temperature of 1200 K [182].

5.1.3.2 Off-Design Performance

For the simulation of turbo component operational behavior, standard component maps from GasTurb [191] are utilized for all power plant types investigated. The placement of the reference point within component maps is defined through prescription of reference values for relative corrected speed and beta (β) values.[37] Map scaling including component map Reynolds number correction refers to the procedure described in Reference [170]. During off-design calculation, steady-state performance is considered.

In order to ensure proper operability of compressors throughout the engine operating envelope, compressors of gas turbine propulsion systems typically utilize features such as Variable Guide Vanes (VGV) and handling bleed extraction. While the consideration of VGV is disregarded, in the first instance, compressor handling bleed extraction is mapped according to the approach proposed in Reference [182, p. 89], where β values are used as a first indication of compressor surge margin. The required relative handling bleed flow is described by the empirical formulation given in Reference [182].

From the engine performance model, important off-design characteristics relevant for the aircraft-integrated assessment such as TSFC may be computed at arbitrary points within the flight envelope. Engine operational input variables typically include flight Mach number, altitude, ISA temperature deviation and relative thrust setting. The latter is modeled via the Power Lever Angle (PLA) parameter, which, in case of turbofan engines, is directly correlated to the relative mechanical speed of the fan [191].[38] Typical limiters may be applied to model engine rated performance including cycle temperature levels, corrected spool speeds and maximum AN^2 values. Minimum feasible thrust settings are typically governed by various factors involving required engine spool-up time, combustor flame-out boundaries, compressor stability aspects and customer offtake requirements. Since the use of TSFC for fuel burn calculation becomes infeasible during idle operation, it is therefore replaced by a minimum feasible fuel flow [182]. In order to allow for improved operational flexibility concerning engine stability at low-speed operation, which is typically impaired in case of very low specific thrust designs, the setting of the bypass nozzle exit area relative to its design value, i.e. the ratio $A_{18}/A_{18,ds}$ is treated as an input variable during performance evaluation.

5.1.4 Turbo Component Design Efficiency Determination

Within the frame of conceptual studies, the primary physical effects determining turbo component design point efficiency should be captured. According to Reference [175], these include the component mean aerodynamic loading, the impact of machine size, Reynolds number implications, optional cooling air insertion effects as well as the considered technology level. In the present context, the prediction of turbo component design efficiencies is based on the empirical data presented by Grieb [175, Sec. 5.2] who published a comprehensive set of relations and graphs covering a wide range of design and performance characteristics of existing and projected propulsion system components. As most information was derived from a proprietary database, the data is displayed in a normalized way. The contained data includes engine samples with EIS years between 1970 and 1996. The statistical information and correspondingly derived trends are presented separately for all relevant components including outer and inner fans, IPCs and boosters, HPCs, HPTs and LPTs. Intermediate-pressure turbines (IPTs) are treated as HPTs. In this work, emphasis has been placed on transforming the available data and relations in a way suitable for the parametric evaluation in the context of integrated design studies. In this respect, the objective is to ensure consistent mapping of turbo component

[37] Auxiliary coordinate commonly employed to avoid ambiguity in component maps during numerical calculation.

[38] For the studies in Chapter 6, PLA is defined between non-dimensional fan speeds ranging from 0.75 and 1.02, respectively, which allows for complete thrust mapping within typical operating ranges.

efficiency implications emanating from alternative power plant arrangements with different design settings such as sizing net thrusts (see Chapter 6). This approach is preferred over analytical loss models[39] (cf. Reference [214]) typically requiring detailed knowledge of the stage geometry as well as the flow characteristics within the rows, which are only available upon a mean line analysis.

The basic approach is based on expressing the overall component polytropic design efficiency, η_{pol}, as a superposition of the individual, component-dependent physical effects. A normalized baseline efficiency value,[40] η'_{pol}, incorporates the influence of the aero-thermodynamic and mechanical design parameters such as the aerodynamic loading, non-dimensional flow coefficient, mean stage pressure ratio, axial Mach number and blade aspect ratio [175]. Since aerodynamic loading is considered decisive for the attainable baseline efficiency level, this parameter is used for the mapping of η'_{pol}. Accordingly, η'_{pol} is determined based on the mean stage loading parameter,

$$\bar{\psi}_m = \frac{2\Delta h_t}{\bar{U}_m^2 \cdot n_{st}} \tag{5.3}$$

where Δh_t denotes the change of total specific enthalpy across the component assuming equal specific work done in each of the n_{st} stages, and $\bar{U}_m$ symbolizes the circumferential speed at the representative area-averaged radius, which is defined as the mean value between inlet and outlet,

$$\bar{r}_m = \frac{1}{2}\left(\sqrt{\frac{A_i}{2\pi}} \cdot \sqrt{\frac{1+\nu_i^2}{1-\nu_i^2}} + \sqrt{\frac{A_o}{2\pi}} \cdot \sqrt{\frac{1+\nu_o^2}{1-\nu_o^2}}\right) \tag{5.4}$$

In equation (5.4), A represents the flow path annulus area and ν the hub/tip ratio, both evaluated at the inlet (i) and outlet (o) station, respectively. From the empirical data given in Reference [175], regression functions of the form $\eta'_{pol} = f(\bar{\psi}_m)$ have been derived separately for each component type. The respective sources constituting the basis for the curve fitting are summarized in Table 5.2.

Component	Sources for determination of η'_{pol}
Outer and inner Fan	[175, Fig. 5.2.2.2]
Booster, IPC	[175, Fig. 5.2.2.32]
HPC [a]	[175, Fig. 5.2.2.44]
HPT [b], IPT [b]	[175, Fig. 5.2.3.19]
LPT	[175, Fig. 5.2.3.3]

[a] axial flow type
[b] excluding impact of turbine cooling air

Table 5.2:Overview of sources constituting basis for determination of baseline efficiency values

Using the baseline efficiency value, increments or decrements are applied capturing successively the implications of component size, Reynolds number, turbine cooling, if applicable, and technology level. The respective implications and modeling approaches are shortly summarized in the following.

5.1.4.1 Component size effects

As a typical trending behavior, smaller turbo component sizes yield degradations in the attainable efficiency level. According to Reference [175], this results from a number of physical effects including the relative radial tip clearance, which tends to become larger for smaller component sizes,[41] the blade profile quality, i.e. manufacturing tolerances relative to the profile dimensions, the blade aspect ratio in case of turbines, and the general design standard, i.e. the smoothness of the hub and casing contours.

[39] Relevant losses typically include profile, trailing edge and shock-induced losses as well as losses due to radial and axial gaps [170].
[40] Reference conditions: standard day corrected inlet mass flow: 70.0 kg/s, EIS year 1995, Reynolds number index = 1.0
[41] Typical exchange rates for the efficiency loss due to tip clearance in compressors and turbines are given in Reference [215]

Since geometric dimensions of the flow path are governed through the inlet corrected mass flow, this parameter is considered the dominating scaling variable [175]. As suggested in Reference [175], the dependency of efficiency on size can be neglected for corrected mass flows greater than 70 kg/s. The efficiency is scaled according to the following relation:

$$\eta_{pol,w} = 1 - \left(1 - \eta_{pol,ref}\right) \cdot \left(\frac{\dot{m}_{corr}}{\dot{m}_{corr,ref}}\right)^{-m} \tag{5.5}$$

The reference values and the exponent in equation (5.5) are given in Reference [175] for compressors and turbines. A summary of the suggested values is provided in Table C.3 in Annex C. Additional size-related factors influencing efficiency levels, which are not considered here include dynamic changes of radial gaps during transient maneuvers emanating from heat transfer dynamics and associated differences in thermal expansion as well as casing deformation due to external forces causing localized tip clearance changes [215].

5.1.4.2 Impact of Reynolds number

The implications of the blade surface roughness are captured by relating the representative component Reynolds number to the critical Reynolds number, Re_{crit}, formulated with respect to the material surface roughness, above which the impact of Reynolds number can be considered as non-existent [175]. Guidelines for the determination of Re_{crit} are given in Reference [175, p. 160] for compressors and turbines, as is an approximation procedure for the representative component Reynolds number with respect to the surface roughness. Herein, the formulation includes a weighting of the aerodynamic effectiveness of rotor and stator via the reaction ratio. The weighting term is mapped based on $\bar{\psi}_m$ and the mean flow coefficient, $\bar{\varphi}_m = \bar{c}_m / \bar{U}_m$.[42] Through averaging between inlet and outlet conditions, the formulation is also applicable to multi-stage turbo arrangements. Auxiliary functions for the determination of the representative, component-averaged kinematic viscosity of multi-stage turbo components are displayed in Reference [175, Fig. 5.2.1.8] for compressors and turbines. The data contained therein has been approximated through nonlinear regression functions. Similar to the mapping of the size effect, the scaling procedure of the Reynolds number impact reads:

$$\eta_{pol,Re} = 1 - \left(1 - \eta_{pol,ref}\right) \cdot \left(\frac{\mathrm{Re}}{\mathrm{Re}_{ref}}\right)^{-n} \tag{5.6}$$

Again, the reference values and exponent suggested in Reference [175] are tabulated in Table C.3 in Annex C.

5.1.4.3 Influence of technology level

The influence of the technology level available for each component (e.g. due to design techniques, employed materials and manufacturing processes) is mapped through the correlations given in Reference [175, Fig. 5.2.1.4]. Accordingly, component type-dependent efficiency increments, $\Delta\eta_{pol,tech}$, are applied. The technology level is correlated to the EIS year, in the first instance, where the reference point is set as year 1995. These characteristics have been fitted and subsequently applied to the efficiency prediction.

5.1.4.4 Impact of cooling air

The implications of turbine airfoil cooling typically employed in a HPT and IPT has a significant effect on the attainable turbine efficiency due to increased aerodynamic losses. In the present context, this impact is parametrically described using a characteristic presented in Reference [175, Fig. 5.2.3.18] indicating the relative efficiency loss, $\Delta\eta_{pol,c}$, depending on the relative cooling mass flow required for stator and rotor cooling with respect to the HPC inlet flow. In contrast to alternative modeling approaches (cf. e.g. Reference [170], [196]) the individual contributions of different cooling

[42] $\bar{c}_m$ symbolizes the mean axial flow velocity averaged between inlet and outlet

mechanisms are not resolved but rather the integrated effect of the entire amount of cooling air is considered. For the conceptual studies of technologically similar turbines in the present context, this is considered appropriate.

The individual contributions outlined above are expressed as increments relative to the reference efficiency values [175]. The resulting polytropic efficiency is then determined from

$$\eta_{pol} = \eta'_{pol} - \Delta\eta_{pol,w} - \Delta\eta_{pol,Re} - \Delta\eta_{pol,tech} \ \left(-\Delta\eta_{pol,c}\right) \tag{5.7}$$

where the last term in parentheses is only applicable in case of cooled turbines.

The implemented model has been validated against published data of experimentally investigated turbo components. For each component type, at least one sample has been considered. Most of the data employed for validation purposes has been derived from the "Energy Efficient Engine Component Development and Integration Program" conducted in parallel by Pratt & Whitney and General Electric under NASA contract [216]–[223]. Additional validation cases were taken from other experimental studies described in References [224]–[226]. The complete set of validation data captures a period between 1954 and 2004, thus partially requiring extrapolation of the EIS-dependent mapping of available technology level. For HPTs, the impact of cooling air is included in the comparison. In Figure B.5 in Annex B, the validation results are visualized indicating good agreement between the computed prediction and the experimentally measured data. As can be seen, all sample points are clearly below a 2.0 percentage point deviation threshold from the published values, and the root mean squared error is 1.0 percentage point. The agreement is consistent for all considered component types, considered machine sizes and technology levels, and thus the proposed model is considered valid.

An evaluation of the implemented efficiency prediction model is provided in Figure 5.2 for a commercial two-spool turbofan application case. The considered model input parameters are $\bar{\psi}_m$, $\bar{\varphi}_m$, the corrected inlet mass flow, $\dot{m}_{corr}$, and the relative cooling mass flow, $\dot{m}_c/\dot{m}_{25}$, if applicable. For the aerodynamic characteristics, typical parameter ranges are selected as suggested in Reference [175], while the ranges of corrected mass flow are adjusted to cover a large scope of thrust classes. The pivot settings refer to typical values associated with the investigated medium-to-long range application scenario. For mapping the impact of advanced technologies, an extrapolation of the characteristics given in Reference [175] is not considered appropriate for technology levels significantly beyond the underlying empirical data. Instead, a simple scaling of the integrated component losses has been introduced, where the technology dependent loss-scaling parameter is denoted as $f_{tech,TC}$. The parameter has been calibrated such that $f_{tech,TC}$ of unity correlates to the reference conditions indicated in Reference [175]. The obtained model responses shown in Figure 5.2 feature intuitive behaviors. As an example, the impact of component loading of compressor and fan efficiency is in good qualitative agreement with the characteristics presented by Walsh and Fletcher [196, Fig. 5.1 and 5.4]. For booster and HPC components, the calculated Reynolds numbers are greater than the critical values within the entire bandwidth of considered input values, thus yielding for the applied nominal input settings at the pivot points invariant efficiencies against variations of $\bar{\varphi}_m$. This is primarily due to the fact that in case of multi-stage compressors the mean kinematic viscosity reduces for larger pressure ratios relative to the inlet value, whereas, for turbines it increases [175, Fig. 5.2.1.1]. For core engine components and the LPT, a strong impact of the corrected mass flow is visible. Similarly, the HPT relative cooling mass flow has a pronounced effect on η_{pol}.

Additional effects affecting the attainable efficiency level such as humidity and flow distortion (see Reference [215]) are considered of secondary importance for conventionally installed power plants and thus neglected. Adaptations to the efficiency prediction of the FF propulsion system are described in Section 5.2.3.

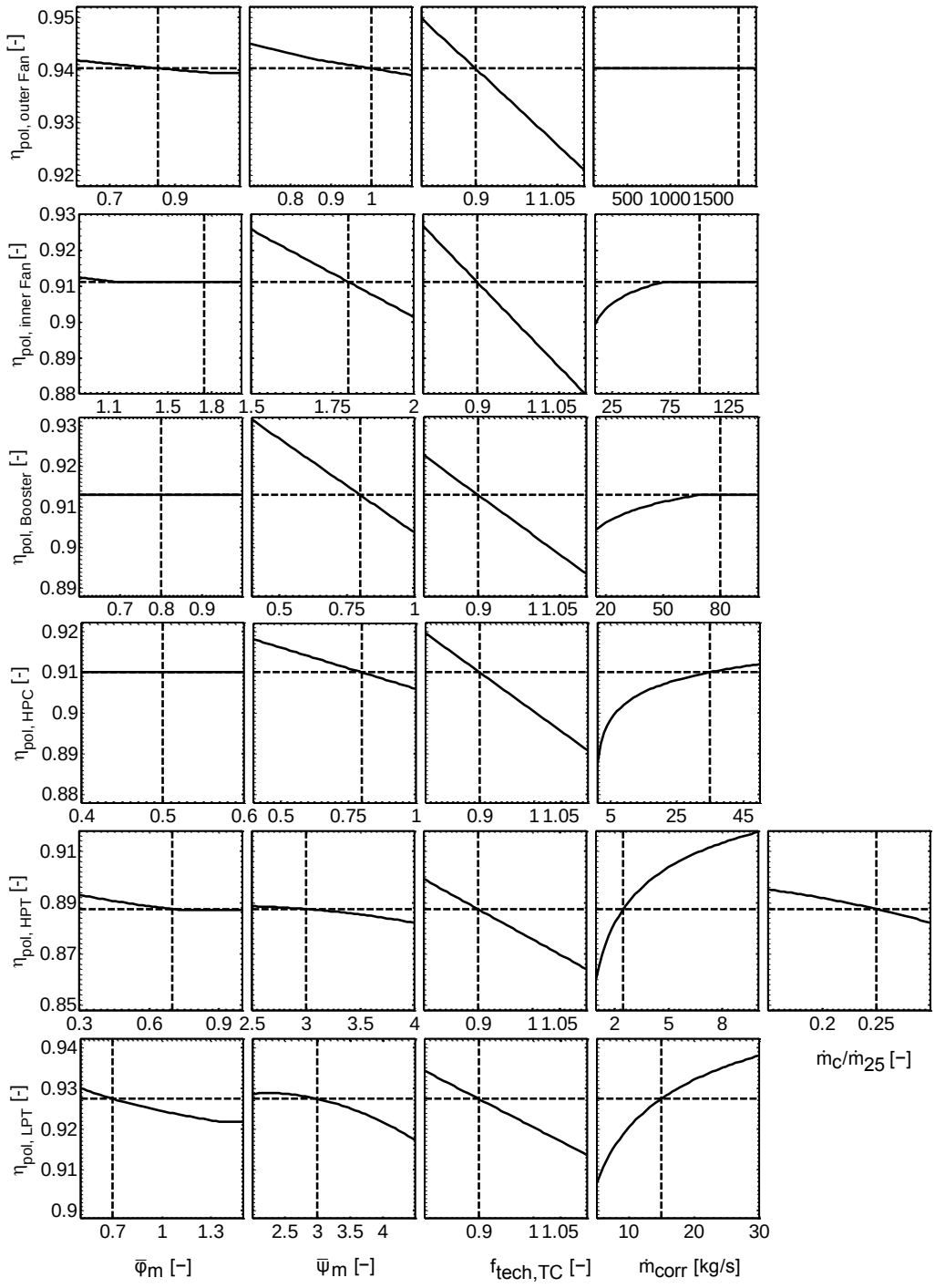

Figure 5.2: Evaluation of turbo component design efficiency prediction model

5.1.5 Duct Pressure Loss Mapping

Pressure losses occurring in the engine intake, nozzles and inter-component ducts may have a pronounced impact on the performance of the propulsion system. In the following, the implemented methods used for the mapping of duct losses are described. Components with explicitly mapped losses comprise the air intake, bypass duct and nozzles. For engine inter-ducts[43] and combustors, constant

[43] i.e. compressor inter-duct, turbine inter-duct and turbine exit casing

design pressure ratios are assumed according to References [34], [175], [196]. For the PFC, the mapping of pressure losses in the s-duct core intake is separately discussed in Section 5.3.4, while the modeling of FF intake pressure losses was described as part of Chapter 4. At off-design conditions, bypass, combustor and inter-duct pressure losses are assumed to vary with the square of the duct flow capacity normalized by the respective design value [191, Sec. 4.6].

5.1.5.1 Air intake

The design of subsonic air intakes of conventionally installed turbofans is driven by a variety of criteria: most importantly, the shaping of the inlet lip needs to be balanced between minimizing localized supersonic regions at the nacelle exterior and associated losses at high-speed cruise, while avoiding super-velocities and flow separation during low-speed operation [209]. While for minimum cruise drag a rather thin geometry is required, the latter aspect can only be achieved with well-rounded lip shapes, thereby illustrating a classic need for compromise [227]. Relevant sizing criteria involve the evaluation of high angle-of-attack, crosswind and engine-out (i.e. windmilling) situations [207]. Well-designed intakes reach cruise intake pressure recovery ratios, π_{int}, very close to unity and are typically between 0.996 and 0.998 [175]. However, at flight conditions where an increased streamtube capture ratio (A_0/A_1) causes the intake highlight and throat Mach number to increase, strong adverse pressure gradients may cause separation and hence the pressure recovery is typically degraded [178, p. 72]. This occurs e.g. at initial climb conditions. The highly optimized shaping of modern intakes, however, only yields moderate degradations within the typical operating envelope.

For the description of the design intake total pressure recovery ratio of conventionally installed power plants, the characteristics given by Rick [177, Fig. 3.2-3] presenting π_{int} as a function of the highlight/throat area ratio, A_{hl}/A_{th}, and the nacelle incidence angle for a capture ratio typical for cruise condition are employed. In the present context, the ratio A_{hl}/A_{th} is optimized to yield maximum cruise pressure recovery. For the mapping of intake off-design performance, characteristics of typical subsonic intakes have been adopted from Mattingly *et al.* [207, Fig. 10.3] presenting π_{int} as a function of engine power setting (expressed in terms of corrected engine airflow) and the free stream Mach number, which exhibit increasing π_{int} against reducing $\dot{m}_{corr}$ and growing free stream Mach numbers. Following the approach proposed in Reference [54], the intake performance characteristics have been transformed into non-dimensional form and the interpolated data subsequently superimposed with the design values. Once the nacelle is operated at incidence angles, the main parameters determining the intake total pressure loss involve, apart from the incidence angle itself, the intake contraction ratio, A_{hl}/A_{th} and operating throat Mach number, M_{th} [178]. While the complex phenomena associated with intake flow at high incidence angles including potential lip flow separation effects are not explicitly resolved in the present context, as an initial approach, the impact of incidence on π_{int} is mapped using data given in [178, Fig. 13.13], which describes intake total pressure loss as a function of throat Mach number, contraction ratio, and incidence angle.

The implemented approach has been validated for a conventional intake of a turbofan for a short-to-medium range transport with characteristics similar to the IAE V2500 series propulsion system. Low-speed intake pressure loss data obtained from high-fidelity coupled intake and propulsor numerical computations given in Reference [228, Fig. 6] is used as a validation basis. The data herein shows good agreement with the corresponding total pressure recovery results calculated with the present approach. Table C.4 in Annex C shows an overview of the prediction results at important operating conditions including the flow path sizing point, typical takeoff and representative cruise. For validating the modeled intake performance at incidence, experimental data presented in Reference [229, Fig. 16a] has been employed comprising measured values of π_{int} against M_{th} for various incidence angles and contraction ratios. The selected validation point at M0.2 and an incidence angle of 20° is considered representative for a typical takeoff condition. Although from a 0.1% error exhibited at zero incidence

the deviation increases to 1.2% at 20° incidence, the trend is considered to be correctly captured by the model. An overview of the validation results is provided in Table C.5 in Annex C.

5.1.5.2 Bypass duct

For high-bypass turbofans, the bypass duct pressure ratio has a pronounced impact on the fuel efficiency of the power plant [196]. As noted by Kurzke and Halliwell [170], the assumption of constant pressure losses during parametric studies may be inappropriate to accurately predict cycle behavior. Duct pressure ratio is influenced by wall friction along the wetted duct surface including the fan struts but even more importantly by additional flow interference and pressure losses due to equipment installed within the bypass duct obstructing the flow. This refers in particular to accessory systems such as oil cooler, fuel, oil, cooling air and drain lines as well as probes and other engine monitoring systems, which may cause considerable blockage within the duct. According to Reference [175], these losses may be described by a single pressure loss coefficient, ζ_{BP}, based on the dynamic pressure at the bypass duct inlet. For the mapping of ζ_{BP}, the empirical data of existing civil mixed and unmixed flow turbofans given by Grieb [175, Fig. 5.5.12] has been fitted as a function of the design bypass ratio. The regression result is given in the left part of Figure 5.3. As can be seen, ζ_{BP} reduces against increasing bypass ratios due to the reducing relative duct length and decreasing blockage effects, cf. also Reference [175, Fig. 5.5.13 and 5.5.14]. Using this correlation, the bypass duct total pressure ratio, $\pi_{BP} = p_{16}/p_{13}$, is calculated from rearranging the definition of the pressure loss coefficient, yielding

$$\pi_{BP} = 1 - \zeta_{BP}(BPR_{ds}) \cdot \left(1 - \left(1 + \frac{\gamma - 1}{2} M_{13}^2 \right)^{\frac{-\gamma}{\gamma - 1}} \right) \tag{5.8}$$

where γ denotes the ratio of specific heats. In the right part of Figure 5.3, an evaluation of Equation (5.8) is visualized, where the bypass duct inlet Mach number, M_{13}, is used as a study variable.

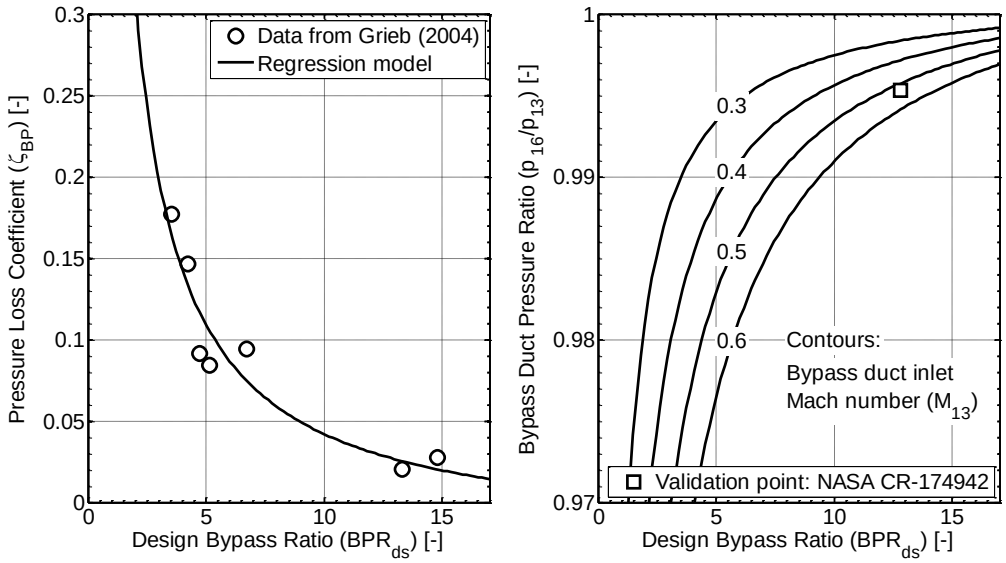

Figure 5.3: Regression model of bypass duct pressure loss coefficient based on data from Reference [175, Fig. 5.5.12] (left), and evaluation of implemented pressure ratio model, γ = 1.4

As expected, increased values of M_{13} yield higher losses and hence a degradation of π_{BP} occurs. Note that for typical turbofans the bypass duct inlet Mach number is between 0.3 and 0.5 [175, Fig. 5.2.2.10]. For increasing BPRs the ratio of wetted wall surface to flow annulus area reduces, which is reflected in improving values of π_{BP} [170]. Additional loss sources due to cooling systems potentially required in case of fan drive gear systems are disregarded, in the first instance. The model yields good agreement

with results published for a UHBR turbofan investigated as part of the NASA/Pratt & Whitney "Energy Efficient Engine" program [230], see Figure 5.3.

5.1.5.3 Nozzles

Loss characteristics of core and bypass nozzle are described through nozzle gross thrust coefficients (c_{FG}) and discharge coefficients (c_D). As described in Reference [182], c_{FG} relates the attained effective jet velocity at the nozzle exit to the ideal jet velocity corresponding to isentropic expansion. The reduction of the effective flow area available to nozzle stream due to aerodynamic blockage effects is accounted for using the discharge coefficient, which measures the ratio of effective and geometric nozzle exit area. For the parametric mapping of c_{FG} and c_D, characteristics presented in Reference [182, Fig. 5.7] based on data from Grieb [175] have been employed.

5.1.6 Nacelle Shape Parameterization

For the mapping of nacelle external dimensions of conventionally installed turbofans, the nacelle length and maximum diameter are considered the essential geometric properties. The calculation approach for the ratio of nacelle length to maximum diameter, L_N/D_N, of SDSF nacelles refers to the empirical relation given in Reference [182, p. 96], which features dependency on the design outer fan pressure ratio. For the prediction of the nacelle maximum diameter, an empirical formulation has been derived in the present context relating the nacelle maximum diameter to the fan inlet tip diameter, D_{Fan}. The model is based on the nonlinear regression of data derived from a broad range of existing turbofan engines of SDSF and Long Duct Mixed Flow (LDMF) types. The necessary information has been graphically approximated from References [231]–[237].[44] Nacelle maximum diameter is based on averaging height and width of the nacelle. The derived formulation is described by the equation (D_{Fan} in [m]):

$$\frac{D_N}{D_{Fan}} = 1.170 + \frac{0.283}{D_{Fan}} \tag{5.9}$$

An evaluation of equation (5.9) is presented in Figure B.6 in Annex B along with the regression data. As can be seen, larger fan diameters yield growing values of absolute nacelle thickness, which may be driven by the requirement of realizing sufficiently large nose lip radii in order to avoid separation at high angles of attack [209]. Moreover, larger engines typically require more space for accessory systems located inside the nacelle. The trending of the ratio D_N/D_{Fan}, however, shows a decreasing behavior against increasing fan diameters. As can be seen, most sample points are within a ±5% error bandwidth.[45] The correlation has been validated using separately sampled nacelle characteristics of a set of representative turbofan engines of three different thrust classes including the BR715 power plant [238], a design similar to the CFM LEAP engine [239], and the GE90-115B turbofan [231]. In addition, the properties of projected Ultra High Bypass Ratio turbofan designs are included in Figure B.6, which have been read from Reference [240]. Both existing and projected engines show good agreement with the implemented model. The nacelle length of LDMF types is equal to the distance between intake highlight and the end of the common nozzle assembly.

A large share of the fan cowling length is composed of the intake length, L_{Int}. For the determination of L_{Int}, a constant length-to-diameter ratio with respect to the fan tip is chosen based on Reference [53]. Bypass nozzle exit hub/tip ratio is mapped based on a nonlinear regression of existing SDSF turbofan engines [231] as a function of BPR, thus yielding the radial position of the bypass nozzle exit:

$$\nu_{18} = 1.092 \cdot BPR^{-0.210} \tag{5.10}$$

[44] cf. also Reference [23] published by the author
[45] root mean squared error: 1.6%

Accordingly, for higher BPR designs ν_{18} decreases as FPR reduces and hence the required bypass nozzle area increases. For the determination of SDSF nozzle aft-body and plug lengths, typical external flow angles approximated from Reference [231] are applied. Nacelle wetted area is calculated according to Reference [241] using the above described geometric properties. The overall propulsion system length is defined between the intake highlight position and the end of the core nozzle plug and results from the summation of the intake, bare engine and core nozzle including plug lengths, where the bare engine length is determined from the summation of component lengths between fan inlet and LPT exit planes (see Figure 5.4).

5.1.7 Fan Drive Gear System

For the optimum matching of the rotational speeds of propulsor and LP spool, a reduction gear system may be required. While this has been the standard practice for many turboprop applications, for turbofans, apart from few exemptions,[46] gear systems have found their way into commercial products only recently. Due to the high efficiency, superior power density and beneficial volume characteristics compared to other transmission types such as spur gears [242], epicyclic gear systems are typically employed in aero-propulsion applications. While the high transmission ratios intrinsic to turboprop applications often require multiple stages (coupled planetary or offset-planetary solutions), existing and projected GTF applications are equipped with inline epicyclic gear systems, thereby benefitting from the coaxial shaft arrangement.[47]

Now, the calculation of Fan Drive Gear System (FDGS) design efficiency requires specification of a variety of detailed parameters determining the gearbox configuration. Approaches to gearbox sizing and efficiency prediction can be found in References [242] and [243]. A breakdown of different loss mechanisms determining the design efficiency is presented in Reference [244]. In the present context, the assumption of constant FDGS design point efficiency is considered satisfactory, in the first instance. The design efficiency, η_{TO}, refers to the FDGS sizing point, which is considered the operating point where maximum power, P_{TO}, is transmitted, i.e. hot-day takeoff condition. Based on References [245]–[248] a value exceeding 99% appears feasible for turbofan applications. During part power operation, however, different loss sources including windage and gear sliding effects outlined in [243] become dominant and cause the operational efficiency to decline. Corresponding characteristics of experimental and computed aircraft engine applications are provided in Reference [243, Fig. 10], which are considered representative for the present studies. The data contained therein has been normalized, averaged and used to derive a nonlinear correlation function depending on the relative power setting, P/P_{TO}, which is given as:

$$\eta/\eta_{TO} = 1.000 - 2.354 \cdot 10^{-4} \cdot \exp\left(\left(2.101 - \frac{P}{P_{TO}}\right)^{2.455}\right) \tag{5.11}$$

The required gear ratio results from the individual rotational speeds of fan and LP spool (see Section 5.1.3). The mapping of the FDGS external dimension refers to the semi-empirical approach given by Grieb [175, p. 407], which assumes the overall size to be widely determined through the properties of the ring gear. Accordingly, the ring gear diameter is calculated based on the gear ratio, the maximum power transmitted and an empirical, power-sensitive similarity parameter depending on the gear system type and stage configuration. Furthermore, ring gear width is assumed linearly proportional to the ring

[46] An example refers to the Lycoming ALF502/LF507 geared turbofan engine.

[47] For gear ratios up to approximately 3, a star arrangement is best suited, while for higher ratios the planetary system becomes advantageous [249]. Further characteristics of both transmission types are outlined in Reference [249, Ch. 11].

gear diameter.[48] In the present context, the similarity parameter has been calibrated using approximate information of the PW1100G gear system given in References [249], [250].

5.1.8 Validation of Propulsion System Synthesis

For purposes of validating the implemented methods for propulsion system synthesis as well as dimension and weight prediction, three cases are considered. The methodology is demonstrated for three different turbofan architectures covering various thrust classes, specifically a

- three-spool, mixed flow architecture in the 70 klbf thrust class,
- two-spool, unmixed flow architecture in the 85 klbf thrust class,
- two-spool, mixed flow architecture in the 30 klbf thrust class.

The Rolls-Royce Trent 700 series propulsion system has been chosen as a typical representative of a high-bypass ratio turbofan in three-spool arrangement and LDMF nacelle design, while the General Electric GE90-85B with SDSF nacelle layout has been employed as validation case for a typical two-spool turbofan. In addition, the IAE V2530-A5 propulsion system featuring a two-spool, LDMF layout has been considered.

The Trent 700 engine (see Table 5.3) is in service powering the Airbus A330-200 and -300 aircraft with the highest market share compared to other available engine options [251]. As such, it is considered representative of a year 2000 status for the medium-to-long range application scenario considered in this thesis. One of its latest variants, the Trent 772B, delivers 316.3 kN (71.1 klbf) sea level static thrust and is flat-rated to ISA+22 K and 2,000 ft altitude [252]. Engine certification of the baseline variant was achieved in 1994 [231]. The engine is characterized by a four-stage LPT driving the fan, while the eight-stage IPC and the six-stage HPC are each powered by a single-stage IPT and HPT, respectively. The GE90-85B[49] delivering 395.3 kN (88.9 klbf) static thrust [253] is one of the engine options of the Boeing 777-200 aircraft. Regarding its architecture, a six-stage LPT drives a three-stage booster, while the core engine consists of a two-stage HPT driving a ten-stage HPC. The IAE V2500 series powers the Airbus A320 family, the Boeing MD90 airliner as well as the Embraer KC-390 military transport aircraft [231]. Thrust ratings range up to 147 kN (33 klbf) takeoff thrust [254]. The -A5 model features a four-stage booster, a ten-stage HPC, a two-stage HPT and a five-stage LPT [231].

The validation of the propulsion system synthesis has been conducted utilizing the methods presented in Section 5.1. In this respect, the parameter describing the technology-dependent impact on the turbo component design efficiency prediction has been set in accordance with the EIS year of the first Trent 700 and GE90 version, respectively, while for the V2500 power plant the models have been adjusted to match the component efficiencies and pressure losses given in Reference [34]. Since input settings available in the public domain include different operating conditions, the discussed multi-point sizing procedure has been applied accordingly. Turbo component axial Mach numbers are set based on References [34], [175], while the hub/tip ratios at the turbo component inlets and outlets have been graphically approximated from two-dimensional general arrangements provided in Reference [231]. The settings for mechanical and customer bleed power offtake refer to References [255] and [256], respectively,[50] and the turbo component stage configuration is treated as a model input. As described in Section 5.1, engine flow path sizing is conducted at the ToC point. While for the GE90 and V2500 engines MCL thrust values are available, due to lack of reliable data for the Trent 700 power plant a

[48] Width/diameter ratios between 0.13 and 0.20 [175, p. 411].
[49] The -85B engine version is selected due to the comparatively large amount of information available in the public domain.
[50] Airworthiness requirements demand 0.55 lb/min fresh air supply per passenger [256].

typical net thrust ratio between the typical cruise requirement given in Reference [231] and the sizing thrust is assumed as well as invariant flight conditions.

	Unit	Calculated Value	Error [%]	Reference
Stage configuration [a]		1 / 8 / 6 / B / 1 / 1 / 4		[231]
Geometry				
Fan inlet tip radius	m	1.237	±0.0[c]	[231]
IPC inlet tip radius [b]	m	0.609	+1.1	[231]
HPC inlet tip radius [b]	m	0.355	–2.8	[231]
HPT exit tip radius [b]	m	0.431	–2.1	[231]
IPT exit tip radius [b]	m	0.526	–1.1	[231]
LPT exit tip radius [b]	m	0.700	–1.2	[231]
Propulsion system length	m	7.21	–1.4	[233]
Nacelle maximum diameter [d]	m	3.18	–0.7	[233]
Performance at Cruise (10,668m, M0.82, ISA+10 K)				
Net thrust	kN	53.51	±0.0[c]	[231]
Bypass Ratio	-	5.03	+0.7	[231]
Fan Pressure Ratio [e]	-	1.61	–	–
TSFC [f]	g/(s·kN)	16.10	+1.5	[231]
Performance at Sea Level Static, ISA				
Net thrust	kN	316.3	±0.0[c]	[231]
Overall Pressure Ratio	-	35.8	+1.0	[231]
Engine inlet mass flow	kg/s	913.5	–0.8	[231]
HPC inlet mass flow	kg/s	156.3	+2.0	[231]
Performance at Max. Takeoff Point (2,000 ft, M0.0, ISA+22 K)				
IP spool speed	RPM	7,231	±0.0[c]	[252]
HP spool speed	RPM	10,611	±0.0[c]	[252]
Masses				
Bare engine	kg	4,959	–0.8	[252]
Propulsion system [g]	kg	6,763	+3.8	[252]

[a] Nomenclature: stage counts of fan, IPC, HPC, HPT, IPT and LPT
[b] reference geometries graphically approximated from two-dimensional general arrangement
[c] input value
[d] mean value of nacelle maximum width and height
[e] reference value not available
[f] published value taken as uninstalled
[g] dry mass (excluding operating fluids)

Table 5.3:Validation results of propulsion system synthesis and weight estimation based on Rolls-Royce Trent 772B power plant

In Table 5.3, an overview of the validation results is presented for the Trent 772B engine, while corresponding result tables for the GE90-85B and V2530-A5 are provided in Table C.6 and Table C.7 in Annex C. For the validation of the propulsion system geometric description, turbo component tip radii, bare engine and/or overall propulsion system length and maximum nacelle diameter are considered important. The turbo component radial dimensions are within -2.8% and +0.5% deviation. With regards to performance validation, the properties used for comparison depend on the available reference data and include TSFC at cruise condition. In addition, the model results of important parameters at sea level static condition including OPR and mass flow rates have been examined for the given thrust requirement. At a MTO condition stated in the engine certification document [252],

maximum spool speeds are considered to occur,[51] thus feeding back via the implemented sizing procedure to the engine design point. Also included in the validation tables are the calculated bare engine mass and propulsion system total mass using the methods described in the subsequent Section 5.3, which are considered to yield satisfactory accuracy for the conceptual studies presented herein.

5.2 Design Aspects Specific to BLI Power Plants

The unconventional nature of the FF power plant necessitates the consideration of a series of specific design aspects. In particular, the geometric arrangement is significantly affected by the airframe integration. The installation in the BL flow also results in several propulsion related loss effects to be taken into account during conceptual studies, which are addressed in this section.

5.2.1 Fuselage Fan Power Plant Geometric Description

In general, different options are conceivable for installing the FF power plant within the fuselage. Following the outcome of a comprehensive down-selection activity outlined in Reference [114], a best and balanced solution, which is also considered in this thesis, is described by an arrangement where the FF propulsion system is positioned behind the fuselage rear pressure bulkhead. The turbo core engine is located in the fuselage aft-cone with the LP shaft connected to the FDGS. Air supply to the core engine is realized through an eccentrical s-duct intake. Targeting maximization of the BLI effect, the propulsor is positioned as far aft as possible. The longitudinal positioning, however, is constrained by feasible core intake curvature radii and appropriate fan disk burst corridors with respect to tail plane control surfaces [118]. For the determination of FF power plant longitudinal dimensions, a parameterized model has been implemented. A schematic of the FF power plant geometric arrangement is presented in Figure 5.4, which shows the FF arrangement on the upper half section compared to a

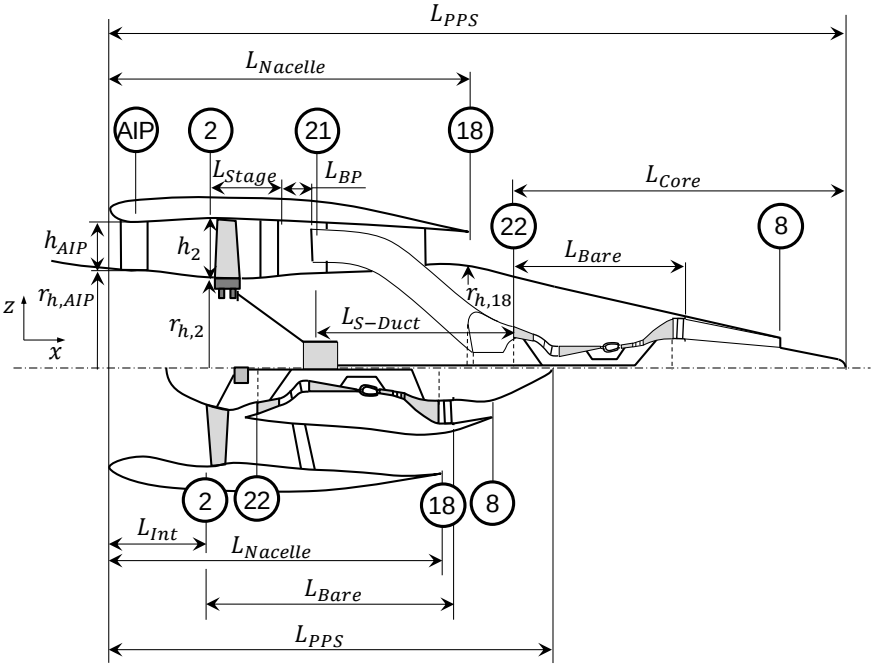

Figure 5.4: Geometric arrangement of FF propulsion system (upper section) and conventionally installed Geared Turbofan (lower section)

[51] Increments between maximum permissible speeds specified in the type certificate and normal operation are not considered.

conventional GTF layout featuring a SDSF design displayed on the lower half section. The station nomenclature indicated in the figure refers to standard recommended practice [257] and has been coherently applied to both the conventional layout and the FF GTF. Main dimension definitions are also displayed in the figure. Accordingly, the overall FF propulsion system length results from the summation of the axial dimensions of the intake, L_{Int}, fan stage, L_{Stage}, bypass duct, L_{BP}, s-duct intake, L_{S-Duct}, and core engine, L_{Core}. The latter consists of the bare core engine power plant including all components between the booster inlet and the turbine exit casing behind the LPT exit, and the core nozzle including plug. The FF stage length calculation is described in Section 5.3.1. In order to ensure consistency between the aero-numerical calculations and the aircraft-integrated propulsion system calculations, the FF nacelle length is kept invariant throughout the studies. The duct height at the AIP, h_{AIP}, is defined as the difference of tip and hub radii at the AIP. A similar quantity can be defined at the fan inlet plane, h_2. The fuselage hub dimensions at stations AIP, 2 and 18 have been derived from the fuselage contour and retained constant. Generally, the radial size of turbofan propulsors is governed by the mass flow density processed by the fan. In order to maintain acceptable fan diameters, reductions in specific thrust levels have traditionally been associated with the attempt to increase the corrected flow per frontal area through realizing combinations of reduced fan inlet hub/tip ratios and increased axial fan inlet Mach numbers.[52] A visualization of this trend in depicted in Figure B.7 in Annex B. Now, in case of the FF power plant, axial Mach numbers at the fan face are significantly reduced due to the BL flow, while the fan hub/tip ratio is strongly increased compared to conventional fan designs. Therefore, as illustrated in Figure B.7, a reduced area-specific corrected flow is obtained requiring for a given flow rate larger annulus areas. The implications on the design and performance will be discussed in Section 6.2. In order to allow for parametric studies, the flow area and thus tip diameter at the AIP is adjusted in order to achieve appropriate Mach numbers in the throat section. For model calibration, the settings used in the representative design of the DisPURSAL project are applied [114].

In order to yield adequately large duct cross section areas and hence minimize friction losses, an eccentrical s-duct core engine intake is preferred over alternative annular inlet designs [118]. This arrangement necessitates deflection of the flow from the bypass duct towards the interface with the booster entry located at the aft-fuselage centerline. Traditionally, the chord line of serpentine-shaped

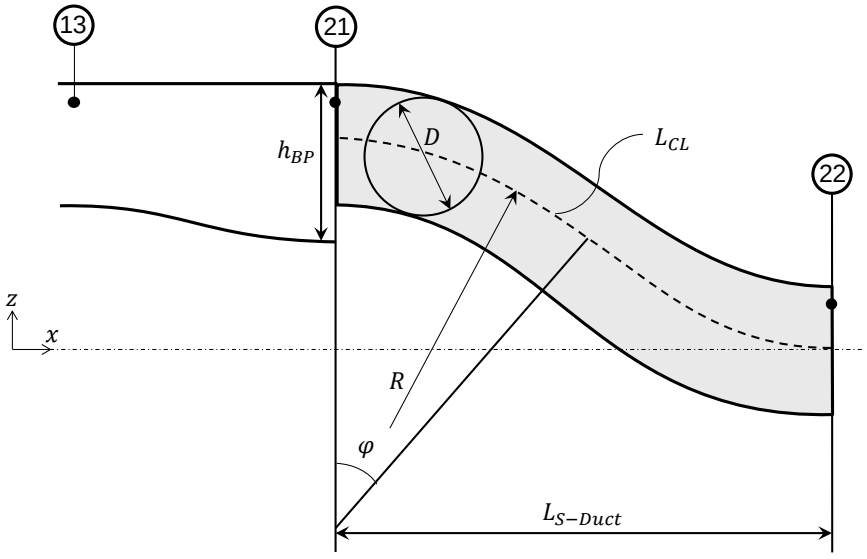

Figure 5.5: Geometric parameterization of the core intake

[52] This trend may eventually culminate in novel counter-rotating fan arrangements offering superior corrected flow per frontal area [175].

duct geometries can be described through two consecutive circular arc segments with opposed orientation [29], [258], [259]. Irrespective of alternative, more sophisticated shapes, this approach has been implemented for the parametric description of the core inlet geometry. The arc central angles, φ, situated in the xz-plane (see Figure 5.5) are calculated from basic geometric relations assuming point symmetry, i.e. identical curvature radii, R, of the two segments. The axial length of the duct installation, L_{S-Duct}, results from the given radial offset and appropriate arc angles. The bypass duct height at the core intake position, h_{BP}, is an input parameter to the model, while the length of the chord line, L_{CL}, is a result. The cross sectional areas perpendicular to the duct centerline are modeled as circular areas and assumed constant. In Figure 5.5, the parameterization of the geometric arrangement is illustrated.

5.2.2 Fuselage Fan Intake Strut Aerodynamic Blockage

For the considered geometric arrangement, the transmission of aft-fuselage related loads requires the installation of intake struts located within the FF intake (see Figure 5.4). The aerodynamic blockage due to the presence of the struts is considered in the cycle calculation. The geometric mapping of the strut and the weight prediction will be discussed in Section 5.3.1. In the first instance, the area of the struts projected to the yz-plane is determined based on the approach given in Section 5.3.1 and the tip diameter accordingly increased in order to allow the required mass flow rate to be processed by the intake. Moreover, an additional total pressure loss factor due to additional viscous flow effects emanating from the presence of the struts is applied to the intake total pressure ratio derived from the regression models described in Chapter 4.

5.2.3 Modification to Fan Design Efficiency Prediction

As an intrinsic characteristic of propulsive devices installed in the fuselage BL flow, a pressure distortion of the inflow field is observed relative to propulsors working in free stream. While this is expected to have an adverse effect on fan polytropic efficiency, determination of the impact of the presence of BL flow on fan efficiency is out of the scope of the present thesis. Several high-fidelity numerical [78], [149], [260]–[262] and experimental [263]–[265] investigations have focused on the detailed analysis of loss mechanisms associated with distorted flow and provided insight into the quantitative degradation in fan efficiency. In summary, there is indication [157] that by introducing a dedicated three-dimensional fan design adjusted to the prevailing flow profile allows for the minimization of performance loss due to BLI distortion. It should be noted that the efficiency impact depends on the type of flow distortion, which, in turn is strongly influenced by the propulsor-airframe integration strategy. As indicated in a study by Liu *et al.* [266, Fig. 7], distortion caused by circumferential cross flow tends to have a far higher impact on the fan efficiency degradation than radially induced distortion. As a summary of a literature survey, BLI fans operating in a flow field exhibiting both radial and circumferential distortion patterns have been assessed to be impaired by approximately 0.5 to 1.5% relative to the free stream installation case. Within the studies presented in Chapter 6, a decrement in FF polytropic design efficiency is applied to the value predicted by the implemented efficiency model (see Section 5.1.4), which is nominally set to -1%. It is assumed that behind the fan pressure distortion effects are sufficiently attenuated and therefore no efficiency impact on the downstream-located turbo components is assumed. As an additional effect, the fan blading may require increased relative thickness to structurally cope with distortion and to mitigate potentially associated aero-elastic excitation effects [78]. The complex trade between the attainable design fan efficiency, blade relative thickness and its impact on fan stability is not considered in the present context.

5.2.4 Core Intake Pressure Losses

For serpentine-shaped intake geometries total pressure losses can be expected to exceed those of typical pitot type intakes [178] due to curvature-induced flow separation effects and secondary flow phenomena [258]. Within the present work, a simplified model for the mapping of core intake pressure losses has been implemented for the s-shaped duct geometry described in Section 5.2.1. The model is based on one-dimensional compressible flow theory assuming steady flow [267].[53] The friction-induced pressure loss between inlet (i) and outlet (o) results from the analytical solution of the differential equation for the compressible pressure evolution along the duct assuming adiabatic walls, a constant flow area and an invariant flow coefficient, λ_D,[54] yielding [267, Sec. 5.5]:

$$\frac{p_{s,i}^2 - p_{s,o}^2}{2p_{s,i}} = \lambda_D \cdot \frac{L_{CL}}{D} \cdot \rho_i \cdot \frac{v_i^2}{2} \cdot \frac{\bar{T}_s}{T_{s,i}} \tag{5.12}$$

where $\bar{T}_s$ represents the average static temperature in the duct between inlet and outlet, ρ_i the density, v_i the velocity, $p_{s,i}$ and $T_{s,i}$ the static pressure and temperature. The geometric properties L_{CL} and D refer to Figure 5.5. The parameter λ_D results from evaluating the Darcy friction factor formulae subject to the existing flow characteristics. According to Reference [267], the selection of the appropriate correlation for λ_D depends on the flow regime (i.e. laminar or turbulent) and the duct's relative surface roughness. A series of implemented empirical models are summarized in Table C.8 in Annex C. Since the static outlet temperature depends on the outlet pressure, Equation (5.12) requires iterative solving. Any potentially required diffusion towards the downstream compressor face is assumed to be accomplished outside the duct, i.e. in the interfacing plenum. In addition to pressure losses caused by friction on wetted surface, a pressure decrement results from the redirection of streamlines due to a localized change in wall geometry causing flow separation and secondary flow effects. The corresponding losses are mapped using an appropriate loss coefficient, ζ. In Reference [268] a tabulation of ζ is given depending on important geometric properties including the arc angle, which is used as a basis for interpolation. The loss contributions from friction and flow deflection are then used to determine an overall core intake total pressure ratio, $\pi_{CI} = p_o/p_i$. More-dimensional swirl effects are neglected, in the first instance.

The implemented model has been calibrated using experimental data measured during a test campaign of the M2129 s-shaped duct investigated in a joint effort by NASA and the UK Ministry of Defense featuring circular cross section [269]. Corresponding geometric settings and total pressure ratios have been read from Reference [270, Fig. 21]. For model validation purposes, the calculated characteristics of π_{CI} have been compared to test data obtained from transonic wind tunnel tests at NASA Langley Research Center examining a flush-mounted s-duct intake at Reynolds numbers representative for full-scale aircraft application. The validation data has been read from Reference [271, Fig. 24B] and is available for a variety of geometric configurations and operating conditions. Comparison to the model prediction yields good agreement. The validation results are shown in Figure B.8 in Annex B for a wide range of inlet Mach numbers, M_i. The maximum error is 1.9%, while the root-mean-squared error amounts to 0.6%. The deviation may be caused by complex secondary flow effects not entirely captured in the simplified model.

In Figure 5.6 the characteristics of π_{CI} obtained from the implemented model are displayed for variations of key operating conditions (M_i) and geometric parameters outlined in Section 5.2.1 for a fixed duct diameter. The dimensionless quantity f_ζ denotes a technology scaling factor applied to the calculated pressure loss caused by localized flow deflection. Potential improvements mapped through a reduced f_ζ below unity might e.g. be realized by introducing flow straightening devices within the

[53] cf. also discussion by Bijewitz *et al.* [29]
[54] also referred to as Darcy friction factor

duct such as vane effectors as suggested e.g. in References [269], [270]. Inspection of the results indicates the significant impact of the inlet Mach number on the friction caused pressure losses. Variations of h_{BP} influence the radial position of the duct entry and hence alter the arc angles. A similar effect is triggered by changing values of L_{Duct}, thus directly impacting on the duct loss coefficient. The observed interplay between duct dimensions and pressure loss illustrates the complex trade-off necessary between the desire for a short intake length and the associated minimized installation volume and weight, and the sacrifice in intake performance with regards to pressure loss. The behavior of π_{CI} against variations of f_ζ is intuitive.

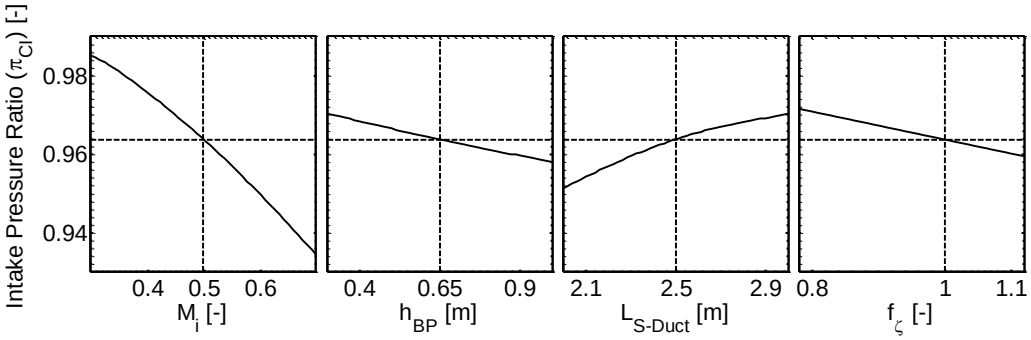

Figure 5.6: Evaluation of core intake pressure loss model (geometry: s-duct described by two consecutive arc segments), adapted from Bijewitz *et al.* [29]

Complex three-dimensional effects from secondary flow phenomena could result in a distorted compressor inflow field and hence degrade the performance of the core engine. For the core intake, however, these loss effects are assumed to be minimized through careful aerodynamic shaping (see e.g. Reference [145]) and hence, not explicitly considered, in the first instance.

5.2.5 Mapping of Intake Pressure Distortion

Intake distortion in general describes a spatial and temporal variation of flow properties and arises when the airflow delivered by the intake to the fan departs from the ideally uniform distribution in total pressure or temperature. Most practical significance is typically associated with the variation of total pressure across the engine face [178]. For conventionally installed turbofan engines, circumferential distortion may occur at flight conditions producing separated inlet flows such as strong crosswind situations, when the engine is operated at high incidence angles and during abnormal operation, thereby creating angular sectors where inlet pressure is significantly lower than the average value [196]. Radial non-uniformities due to the BL profile inside the inlet duct are typically approximately one order of magnitude smaller than circumferential distortion (cf. Reference [227]) and can be neglected for most practical cases [178]. Although the upstream suction effect of the fan greatly increases the critical lip separation angle and thus tends to delay flow separation at the lower intake lip [227], as a most important impact of pressure distortion, a shift in operating point in the fan map towards stall is encountered, thus causing performance degradation of the engine as a whole.

For conventionally installed turbofans in commercial transports, the highly optimized intake geometries yield only small inlet distortion effects within the normal engine operating envelope even at high incidence angles [178]. In case of more integrated arrangements where the BL developing along airframe surfaces is in close vicinity or even ingested into the propulsor, the inflow conditions may be significantly altered relative to the case of freestream installation. Different from semi-buried or flush-mounted propulsion systems with strongly coupled circumferential and radial flow distortion throughout the flight, at zero-to-low incidence angles (i.e. during cruise) the intrinsically symmetrical

installation of the FF intake is expected to restrict distortion effects to the radial type induced by the BL flow. Since a major portion of the flight is conducted within cruise, the rotor blading design is assumed to account for the radial velocity and pressure profile and hence limit the adverse effect to a small decrement in design efficiency. However, during low-speed operation at angle-of-attack, the asymmetric flow around the fuselage will cause circumferential distortion patterns. Although distortion is in general a three-dimensional phenomenon, for computational reasons, radial and circumferential distortion are frequently assessed separately and subsequently super-positioned [272]. Accordingly, as an initial step towards characterization of non-uniform inlet conditions, both effects are individually discussed in the following. Potentially beneficial flow-straightening effects due to the FF intake struts are not considered, as are additional distortion effects emanating from the wing-induced flow field.

The radial distributions in flow parameters are derived from the CFD computations discussed in Section 4.1 and the BL thickness is corrected for takeoff conditions using an empirical correlation for turbulent flow [172]. This radial distribution is assumed to be uniformly spread around the circumference. Due to the lack of numerical or experimental three-dimensional data for the investigated configuration, for the consideration of two-dimensional pressure variations, similarity with a flush-mounted turbofan installation is assumed, in the first instance. Specifically, the relative pressure loss in the lee-oriented inlet sector (i.e. the angular sector hidden by the fuselage during positive angle-of-attack operation) is treated in similarity to the two-dimensional profile exhibited in flush mounted arrangements. Experiments with ogive cylinder bodies have shown that this is the origin of vortex fields and pressure deficits [273]. Extensive wind tunnel data with Reynolds numbers representative of full scale transport aircraft applications covering a wide range of inlet Mach numbers and engine operating conditions at zero incidence are presented in Reference [271, Fig. 19]. The extracted data containing steady-state (i.e. time-averaged) values has been transformed in non-dimensional form and interpolated using a representative takeoff Mach number assuming the takeoff rotation point as the critical operating condition. Subsequently, the circumferential distortion characteristics are super-positioned with the radial characteristics.

A typical metric quantifying the amount of circumferential distortion is the DC_θ index [178],

$$\mathrm{DC}_\theta = \frac{\bar{p} - p_\theta}{\bar{q}} \tag{5.13}$$

where $\bar{p}$ indicates the total pressure averaged across the fan face, $\bar{q}$ is the corresponding dynamic pressure and p_θ represents the mean pressure in the sector of angle θ where the lowest pressure is exhibited. According to Seddon and Goldsmith [178], a commonly used sector angle is 60°. The quantity of DC_{60} is computed from the two-dimensional pressure profile, $p = f(r, \theta)$, by identifying the sector with the lowest averaged total pressure. As an initial estimation, the sensitivity of DC_{60} with angle-of-attack is mapped by applying the characteristic of a serpentine-shaped inlet duct given in Reference [178, Fig. 11.17] to the calculated characteristics.

The discussed distortion modeling approach has been validated against three-dimensional RANS computations of a PFC configuration described in Reference [121]. The data basis for validation refers to Reference [274, Fig. 10f].[55] The comparison has been conducted for a takeoff case at 8° angle-of-attack. Key geometric settings of the fuselage and propulsor as well as operating conditions have been set as given in References [125], [55, Fig. 5.21] and [274, p. 6]. The relative error of the implemented method with respect to DC_{60} has been determined as -5.9%, which is considered acceptable considering the simplicity of the implemented approach. Additional data of the validation case is summarized in Table C.9 and in Figure 5.7.

[55] The value of the DC_{60} metric has been derived from the published total pressure contours at the fan face using graphical image processing [323].

The implications of pressure distortion on the performance of the FF are modeled using parallel compressor theory originally proposed by Pearson and McKenzie [275]. As a key assumption, the distorted flow field upstream of the fan is modeled by angularly separated streams featuring different but uniform total pressures constituting the inlet conditions of the separate sub-compressors. In the formulation considered here, two separate streams are applied and the flow capacity of each sector is scaled with the angular width of the considered sector angle, i.e. $\theta/(2\pi)$ and $1-\theta/(2\pi)$, respectively [276]. Both compressors are assumed to work against the same static pressure in the downstream duct. Hence, the compressor handling the sector exhibiting lower total inlet pressure is required to produce an increased total pressure ratio, thus yielding an operating point closer to the stall line than the other compressor. As suggested in the formulation of parallel compressor theory, the entire compressor becomes unstable once the operating point in the distorted sector reaches the stall line [276]. Since in the short compressor inter-ducts of conventionally installed turbofans limited opportunity is given for achieving the static pressure balance postulated in the theory, this boundary condition is often replaced by a condition preventing the balance of mass flow between the distorted and undistorted sectors downstream the compressor, also referred to as "compressor coupling" [276]. Different from conventional turbofans, the long core engine intake duct intrinsic to the FF propulsion system design is considered to allow for sufficient redistribution of flow downstream the FF and thus no compressor coupling is considered here.

An exemplified evaluation of the implemented model is shown in Figure 5.7. The study settings correspond to the validation case previously discussed. The right part indicates the modeled sensitivity of DC_{60} with angle-of-attack while the left part shows the implications on FF surge margin (SM_{FF}).[56] The relative change of FF bypass nozzle area, $\Delta A_{18}/A_{18,ds}$, is shown as a contour parameter. The operating intake pressure ratio, $\pi_{int,TO}$, is parametrically mapped based on the methods presented in Chapter 4 (see Figure 4.16). As expected, increasing values of DC_{60} yield a shift in the operating point towards the stall line and thus a decline in SM_{FF} is observed. The increase of the bypass nozzle area strongly de-throttles the fan and hence moves the working line to higher corrected flows and lower pressure ratios. While at low incidence angles intake pressure ratios greatly exceeding the respective design values contribute to ample surge margins, at higher incidence angles the increasing level of distortion and the decay in $\pi_{int,TO}$ cause SM_{FF} to deteriorate strongly. Accordingly, at incidence angles typical for takeoff rotation an increase of the bypass nozzle area may be required to attain acceptable

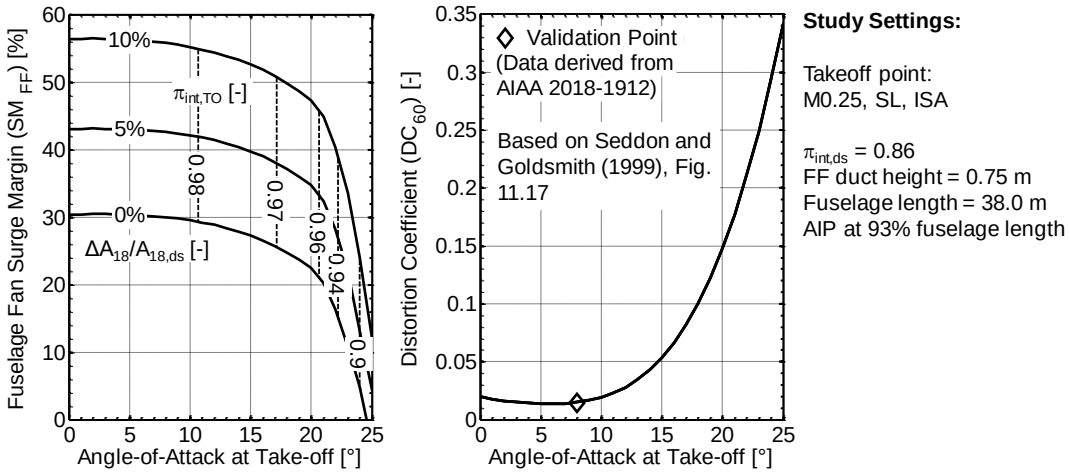

Figure 5.7: Exemplified prediction of FF surge margin (left) and distortion coefficient as a function of takeoff angle-of-attack

[56] In the present context, the surge margin definition at constant flow utilized e.g. in the software GasTurb [191, Sec. 4.19.2.4] is employed.

stability margin. As suggested by Walsh and Fletcher [196, p. 460], at least 15% margin is required for commercial fan applications.

Further effects yielding additional deviations from the symmetrical propulsor inflow such as operation at angle-of-sideslip, crosswind, and wing-induced wash are not considered. Also, total temperature distortion occurring e.g. from exhaust gas ingestion[57] and transient distortion effects are neglected. The impact of dynamic deformations of the FF nacelle during maneuvers on fan tip clearance and associated aerodynamic stability is not considered in the present work.

5.3 Power Plant Weight Prediction

The estimation of power plant weight constitutes a central aspect in the conceptual design phase since mass characteristics are crucial for determining the technical feasibility and important attributes including mission fuel consumption. A significant aspect of the investigated aircraft configuration is associated with the weight implications of the propulsion system installation. As a result of the unconventional nature of the fuselage-encircling propulsion system installation, no empirical database for crucial system component weights is available. Hence, a set of simplified, physics-based methods for the parametric estimation of major systems has been developed. The estimation of the weight properties of conventional turbofan power plants refers to Section 5.3.5.

For the weight prediction of the FF propulsion system, a component build-up approach is introduced breaking down major systems into several components. The increased integration of the considered propulsion system requires definition of the interfaces between propulsion and airframe related systems, which are visualized in Figure 5.8. The control volume encompassing the FF propulsion system includes the fan module, the FF drive gear system, the core intake, the core engine, and the nacelle. The term “core engine”, here, refers to the components between the booster inlet and the core nozzle exit. The different systems are broken down into components and subcomponents according to the scheme indicated in Figure 5.9. The systems outside the control volume shown in Figure 5.8 are considered to be part of the airframe weight accounting.

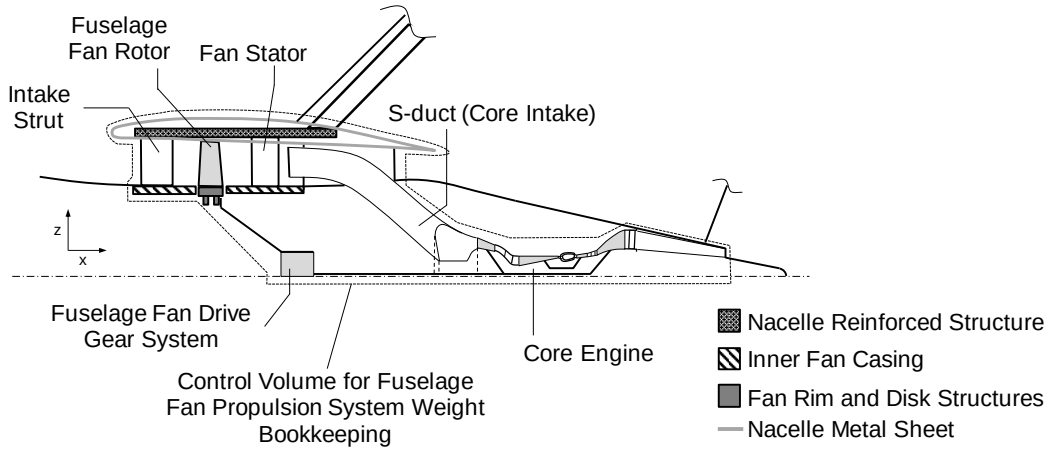

Figure 5.8: Schematic overview of control volumes for FF module weight accounting

Targeting coherence between the FF propulsion system and conventionally installed power plants, a hierarchical component build-up structure has been introduced which is visualized in Figure 5.9. The scheme adheres to the typical division of the overall power plant weight into bare engine weight and

[57] primarily relevant for military and vertical takeoff and landing applications and during thrust reverser operation [276]

nacelle weight. Accordingly, the bare engine weight includes the FF module, the FF drive gear system,[58] the core intake and the core engine as well as operating fluids. The notion of thrust reversing is not considered for the FF power plant due to the anticipated complex installation of reverser systems. With respect to conventionally installed turbofan propulsion systems, the bare engine includes the fan assembly, an optional fan drive gear system, the core inlet and the core engine, while the sum of bare engine and nacelle component weights constitute the propulsion system weight. A visualization of a typical component build-up is provided in Reference [182, Fig. 5.12]. A description of the modeling approaches of the individual constituents of bare engine and nacelle weight is given in the following sections.

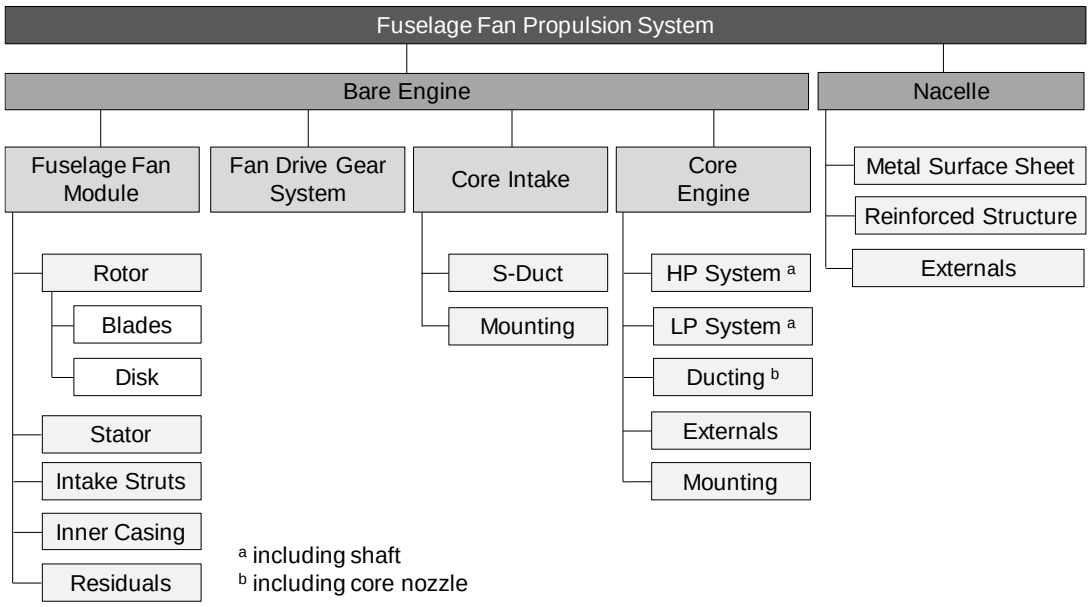

Figure 5.9: Weight breakdown of FF propulsion system

5.3.1 Fuselage Fan Module

In case of conventional turbofans, the mass of rotating parts is closely correlated to the centrifugal stress exhibited at the blade roots and connected disks. Centrifugal stress can suitably be described through the AN^2 metric. While for state-of-the-art conventional fans the inlet hub/tip ratio is typically approximately between 0.26 and 0.30 [175], the FF module is intrinsically characterized through significantly higher values resulting from the increased hub radius. In Annex A, it is analytically demonstrated that in this case the airfoil centrifugal stress is greatly reduced for a given material density and representative blade tip speed compared to existing conventional fans. As a result, centrifugal stress is considered a less dominating sizing case for the design of the rotating components compared to other loads such as bending in reaction to gas loads and torsion. Due to the fundamentally different load situation and geometric arrangement compared to conventional fans, the applicability of existing empirical methods for mass estimation is considered inappropriate. Instead, a simplistic parametric model involving evaluation of the displaced material volume of major subcomponents of the fan module is used as an initial estimation. The model is based on References [29], [113] and has been extended as part of the present work. The considered subcomponents are parametrically scaled based on essential geometric dimensions and include rotor blades and the connected disk, stator vanes, intake struts as well as the inner fan casing (see Figure 5.8). The outer fan casing is bookkept as part of the nacelle reinforcing structure (see Section 5.3.2).

[58] FF module and FF drive gear system may be subsumed as “propulsive device”.

Fan blades, stator vanes and intake struts are approximated through solid polyhedrons of rectangular cross section, irrespective of perspectives for manufacturing techniques based on advanced hollow structures and more sophisticated shapes. For rotor blades, a polynomial chord length distribution of second degree is assumed[59] (cf. Reference [277]), while vanes and struts are considered of constant cross section. Key properties of the individual components including solidities, σ, thickness/chord ratios, t/c, and taper ratios, τ, are model input parameters. Similar to conventionally installed fans, the rotor blade aspect ratio, Λ, is parametrically mapped as a function of corrected flow based on empirical data given in Reference [175, Fig. 5.2.2.14b]. The inner fan casing is modeled as an annular volume of constant cross section. For reasons of reduced tonal interaction noise between stationary and rotating components, based on the empirical data given in Reference [175, p. 460], a relative axial spacing, s/c, of 1.5 between the blades and the stator vanes is applied for the scaling of the casing length, while for the relative spacing between intake struts and the rotor plane a value of 1.0 is assumed. Due to the generally higher hub/tip ratio of the fan rotor, the external load on the disk module is greatly reduced. This beneficial effect, however, is diminished by an increased centrifugal force exhibited by the disk material itself resulting from the increased hub diameter. In total, the utilization of a preliminary rim and disk sizing method presented by Mattingly *et al.* [207, Sec. 8.2.3.3] in conjunction with a first-order calculation for airfoil centrifugal stress[60] shows that for typical rim and disk shape parameters centrifugal stress is not a dominating sizing case for the present application and is therefore not considered. Instead, a simple geometric parameterization is introduced. The disk module is considered to be composed of the rim and disk itself. For the determination of rim and disk volumes, similarity in the fan disk shape with state-of-the-art turbofans is assumed, in the first instance. The disk module cross sectional shape is approximated to be composed of a series of annular volumes (a schematic is given in Annex A). For the rim, a rectangular body of revolution with an aspect ratio derived from Reference [278] is used, where the rim width is correlated to the length of the blade root chord length projected to the xz-plane. The ratio of disk height to rim width is parametrically mapped as a function of the fan hub radius based on empirical data graphically derived from a compilation of existing turbofan engines [231] employing the specific disk shape considered representative in the present context. The ratio of disk width to rim width is derived from Reference [278] and retained constant. Basic plausibility has been checked by comparing the total disk mass to the approximate mass of the V2500-A5 series fan disk derived from the weight breakdowns given in Reference [213, Fig. 5.3 and D.1], which yielded satisfactory agreement (+2.6% deviation). The length of the fan stage, L_{Stage}, is determined based on the sum of area-averaged projected chord lengths of rotor blade, stator vane and the corresponding spacing between the components. Similarly, the intake length, L_{Int}, is computed.

The subcomponent masses are obtained from the summation of the products of density, ρ, and material volume, V, of the respective p subcomponents featuring n_i blade elements, and the disk (index D) as well as the casing (index C):

$$W_{FF,bare} = \sum_{i=1}^{p} \rho_i V_i n_i + (\rho V)_D + (\rho V)_C + W_{Res} \tag{5.14}$$

Residual components (W_{Res}) such as air sealings, bearings and supports are not explicitly modeled but treated as constant model inputs. The respective number of blade units, n, is computed from the area-averaged mean annulus radius, r_m, and the chord length, which can be conveniently expressed as a function of the hub/tip ratio, solidity, σ, and aspect ratio:[61]

$$n = \text{ceil}\left(\frac{2\pi r_m \sigma}{c}\right) = \text{ceil}\left(\pi \frac{1+\nu}{1-\nu} \sigma \Lambda\right) \tag{5.15}$$

[59] see also Annex A
[60] Involving the numerical integration of the product of local cross sectional area and local radius [318].
[61] As a conservative assumption, the ceiling function is employed here.

As part of the implemented procedure, it is verified that the ratio of vane and blade numbers is above a critical threshold specified in Reference [175, Fig. 461],[62] thereby causing the partial cancellation of tonal noise propagation. In addition, based on practical guidelines given in Reference [209], if necessary, the rotor blade count is adjusted to be an adjacent even number, thus easing rotor balancing upon blade failure. Similarly, for reasons of avoiding aero-acoustic excitation, it is verified that the resulting stator count is not an integer multiple of the number of rotor blades.

In Figure 5.10, an evaluation of the implemented model is shown for a range of FF blade heights. For the purpose of the study, a material mix consisting of 80% Carbon Fiber Reinforced Polymer (CFRP) and 20% titanium[63] is assumed for rotor blades [279]. Material properties have been taken from Reference [194]. Reflecting the requirement for superior robustness against foreign object damage, the intake struts are considered to feature 30% titanium, while the inner fan casing is assumed to be solely consisting of CFRP. For the disk, a solid titanium volume is assumed. In order to account for intake distortion effects, potential mechanical excitation and thus higher required robustness, the value for the pitchline t/c of rotor blades of typical transonic compressors [176, p. 376] is assumed to be increased by 50%. Due to the assumedly combined stator and strut functionality, for the vanes a higher value is chosen for t/c. Acknowledging the need to pass fluid lines and electric wiring through the intake struts, a t/c of 0.1 is selected for these subcomponents and a lower limit for the absolute thickness is applied. The chosen solidity of the fan blades and stator vanes refers to Reference [175, Fig. 6.11.7]. Further geometric model settings used for the study are tabulated in Figure 5.10. The partially discontinuous characteristics emanate from discrete changes in the calculated number of blade, vane and strut units (equation (5.15)). Intuitively, elements with high relative thickness result in a large share of the overall mass. A supplementary evaluation with respect to important sizing parameters of the implemented model including design net thrust, specific thrust and design free stream Mach number is provided in Figure B.9 in Annex B. It is noted that detailed mechanical sizing

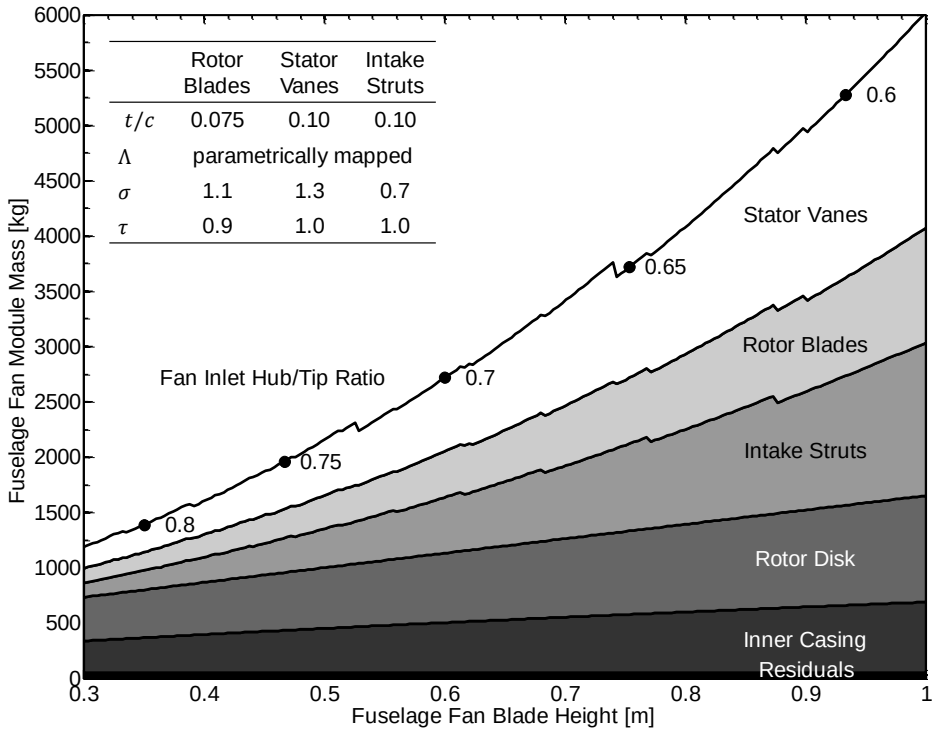

Figure 5.10: Exemplary evaluation of FF module weight prediction model (hub radius: 1.40 m)

[62] Also referred to as „cut-off condition“ [176]
[63] Ti-6Al-4V alloy is considered

and corresponding weight prediction of the fan module requires in-depth analysis of all relevant load case scenarios including discrete loading events resulting e.g. from foreign object damage.

5.3.2 Fuselage Fan Nacelle

As an intrinsic characteristic of the synergistic propulsion integration approach of the PFC, the FF nacelle serves multiple functions. Apart from its aero-propulsion related purpose and different from nacelles of conventional turbofans, a fundamental role is also associated with the transmission of aft-fuselage related forces into the fuselage center section, thus being essential for the structural integrity of the aft-fuselage segment.

Similar to the FF module, for the targeted installation type no empirical method for the prediction of FF nacelle structural weight is available. Hence, as an initial approach to the parametric mapping of nacelle structural weight, a simplified physics-based model has been developed. Now, the detailed structural dimensioning of the nacelle involves analysis of all relevant load cases and potential failure modes. Significant aspects include inertial and maneuver loads of the empennage, low and high cycle fatigue considerations, gyroscopic forces emanating from the rotating fan rotor, aerodynamic forces caused by the pressure differential of external and internal nacelle flow and discrete loads resulting e.g. from blade-off events and foreign object damage. In the present context, loads emanating from inertial and tailplane related aerodynamic forces are considered of primary significance, in the first instance. Inertial forces refer to the vertical and horizontal tail, the fuselage-installed power plant and the nacelle itself. In addition, reaction loads due to FF blade-off are conceptually considered. For the estimation of aerodynamic forces, the most critical static load cases with respect to the tail plane structures are considered and the corresponding forces and moments determined. This requires the conceptual dimensioning of the control surfaces, i.e. the rudder and elevator, respectively, which is outlined in the following paragraphs.

5.3.2.1 Vertical tail loads

Significant critical loads on the vertical tail (VT) result from the side force produced by rudder deflection and from lateral gusts [280].[64] Now, for transport category aircraft, the most critical scenario determining the size of the rudder is typically associated with the requirement to maintain directional trim while operating with asymmetric thrust following a One Engine Inoperative (OEI) condition at the critical takeoff condition [35].[65] Similarly important, the available rudder side force must be sufficient to ensure proper alignment with the runway during crosswind landing up to a wind speed specified by airworthiness standards. In the present context, the calculation of the required rudder size is based on evaluating the maximum required yawing moment to directionally control the aircraft in the most critical condition following the procedure outlined by Sadraey [35, Sec. 12.6.3.1] assuming maximum rudder deflection, $\delta_{R,max}$.[66] The resulting rudder control derivative strongly depends on the thrust of the remaining propulsion system and the lateral distance to the aircraft centerline. The windmilling drag of the failed engine is accounted for using the empirical formulation of Reference [281, p. 218]. The rudder effectiveness is determined from Reference [35] and used to determine the required rudder-to-vertical tail chord ratio, c_R/c_{VT}, using empirical data given in Reference [35, Fig. 12.12]. The VT side force coefficient due to rudder deflection is determined from the lift curve characteristic of the Fokker F29 T-tail conceptual design given in Reference [282, Fig. 33.1] exhibiting sensitivity with c_R/c_{VT} and δ_R. Using a similar approach, the required rudder side force to satisfy the requirements for a safe crosswind landing is calculated based on Reference [35, Sec. 12.6.3.2]

[64] Further load cases neglected here include sudden aileron deflection [280].
[65] Information on the critical takeoff velocity for transport aircraft is provided in Reference [181, p. 437].
[66] Typical maximum rudder deflection angles are given in Reference [35, p. 687] for various types of transports.

assuming the most critical condition, i.e. a crosswind direction perpendicular to the runway heading.[67] Typical aircraft sideslip derivatives for transport aircraft are provided in Reference [35]. As part of the implemented method, the magnitude of the critical gust load is estimated as well. The detailed computation of gust loads requires evaluation of all relevant combinations of design flight speeds, gust velocities and altitudes. Following guidelines given in Reference [171, p. 325], as an initial approach, the design cruise speed at 20,000 ft altitude and a gust velocity of 15 m/s may be selected as the critical condition. An analytical formulation for the critical gust load on the vertical tail is given in Reference [280, p. 63].[68]

5.3.2.2 Horizontal tail loads

For the load prediction of the horizontal tail (HT), a corresponding model has been implemented. Similarly as for the rudder, the elevator dimensions are determined based on the design procedure suggested in Reference [35, Sec. 12.5]. Taking transport aircraft with standard tricycle landing gear arrangement, the most critical condition for the sizing of the elevator is typically associated with the requirement to induce a sufficient aircraft angular acceleration about the main landing gear rotation point during takeoff rotation. Typical rotational acceleration rates along with recommendations for the corresponding aircraft speed can be found in Reference [35, p. 645]. The aircraft mass moment of inertia around the lateral axis is estimated utilizing the empirical formulation given by Roskam [283, Ch. 3]. Now, for the calculation of the required elevator size, the equations of motion at the instant of rotation, i.e. the force balances in vertical and axial direction, and the moment balance around the aircraft center of gravity [35, p. 677] are solved for the horizontal lift force. Contributions from wing/fuselage lift, aerodynamic drag forces, wing/fuselage pitching moment, engine thrust, linear acceleration, runway friction as well as the corresponding lever arms are inputs to the parameterized model. The elevator effectiveness is computed assuming maximum negative elevator deflection[69] based on Reference [35, p. 679] and used to determine the relative elevator chord ratio expressed as fraction of the HT chord length, c_E/c_{HT}, from data given in Reference [35, Fig. 12.12]. As part of the implemented procedure, it is verified that the calculated elevator design does not cause the HT to stall during takeoff rotation by comparing the maximum operating HT angle with the HT stall angle taking into account the stall angle decrement due to elevator deflection [35]. In analogy to the load prediction of the VT, the critical gust load is estimated based on References [171] and [280, p. 63]. As detailed by Torenbeek [171], maneuver loads may even constitute a more critical load scenario for the structural sizing of lifting surfaces of large commercial aircraft. Hence, for the initial mapping of HT maneuver loads, the approach given in References [280] and [284] has been employed targeting the calculation of the balancing tail load for a steady-state pull-up maneuver at maximum takeoff weight, maximum operating Mach number[70] and limit load factor.

During both rudder and elevator sizing, the basic plausibility of the obtained designs is monitored by verifying that the effectiveness of the control surfaces does not exceed unity, and, that the obtained relative geometric characteristics c_R/c_{VT} and c_E/c_{HT} are consistent with typical ranges recommended in Reference [35]. The VT and HT induced critical loads relevant for the structural dimensioning of the nacelle are subsequently treated as inputs in the superordinate nacelle structure sizing model.

5.3.2.3 Approach to nacelle structure dimensioning

The approach is based on the dimensioning of the load carrying nacelle structure (Figure 5.8) considering the relevant acting forces and moments exerted on it. As an initial approach, the complex load situation in the aft-fuselage section is divided into separately acting tailplane related aerodynamic ($F_{HT,a}$ and $F_{VT,a}$, respectively) and weight forces ($F_{HT,w}$ and $F_{VT,w}$), as well as the aft-fuselage related

[67] Regulatory requirements regarding the magnitude of wind speed are specified in the airworthiness standards (CS 25.233).
[68] The formulation for an empirical gust alleviation factor to account for dynamic effects is provided in Reference [171].
[69] Typical maximum negative and positive elevator deflection angles are provided in Reference [35, p. 637].
[70] The value of an in-service commercial widebody transport (Airbus A330) of M0.86 is applied [187].

weight force, $F_{AF,w}$. The parameter $F_{AF,w}$ comprises the weight force of the aft-fuselage power plant and the structural weight of the aft-fuselage section, which is, as a simplification, scaled with the corresponding fuselage length fraction. In addition, forces emanating from unsteady rotor loads are considered. Weight forces are approximated as point forces acting in the respective centers of gravity and scaled using the ultimate design load factor, while aerodynamic forces are assumed to act in the tailplane aerodynamic centers. Rotor loads refer to the simplified computation of the reaction forces to be transmitted through the structure as a consequence of a rotor imbalance following a FF blade-off event. Both centrifugal and weight forces of a single FF blade element (see Section 5.3.1) treated as a point mass are considered. The failed blade is assumed to be oriented such that the resulting reaction force is acting in the most critical angular direction with respect to the overall load situation. The forces $F_{BO,1}$ and $F_{BO,2}$ are assumed to be induced in equal shares before and aft of the FF plane of rotation, in the first instance. The nacelle's own weight force, $F_{Nac,w}$, is taken to be concentrated in the nacelle center of gravity. Gyroscopic loads and discrete loads emanating from blade-off debris acting on the nacelle inner surface are neglected. A graphical representation of the considered load condition is given in Figure 5.11 for the FF power plant displayed in Figure 5.4.

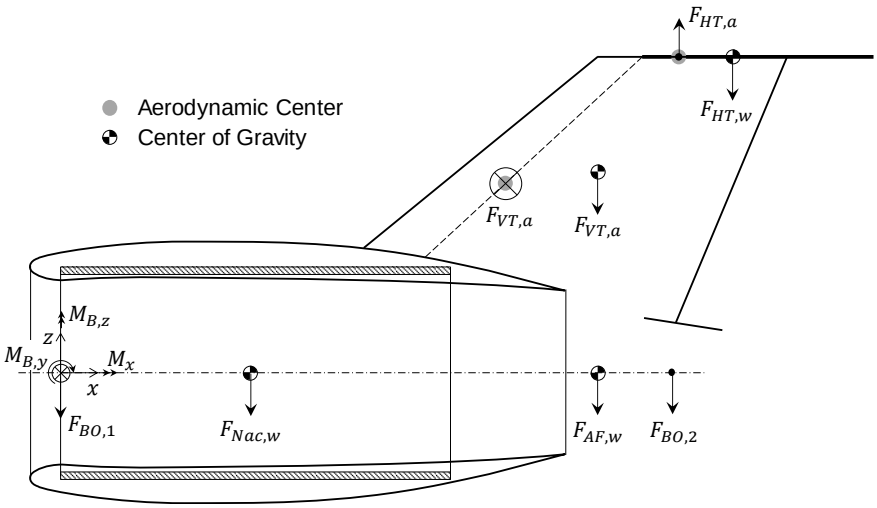

Figure 5.11: Schematic representation of considered forces and moments for FF nacelle structural weight estimation

The transmission of forces is considered to be realized by a load carrying structure (cf. also Figure 5.9), which is approximated as an annular cylindrical body. As a conservative approach, any perspectives for establishing a secondary load path through the FF drive gear system are disregarded, in the first instance. Similarly, potential improvements to the structure's rigidity offered by stiffeners, spars or more topologically optimized shapes are not considered. The dimensioning of the nacelle load carrying structure is based on the computation of the considered three-dimensional stress condition and refers to the basic mechanical engineering practice presented in Reference [285]. The forces described above result in bending moments around the lateral and vertical axis ($M_{B,y}$, $M_{B,z}$, respectively), as well as torsional moments M_x which are evaluated at the forward attachment point of the structure (see Figure 5.11). The bending stress components with respect to the vertical and lateral axis are computed based on the individual bending moments acting in the respective planes and the section moduli of a circular hollow element of constant thickness (cf. Reference [285, Fig. 3.9]). The total bending stress, σ_b, results from the superposition of the partial bending stresses [286]. Similarly, shear stress is composed of a stress component due to torsional moment, τ_t, requiring consideration of the polar section modulus, and stress due to eccentrically acting cross forces, τ_s.

Now, according to Reference [285, Sec. 3.5.4], the proper assessment of structural integrity against static failure requires evaluation of both the separate contributions of bending, shear and torsional stresses, as well as the equivalent stress. Equivalent stress is computed from the individual contributions of σ_b, τ_t and τ_s according to Reference [285, Sec. 3.5.4.2]. For the determination of the applicable material strength, a procedure for a variety of material groups is provided in References [285] and [287]. For the studies presented in Chapter 6, typical aluminum alloy is assumed, i.e. advanced material options such as for CFRP are disregarded.

Since the wall thickness, t, is expected to be small compared to the mean radius, r, in addition to the discussed classic load scenarios buckling cases are included in the model. The material resistance to buckling is analytically calculated according to Reference [288] assuming isotropic material. This involves parametric evaluation of empirical correlation factors based on the load situation, material properties and basic geometry relations. For bending,

$$\sigma_B = \frac{\gamma E}{\sqrt{3(1-\mu^2)}} \cdot \frac{t}{r} \tag{5.16}$$

applies, where γ constitutes an empirical buckling correlation coefficient:

$$\gamma = 1 - 0.731\left(1 - \exp\left(-\frac{1}{16}\sqrt{\frac{r}{t}}\right)\right) \tag{5.17}$$

For shear or torsion, Reference [288, Sec. 3.1.1.6] suggests:

$$\tau = 0.747\frac{Et^2}{l^2}\left(\frac{l}{\sqrt{r \cdot t}}\right)^{3/2} \tag{5.18}$$

In Equations (5.16) and (5.18), E represents Young's modulus, μ Poisson's ratio, and l the nacelle structure length. For the superposition of the interacting buckling loads, a conservative estimation for isotropic, unpressurized cylinders presented in [288, Sec. 3.1.1.8] based on a classic stress ratio equation is used:

$$R_1^x + R_2^y + R_3^z = 1 \tag{5.19}$$

where the quantities R_i represent the ratio of applied to permissible stress with respect to a particular type of loading such as bending, shear and torsion, respectively. The exponents x, y and z are typically empirically derived. Guidelines are provided in Reference [288, Sec. 3.1.1.8].

In the present approach, the most critical load scenario is considered decisive for the structural sizing. During an iterative routine, the structure thickness is adjusted such that the resulting stress corresponding to the most critical load condition satisfies the material strength regarding the respective loading situation, thereby affecting the nacelle's own weight. The inner diameter of the ring structure is approximated as the fan tip diameter, while the nacelle length is an input parameter to the model. The nacelle external and inner surface is modeled as a thin sheet with a given thickness and considered not load carrying. The outer wetted surface area is calculated according to Section 5.5.1, while the inner surface area towards the bypass duct is treated as a cylinder of constant diameter. The mass is computed from the required volume and the material density. A residual mass increment is added capturing potential subcomponents located inside the nacelle.[71]

A parametric evaluation of the implemented model is presented in Figure 5.12. Here, both the FF power plant mass, $W_{FF\ PPS}$, and the FF tip diameter (considered equivalent to nacelle inner diameter, D_i) have been selected as study variables. The ordinate shows the nacelle weight, while a secondary contour parameter is used to visualize the required nacelle thickness. For the sake of this example, tailplane weights, lever arms, FF tip speed, takeoff and landing operating conditions, and the nacelle length have

[71] An overview of ancillary systems typically located inside conventional nacelles such as anti-icing systems, air sealing, nacelle ventilation and compartment cooling, drain lines and attachment structures is given in Reference [208].

been set typical for the targeted widebody application and retained constant.[72] Intuitively, the increasing bending stress caused by increasing power plant masses result in a growing nacelle mass. Inspection of the stress situation reveals that for the given settings the buckling case is most critical. The stresses σ_b as well as τ_t initially decrease for increasing D_i due to the section moduli being highly sensitive to D_i, while τ_s relating the combined cross force to the cross sectional area increases. Towards the higher end of the considered range of D_i, loads due to blade-off reaction become dominant. Here, the key driver is the increasing mass of the individual FF blades against increasing D_i (see also Figure 5.10). Moreover, the material resistance against buckling is strongly nonlinear (cf. equations (5.16) and (5.18)) with respect to the geometry, thus affecting the ratio of maximum combined loading and permissible loading. In the exemplified study, the metal sheet mass, which ranges between approximately 320 and 450 kg, is subdominant.

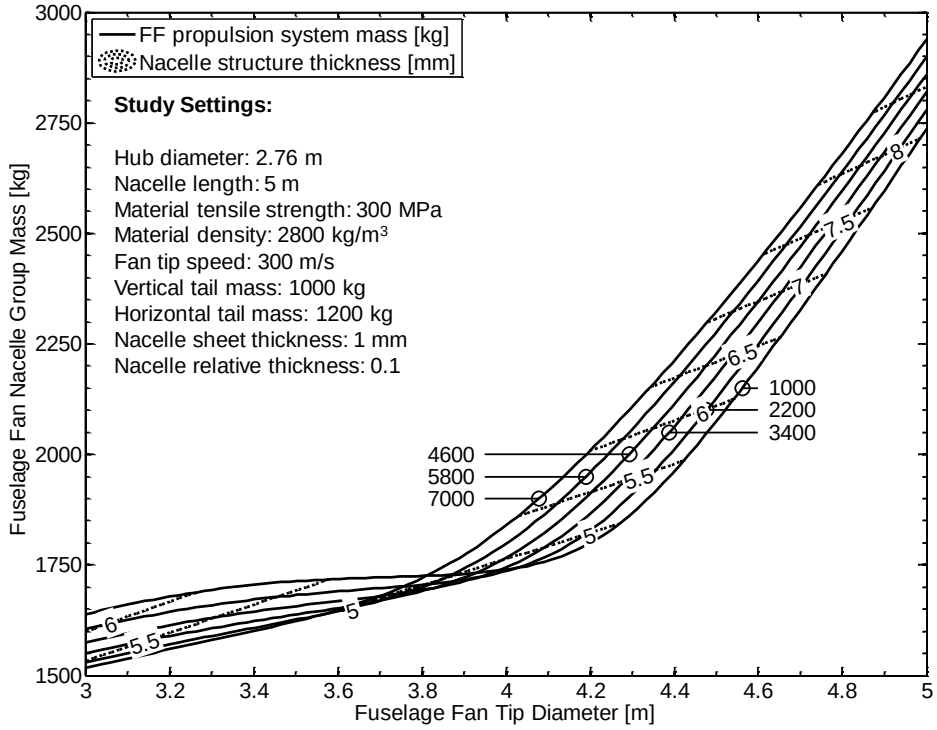

Figure 5.12: Evaluation of FF nacelle weight estimation model

5.3.3 Fan Drive Gear System

The large geometric dimension connected to the FF results in a particularly pronounced asynchronism in the optimum rotational speeds of the fan, booster and LPT, thus necessitating the installation of a reduction gear system. The weight of epicyclic gear systems typically scales proportionally with the output torque [289]. For the parametric mapping of gear system weight in the considered power and torque regime, different empirical approaches are available in the literature. In Reference [289], the torque-specific mass of existing industrial planetary reduction gear systems comprising single and multiple-stage designs was analyzed and a power based correlation with respect to output torque derived (see Figure 5.13). More specifically targeting airborne applications, parametric scaling laws for mass and geometry were proposed by Reynolds [290, Fig. 4.3.3-23], which are valid within a power range of approximately 3,700 and 16,400 kW. More recently, Hendricks and Tong [291] presented a

[72] This means that the HT and VT aerodynamic forces are invariant within this study.

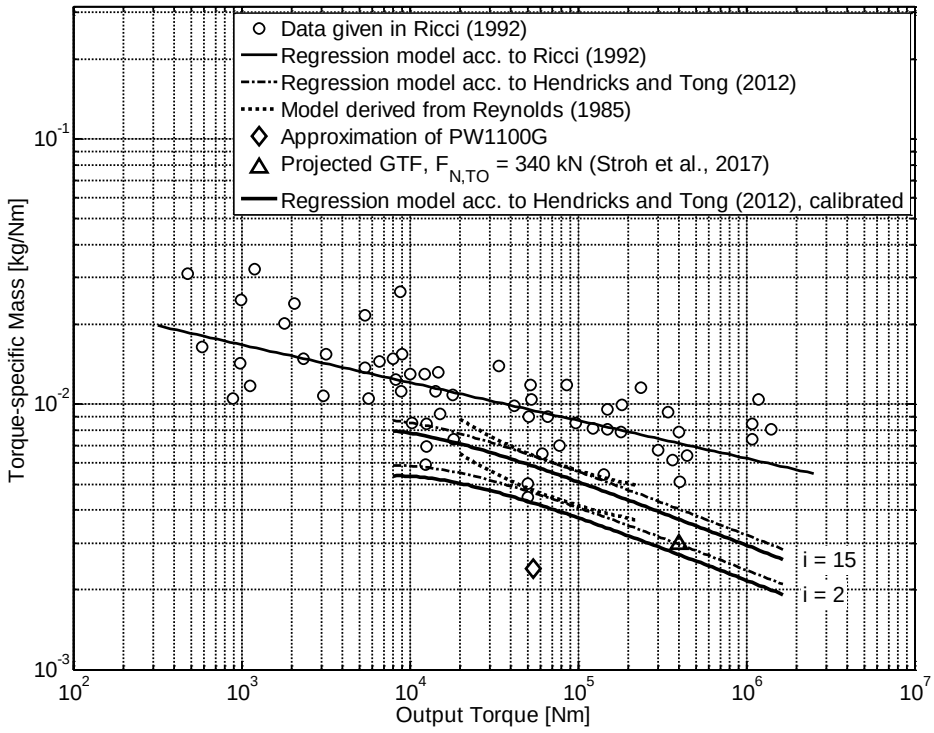

Figure 5.13: Summary of selected empirical models for the weight estimation of fan drive gear systems (modified from Reference [289])

parametric correlation derived from data of a variety of existing turboprop and rotorcraft applications featuring sensitivity with the gearbox output torque and the transmission ratio, i:

$$W_{GB} = -37.426 + 116.330 \cdot \left(\left(\frac{P_{out}}{N_{out}} \right)^{0.75} \cdot i^{0.15} \right), \qquad (5.20)$$

P_{out} in [hp], N_{out} in [RPM], W_{GB} in [lb]

Due to the large data basis and corresponding validity range up to approximately 1,680 kNm as well as the fact that additional weight of the gearbox lubrication system is readily included in equation (5.20), this relation is preferred over alternative empirical relations. A graphical synopsis of the approaches discussed above is provided in Figure 5.13 for a range of transmission ratios between 2 and 15. As can be seen, all considered models yield slightly decreasing torque-specific masses against increasing values of torque. The requirement of high torque densities for aircraft applications and technological advances over the sample designs of Ricci's model are echoed in significantly decreased specific masses of the models given by Reynolds and Hendricks and Tong. In order to account for advances in design techniques, material and lubrication/cooling technology, the model of Hendricks and Tong has been calibrated using the characteristics of a projected UHBR geared turbofan [248, Fig. 4] featuring approximately 340 kN takeoff thrust. The obtained characteristics are included in Figure 5.13. Finally, the approximate settings of the Pratt & Whitney PW1100G fan drive gear system derived from data given in References [209], [249] is included. As can be seen, with the present correlation a considerable overestimation of the published mass is obtained. This may be attributed to unknown differences in the weight bookkeeping schemes, in particular in the masses of the cooling and lubrication system, which, in contrast to the presented regression function, is not included in the derived sample point.

5.3.4 Core Engine Intake

Based on the geometric parameterization described in Section 5.2.1 the core intake mass is computed using an empirical method. Similarity to the air induction systems of buried engine installations of commercial transports is assumed. The approach presented by Roskam [283, Sec. 6.2.2] is preferred over alternative formulations due to the consideration of additional sensitivities included in the model such as the inlet static pressure at the compressor face. The weight prediction is further influenced by the duct length, inlet flow path area, basic shape factors and operating conditions. According to the formulation given in [283], the core intake system mass is composed of the s-duct and the duct support structure.

5.3.5 Conventionally Installed Turbofan Power Plant

In general, the accurate estimation of propulsion system mass is a complex task due to the interrelating effects of flow path design, thermal and mechanical loads, component reliability and life requirements, available material options and cost aspects. Further aspects affecting the required material volume and hence mass involve component dynamics, thermo-mechanical stress such as creeping, corrosion and erosion phenomena [175]. For the estimation of power plant weight, different approaches featuring varying levels of fidelity are available in the literature. Since methods based on purely statistical data such as provided in Reference [292] typically do not account for technical advances or even unconventional solutions and inherently suffer from relatively low accuracy, even in the conceptual design phase more sophisticated approaches relying on physics-based elements are generally considered necessary [293]. Examples include the WATE[73] computer program developed by Boeing under NASA contract [294] and the built-in weight estimation routine of the software GasTurb [191]. However, due to the large number of input parameters for each component, the applicability of these methods is mostly limited [182]. For conceptual studies of different propulsion system architectural arrangements, Seitz [182] presented a component-based weight prediction methodology. Owing to the comparatively small set of input parameters and appropriate extensibility to other design tasks, this method has been selected for the present work. Herein, turbo component weight is separately assessed for stationary parts such as casings, vanes, struts, bearings, and rotating elements including the disk and blade masses, where both fractions are calculated on a stage-resolved basis. In general, the component stage configuration, annular geometry and the material properties pose primary input parameters. For rotating parts, in addition, the component specific strength[74] at the local material bulk temperature and the AN^2 metric is applied as a scaling parameter. For the evaluation of the component weights, the operating conditions prevailing during the takeoff case – in particular component rotational velocities, power levels and temperatures – are considered representative. Further engine components including ducts, combustor, nozzles, nacelle components (intake, cowling, thrust reverser, engine mounts), shafts and accessories are computed based on a scaling procedure of values given in the public domain considering the primary weight-driving design parameters. Further details on the modeling approach including model validation can be found in Reference [182]. The weight prediction of the Fan Drive Gear System refers to Section 5.3.3. Following assumptions commonly employed in the literature [295], [296], in case of fan nozzle variability the weight of the nozzle assembly mass is assumed to be increased by 10%.

[73] „Weight Analysis of Turbine Engines“, later revisions include the “WATE++” framework [333]
[74] Yield strength divided by material density

5.3.6 Fuselage Fan Core Engine

The component weights associated with the FF core engine (see Figure 5.9) are treated in similarity to the components of conventionally installed turbofans. As such, the method used for the weight prediction of the components located between booster and core nozzle exit refers to the previous section and similar material properties are adopted.

5.4 Surrogate-Based Integration of Propulsion System Characteristics

Generally, surrogate models are regarded as a crucial contributor for the efficient handling of complex systems in the context of multidisciplinary design and optimization (MDO). As a key characteristic, instead of directly evaluating a computationally expensive disciplinary model within the MDO task, a surrogate model (also referred to as "metamodel" [297]) approximates the behavior of the original model by means of mathematical techniques. In the context of this work, direct simulation of propulsion system characteristics within the aircraft sizing loop is considered prohibitive for ensuring efficient, fast responding design space exploration capability during the conceptual design stage. Different strategies for the design of surrogate models can be found in the literature ranging from polynomial response surface approaches to elaborate non-parametric models. General recommendations for the utilization of surrogate modeling techniques in computer-based engineering design were provided by Simpson *et al.* [298]. A comprehensive synopsis of contemporary modeling techniques is given in Reference [299]. In the context of advanced propulsion system integration, the application of artificial neural networks and specifically Feedforward Neural Networks (FNN) was identified as a well-balanced trade-off between response fitting accuracy and required computational effort during surrogate model generation [182]. A practical approach and demonstration of the applicability of FNN-based surrogate modeling techniques in advanced propulsion system integration was provided in Reference [182], which constitutes the methodological basis for the surrogate model creation process employed in the present work.[75] Now, the creation of FNN surrogates requires computational effort to be expended prior to evaluation within a superordinate model. A typical FNN-based surrogate model creation process may be structured into four consecutive tasks, which are briefly characterized in the following [182] including adaptations introduced in the present context.

- **Generation of sample data**: As part of the preparatory work, prior to surrogate creation samples of the response behavior produced by the original model to be approximated are recorded based on predefined model input conditions. Upon selecting the free input variables, sampling plans defining the distribution of input values of each variable within the variable space need to be fashioned. In general, randomized and deterministic sampling plans can be distinguished. The latter is often referred to as "Design of Experiments" (DoE). The required number of sample points depends on various aspects including the degree of non-linearity of the model response and the dimensionality of the investigated problem, i.e. the number of input variables. With rising number of input variables, sampling plans based on full-factorial design quickly yield excessive points to be simulated and are therefore inappropriate for most practical cases, thus motivating consideration of fractional-factorial design or more sophisticated methods including quasi-random methods.[76] A prominent example is the Latin Hypercube Sampling (LHS) approach [300], which inherently features high flexibility by offering a decoupling of the number of sample points and the dimensionality of the design space. A practical approach towards LHS plan generation including means to ensure

[75] Details on the simulation setup (i.e. neuron configuration, transfer function, etc.) can be found in Reference [182, Sec. 3.3.2].
[76] A review of space filling experimental designs can be found in Reference [334].

appropriate space filling quality in each dimension was presented in Reference [182]. In the present context, the input variables include both sizing and operational variables. Consequently, a parallelized simulation of sizing and operational modes has been implemented, thereby not relying on the scaling of a given generic off-design deck. The employed set of design and operational variables will be outlined in Section 0.

- **Simulation:** Prior to executing the computation of the sample plan, essential cycle settings have to be defined, suitable design and off-design heuristics are chosen and iteration settings selected based on the scope of the investigation. As part of the present work, a wrapping process for the propulsion system simulation framework APSS (see Section 5.1) has been developed. The design and off-design laws refer to the multi-point based sizing procedure discussed in Section 5.1.2. Once all simulation settings have been defined, the propulsion synthesis model is evaluated at the input conditions defined within the sampling plan. The model results are logged together with the respective input settings.

- **Analysis of simulation results**: Upon completed simulation, this step involves the inspection of the simulation results in order to ensure the numerical validity of the obtained results. As part of the quality assurance process, the physical plausibility of the model response is verified.

- **Creation of surrogate models:** As part of the process for FNN-based surrogate model creation described in Reference [182], an automated procedure for the iterative adaptation of neuron settings targeting the minimization of the overall FNN prediction error is employed [301]. This procedural step is often referred to as "surrogate training". Starting from the definition of basic surrogate settings,[77] surrogate training, i.e. the regression procedure, is executed. Repetition may be required to adapt the training setup for optimum fitting quality. This step also involves the validation of the surrogate model using an independent set of simulation data gained from applying the previous procedural steps.

5.5 Conceptual Aircraft Design Methods

In this section, the aircraft conceptual design framework employed for the aircraft-integrated studies in this work is briefly characterized and necessary adaptations introduced for the analysis of PFC configurations are highlighted. In addition, the parameterization of the propulsion system synthesis models is discussed.

5.5.1 Overview of Employed Framework

For aircraft-integrated sizing and performance evaluation, the conceptual design framework presented by Seitz [182] is employed. The design synthesis features a modular, discipline-oriented setup for the iterative evaluation of aircraft component geometric description, estimation of structural weights and aircraft center-of-gravity, high-speed and low-speed drag polar prediction as well as integrated mission performance simulation. A comprehensive validation of the framework can be found in Reference [182]. In the following, based on Reference [182] essential aspects relevant in the context of the studied turbofan-powered configuration are outlined and adaptations introduced for the treatment of the studied PFC architecture discussed.

The geometric representation of lifting surfaces refers to a simple trapezoidal planform. The parameterization is configured to calculate basic geometric properties such as span, thicknesses, inner

[77] Guidelines for surrogate model settings in case of FNN can be found in Reference [182, Sec. 3.3.2].

volumes, Mean Aerodynamic Chord (MAC) lengths, wetted areas and the position of the aerodynamic centers based on the reference areas, aspect ratios, dihedral angles as well as volume coefficients in case of tail planes. Wing sweep is adjusted according to simple sweep theory based on an effective design incidence Mach number for the wing airfoils, while empennage sweep angles are correlated to wing sweep based on fixed increments. Fuselage geometry is determined from a simplified parameterization. In case of the PFC, owing to the axisymmetric shaping of the fuselage geometry assumed in the CFD setup, the fuselage geometry can be conveniently described through a pair of coordinates in longitudinal (x) and radial direction, y. The wetted surface area is determined based on the evaluation of the following integral generally applicably to describing the surface area of a function $y = f(x), x \in [a; b]$ revolved around the x-axis [302]:

$$S_{wet} = \int_a^b 2\pi y \cdot \sqrt{1 + \left(\frac{\mathrm{d}y}{\mathrm{d}x}\right)^2}\ \mathrm{d}x \tag{5.21}$$

A similar procedure is followed to determine the wetted area of the FF nacelle external surface. Landing gear height determination results from the consideration of an array of geometric constraints including roll clearances of wing-mounted engine nacelles and wing tip and pitch clearances of the fuselage contour and, in case of the PFC, the nacelle of the FF power plant.[78] Propulsion system geometric parameterization including the consideration of aero-propulsive interaction effects in case of the PFC refers to the approach described in Sections 5.1 and 5.2, see also Section 0.

Drag prediction is mainly based on established semi-empirical handbook methods [181], [183], [303], [304], and a symmetric polar approach is employed. The high-speed drag buildup distinguishes between parasite drag (skin friction and pressure drag, interference and transonic compressibility drag) and lift-induced drag of the wing, while trim drag is included as a residual drag share. Miscellaneous drag contributions e.g. due to protuberances and surface imperfections are also captured in this residual. Low-speed aerodynamic performance is modeled according to Loftin [305]. The effects on additional drag due to windmilling in engine-out conditions is mapped based on a simple parametric model. Essential modeling aspects for high-speed and low-speed aerodynamics are itemized in Table C.10 in Annex C.

Airframe structural weight estimation is based on a combination of suitably calibrated, semi-empirical textbook heuristics and analytical methods developed in Reference [182], which are outlined in Table C.10. Generally, the methods feature sensitivity with the configurational setup (i.e. conventional versus T-tail empennage layout) and important physical effects associated with the PFC configuration are covered. As an example, the mapping of fuselage structural weight accounts for the increased bending moment exhibited in case of aft-fuselage power plant installation, while the effects of varying underwing-podded power plant weights on wing bending relief influence the structural weight of the wing. The calculation of propulsion system weights utilized in the present work was described in Section 5.3. The weight of aircraft subsystem, cabin outfitting and operational items is not explicitly mapped but captured through a residual weight term. The computation of the aircraft longitudinal center of gravity is based on the individual component masses and gravity centers. In case of the PFC, the procedure has been extended to include the properties of the FF power plant.

As described in Section 5.1, power plant geometric sizing is conducted at ToC, which is typically the most demanding condition for flow path sizing of high-bypass turbofans. However, in case of stringent takeoff requirements, or due to restrictions of engine peak temperature levels e.g. due to strict NO_x emission requirements, the criticality of takeoff performance may become a dominating factor, thus requiring oversizing of the power plant at ToC conditions relative to the actual climb thrust

[78] As described in Reference [182], the treatment of multiple constraints is handled through a single composite constraint via the Kreisselmeier-Steinhauser function [335].

requirements. This circumstance is handled by an engine scaling factor [182], which, in the present context, is correlated to the engine Power Lever Angle as $c_{N,MCL} = PLA_{MCL}/PLA_{ds}$. Accordingly, for an engine characterized by $c_{N,MCL}$ = 1, the ToC point is the relevant thrust sizing case, while in case low-speed thrust requirements become critical, $c_{N,MCL} < 1$ is obtained.

Mission simulation is based on the evaluation of point performances along consecutive mission phases utilizing basic flight mechanical relations, where the aircraft is treated as a point mass. This involves the parametric mapping of typical climb schedules, a stationary, level cruise segment and a continuous descent and approach phase. For the calculation of trip fuel burn, propulsion system characteristics are evaluated during each mission time step. In accordance with the bookkeeping standard introduced in Section 4.2, the instantaneous fuel flow per simulation step is computed from the product of TSFC and net thrust of the individual power plant types installed on the aircraft. In case of the PFC, this involves the continuous evaluation of key operating parameters related to the aero-propulsive integration of the FF power plant such as π_{int} and the ΔF_X metric according to the scheme presented in Section 4.9. The evaluation is conducted based on similar PLA settings for each power plant type, in the first instance. The fuel required for Landing and Takeoff (LTO) mission segments is handled by prescribed aircraft mass fractions. The corresponding fuel burns added to the trip fuel constitutes the block fuel. Essential metrics describing aircraft low-speed performance including Takeoff Field Length (TOFL), Landing Field Length (LFL) as well as climb gradients during OEI cases relevant with respect to airworthiness requirements are mapped according to References [181], [305].

The subsequently evaluated disciplinary modules are wrapped in an iterative procedure targeting the minimization of the root mean square error from a set of iteration variables. Beyond default parameters, variables added to the iteration scheme include e.g. FF intake and core intake total pressure ratios at design and takeoff conditions as well as the engine related parameters associated with the implemented multi-point sizing strategy, see Section 5.1.2. Aspects on the parametrization of the propulsion system synthesis models are elaborated in the following section.

5.5.2 Parameterization of Propulsion Synthesis Models

For the system analysis studies presented in Chapter 6, an appropriate parameterization of the propulsion system synthesis models is required, which is indicated in Table 5.4 for the individual power plant architectures of the PFC. Design specific thrust constitutes a typical free input parameter for aircraft-integrated sizing, $\vec{X}_{fr,ds}$. Targeting the execution of speed sensitivity studies, design free stream Mach number is also declared as an input. In addition, technology enhancements to the

Variable Type	Variable
Free design variables, $\vec{X}_{fr,ds}$	$M_0, F_N/w_2, f_{tech,TC}, \Delta\eta_{Fan}$ [a]
Aircraft-iterated design variables, $\vec{X}_{it,ds}$ [b]	$F_N, \dot{m}_c/\dot{m}_{25}, \eta_{GB,MCL}, U_{t,LPT}, U_{t,HPC}, \pi_{int}$ [a], p_{22}/p_{21} [a]
Free off-design variables, $\vec{X}_{fr,od}$	$\Delta T_{ISA}, H_0, M_0, A_{18}/A_{18,ds}$
Aircraft-iterated off-design variables, $\vec{X}_{it,od}$ [b]	PLA, π_{int} [a]

[a] only applicable to parameterization of FF power plant
[b] only relevant for studies presented in Section 6.3

Table 5.4: Parameterization of power plant synthesis models for studies presented in Chapter 6

propulsion system are simulated through manipulation of the turbo component loss-scaling factor $f_{tech,TC}$ introduced in Section 5.1.4, which is applied collectively to all turbo components. Similarly, for the FF, the decrement in fan design efficiency, $\Delta\eta_{Fan}$, is considered. The vector of power plant design variables requiring iteration at aircraft level, $\vec{X}_{it,ds}$, refers to the variables relevant for multi-point sizing (see Section 5.1.2) and includes apart from the design net thrust, F_N, the relative HPT cooling air mass flow, $\dot{m}_c/\dot{m}_{25}$, the FDGS efficiency at the MCL point, $\eta_{GB,MCL}$ and LPT and HPC design tip speeds, $U_{t,LPT}$ and $U_{t,HPC}$. Additionally, for the FF power plant, the parameters π_{int} and p_{22}/p_{21} are covered. The free off-design variables, $\vec{X}_{fr,od}$ were discussed in Section 5.1.3.2. The off-design intake total pressure ratio of the FF power plant is also employed as an input and is iteratively adjusted during aircraft-level studies.

5.6 Metrics for System and Aircraft Level Performance Assessment

At propulsion system level, fuel efficiency is assessed based on power plant overall efficiency, which incorporates the individual efficiency shares of thermal and propulsive efficiency (see Section 3.1.2). Aircraft-integrated performance is assessed based on block fuel, which is directly correlated to CO_2 emissions. Relevant input values for the initial estimation of NO_x[79] and noise emissions may be derived along the mission by evaluating the propulsion system surrogate models. For the evaluation of aircraft point performance, the Specific Air Range, SAR, constitutes a meaningful metric (see Section 3.1.5). Now, in particular for long-range applications, fuel burn is closely correlated to the SAR exhibited during cruise. As will be demonstrated quantitatively in Section 6.4, evaluating the change in SAR at a typical cruise condition relative to a reference is representative of the integrated change in block fuel, ΔW_F, i.e.

$$SAR/SAR_{ref} \approx 1/(1 + \Delta W_F) \tag{5.22}$$

assuming invariant range covered. Accordingly, the fractional changes in aerodynamic efficiency, propulsion performance and aircraft gross weight at a suitable cruise condition can be utilized to approximately gauge the impact on fuel burn relative to a reference.

Now, the impact of BLI propulsion system integration expressed in the present context via the proposed integration impact metric ΔF_X can be included in the contributions of SAR based on different approaches. As such, ΔF_X may be incorporated in the total aircraft TSFC, which relates the bookkeeping-invariant fuel flows of the wing and fuselage-installed power plants, $\dot{m}_{F,W}$ and $\dot{m}_{F,F}$, respectively, to the total propulsive force:

$$TSFC_{tot} = \frac{\dot{m}_{F,W} + \dot{m}_{F,F}}{F_{N,W} + F_{N,F} + \Delta F_X} \tag{5.23}$$

As a consequence, decreased values of total vehicular TSFC are obtained compared to a conventional reference case. In this scheme, the accounting of L/D is unaffected. An alternative approach is linked to the concept of the relative integration impact metric, $\tilde{\beta}$, introduced in Section 3.1.3. Accordingly, the lift-to-drag ratio synthetically increases,

$$\widetilde{L/D} = \frac{L}{D(1 - \tilde{\beta})} \tag{5.24}$$

while total aircraft TSFC remains as in the commonly used definition:

$$\widetilde{TSFC}_{tot} = \frac{\dot{m}_{F,W} + \dot{m}_{F,F}}{F_{N,W} + F_{N,F}} \tag{5.25}$$

[79] A commonly used estimation of the production of nitrogen oxides in the combustor refers to the "NO_x severity index" [336].

It will be shown in Section 6.4 that with both approaches coherently similar values in SAR are obtained compared to calculating this metric based on the integrated fuel burn (equation (5.22)), thus rendering both approaches feasible options. In the studies presented in Chapter 6, the approach expressed through equation (5.23) will be employed.

6 Discussion of Study Results

This chapter serves the purpose of demonstrating the applicability of the presented methods to a practical propulsion system integration study. In this respect, the suitability of the aero-propulsive bookkeeping approach, the propulsion system design and performance methods and the aircraft-integrated evaluation is demonstrated through the discussion of conceptual sizing and performance studies of the considered PFC configuration aiming at the exploration of system and aircraft level characteristics. The chapter commences with the description of the demonstration case upon which the studies will be based on. As an initial parametric study, the cycle characteristics of the FF propulsion system will be compared to those of a conventionally installed geared turbofan architecture. Having derived the specific trending behavior, aircraft-integrated studies are discussed. Upon introduction of settings and assumptions related to key inputs of the underlying aircraft and propulsion system synthesis models, a series of parametric, aircraft-integrated studies are presented and the aircraft-level sensitivities to essential design and operating parameters are highlighted. Finally, the key characteristics including the integrated efficiency potential of the studied PFC configuration offered through adoption of different sizing strategies are discussed.

6.1 Description of Demonstration Case

The application scenario considered for the demonstration of the developed methodology is largely geared to the configurational arrangement and corresponding aero-numerical data gained from the research project DisPURSAL (cf. Section 4.1). Therefore, a widebody aircraft layout featuring a gas turbine powered ducted FF power plant in conjunction with two turbofan engines in underwing-podded installation is considered. The technology level refers to a potential EIS of year 2035. As described in Reference [114], based on analysis of forecast data it had been projected that by this EIS year the medium-to-long range stage lengths will have the highest impact on overall air transport system cumulative fuel consumption, thus motivating the selection of a 4,800 nm design range at a cabin capacity of 340 passengers in two-class arrangement. Corresponding key aircraft requirements were adopted from Reference [114]. In similarity to an Airbus A330, which is a typical year 2000 representative of these specifications, in the present work, the design cruise Mach number was set at 0.82 [306]. In addition, airport compatibility with ICAO Aerodrome Reference Code E was ensured, thus restricting wingspans to an upper limit of 65 m [307].[80] While small fuselage length variations due to length changes of the FF power plant are parametrically captured, the local fuselage radial coordinates were kept constant, in particular the hub radii at the various thermodynamic stations of the FF power plant.

6.2 Fuselage Fan Propulsion System Parametric Studies

Prior to studying aircraft-integrated characteristics, in this section the design and performance features of the FF power plant are explored. The characteristics are compared and contrasted to the attributes of a conventionally installed, Underwing-Podded Geared Turbofan (UP-GTF) in SDSF nacelle layout,

[80] The specification of admissible outer main gear wheel spans correspondingly defined in ICAO Annex 14 is not explicitly considered.

which is considered representative for both the reference power plant and the underwing-podded engines of the PFC. A typical sizing chart of a turbofan propulsion system indicates a power plant efficiency metric such as η_{ov} or TSFC against the fan tip diameter for various combinations of sizing net thrusts and bypass ratios, thus allowing for the direct trade-off between installation size and engine efficiency. In Figure 6.1, this visualization strategy has been generalized for the quantitative comparison with the FF propulsion system. Therefore, the abscissa presents the fan inlet flow area (A_2), while η_{ov} shown on the ordinate was chosen as a metric to compare the fuel efficiency of both power plant types. Design net thrust and specific thrust were chosen as study variables, where the latter parameter was preferred over BPR due to the more direct relation to propulsive efficiency compared to BPR. Key cycle settings including OPR_{ds} and $T_{4,ds}$ were derived from a parametric study associated with the reference propulsion system (see Section 6.3.2) and retained constant within the study and between both power plant types. The takeoff performance implicitly included in the sizing was evaluated at M0.25, SL, ISA+15 K and a constant ratio of takeoff and sizing thrust was applied for the purpose of this study. The propulsion system sizing and performance evaluation was based on the methods and heuristics presented in Chapter 5. Further assumptions for losses and efficiencies are tabulated in Table C.11.

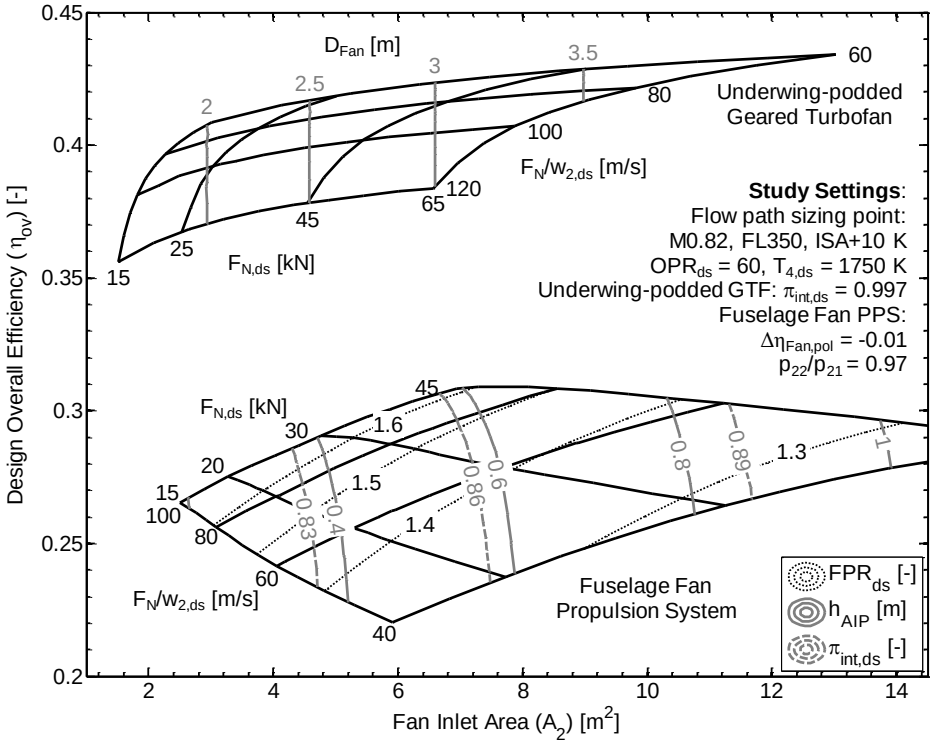

Figure 6.1: Comparative sizing chart for conventionally installed GTF and FF propulsion system

As discussed in Section 4.1, for the FF power plant, the axial design Mach number at the fan face is approximately 20% smaller than the value typical for conventionally installed advanced turbofans. The intake duct height at the aerodynamic interface plane (h_{AIP}) results from the local fuselage radius and the required annular flow area, which was iteratively adjusted to yield appropriate axial Mach numbers in the throat. For the purpose of this particular study, the core intake pressure ratio, p_{22}/p_{21}, was kept constant at 0.970 and a decrement in fan design polytropic efficiency of 1.0% was assumed relative to the fan of the UP-GTF. The characteristics of FF design intake total pressure recovery ratio, π_{int}, refer to the parametric model introduced in Section 4.4.1.

Inspection of the characteristics of the UP-GTF reveals the trends typically expected for turbofan engines. As a result of increasing corrected flow of the turbomachinery, increasing $F_{N,ds}$ translate into

improving turbo component efficiency levels, while reducing values of F_N/w_2 are associated with improving propulsive efficiency. The shown contours of fan diameter directly correlate with A_2. As expected, for the UP-GTF, reducing F_N/w_2 directly translates into reducing FPRs. Therefore, for reducing FPR the impact of pressure losses in the transmission system (primarily the intake and bypass duct) increases as F_N/w_2 is reduced, and hence transmission efficiency, η_{tr}, degrades. This eventually causes the characteristics of η_{ov} to flatten towards the lower end of F_N/w_2 values investigated. For a given net thrust, decreasing F_N/w_2 triggers growing fan dimensions.

Examination of the characteristics associated with the FF power plant shows significant differences in the trending behaviors compared to the underwing-installed GTF. Different from the UP-GTF exhibiting approximately constant levels of intake pressure ratio at MCL, for the FF power plant a strong sensitivity of π_{int} with fan size is obtained. The carpet in Figure 6.1 is supplemented with contour lines of π_{int}, showing for a given free stream Mach number a direct correlation to h_{AIP}. The strong degradation in π_{int} of approximately 9% to 18% in conjunction with the fan efficiency penalty and penalized core intake pressure ratio is the main contributor of the carpet being generally found at lower overall efficiencies compared to the UP-GTF power plant. For a given specific thrust, increasing values of F_N yield – as a result of improving intake pressure ratios and due to enhancements in core efficiency – improving η_{ov}. For variations of F_N/w_2, however, a different trending behavior is observed for the FF propulsion system compared to the UP-GTF. Within the ranges analyzed, reducing F_N/w_2 at a given F_N yields a degradation in η_{ov}. This initially counter-intuitive trending stems from the superposing effects of core, transmission and propulsive efficiencies. In case of the FF with strong pressure losses in the intake, the impact of transmission efficiency degradations with reducing FPRs (see contour lines in Figure 6.1) is much more pronounced than for the UP-GTF. While in case of the conventionally installed GTF losses in η_{tr} are still outweighed by monotonically improving η_{pr}, the implications of η_{tr} clearly dominate for the FF power plant. As can be gleaned from the chart, for the FF propulsion system the typically observed coupling of FPR with F_N/w_2 is no longer present. For given F_N/w_2, increasing net thrusts yield a slight reduction in design FPR, which is driven by the improving π_{int} leading to increasing total pressure levels processed by the fan and hence requiring the FPR to reduce in order to maintain the optimum nozzle exit velocity ratio. This is connected to increasing BPRs.

For purposes of further elaborating the differences between both power plant types, Table 6.1 compares key characteristics for exemplary design settings. The designs are evaluated for identical fan face areas and common design specific thrusts of 90 m/s. To satisfy this condition, FPR needs to be increased for the FF power plant to cater for the impaired intake total pressure, while BPR is reduced. At equal maximum levels of AN^2 exhibited by the last LPT rotor, the significantly larger fan diameter requires the gear ratio to increase compared to the UP-GTF, although the increased fan tip speed associated with the larger FPR partly counteracts this trend. The reduced mass flow connected to the smaller fan inlet Mach number directly translates into reduced net thrust. For given specific thrust, η_{pr} remains invariant, while, as discussed above, η_{tr} is significantly penalized compared to the UP-GTF. Core efficiency is almost neutral due to the opposing effects of increased core intake pressure losses and a larger core size. As a net result, overall efficiency is strongly affected by transmission efficiency and in relative terms impaired by 27.6%. From an efficiency perspective, the impact of ingesting the BL flow on propulsion system design point performance appears large. It should be noted, however, that for realistic PFC configurations the fuselage-installed propulsion system only accounts for a portion of the installed power plant total power, hence reducing the impact at aircraft level.

Parameter	Unit	UP-GTF	FF PPS	Difference [a] [%]
Specific thrust, F_N/w_2	m/s	90	90	±0.0
Fan inlet area, A_2	m^2	6.05	6.05	±0.0
Net thrust, F_N [b]	kN	45.0	34.8	–22.7
Fan Pressure Ratio, FPR	-	1.41	1.59	+12.1
Bypass Ratio, BPR	-	14.9	10.8	–27.5
Core size [c]	kg/s	2.57	3.15	+22.6
Gear ratio	-	3.9	4.5	+15.4
Fan inlet hub/tip ratio	-	0.26	0.71	+173.1
Fan inlet axial Mach number	-	0.68	0.56	–17.7
Propulsive efficiency, η_{pr}	-	0.848	0.848	±0.0
Transmission efficiency, η_{tr}	-	0.857	0.627	–26.8
Core efficiency, η_{co}	-	0.564	0.558	–1.1
Overall efficiency, η_{ov}	-	0.410	0.297	–27.6

[a] FF PPS relative to UP-GTF
[b] streamtube definition (cf. Section 4.2)
[c] defined as $\dot{m}_{25}\sqrt{T_3/T_{std}}/(p_3/p_{std})$

Table 6.1:Comparison of design characteristics between conventionally installed GTF and FF propulsion system sized for identical specific thrust and fan inlet area. For study settings, see Figure 6.1

In order to provide more detailed insight into the effects of BL ingesting installation on the propulsion system design characteristics, Figure 6.2 presents the impact of F_N, F_N/w_2, $f_{tech,TC}$ and M_0 on the individual efficiency metrics as well as BPR and FPR. The study settings refer to Figure 6.1. The first column illustrates the above-discussed interplay between F_N and FPR induced by variations of π_{int} and its impact on thermal efficiency. The reduction in core efficiency observed for increasing F_N/w_2 results from the increasing cooling air demand. As an intrinsic characteristic of turbofan propulsion systems, a reduction of $F_N/w_{2,ds}$ triggers a stronger thrust lapse between takeoff and operation at altitude. Hence, with the flow path sizing being conducted at MCL conditions, takeoff performance is significantly affected by F_N/w_2. Now, assuming prescribed thrust ratios between takeoff and MCL this yields increasing required power settings at takeoff for high F_N/w_2 designs. The correspondingly increased cooling air demand translates into a η_{ov} penalty at MCL conditions. As expected, $f_{tech,TC}$ has a direct effect on η_{co}. The rise in FPR associated with increasing free stream Mach numbers results from the higher required nozzle exit velocities required to maintain the specific thrust in presence of increasing values of V_0 and intensifying intake total pressure losses.

As a key result gained of the discussed propulsion system studies, it is established that the trending behavior of the BLI power plant varies from the corresponding characteristics of conventionally installed turbofans. As will be demonstrated in the following section focusing on the investigation of the aircraft-integrated characteristics, this considerably influences the optimality of the PFC designs at the vehicular level.

6.3 Aircraft-Integrated Studies

The present section focuses on demonstrating the methodological approach for the modeling of aero-propulsive interaction effects, propulsion system sizing and performance as well as aircraft-level integration expounded in Chapters 4 and 5 through discussion of sizing and optimization studies of a

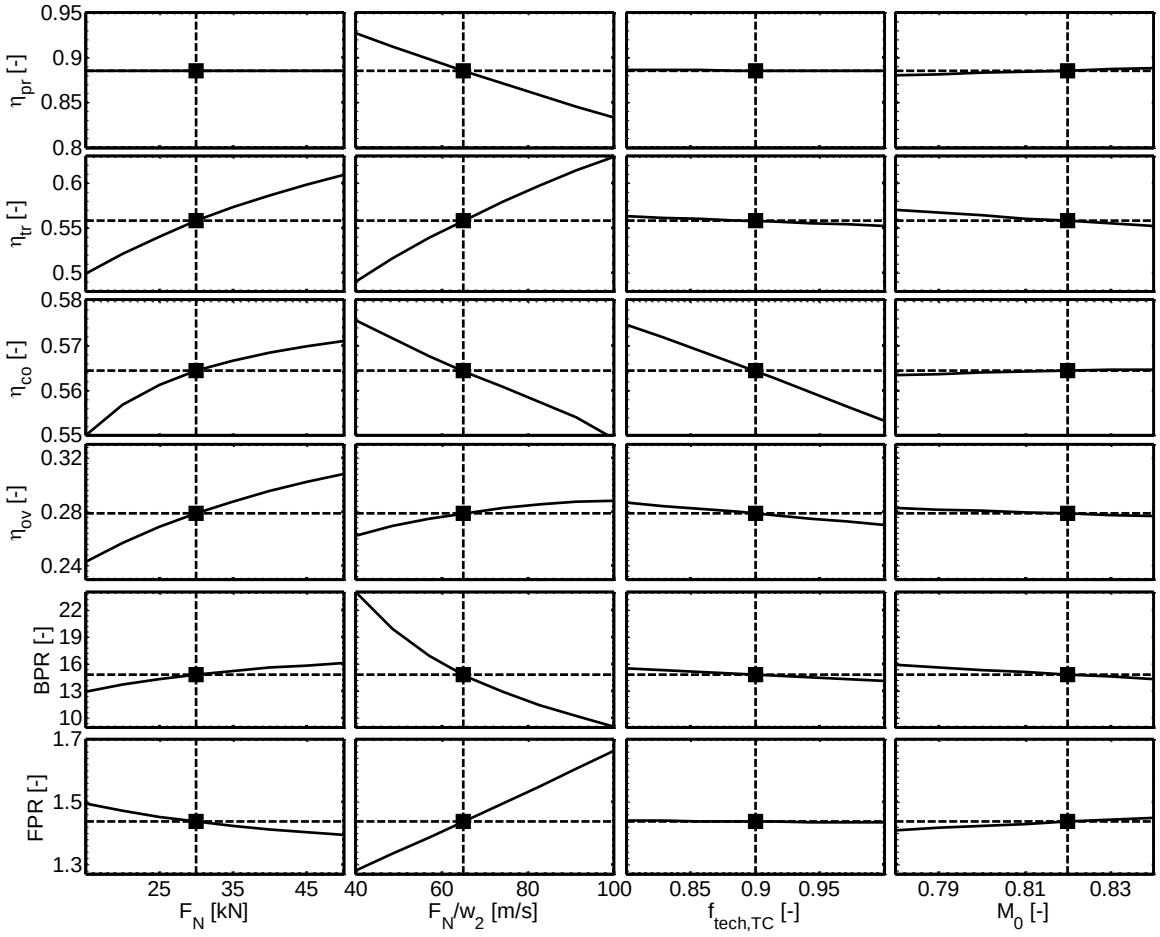

Figure 6.2: Impact of essential propulsion system sizing parameters on propulsive, transmission and core efficiency as well as design Bypass Ratio and Fan Pressure Ratio of FF propulsion system

concrete PFC layout. Upon the discussion of commonly applied study settings (Section 6.3.1), the characteristics of a suitable reference aircraft and propulsion system platform employed for comparing and contrasting the characteristics of the PFC designs will be discussed in Section 6.3.2. Thereafter, aiming at the substantiation of the presented integrated results, a basic analysis is presented in Section 6.3.3 involving the comparison of integrated aircraft characteristics against case study data for several PFC configurations available in the public domain.

Now, at this stage of technology evaluation, it is necessary to impose assumptions for a number of technological parameters associated with the PFC. In addition, in the conceptual phase the calculation methods are inherently characterized by certain degrees of uncertainty. A commonly used method to quantify the impact of parameter changes constitutes a sensitivity analysis. While a derivative-based approach is inexpensive from a computational perspective, these sensitivities are strictly valid at the point of measurement and therefore it is not possible to predict the system behavior at other values within the input space. Hence, the information gained is limited in case of large model non-linearity. Moreover, sensitivities inherently lack exploration capability of the entire input space in a sense that simultaneous variations of input variables are neglected and thus this technique is unable to detect the presence of interactions between input variables [308]. Hence, it is considered of paramount importance to supplement sensitivity analyses with a parametric design space exploration activity. Consequently, initially a series of parametric trade studies of key sizing parameters connected to the investigated configuration aiming at the exploration of the entire space of interest will be discussed in Section 6.3.4. These serve the purpose of deriving the relevant trends of this propulsion system integration approach with respect to typical system and aircraft-level performance metrics and target

the identification of optimality settings at the vehicular level. Thereafter, based on a best-and-balanced array of design settings identified as part of this exploratory analysis, sensitivities are presented in Section 6.3.5 to provide guidance as to what the change will be once uncertainty or varying technical assumptions may change the respective baseline value.

6.3.1 Setup of Studies

Targeting appropriate comparability between the aircraft designs studied in the present work, a series of design and simulation settings were commonly applied. The studies presented in Sections 6.3.2 to 6.3.5 were based on a common set of TLARs outlined in Section 6.1. As such, design range was set at 4,800 nm at a design (maximum structural) payload corresponding to 340 passengers at 102 kg/PAX [114].

Wing sizing was conducted based on a prescribed maximum wing loading, MTOW/S_{Ref}, of 650 kg/m², in the first instance, which was assessed as typical for the considered utilization spectrum [118] and provides margin for potential stretch variants. Hence, wing reference area was iteratively adjusted in case of MTOW variations. A combined upper constraint on the aspect ratio and wing span of 12.0 and 65 m, respectively, was applied, hence yielding reduced aspect ratios for excessive gross weight growth. Another constraint, which may determine wing size may include the required fuel tank volume available within the wing. All designs employed similar parameters for wing relative thickness and dihedral. As outlined in Section 2.4.2, for the PFC the empennage preferably features a T-tail design, while the reference aircraft is arranged with a classic tail design. The settings for horizontal and vertical tail aspect and taper ratios were chosen as typical for conventional and T-tail arrangements, respectively, according to textbook guidelines [181], [282]. As a conservative approach, no credit for reduced tail volume coefficients was granted for the T-tail layout. Potentially beneficial effects in static stability due to the presence of the FF nacelle, which may allow for reduced tail volume, were not considered. For the PFC horizontal tail, a dihedral angle of -5° was selected [114]. Similar angular clearances with respect to roll and pitch freedom during ground operation were applied. All studied vehicles employed equal static stability margins. The potential impact of changes in the fuselage pressure distribution on stability and handling characteristics was neglected. The diameter of the cylindrical fuselage section was kept constant, while fuselage length of the PFC was parametrically adapted as a function of FF total power plant length (see Section 5.2.1). A residual weight covering aircraft equipment, cabin outfitting and subsystems was derived from Reference [118] and considered constant, in the first instance.[81] Additional weight due to noise insulation materials in the cabin potentially required for the PFC was not considered.

With the semi-empirical calculation of low-speed aerodynamic performance applied here (see Section 5.5.1), similarity in landing performance, i.e. approach speed and LFL, is ensured in case of similar wing loadings.[82] With regards to takeoff performance, a TOFL constraint of 2,500 m was considered appropriate, which was derived from a number of contemporary widebody, twin-engine aircraft types. This value agrees with the field length limit specified in Reference [309] for an application of similar gross weight. For LFL, 2,000 m was chosen as a limit [310]. Required climb gradients at takeoff, missed approach during OEI events and at the ToC point as well as stall speed margins at takeoff and approach were taken into account according to transport aircraft airworthiness regulations [311]. With respect to required climb gradients, the PFC configuration was treated as a three-engine aircraft, which is a conservative assumption in comparison to the reference aircraft. The fuel reserve policy referred

[81] Includes electrical system, flight control, environmental control, ice and rain protection, instruments, fuel system, furnishing, operational items and auxiliary power.
[82] For given flight conditions and lift coefficient in the landing configuration.

to generic international rules including contingencies for 30 minutes holding,[83] 200 nm diversion at FL250 and 5% trip fuel as final reserves.

Similarity during the mission calculation was ensured by retaining relevant simulation settings and inputs to the flight profile parameterization. Constant fuel mass fractions for aircraft ground operation were applied. A typical climb schedule was adopted from Reference [182] consisting of four consecutive segments, i.e. 1) a climb and acceleration phase at constant CAS of 250 kts below 10,000 ft governed by Air Traffic Control rules, 2) an acceleration phase to 300 kts CAS, 3) a segment of climb and acceleration at constant CAS until the initial cruise Mach number is reached, and, 4) above the crossover altitude a phase of constant Mach number climb until the ToC is reached. The ToC point was characterized through a common residual climb capacity of 500 ft/min and was considered to be operated at the design cruise Mach number. Cruise was simulated based on a flat cruise profile at constant Mach number, thereby disregarding step cruise flight techniques. Descent was considered to be conducted at a constant descent angle of 3°. Still air was assumed during the entire mission. The ambient conditions at takeoff (SL, ISA+15 K) and ToC (FL350, ISA+10 K) were kept invariant throughout the studies, while variations from the nominal cruise Mach number were studied as indicated. During result inspection, it was verified that the climb time to initial cruising altitude was below a threshold of 25 minutes, which is considered an appropriate limit for the present application [114].

Settings for interference drag factors applied to the zero-lift drag calculation, f_{interf}, were derived from Reference [181]. This included interference effects between the FF nacelle and the empennage not considered in the CFD setup. Technology-dependent aerodynamic model inputs for high-speed drag polar estimation including the Korn factor, the relative longitudinal position of the flow transition points along wetted surfaces and the technology scaling factor to Oswald's efficiency [182] were kept invariant. A maximum lift coefficient was applied according to Reference [305], as were increments to the drag breakdown due to extension of high-lift devices and the landing gear.

Advanced GTF power plants in two-spool, boosted arrangement featuring a SDSF nacelle layout were considered for the wing-installed power plants. The geometrical and technological similarity of the calculated propulsion system designs was ensured by applying identical key input parameters including e.g. component hub/tip ratios[84] and axial Mach numbers at inlet and outlet, allowable material temperature levels, the cooling air technology constant and mechanical shaft efficiencies. Primary parameters of the thermodynamic cycle including OPR_{ds} and $T_{4,ds}$ were adopted from the propulsion system of the reference aircraft and kept constant throughout the studies, thereby disregarding prospective potential attainable from individually optimized cycle settings.[85] The turbo component loss-scaling factor (see Section 5.1.4) was set according to the advanced technology level and kept constant unless investigated as a study parameter. Nominally, for $f_{tech,TC}$, a value of 0.9 was chosen. Pressure losses for compressor and turbine inter-ducts and the combustion chamber were adopted from References [34] and [196] (see Table C.11). Further duct pressure losses applicable to the individual power plants were parametrically evaluated using the methods described in Chapters 4 and 5. For the design efficiency of the FDGS, a value of 0.994 was chosen [248, p. 5]. The power offtake was assumed to refer to a mean value representative of the design mission. Advancements in engine material technology were implicitly considered through the settings applied for the allowable material temperature and AN^2 values. During off-design calculation, equal maximum values for gas temperature levels at HPC outlet and turbine inlets, corrected spool speeds and prescribed mechanical loadings were applied. A common set of turbo component maps was utilized across all engine designs

[83] Holding is considered to be performed at the top-of-descent flight condition of the diversion mission.
[84] Exemptions include the FF and HPC inlet hub/tip ratios, which are iteratively adjusted.
[85] See also discussion in Section 6.3.2.

including the settings for the map reference points. The bypass nozzle was considered to be opened only at the takeoff point, thereby decreasing temperature levels, reducing jet velocities for decreased noise and improving engine operating stability, and was kept unchanged unless stated otherwise. A synopsis of further essential propulsion system input settings is provided in Table C.11. With respect to the FF power plant, a nominal fan polytropic design efficiency degradation due to BLI induced non-uniformity effects of 1% was assumed relative to underwing-podded fan designs (see also Section 5.2.3). The geometric model input settings of the FF module were applied as described in Section 5.3.1 and kept invariant throughout the studies.

The studies presented in the following target the identification of optimum design settings for the PFC. Typical objective functions in the conceptual design phase include block fuel demand at design and operational missions,[86] aircraft empty or gross weight, noise, emissions, economic metrics as well as weighted combinations [171]. The present context focusses on design mission block fuel and Maximum Takeoff Weight (MTOW), which both constitute important inputs to any cost related aspects. Aircraft operational performance on off-design stage lengths is analyzed within the frame of integrated benchmarking presented in Section 6.4. Now, primary design variables considered during parametric, constrained optimization studies include:

- The design specific thrust level of fuselage and wing-installed power plants, $F_N/w_{2,ds}$
- The design power split between fuselage and wing-installed power plants, Θ_{ds}
- The design cruise Mach number, $M_{cr,ds}$

In particular, $F_N/w_{2,ds}$ and Θ_{ds} are expected to have strong effects on various disciplines connected to the PFC layout including power plant thermodynamic performance, dimensions and weight, and ultimately overall system characteristics. The investigation of PFC design speed trends relative to those of a conventional aircraft is considered an important aspect for the performance evaluation of the PFC.

The considered aircraft constraints include TOFL as well as above-mentioned climb gradients, while LFL requirements are inherently satisfied due to invariant wing loadings. Therefore, the engine scaling factor was employed as an auxiliary free variable as a means to adapt the engine sizing thrust relative to the ToC requirement. In order to reduce the number of free variables, the values of $c_{N,MCL}$ were adopted for both power plant types. The bypass nozzle area setting, $A_{18}/A_{18,ds}$ at the takeoff point was treated as an operational variable, where the repercussive effects on engine and eventually aircraft design were incorporated in overall system sizing. Optimization was performed based on a set of aircraft designs distributed across the design space using a standard algorithm for multivariate, constrained optimization [312].

6.3.2 Reference Aircraft Sizing Study

For purposes of establishing a consistent basis for comparing the characteristics of the PFC to those of a conventional aircraft layout, it is necessary to define appropriate reference systems for aircraft and propulsion system. Accordingly, an advanced but conventionally arranged twin-engine aircraft with identical Top-Level Aircraft Requirements (TLARs) was conceptually sized using the same methodological framework as for the PFC. The aircraft layout referred to a classic tube-and-wing design with two underwing-podded GTF engines. Fuselage external dimensions, in particular length and cylindrical diameter were adopted from Reference [114].

[86] The operational performance at smaller stage lengths (e.g. maximum utilization distance) typically constitutes important elements of a complete performance assessment.

Key thermodynamic cycle settings including design levels of combustor exit temperature, $T_{4,ds}$, and OPR_{ds} were derived from a two-dimensional parametric study at given design specific thrust of 90 m/s[87] using the multi-point sizing approach discussed in Section 5.1.2. The results are presented in Figure B.11 in Annex B indicating TSFC-optimum $T_{4,ds}$ at approximately 1800 K, which is in good agreement with the results presented in Reference [212]. In deference to the indicated limits of HPC exit temperature, combustor exit temperature and LPT inlet temperature exhibited at takeoff conditions, best and balanced settings at OPR_{ds} = 60 and $T_{4,ds}$ = 1750 K were chosen, which are characterized by sufficient margin to the limiter settings, especially considering possible performance requirements at hot-and-high conditions[88] as well as production scatter, deterioration and growth potential. The selected characteristics are similar to those of NASA's N+3 technology level reference turbofan [42] and the obtained TSFC at cruise condition is in good quantitative agreement with the advanced, long-range GTF designs published in Reference [9].

An essential design attribute of a turbofan power plant refers to the BPR or specific thrust, $F_N/w_{2,ds}$. The proper selection of this parameter requires an array of trade-offs to be made at the vehicular level involving basic thermodynamic characteristics, power plant weight effects, nacelle wetted area implications and the corresponding aircraft-level cascade effects resulting from the engine installation (see Section 2.2). Therefore, based on an aircraft-integrated study, design specific thrust levels were varied across a broad range, while power plant cycle settings including OPR_{ds} and $T_{4,ds}$ were kept invariant. Technology dependent settings were also retained. Essential results are presented in Figure B.12. From the integrated study, a fuel burn-optimum $F_N/w_{2,ds}$ of 90 m/s is identified. Beyond the characteristic of design mission block fuel, which are normalized with the selected design, Figure B.12 presents the trends of relative TSFC at flow path sizing point, fan diameter and design BPR. As can be seen, the chosen level of $F_N/w_{2,ds}$ correlates with a design BPR of 15.2 and a fan diameter of 3.28 m. In the investigated range of $F_N/w_{2,ds}$, TSFC maintains a monotonic trend and is primarily influenced by the improving propulsive efficiency levels. As part of aircraft-integrated assessment, basic aircraft performance constraints are considered. Since lower $F_N/w_{2,ds}$ trigger a stronger thrust lapse between takeoff and maximum climb points and hence towards the higher end of $F_N/w_{2,ds}$ values the takeoff performance would become increasingly impaired due to the reducing available takeoff thrust, oversizing of the power plants relative to the MCL thrust requirement is required. For $F_N/w_{2,ds}$ smaller than approximately 90 m/s the TOFL constraint becomes uncritical and thrust sizing is solely conducted for the climb requirement. Second segment climb gradients with OEI at takeoff and missed approach were uncritical throughout the range of $F_N/w_{2,ds}$ investigated. As explained above, landing field lengths are constant due to constant wing loading. The necessary fuel tank volume, which may constitute a further constraint for wing sizing, was consistently satisfied.

6.3.3 Plausibility Analysis of Overall Methodology

Due to the novel technology status of the considered propulsion integration concept, higher-order integrated simulation results or even test data is not available in the public domain. Therefore, to substantiate the plausibility of the integrated results to be discussed, a basic analysis is presented in this section involving the comparison of integrated aircraft characteristics against publically available case study results of the PFC. Since assumptions in system level design necessary at this stage of technology evaluation propagate to varying aircraft-level results and many parameters and assumptions made in the studies available in the literature remain undisclosed, it is considered useful to employ a

[87] This means that propulsive efficiency is approximately constant, i.e. TSFC contours are directly proportional to the characteristics of thermal efficiency, while BPR varies with the specific power developed by the core engine.
[88] A typical hot-and-high condition refers to 5,000 ft altitude at ISA+20 K.

systematically randomized distribution of design settings. Therefore, an LHS distributed experimental plan was set up comprising 2,000 different aircraft designs. The variables selected include parameters subject to assumptions as well as parameters predicted by models implemented in the present work, and comprise thermodynamic, weight related and aerodynamic aspects. Given that FF design specific thrust and the thrust split ratio constitute important design parameters for the considered application and vary across the set of comparison data, these two variables were included in the array of design parameters. In Table 6.2, an overview of the parameters is presented including the chosen parameter ranges. The cycle parameters and specific thrust levels of the underwing-podded power plants were retained constant. In addition, mission requirements including cruise settings were kept constant as described in Section 6.3.1.

Parameter	Unit	Nominal	Minimum	Maximum
Design variables				
FF design specific thrust, $F_N/w_{2,F}$	m/s	n/a	45	110
Design power split ratio, Θ_{ds}	-	n/a	0.10	0.55
Technological settings				
Fuselage/nacelle interference coefficient, f_{interf}	-	1.05	1.00	1.15
Turbo component loss-scaling factor, $f_{tech,TC}$	-	0.90	0.85	0.95
FF design polytropic fan efficiency, $\Delta\eta_{Fan,ds,F}$ [a]	-	–0.01	–0.05	±0.0
FF design intake-PR scaling factor, $f_{p2/p0}$ [b]	-	1.00	0.90	1.10
FF design core intake-PR scaling factor, $f_{p22/p21}$ [b]	-	1.00	0.93	1.03
FF power plant mass increment, $\Delta W_{PPS,F}$ [b]	kg	±0	–1,000	+1,000

[a] relative to underwing-podded fan
[b] expressed relative to model prediction value

Table 6.2:Overview of selected variable ranges chosen for plausibility analysis

In Figure 6.3, the simulation results are presented. For result presentation, non-dimensional properties were chosen as axes parameters, thus allowing for the visualization of a large scope of application cases. The PSC (cf. Section 3.1.5) shown at the ordinate refers to the total design power of the LPT, thus incorporating all sources of aircraft motive power and is thus considered to be as well applicable to non-mechanically driven FFs such as partial turbo-electric power trains.[89] The reference condition refers to the reference systems discussed in Section 6.3.2. For the comparative study cases, each reference condition corresponds to the reference aircraft of the respective concept design, which are itemized below. The effects of varying design cruise conditions amongst the comparison samples on the respective relative power savings is considered subdominant compared to the large impact of Θ_{ds} and $F_N/w_{2,F}$ and therefore not explicitly resolved in this study. Furthermore, effects stemming from varying relative longitudinal installation positions of the fuselage propulsive device are disregarded. Again, serving the purpose of generalization with respect to the power source, the abscissa shows the fuselage-installed fan power relative to the total power of all fans installed, $P_{rel} = P_{Fan,F}/(P_{Fan,F} + P_{Fan,W})$. Each dot symbolizes a converged aircraft design, while the further symbols indicate the outcome of the comparative published studies. The level of shading indicates the respective FF intake duct height, which serves as an indicator for the amount of ingested momentum deficit and correlates with the fuselage-installed power plant mass.

[89] i.e. the LPT total power includes the power demand of the turbofan LP components plus LP spool generator offtakes

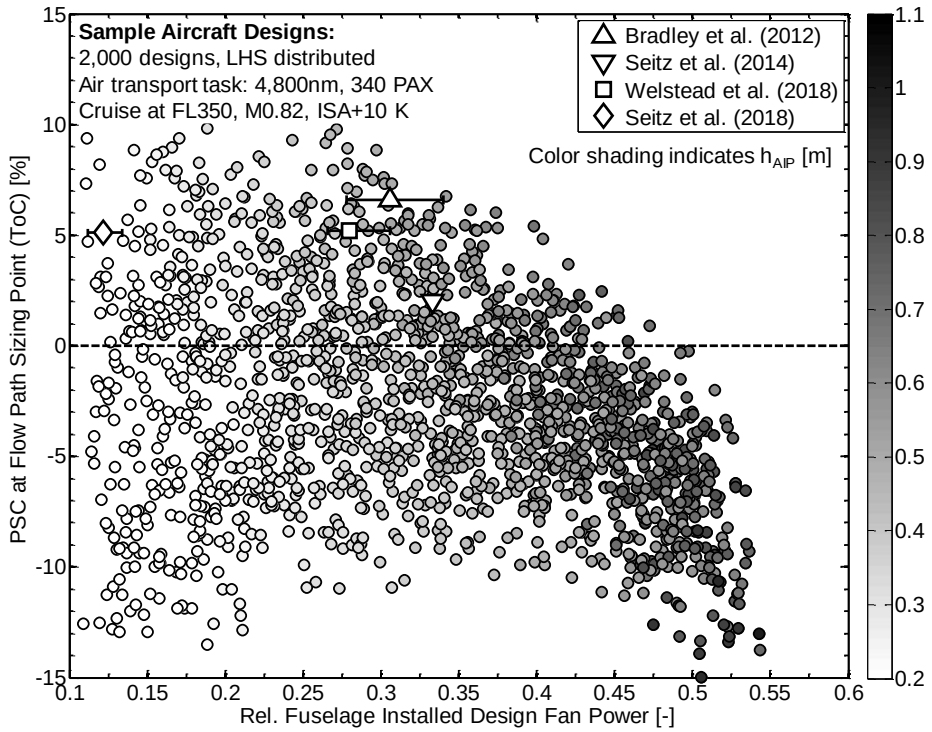

Figure 6.3: Results of plausibility analysis, 2,000 sampled aircraft designs

The following PFC concept design samples obtained from the literature were included for comparison purposes:

- The Boeing "SUGAR Freeze" concept in its variant with a BLI propulsor (3,500 nm, 154 PAX, cruise at M0.70, see Section 2.4.2.3) published by Bradley *et al.* [49], PSC expressed relative to baseline "SUGAR Freeze" version evaluated for 900 nm mission.

- The investigation of a gas turbine powered FF presented by Seitz *et al.* (2014) [118] conducted as part of the EC FP7 DisPURSAL project (4,800 nm, 340 PAX, cruise at M0.80, see Section 2.4.2.5), PSC expressed relative to advanced year 2035 reference aircraft with similar technology standard.

- The NASA STARC-ABL concept (revision published in 2018, 3,500 nm, 154 PAX, cruise at M0.785, see Section 2.4.2.6) presented by Welstead *et al.* [125], PSC expressed relative to NASA's N3CC Rev. B2.0 reference aircraft.

- A preliminary status of the turbo electric PFC configuration investigated by Seitz *et al.* (2018) within the EC H2020 CENTRELINE project (6,500 nm, 340 PAX, cruise at M0.82, see Section 2.4.2.7) [123], PSC expressed relative to advanced year 2035 reference aircraft with similar technology standard.

Note that for some of the comparison cases not the entire information necessary to determine PSC and P_{rel} is publically available. Therefore, imposed assumptions are listed in Table C.12 in Annex C. The error bars indicate a spread in the assumption values as discussed in Table C.12. It can be seen that the design results obtained from the implemented methodology are bound by frontiers of minimum and maximum PSC values. While there is a correlation of increasing P_{rel} with increasing duct height this also yields weight increase and therefore the general trend in PSC is seen to diminish against P_{rel}. In general, a noticeable proportion of the samples yields negative PSC, i.e. combinations of technological

and design settings offering no benefit against the reference systems. The corresponding trends will be elaborated in detail in Section 6.3.4. The shown comparison cases are found to reside well in the region of obtained result values.

6.3.4 Parametric Design Studies

In general, parametric studies serve the purpose of determining functional characteristics over the entire range of interest, thereby allowing for the identification of potential extrema and their location with respect to the study variables [313]. Primary design variables in the context of the PFC were declared in Section 6.3.1. Regarding the relative share of aircraft motive power installed at the fuselage power plant, different strategies will be analyzed in the following. From an economic perspective, contemporary aircraft design strategy seeks a high degree of commonality between assemblies and systems amongst different family members.[90] By allowing for the introduction of derivative designs from the outset, market flexibility is enhanced and beneficial cost effects may be exploited [171]. In the context of aero propulsion in particular, it is traditional practice to take commonality considerations into account. Frequently, the gas generator is sized to meet requirements for a range of thrust classes and even intended to cover varying application scenarios,[91] thereby significantly reducing development and manufacturing cost [314]. From an aircraft operator's view, common parts of the propulsion system translates into streamlined inventory management, reduced total propulsion costs and simplified maintenance procedures [171]. Consequently, an economic advantage is expected to occur for a PFC arrangement consisting of three similarly sized turbofan core engines, which in the present context refers to the components between the booster inlet and the LPT outlet. In the studies presented in this section, identical LPT powers are utilized as an approximate design criterion to indicate commonality in engine cores, in the first instance. As outlined in Section 6.3.1, geometric similarity of the core power plants is ensured. Besides this common core strategy (CCS), also the implications of varying the power split will be investigated.

6.3.4.1 Investigation of FF power plant specific thrust

One of the most influential design variables of the PFC refers to the design specific thrust of the fuselage-installed power plant. Therefore, the aircraft-level implications of this parameter were investigated in a parametric study, where $F_N/w_{2,F}$ was varied across a large range between 45 and 110 m/s. As a direct result, both duct height and design FPR vary approximately inversely. In this study, the power split ratio was retained at settings associated with a common core strategy, i.e. Θ_{ds} = 1/3. Key power plant cycle and technology settings (in particular $\Delta\eta_{Fan,ds,F}$) were kept constant. In order to maintain proper comparability with the reference aircraft, the design specific thrust of the wing-installed power plants was adopted from the reference aircraft and retained invariant. Expecting varying available thrust levels at takeoff due to $F_N/w_{2,F}$ variations, the engine scaling factor $c_{N,MCL}$ was added as a study parameter.

The study results are visualized in Figure 6.4 presenting the change in design mission block fuel, $\Delta W_{F,ds}$, relative to the reference aircraft against h_{AIP} for several levels of $c_{N,MCL}$. The carpet indicates the intuitively degrading block fuel benefit in case the power plants are oversized with respect to the MCL thrust requirements, i.e. $c_{N,MCL} < 1$. For a given $c_{N,MCL}$, reducing values of $F_N/w_{2,F}$ initially yield improving fuel burn savings due to an increasing share of momentum deficit being recovered through fuselage BLI/WF, which is reflected in growing values of ΔF_X, thereby yielding reductions in total engine sizing thrust (see Figure B.13 in Annex B for supplementary visualizations). In addition, intake pressure ratio increases with larger duct heights (see also Figure 4.7). Although propulsive

[90] Typically relates to tailplanes, power plant and wing [171].
[91] e.g. civil and military applications

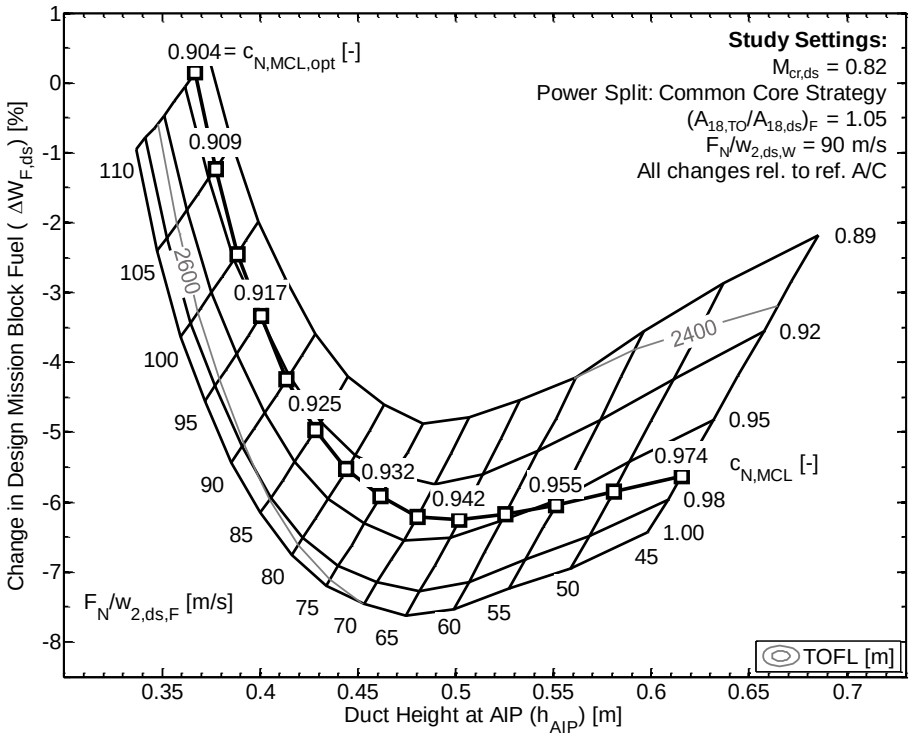

Figure 6.4: Parametric study of fuel burn optimum FF power plant design specific thrust levels

efficiency improves through reduced specific thrusts, the strong impact of pressure losses becomes increasingly dominant as FPR decreases (see also Section 6.2) and hence propulsive device efficiency, $\eta_{pr} \cdot \eta_{tr}$, degrades against h_{AIP}. This translates into reducing overall efficiencies of the fuselage-installed power plant, while η_{ov} of the wing-installed turbofans only reduces insignificantly for increasing h_{AIP} due to core size effects. The improvement in $\Delta W_{F,ds}$, however, is gradually counteracted by strongly increasing FF propulsion system weight, which is primarily driven by the increasing dimensions of the propulsive device and propagates into growing OEW including aircraft level cascade effects. As an additional contributor to the degrading η_{ov} and hence fuel burn benefit, temperature levels at takeoff experienced by the FF power plant and thus cooling air demand increases with reducing $F_N/w_{2,F}$. This is primarily caused by the thrust lapse characteristic of the FF propulsion system in connection with the takeoff rating strategy. As discussed before, turbofan designs with low specific thrust, which typically directly correlate with low design FPRs, are characterized by stronger thrust lapse with altitude and Mach number. Therefore, for given design thrust and takeoff limiter settings these engines develop a higher thrust output at takeoff relative to high specific thrust designs. The associated increased turbine power requires increased temperature levels. For the FF propulsion system this effect is partly mitigated by the slightly rising values of π_{int} at TO. As a result of the discussed partially counteracting trends, minima in $\Delta W_{F,ds}$ are encountered, which are located at specific thrust levels between 65 and 75 m/s depending on $c_{N,MCL}$. The takeoff performance represented by TOFL is visualized as contour lines. It is apparent that the global block fuel minimum of the study is associated with engines employing no oversizing and that this optimum is infeasible due to the imposed upper bound of TOFL.

Also presented in the chart is the characteristic of the constrained fuel burn optima, which represents the loci of minimum feasible thrust loadings $F_{N,TO,t}/MTOW$ for the investigated range of $F_N/w_{2,F}$ levels. The corresponding optimum values of the engine scaling factor, $c_{N,MCL,opt}$ are

annotated. It can be seen that for decreasing $F_N/w_{2,F}$ the extent of oversizing monotonically decreases, thereby mitigating the increase in propulsion system weight growth. Yet, for the given study settings all analyzed designs are characterized by $c_{N,MCL} < 1$. This effect is influenced by the dependency of the integration metric ΔF_X from the flight conditions yielding diminished force contributions at low-speed operation. The constrained relative block fuel minimum of -6.3% is obtained at $F_N/w_{2,F}$ = 65 m/s corresponding to a duct height of approximately 0.50 m. As can be gleaned from the chart, a relaxation of the TOFL requirements allowing for $c_{N,MCL}$ = 1 would translate into an additional fuel burn saving of approximately 1.4%. Figure B.13 presents an extended set of fuel burn-optimum characteristics against $F_N/w_{2,F}$. The displayed trend of the change in Operating Weight Empty, ΔOWE, is predominantly determined by the opposite characteristics of wing and fuselage-installed propulsion system weights. While for a given specific thrust of the podded turbofans reductions in sizing thrust translate into reducing power plant weight and hence initially yield decreasing aircraft empty weights, the increasing power plant mass of the FF propulsion system counteracts this trend. Apart from the propulsive device including nacelle, also the FDGS contributes to this due to increasing fan torque and significantly rising gear ratios. The degrading efficiency of the FF power plant is also reflected in a thrust split ratio, ϑ_{ds}, slightly reducing with lower $F_N/w_{2,F}$, however, remaining between 0.234 and 0.261.

As a result of widely unchoked nozzles at takeoff associated with low design FPRs, strong variations in the fan working line occur between cruise and takeoff operation [315]. As a general tendency, due to the reduced capacity of the bypass nozzle the takeoff operating point of low-pressure ratio fan arrangements tends to become shifted towards the surge line. Hence, surge margin of the FF power plant ($SM_{Fan,TO,F}$) becomes increasingly degraded for increasing h_{AIP}. This is further intensified by the circumferential distortion impact at takeoff, which, based on the simplified mapping approach outlined in Section 5.2.5, individually triggers a surge margin deterioration between -3.8 and -5.2%. For larger duct heights, the impact expressed in terms of DC_{60} rises due to larger fan regions generally being affected by distortion. As can be seen from Figure B.13, for $F_N/w_{2,F}$ smaller than approximately 55 m/s, $SM_{Fan,TO,F}$ would yield values below 15%, which is typically considered a lower limit for commercial fan applications [196]. Note that the FF application being inherently more susceptible to distortion may potentially require even more surge margin, thereby indicating the necessity of further increasing the area of the FF bypass nozzle at low-speed operation or the introduction of dedicated design measures potentially yielding impaired fan efficiency.

Within the range of parameters studied, L/D at the representative cruise point only varies insignificantly due to wetted area changes. The trend of $\Delta MTOW$ results from the superposing behaviors of ΔOWE and $\Delta W_{F,ds}$ and yields a minimum at an approximately 5% smaller duct height than for $\Delta W_{F,ds}$. The unconstrained characteristics of PSC_{ds} consistently exhibit maxima at h_{AIP} greater than for minimum fuel burn. The shape of the individual PSC_{ds} contours for a given $c_{N,MCL}$ are a direct result of the overall aircraft sizing thrust requirements. The optimum $c_{N,MCL}$ levels yield a characteristic of constrained PSC_{ds} optima, which show a monotonically rising trend of PSC against h_{AIP}. Note that the PSC_{ds} at sizing conditions incorporates the necessary oversizing capacity and hence is inherently smaller than the PSC evaluated e.g. at typical cruise condition.

6.3.4.2 Impact of power split ratio

Apart from FF specific thrust, the power split between fuselage and wing-installed power plants constitutes an important design parameter of the considered configuration. Based on the technological and simulation settings outlined in Section 6.3.1, in a parametric study, Θ_{ds} was varied between 0.1 and 0.6. The parameter $c_{N,MCL}$ was optimized for minimum block fuel subject to the TOFL inequality

constraint. The FF nozzle setting at takeoff, i.e. the relative exhaust area $A_{18}/A_{18,ds}$ was treated as an additional study parameter.

Figure 6.5 presents the impact of Θ_{ds} on $\Delta W_{F,ds}$ and $\Delta MTOW$. The characteristics of the common core strategy are annotated in the figure. It can be gleaned from the chart that within the chosen ranges the influence of $F_N/w_{2,F}$ and Θ_{ds} is similar with respect to $\Delta W_{F,ds}$. Furthermore, it is apparent that minimum block fuel is obtained at a power split slightly larger than 1/3. As an example, taking $A_{18,TO}/A_{18,ds}$ to be 1.05, i.e. the value used in the previously discussed study, a minimum in $\Delta W_{F,ds}$ is attained at Θ_{ds} = 0.41. This is primarily driven by the impact of FF power plant sizing parameters on the BLI/WF potential. Different from the study discussed in Section 6.3.4.1, for retained FF specific thrust, changes in FF pressure ratio are much smaller and only due to the improving intake total pressure recovery ratio. Therefore, as discussed in Chapter 4, this yields characteristics in the aero-propulsive design, which exploit the potential of BLI in an improved way (cf. also Figure 4.8). As a result, the convergence of ΔF_X towards the higher end of h_{AIP} is not as pronounced as in the case of strongly reducing design FPRs associated with reductions in $F_N/w_{2,F}$.

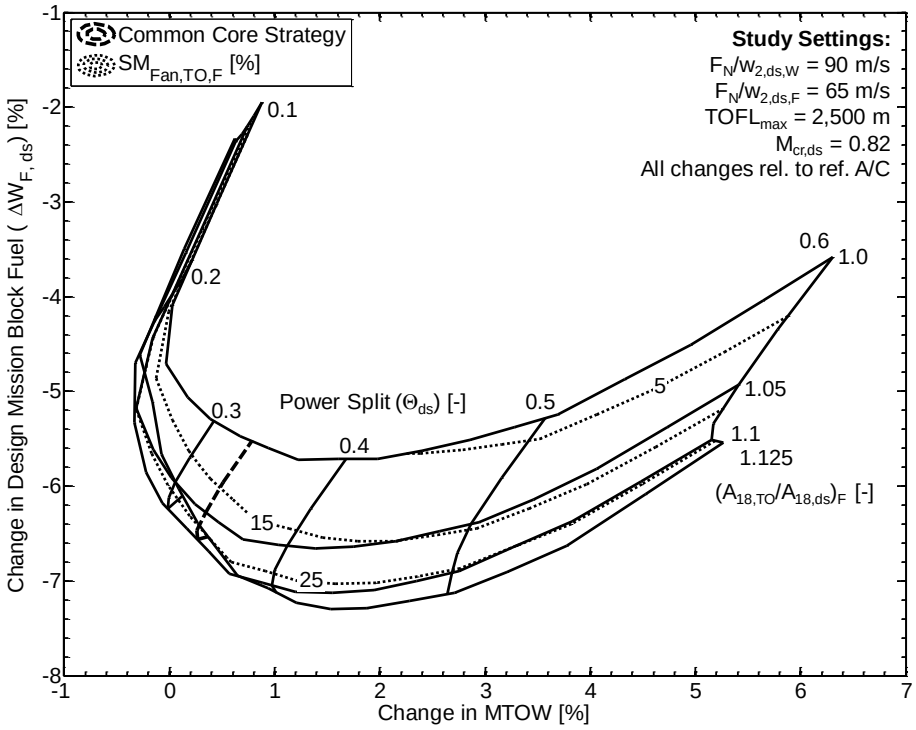

Figure 6.5: Implications of power split on design mission block fuel and MTOW for different FF nozzle settings at takeoff

As an additional effect, the increase in sizing thrust of the FF propulsion system propagates via improving η_{tr} into increasing overall efficiencies. Since $\eta_{ov,F}$ is still significantly degraded compared to the wing-installed power plants and the impact of the FF power plant increases with Θ_{ds} (cf. Figure 3.3), a slight net decrease in total propulsion system efficiency is obtained, specifically from 0.370 at Θ_{ds} = 0.1 to 0.350 at Θ_{ds} = 0.6, which, however, is a smaller decline than exhibited in case of reducing $F_N/w_{2,F}$.

Although specific thrusts are retained in this study, the factor $c_{N,MCL}$ decreases against Θ_{ds}. This is driven by the characteristics of π_{int} of the FF. While π_{int} at the sizing point improves for rising Θ_{ds}, the change in the corresponding value at takeoff is much less pronounced. As a result, the relative

improvement in π_{int} at off-design operation during takeoff is strongly increased for low values of Θ_{ds}, thereby yielding a higher relative net thrust output compared to the sizing thrust and thus allowing for increased $c_{N,MCL}$. This behavior is reflected in the surge margin characteristics of the FF indicated in Figure 6.5, which decreases against Θ_{ds}. This parameter is also influenced by increasing values in the distortion coefficient. It is apparent that for adequate surge margins a de-throttling of the FF at takeoff via fan nozzle area extension is essential. Primarily due to reduced maximum temperature levels requiring less cooling air demand, this triggers a slightly improving TSFC for the FF propulsion system against increasing nozzle area ratios. Figure B.14 in Annex B illustrates the changes in important system and aircraft level parameters against $A_{18,TO}/A_{18,ds}$, exemplified for Θ_{ds} = 1/3. In addition to improved overall power plant efficiency, the size of the core power plant decreases, which translates into increasing $BPR_{ds,F}$ and reduced propulsion system weight. Due to cascading effects at the vehicular level, a benefit in MTOW and block fuel can be obtained relative to the case of inexistent nozzle adaptation. Note that the benefit flattens out and even inverses for larger $A_{18,TO}/A_{18,ds}$, which can be attributed to the location of the operating points in the compressor maps influencing through changing component efficiencies the temperature levels and hence required cooling air. For appropriate comparability, a nominal value of 1.05 is selected for $A_{18,TO}/A_{18,ds}$ since this value yields feasible $SM_{Fan,TO,F}$ for the common core strategy while also supporting minimum $\Delta W_{F,ds}$ with $SM_{Fan,TO,F}$ > 15% and is thus considered a robust choice.

Figure 6.5 suggests that both MTOW and $\Delta W_{F,ds}$ constitute possible targets for minimization. In practice, the choice of Θ_{ds} may result from a trade-off between minimum block fuel and MTOW. It is apparent that the common core strategy may constitute a suitable compromise between both objective functions.

6.3.4.3 Combined investigation of FF power plant specific thrust and power split

Acknowledging the strong impact of the previously discussed parameters Θ_{ds} and $F_N/w_{2,F}$ on the overall system design and performance outcome, those two parameters were collectively investigated in a two-dimensional study, where the range of the individual parameters was chosen as before. The upper part of Figure 6.6 presents iso-contours of $\Delta W_{F,ds}$ against $F_N/w_{2,F}$ and h_{AIP}, while the lower part shows characteristics of MTOW as a function of identical coordinates. Again, $c_{N,MCL}$ was optimized for minimum block fuel. The figures are supplemented with contour lines indicating constant power split ratio, where the line Θ_{ds} = 1/3 corresponding to the common core strategy is explicitly highlighted. In addition, contours of the optimum engine scaling factor, $c_{N,MCL,opt}$, are included. The design space is constrained by two FF power plant related criteria. For the engine scaling factor, a minimum value of 0.89 was considered practically feasible in order to avoid extreme part power operation during cruise.[92] In accordance with the previously discussed studies, for the minimum required FF surge margin, a value of 15% was assumed, which is indicated in Figure 6.6.

Now, as a basic plausibility check, the previously discussed study results may be reproduced by setting one of the study variables constant. As can be gleaned from the chart, maintaining $F_N/w_{2,F}$ at 65 m/s results in a fuel burn optimum at Θ_{ds} = 0.41, while for the common core strategy the fuel burn optimum is, as previously demonstrated, located at a specific thrust of 65 m/s. In practice, the selection of the design solution, i.e. the choice if the common core strategy should be dispensed with in exchange for a relatively small additional fuel burn benefit will be made based on a multi-faceted trade-off analysis including economic aspects.

The iso-contours in Figure 6.6 result from the superposition of the individual effects of $F_N/w_{2,F}$ and Θ_{ds} discussed in the previous sections. Accordingly, the location of minimum block fuel is strongly

[92] see thick dashed-dotted line in Figure 6.6

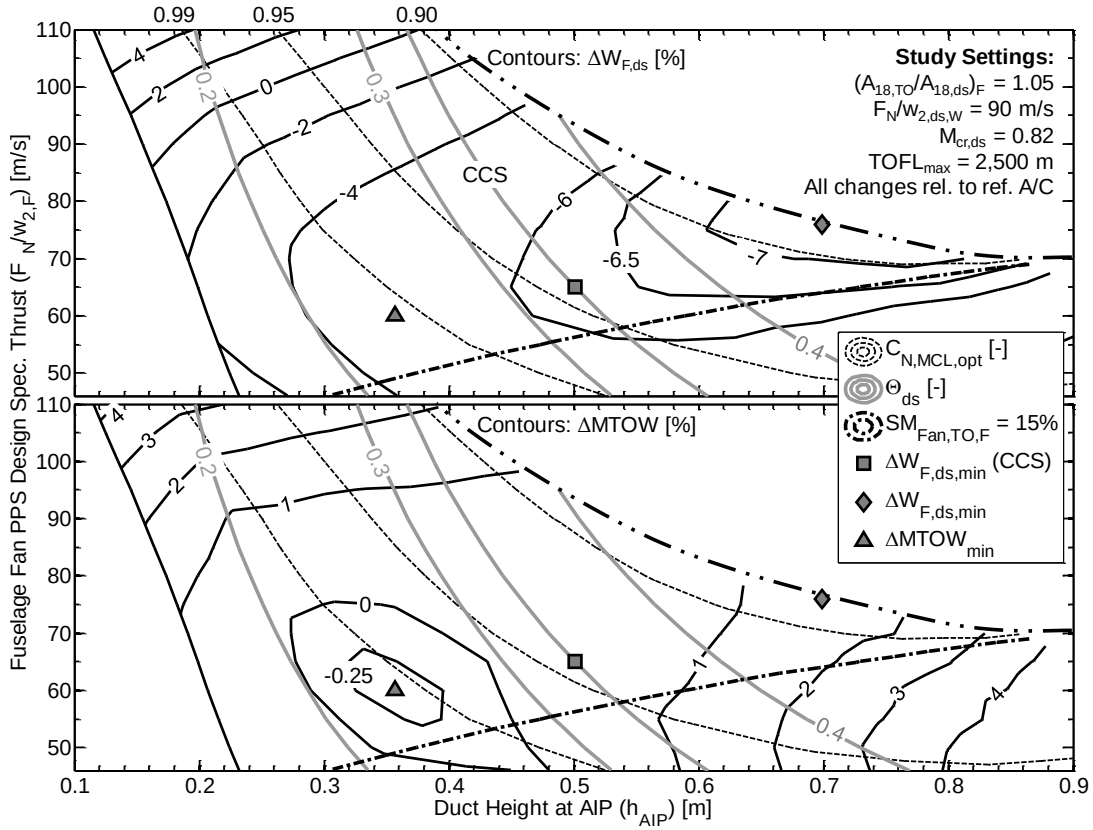

Figure 6.6: Investigation of FF power plant specific thrust and power split ratio on design mission block fuel and MTOW. Settings corresponding to common core strategy (CCS) are explicitly highlighted

influenced by the characteristics of π_{int}, which non-linearly correlate with h_{AIP}. Taking e.g. specific thrusts in excess of 65 m/s, it is observed that fuel burn optimum designs are characterized by larger power splits, thereby yielding greater duct heights and hence improved π_{int}. Reflecting the increased effect at the overall aircraft level associated with increasing power split, for Θ_{ds} > 1/3 fuel burn improvements are obtained for specific thrusts greater than 65 m/s, which, as discussed in Section 6.2, tend to yield in presence of generally penalized intake pressure ratios improved power plant overall efficiencies. Due to the applied lower limit on $c_{N,MCL}$, for $F_N/w_{2,F}$ greater than approximately 75 m/s a monotonic trend in $\Delta W_{F,ds}$ is obtained with increasing Θ_{ds}. The previously discussed tendency of increasing engine oversizing demand as $F_N/w_{2,F}$ is increased is consistently maintained for all investigated Θ_{ds}. The constrained fuel burn optimum is located at Θ_{ds} = 0.49 and $F_N/w_{2,F}$ = 74 m/s culminating in a block fuel reduction of -7.6%. Different from $\Delta W_{F,ds}$, for MTOW, the optimal design is clearly located at power splits smaller than one third. Intuitively, MTOW is driven by aircraft empty weight, which is significantly influenced by the FF power plant weight. The gross weight optimal design is situated at h_{AIP} = 0.35 m and a specific thrust of 60 m/s and yields a minimum value of -0.4% in $\Delta MTOW$. It can be observed from Figure 6.6 that the feasible solution space narrows down for increasing h_{AIP} and no valid solutions are found for h_{AIP} > 0.85 m.

The displayed study results facilitate trade-offs with respect to important sizing parameters of the PFC, i.e. $F_N/w_{2,F}$ and Θ_{ds} depending on the relative importance of the objective function. The studies are therefore considered to constitute a significant basis for follow-on analyses of specialized disciplines such as economic assessments. Furthermore, it is recognized that the common core strategy appears to be a robust design compromise between optimal block fuel and aircraft gross weight reduction potential.

6.3.4.4 Impact of design cruise speed

The implications of varying design cruise Mach numbers, $M_{cr,ds}$, are presented in Figure 6.7, where for varying $M_{cr,ds}$ and $F_N/w_{2,F}$ characteristics of $\Delta W_{F,ds}$ are displayed against h_{AIP}. For $M_{cr,ds}$, a value of 0.78 was considered as lowest acceptable cruise speed judging from an airline operator's perspective, while 0.85 was considered an upper practical limit for the considered medium-to-long haul application. The study was conducted for a common core strategy and, again, $c_{N,MCL}$ was optimized for minimum block fuel. The change in block fuel is expressed with respect to the reference aircraft sized for an identical range of Mach numbers and constant specific thrust. As previously, the thick dash-dot line denotes the boundary at which the minimum permissible value of $c_{N,MCL}$ is obtained.

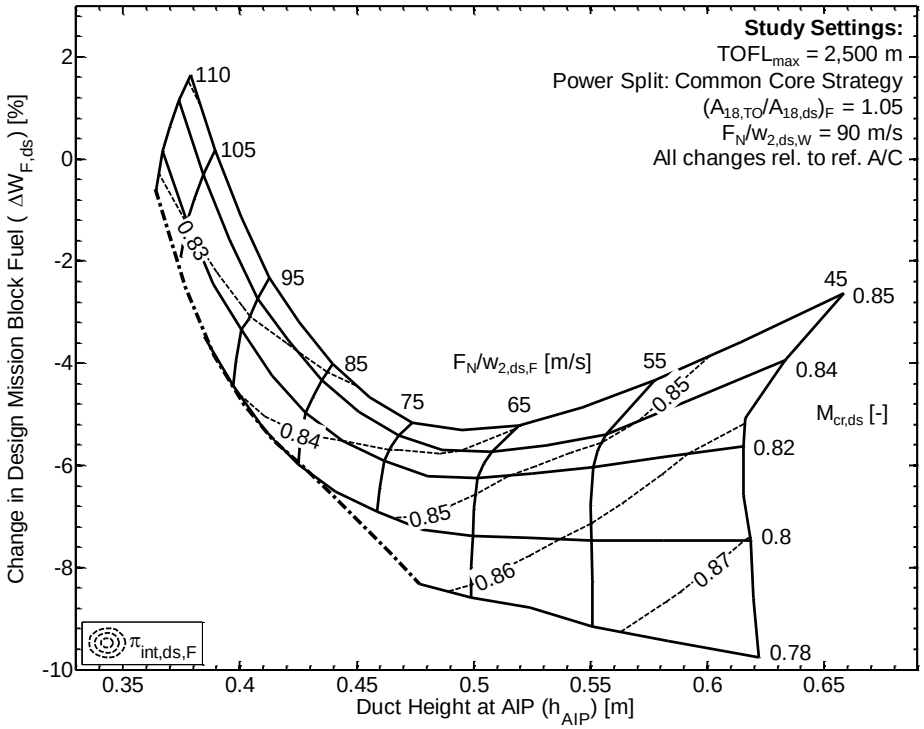

Figure 6.7: Implications of design cruise Mach number and FF power plant design specific thrust on design mission block fuel

As an important trend, it can be observed that generally the block fuel change for varying $M_{cr,ds}$ is disproportionate to the respective change exhibited by the reference aircraft. Irrespective of $F_N/w_{2,F}$, slower cruise speeds tend to increase the fuel burn benefit while the opposite is true for greater $M_{cr,ds}$. At $F_N/w_{2,F}$ = 65 m/s, sizing the aircraft for $M_{cr,ds}$ = 0.78 results in a block fuel reduction of 8.6%, while at $M_{cr,ds}$ = 0.85 the benefit diminishes to 5.2%. This trend is predominantly caused by the distinct Mach number dependency of design intake total pressure ratio of the fuselage-installed power plant (see contour lines in Figure 6.7), which propagates in a strongly non-linear way into propulsion system overall efficiency. As an additional contributor, the thrust growth necessary due to the transonic drag rise associated with increasing $M_{cr,ds}$ translates into increasing aircraft empty weight, where the impact of greater required wing sweep additionally triggers structural weight penalties. In this respect, the fuselage installation of the FF power plant evokes stronger cascading effects resulting from weight and balancing effects at the vehicular level than experienced by the reference aircraft, hence resulting in a net increase in OEW over the reference.

The fuel burn optimal value of $F_N/w_{2,F}$ significantly decreases for smaller $M_{cr,ds}$, which is driven by the Mach number induced variation in the trades of engine efficiency and weights with respect to block

fuel. Designs sized for smaller $M_{cr,ds}$ associated with reduced aircraft empty weight are found to allow for lower optimum specific thrust levels and hence greater propulsor dimensions. Since BL thicknesses inherently increase for reducing $M_{cr,ds}$, this offers improved exploitation of the wake filling potential. For increasing $M_{cr,ds}$, the discontinuity exhibited for $F_N/w_{2,F}$ = 45 m/s at approximately $M_{cr,ds}$ = 0.825 indicates the boundary of the region where no engine oversizing is required. As previously discussed, at given $F_N/w_{2,F}$ the decreasing values of $\pi_{int,ds}$ associated with increasing $M_{cr,ds}$ yield increasing ratios of intake pressure ratio between the sizing point and takeoff conditions, thus resulting in a thrust benefit at low-speed operation.

As discussed, the impact of $M_{cr,ds}$ on the fuel burn reduction potential is non-linear. As an example, for a $F_N/w_{2,F}$ of 65 m/s reducing the design Mach number from a baseline value of 0.82 to 0.80 results in an additional fuel saving of 1.1%, while an increase by the same Mach number increment only produces a penalty of 0.5%. The concave shape of the $\Delta W_{F,ds}$ characteristic as a function of $M_{cr,ds}$,[93] i.e. the tendency of being able to design the aircraft for a higher cruise speed at a relatively small fuel burn penalty is perceived as a beneficial characteristic for commercial operators.

6.3.4.5 Impact of wing-installed power plant design settings

While in the previous sections design specific thrust of the wing-installed GTFs, $F_N/w_{2,W}$, was retained, in this study the implications of varying this parameter are investigated for a range of $F_N/w_{2,F}$. The study settings and optimization strategy refer to Section 6.3.1 and the reference aircraft was kept unchanged. The results are presented in Figure 6.8. The essential parameters describing the size of the individual power plants, i.e. the fan tip diameter of the underwing-podded GTFs, $D_{Fan,W}$, and h_{AIP} were selected as coordinates for visualization. The carpet is supplemented with contours of $\Delta W_{F,ds}$ and $\Delta MTOW$.

The visible impact of $F_N/w_{2,W}$ on $D_{Fan,W}$ is intuitive. It should be noted that the observed deviation of the carpet from a strictly orthogonal shape is due to resizing effects at aircraft level provoking variations in sizing thrust for given specific thrust levels. The fuel burn optimal $F_N/w_{2,W}$ of approximately 79 m/s is found reduced compared to the reference aircraft. This is driven by the inherently smaller and lighter underwing-podded power plants of the PFC, which constitute a smaller share of the overall empty weight, thus allowing for the exploitation of propulsive efficiency benefits associated with a slightly larger fan diameter than resulting for $F_N/w_{2,W}$ = 90 m/s. This optimal point is located on a line connecting the loci of $c_{N,MCL,opt}$ = 1 and is thus associated with the smallest feasible sizing thrust to comply with all thrust requirements. It is characterized by 7.0% block fuel benefit. As established in the previously discussed studies, the location of minimum MTOW is determined to be at generally smaller propulsion dimensions.

The stipulated minimum feasible value of $c_{N,MCL}$ restricts large regions of the design space. The diagonal shape of this boundary is due to the superposition of the thrust lapse characteristic of the individual power plant types. Again, the study results visualized in Figure 6.7 are suitable for directly assessing the trade between the fuel saving potential and minimum aircraft gross weight.

6.3.5 Aircraft-Level Sensitivities

General objective of a sensitivity analysis is to analyze the impact of modeling aspects and assumptions subject to uncertainty on the integrated model response [316]. This construct therefore serves to

[93] This means that the second derivative of $\Delta W_{F,ds}$ with respect to $M_{cr,ds}$ is negative for all $F_N/w_2 \in$ [45…110 m/s], cf. Reference [302].

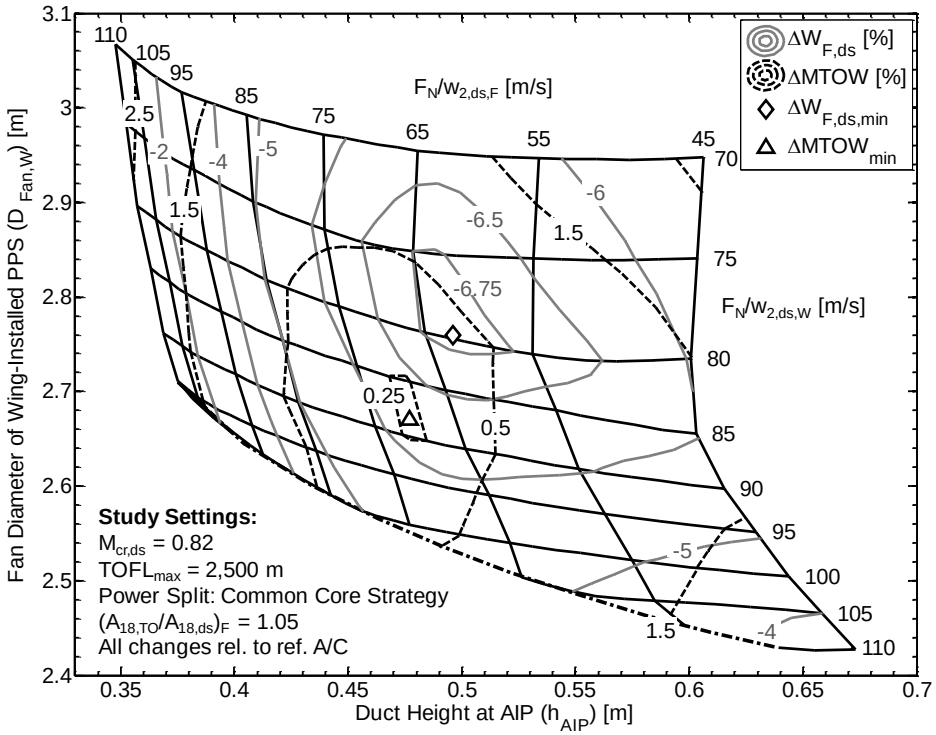

Figure 6.8: Results of variation of wing and fuselage-installed power plant specific thrusts with respect to change in design mission block fuel and MTOW

identify sensitive or important variables and to enhance the understanding of the system by estimating relationships between inputs and outputs of a model. Beyond that, it is useful for inspecting the model for validity and accuracy and for detecting potential modeling errors. Another field of common application of sensitivity analyses refers to the handling of poor or missing data by measuring the impact of assumptions [316]. As pointed out in Reference [313], as a classic task in conceptual design a sensitivity analysis provides insight to "what-if" scenarios. Additional aspects related to sensitivity analyses were outlined by Queipo *et al.* [299].

Now, a sensitivity is commonly understood as the partial derivative $\partial Y_j/\partial X_i$ of a model output Y_j against an input X_i [317], measured at a given local point. In order to capture non-linearity, the graphical representation presented in this section is based on five sample points of the respective input variable. The relative impact of a given variable is measured using a sensitivity index [316]

$$\varepsilon = \frac{\Delta Y_j}{\Delta X_i}\bigg|_{x_0} \tag{6.1}$$

which can be interpreted as the linearized partial derivatives evaluated at the respective nominal design settings chosen as pivot points, x_0. Based on the findings elaborated in Section 6.3.4.3, those settings refer to a common core strategy as well as specific thrust levels of $F_N/w_{2,W}$ = 90 m/s and $F_N/w_{2,F}$ = 65 m/s, while $M_{cr,ds}$ was kept at 0.82.

The method employed here refers to the classic "one-factor-at-a-time" approach [308], i.e. an introduction of local perturbations while keeping all other variables at a baseline value and monitoring the system response with respect to the parameters of interest, for which the linearized partial derivatives are computed. Since all but the current variables are kept at a coherently applied baseline value, adequate comparability of results is ensured. The variables chosen for the sensitivity analysis comprise primarily FF propulsion system related parameters and include thermodynamic, weights related and aerodynamic aspects:

- FF design polytropic efficiency decrement expressed relative to the fan efficiency of underwing-podded turbofan, $\Delta\eta_{Fan,ds,F}$
- FF design intake total pressure ratio, $\pi_{int,ds}$
- FF propulsion system mass increment, $\Delta W_{PPS,F}$
- Turbo component loss-scaling factor applied to all turbo components of the aircraft except the FF component, $f_{tech,TC}$
- Fuselage/nacelle interference drag coefficient, f_{interf}
- FF design core intake total pressure ratio, p_{22}/p_{21}
- FF intake total pressure ratio at takeoff point, $\pi_{int,TO}$
- FF nozzle area setting at takeoff point, $A_{18,TO}/A_{18,ds}$
- Relative mass of final reserve fuel with respect to trip fuel mass, $W_{F,rel,res}$

Figure 6.9 presents the impact on aircraft key metrics including design mission block fuel, OEW and MTOW. For the relative change ΔX_i, an increment of +0.01 was chosen, while the impact of propulsion system weight is typically expressed for an absolute mass increment of +500 kg, cf. e.g. Reference [204]. Negative values of ε signify improvements in $\Delta W_{F,ds}$, ΔOEW and $\Delta MTOW$, while $\varepsilon > 0$ corresponds to diminishing benefits. The pivot settings for $\pi_{int,ds}$, $\pi_{int,TO}$ and p_{22}/p_{21} coincide with the values predicted by the implemented models, while all other settings refer to nominal design assumptions (cf. Section 6.3.1). From inspecting the partial dependencies in Figure 6.9, the following insightful trends can be derived:

- The parameter $\pi_{int,ds}$ is determined to have the strongest impact on block fuel yielding an almost proportional effect on $\Delta W_{F,ds}$. This is understandable considering the over-proportional effect on TSFC, which, as $\pi_{int,ds}$ improves, becomes more dominant at the overall system level. Since power split and specific thrust were retained in the study, improving $\pi_{int,ds}$ triggers an increasing share of fuselage-installed thrust due to enhancing propulsive device efficiencies. While propulsion system total mass slightly increases against $\pi_{int,ds}$, a benefit in MTOW is attained primarily due to the reduction in required fuel and resizing effects e.g. with regards to wing and empennage sizes.
- Quantification of the implications of FF design efficiency variations emanating from inflow distortion effects on the overall system level is considered of particular importance for the present application. Comparison of the exchange rate ε indicates that $\Delta\eta_{Fan,ds,F}$ ranks second with respect to the relative significance of considered design variables. Specifically, a distortion tolerant fan design, i.e. $\Delta\eta_{Fan,ds,F} = 0$, would offer an additional fuel burn benefit of 0.67 percentage points. Conversely, the loss of each additional percentage point in fan efficiency implies a corresponding penalty.
- The relative importance of $\pi_{int,ds}$, $\Delta\eta_{Fan,ds,F}$ and p_{22}/p_{21} with regards to their individual impact on TSFC is found consistent with the trends expected from conventionally installed,

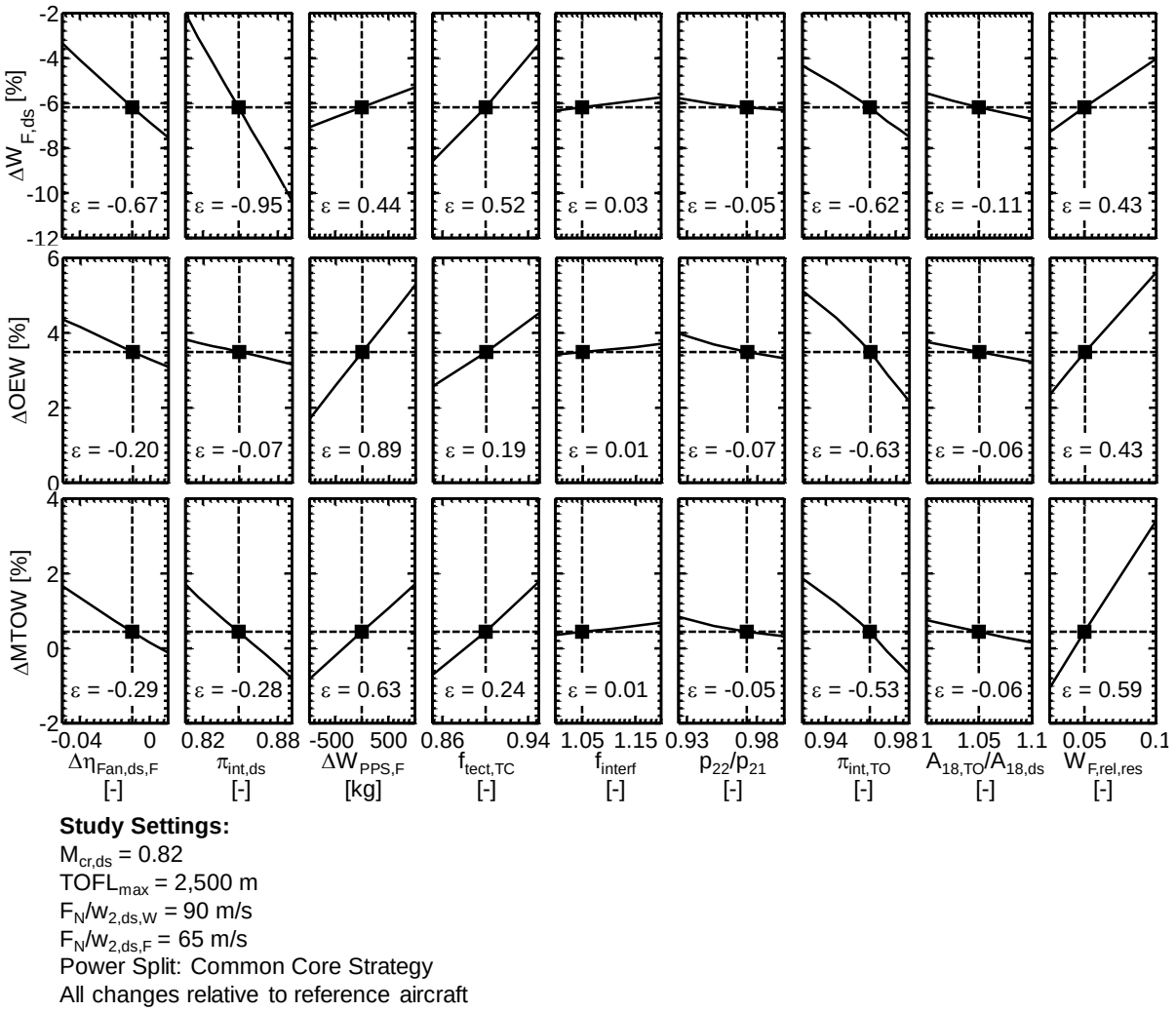

Figure 6.9: Results of aircraft-level sensitivity analysis. The factor ε describes the sensitivity index

very high-bypass turbofans, cf. Reference [196, p. 337]. Due to the lower specific thrust design, the impact of $\Delta\eta_{Fan,ds,F}$ is increased over the value indicated in Reference [196].

- Intuitively, increments in FF power plant mass propagate via changing OEW directly into MTOW including cascading effects.

- The collective adjustment of all turbo component aerodynamic losses except the FF via $f_{tech,TC}$ translates into an over-proportional change in total aircraft propulsion system efficiency, thereby yielding improvements in both $\Delta W_{F,ds}$ and $\Delta MTOW$.

- The impact of FF intake total pressure ratio at takeoff is primarily driven by repercussive effects on the design characteristics of the FF power plant. The improvement of $\pi_{int,TO}$ moves the fan operating point away from the surge line to higher corrected flows, thereby, apart from providing benefits in fan surge margin, yielding a reduction in temperature levels and hence decreased HPT cooling air demand for the fuselage-installed power plant. The reductions in OEW arise due to increasing thrust capability at takeoff allowing for reduced engine oversizing demand.

- While the impact of $A_{18,TO}/A_{18,ds}$ on the integrated performance is modest, it significantly affects the operability of the FF propulsion system. Specifically, for a fixed nozzle area, FF

surge margin at takeoff would decline to inadmissibly low 8.4%. As determined above, a relatively small area increase of 5% provides engine stability that is considered sufficient even considering potentially increased susceptibility due to distortion effects compared to conventional fan designs.

- The final reserve fuel fraction was studied as part of the sensitivity analysis due to potentially different airworthiness rules with respect to fuel contingency planning that might apply to this concept. Given that a thrust loss of the FF power plant might result in excessive windmilling drag, compatibility with current certification standards might require elevated levels of reserves compared to a conventional layout. It can be observed that a doubling of the nominal value of $W_{F,rel,res}$ would result in a penalty in fuel saving of 2.1 percentage points.

- The parameters f_{interf} and p_{22}/p_{21} only have minor effects on the aircraft-integrated performance compared to the other parameters considered.

6.4 Characterization of Propulsive Fuselage Concept

As a synthesis of the studies presented above, the characteristics of the PFC including the propulsion system are compared and contrasted to those of the reference systems. Primary objective of the benchmarking exercise is to facilitate the identification of commonalities and differences in key design parameters and integrated performance characteristics between the alternative sizing strategies. Starting from the reference aircraft denoted as "REF", the impact of successively increasing the design space by consecutively relieving design restrictions is discussed. The sizing strategies are denoted as PFC_1 to PFC_3:

- PFC_1: derived from investigation of FF power plant specific thrust (Section 6.3.4.1) where the specific thrust of the wing-installed power plant was kept constant and power split was set to facilitate a common core strategy.

- PFC_2: derived from combined investigation of FF power plant specific thrust and power split (Section 6.3.4.3) where the specific thrust of the wing-installed power plant was kept constant.

- PFC_3: derived from investigation of fuselage and wing-installed specific thrust levels (Section 6.3.4.5) while a common core strategy was maintained.

For each sizing strategy the aircraft characteristics delivering minimum design mission block fuel and minimum MTOW were derived, which are symbolized using indices *a* and *b*, respectively. The characteristics of the different designs with regards to MTOW and block fuel saving potential are visualized in Figure 6.10, where designs featuring common settings yet different objective functions are connected through lines. The shaded area denotes the undesirable region.

It can be seen that the spread in $\Delta MTOW$ and $\Delta W_{F,ds}$ increases once greater freedom in the choice of design variables is permitted. While for case 1 the optima for minimum block fuel and MTOW are located in close proximity, variations in power split have a strong impact on the location of the design point with respect to the $\Delta MTOW$ and $\Delta W_{F,ds}$ coordinates. It is visible that the respective derivatives $\Delta W_{F,ds}/\Delta MTOW$, which may be approximated by connecting points of equal sizing strategies, change between cases 1 to 3 indicating different trades in aircraft empty weight and fuel demand. In general, the aggregated solutions reside in a corridor offering the possibility to trade enhancements in MTOW against reductions in fuel saving potential. As a key result, it is established that for the given general study settings and application scenario only if the common core strategy is waived a benefit in both

$\Delta W_{F,ds}$ and $\Delta MTOW$ metrics is achievable over the reference. Intermediate solutions (e.g. gross weight neutrality) may constitute a feasible compromise depending on the relative importance of the individual metrics.

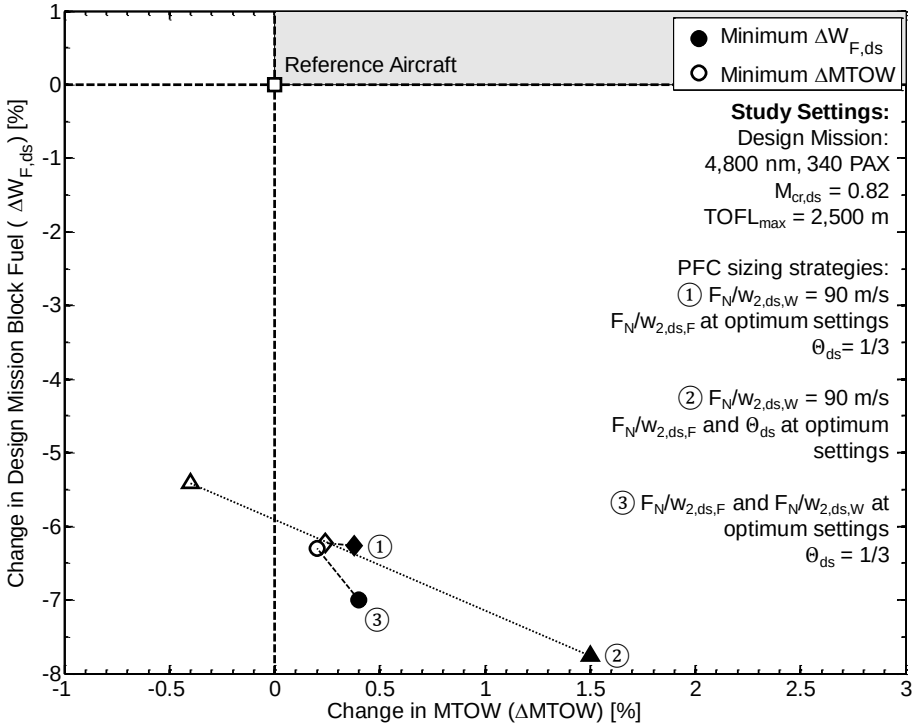

Figure 6.10: Visualization of PFC sizing strategies on integrated performance characteristics relative to reference aircraft

A synopsis of important power plant and aircraft related parameters and performance metrics of the different sizing strategies discussed above is presented in Table 6.3, where for each strategy the characteristics of the designs delivering minimum block fuel and minimum MTOW, respectively, are benchmarked against the reference aircraft. A key design attribute of the power plant types includes the optimal setting for specific thrust, which, in conjunction with the net thrust at the flow path sizing point indicated in the table determines the primary dimensions of the engine. Here, fan tip diameter, D_{Fan}, and h_{AIP}, respectively, were chosen as suitable indicators of propulsion system radial size. As discussed in Section 6.3.4, for a given F_N/w_2, design BPR and FPR strongly depend on the specific power produced by the core engine and on the inlet conditions imposed by the ingested low-momentum BL flow, which is indicated through the levels of π_{int}. The strong impact of the adverse inflow conditions as well as increased component losses on the performance of the FF power plant can be gauged from comparing the levels of overall efficiency indicated in the table to those of the respective wing-installed power plants. Due to the moderate levels of Θ_{ds}, however, the impact on overall propulsion system efficiency at the vehicular level, $\eta_{ov,ds,tot}$, as derived in equation (3.15) is attenuated.

Reflecting the assumption of invariant wing loadings, the indicated values of wing reference area, $S_{Ref,Wing}$, directly scale with MTOW. For all selected designs, the variation in MTOW is below the threshold above which reduced wing aspect ratios would be required to comply with the imposed span constraint. The integration impact metric ΔF_X at the sizing point, which is determined by h_{AIP}, FPR and $M_{0,cr}$ (cf. Section 4.4.2) is also provided in the table. While for the reference aircraft propulsion system thrust sizing is solely defined through the MCL point requirements, for most of the selected

PFC designs the takeoff constraint becomes critical. This is caused by the reduction of the ΔF_X metric at low-speed operation, although improved values of π_{int} alleviate this issue (cf. Section 6.3).

Parameter	Unit	REF [a]	PFC_{1a}	PFC_{1b}	PFC_{2a}	PFC_{2b}	PFC_{3a}	PFC_{3b}
Wing-installed power plants								
$F_N/w_{2,ds}$	m/s	90	90	90	90	90	79	88
$F_{N,ds}$ [b]	kN	58.8	37.9	38.2	30.1	41.3	36.4	38.0
D_{Fan}	m	3.28	2.64	2.65	2.35	2.76	2.76	2.67
BPR_{ds}	-	15.2	14.9	14.9	14.7	15.0	16.9	12.7
W_{PPS} [c]	kg	9017	5373	5424	4121	5937	5559	5463
$\eta_{ov,ds}$	-	0.411	0.406	0.406	0.401	0.406	0.408	0.407
Fuselage Fan propulsion system								
$F_N/w_{2,ds}$	m/s	n/a	65	70	76	60	61	70
$F_{N,ds}$	kN	n/a	24.1	24.7	41.7	15.2	22.3	24.4
FPR_{ds}	-	n/a	1.45	1.48	1.48	1.46	1.43	1.48
h_{AIP}	m	n/a	0.50	0.48	0.70	0.36	0.50	0.48
BPR_{ds}	-	n/a	13.4	12.7	13.1	13.1	14.0	12.7
$\pi_{int,ds}$	-	n/a	0.848	0.845	0.872	0.827	0.848	0.845
W_{PPS} [c]	kg	n/a	9010	8739	12597	6832	8840	8675
$\eta_{ov,ds}$	-	n/a	0.261	0.264	0.289	0.246	0.261	0.265
Θ_{ds}	-	n/a	0.33	0.33	0.49	0.24	0.33	0.33
$\eta_{ov,ds,tot}$	-	0.411	0.358	0.359	0.346	0.367	0.359	0.359
$S_{Ref,Wing}$	m^2	325.9	327.1	326.7	330.8	324.6	327.2	326.6
$c_{N,MCL,opt}$	-	1.000	0.942	0.937	0.887	0.998	1.000	0.946
$\Delta F_{X,ds}$	kN	n/a	21.4	20.7	25.4	17.5	21.5	20.6
Aircraft performance characteristics								
$\Delta TSFC_{tot,cr}$ [d, e]	%	base	–7.1	–6.9	–9.0	–5.4	–8.0	–7.1
$\Delta W_{AC,cr}$ [d]	%	base	+0.4	+0.2	+0.4	–0.4	–0.4	–0.4
$\Delta L/D_{cr}$ [d]	%	base	+0.4	+0.4	+1.1	+0.2	+0.6	+0.4
ΔOEW	%	base	+3.4	+3.2	+5.3	+1.8	+3.5	+3.1
$\Delta MTOW$	%	base	+0.4	+0.2	+1.5	–0.4	+0.4	+0.2
$\Delta W_{F,ds}$ [f]	%	base	–6.3	–6.2	–7.8	–5.4	–7.0	–6.3
$\Delta W_{F,od}$ [g]	%	base	–5.8	–5.9	–7.5	–4.9	–6.6	–6.0

[a] see p. 123 for nomenclature (index *a*: minimum design mission block fuel, index *b*: minimum MTOW)
[b] per engine
[c] total propulsion system mass per engine including operating fluids
[d] typical cruise at M0.82, FL350, ISA + 10 K, c_L = 0.5
[e] definition based on equation (5.23)
[f] design mission block fuel (4,800 nm, 340 passengers) including reserves, cruise at M0.82, ISA + 10 K
[g] off-design mission block fuel (2,000 nm, 340 passengers) including reserves, cruise at M0.82, ISA + 10 K

Table 6.3: Comparative summary of important design and performance parameters of alternative PFC sizing strategies compared to advanced reference aircraft

For immediate identification of the implications of the different sizing strategies, the relative change in important overall system-level performance metrics is provided. These include the parameters necessary for en route point performance evaluation at typical cruise, i.e. the changes relative to the reference aircraft in total aircraft TSFC, L/D and instantaneous gross weight, $W_{AC,cr}$, at a given aircraft lift coefficient, c_L. The total aircraft TSFC refers to the definition outlined in Section 5.6 (equation (5.23)), i.e. incorporates ΔF_X in the total propulsive force. Hence, aero-propulsive interaction effects associated with the power plant integration concept are interpreted as a TSFC benefit. Only slight changes in aerodynamic efficiency at cruise occur relative to the reference aircraft. Minor and partly

counteracting changes in wetted areas constitute the main driver on aircraft form drag, while for the given flight condition lift-induced drag remains constant due to invariant wing aspect ratios and Oswald's efficiency factor. The integrated vehicular performance is assessed through the changes in OEW, MTOW and design mission block fuel. A growth in empty weight is encountered for all studied PFC designs compared to the reference. This is mainly rooted in the increased total power plant weight, which varies between +3.7% and +15.6%. A comparative weight breakdown between the PFC_{1a} design and the reference aircraft is provided in Table 6.4. As can be seen, a heavier fuselage primary structure is obtained emanating from increased fuselage total length (+4% to +5%) as well as from necessary structural reinforcements associated with installation of the fuselage power plant. The intrinsically suffered weight penalty of the vertical stabilizer is compensated for by an increased lever arm between the aerodynamic centers of the wing and the horizontal stabilizer resulting from the T-tail arrangement, although the wing position is shifted aft due to the placement of power plant weight in the rear fuselage. As a net effect, reduced stabilizer area is obtained over the reference aircraft. Landing gear height is driven by the required pitch freedom with respect to the FF nacelle contour, thereby triggering an 8.8% to 10.6% increased height, which translates into a weight growth of the undercarriage. The almost proportional change in wing weight with MTOW is understandable considering the above-mentioned wing scaling law. A relatively small penalty in MTOW over the reference configuration is exhibited by the PFC_{1a} design.

	Unit	REF	PFC_{1a}	Change [a]
Structures	t	78.32	80.80	+3.2%
Wing	t	38.58	38.68	+0.3%
Fuselage	t	29.63	32.41	+9.4%
Empennage	t	1.85	1.77	–4.6%
Pylons	t	2.00	1.39	–30.7%
Landing gear	t	6.25	6.55	+4.7%
Propulsion	t	18.03	19.76	+9.6%
Wing-installed turbofans [b]	t	18.03	10.75	–40.4%
Fuselage Fan propulsion system	t	n/a	9.01	n/a
Residuals [c]	t	26.77	26.77	±0.0%
OEW	t	123.12	127.32	+3.4%
Payload [d]	t	34.68	34.68	±0.0%
Fuel [e]	t	53.83	50.63	–6.3%
MTOW	t	211.63	212.42	+0.4%

[a] PFC_{1a} relative to REF
[b] engine total mass including mounting and operating fluids
[c] refers to systems and components not explicitly modeled including equipment, operational items, furnishing, electrical system, fuel system, flight controls, environmental control, instruments, ice and rain protection and auxiliary power
[d] maximum structural payload
[e] design mission takeoff fuel at maximum structural payload including contingencies for diversion flight, holding and final reserves

Table 6.4: Comparative mass breakdown of advanced conventional reference aircraft (REF) and PFC_{1a} design

For the nominal design settings, the block fuel benefit on the design mission is found between 5.4% and 7.8% depending on the employed sizing strategy. In addition, the block fuel required for an off-design mission of shorter stage length is provided in Table 6.3, where an identical fuel contingency policy was in effect. With reference to [114], a 2,000 nm distance was considered the maximum utilization analogue for the studied application case. As expected, in case of shorter distances where the cruise segment inherently constitutes a smaller fraction of total mission time, the impact of

beneficial aero-propulsive interaction effects reduces and hence a degraded fuel saving potential is obtained.

In order to verify the plausibility of the integrated performance assessment, the outcome of PFC_{1a} against REF with regards to SAR at cruise is compared in the following for the two alternative accounting approaches outlined in Section 5.6. Using the data tabulated in Table 6.3, a ratio in cruise-SAR relative to the reference,

$$\frac{SAR}{SAR_{ref}} = \frac{(L/D)_{cr}}{(L/D)_{cr,ref}} \cdot \frac{1}{TSFC_{tot,cr}/TSFC_{tot,cr,ref}} \cdot \frac{1}{W_{AC,cr}/W_{AC,cr,ref}} \tag{6.2}$$

of 1.0763 is obtained. Now, employing the alternative accounting option results in $\Delta\widetilde{L/D}$ = +34.9% at $\tilde{\beta}$ = 0.256 and $\Delta\widetilde{TSFC}_{tot}$ = +25.0% at cruise and therefore produces a SAR ratio of 1.0757. Both results compare well with the fractional change in SAR determined directly from $\Delta W_{F,ds}$ using equation (5.22), for which a value of 1.0668 has been identified for the PFC_{1a} design.

The identified fuel burn reduction potential appears slightly smaller than previously predicted for similar applications (cf. References [114], [118], [124]). This is primarily attributed to the enhanced level of detail in system modeling in the present work, which is deemed necessary for a realistic assessment, and the consideration of additional sizing constraints previously not included. The presented sensitivity analysis revealed the considerable lever offered by enhancements in the aero-propulsive characteristics on the overall saving potential, which may be realized through optimized aerodynamic shaping of the associated components. The findings presented are considered to constitute relevant contributions for more specialized analyses related to the investigated configuration including the evaluation of operating economics and an in-depth environmental assessment.

7 Conclusion and Outlook

In this thesis, a methodological framework for the conceptual sizing of a novel configurational approach for synergistic propulsion system integration, the Propulsive Fuselage Concept (PFC), was presented. As a result of a comprehensive literature survey, the requirement for an enhanced representation of the aero-propulsive interaction effects and the associated implications on propulsion system and airframe in the conceptual design process was recognized. Therefore, the methodological development included the introduction of methods facilitating efficient incorporation of parameterized numerical data describing the mutual interaction between airframe and engine within aircraft-integrated propulsion system synthesis. In this respect, emphasis was placed on the adequate mapping of design and operational implications associated with the Fuselage Fan (FF) power plant while ensuring compatibility with typical propulsion and aircraft design frameworks. The proposed approach is reasonably general to be applied to varying sets of numerical data and proved adequate to handle the increased complexity associated with intensified aero-propulsive interrelations. Since the investigated configuration is powered by both a FF propulsion system and wing-mounted turbofan power plants, propulsion system synthesis models featuring multidisciplinary methods consistently applicable to conventionally installed and highly integrated arrangements were employed. A series of specific methods were introduced for the mapping of the additional loss and weight effects associated with the FF power plant integration, which were primarily based on simplified physics-based relations. The specific disciplinary methods were validated individually. A conceptual aircraft sizing framework was methodologically supplemented in the present context to account for the physical effects associated with the fuselage wake filling propulsion installation. Attention was paid to allow for the investigation of alternative propulsion system sizing strategies while taking into account typical contemporary sizing requirements and product design practices. The key design parameters associated with the propulsion system integration approach were treated as free variables and studied as part of system and aircraft level design space exploration studies. The presented methodology provides efficient exploration capability of the design space under consideration of multidisciplinary design aspects in the early phases of conceptual design. It therefore facilitates enhanced knowledge gain with regards to the impact of key influential parameters on propulsion system optimality settings at the vehicular level, thereby enabling quantification of the PFC efficiency potential compared to the conventional propulsion system integration practice.

7.1 Summary of Important Results and Findings

In order to demonstrate the implemented methodological framework, several parametric design studies were presented. The application scenario corresponded to the widebody, medium-to-long range aircraft layout for which numerical aerodynamic data was available. For the detailed analysis of the implications connected to the ingestion of the fuselage boundary layer, initially, design studies on power plant level were conducted highlighting important differences in the trending behavior compared to a conventionally installed Geared Turbofan (GTF) architecture. For the FF power plant, intake total pressure recovery ratio was identified to be a decisive design driver, which was found severely penalized due to the low-momentum boundary layer flow ahead the intake. As a result, strongly impaired transmission efficiency levels translated into significantly degraded power plant overall efficiency. Moreover, the optimality of design specific thrust levels was found altered compared to the trends obtained from conventionally installed turbofans.

Acknowledging the strongly coupled propulsion and aircraft characteristics associated with the investigated concept, in a next step, aircraft-integrated studies were presented. In order to establish a suitable basis for comparing and contrasting the characteristics of the PFC, a parametric study of an advanced, conventional twin-engine aircraft accomplishing the same transport task and incorporating similarly advanced technology was conducted. Fuel burn-optimum settings for design specific thrust were found to be 90 m/s corresponding to a design bypass ratio of 15.2.

The PFC aircraft configuration referred to a tube-and-wing arrangement featuring the FF propulsion system in conjunction with two underwing-podded GTF engines. Targeting substantiation of the implemented methodology, a plausibility analysis involving the quasi-randomized distribution of significant input parameters across wide ranges was performed. Comparison of the characteristics of 2,000 computed PFC aircraft design samples with data obtained from published conceptual studies of different PFC layouts showed similar magnitudes in the power saving potential expected from the PFC. Thereafter, parametric studies were presented focusing on identifying the aircraft-level characteristics emanating from the variation of key parameters associated with the FF propulsion system installation. The parameters investigated included the design specific thrust, F_N/w_2, of both power plant types, since this parameter has a pronounced effect on both power plant internal performance, i.e. specific fuel consumption, but also on the external dimensions and weight of the propulsion system. As objective functions for parametric optimization, both design mission block fuel, $W_{F,ds}$, and maximum takeoff weight were considered, while low-speed performance metrics including Takeoff Field Length (TOFL) were treated as constraints. It was found that depending on the study settings, a large share of the investigated PFC designs required oversizing of the power plants relative to the thrust requirements at the top-of-climb point in order to comply with the TOFL limit. As a result, for invariant specific thrust levels of the underwing-podded GTFs, the constrained fuel burn optimal design specific thrust of the FF power plant was identified to be 65 m/s yielding a 6.3% reduction of $W_{F,ds}$ compared to an advanced conventional reference aircraft. From a multi-variate design study it was determined that a relaxation of the TOFL constraint would allow for an additional fuel burn saving of approximately 1.4%. While a system sizing approach under the premise of realizing maximum commonality in the core engines of wing and fuselage-installed power plants is expected to allow for benefits in operating economics, the prescription of fixed design power splits restricts the feasible design space and thus exploitation of the full efficiency potential. Hence, from a conjoint investigation of F_N/w_2 of the fuselage power plant and the design power split between both power plant types, the potential of disregarding a common core strategy was investigated. It was established that the lever of power split on both $W_{F,ds}$ and MTOW is stronger than F_N/w_2. Generally, the location of minimum block fuel was found significantly influenced by the characteristics of intake total pressure ratio. For constant design specific thrust levels of the wing-installed GTFs, the constrained optimum with respect to $W_{F,ds}$ was identified to deliver 7.8% block fuel reduction compared to the reference aircraft, while MTOW was increased by 1.5%. This design was associated with a power split of 0.49, while for minimum MTOW the optimum power split was clearly below one third, thereby reflecting the implications of FF power plant weight on aircraft empty weight. Compared to that, the fuel burn saving associated with the common core strategy yielded 6.3%. The combined investigation for a fixed design power split showed that the in case of the PFC higher BPRs of the wing-installed power plants than identified for the reference aircraft are optimum with respect to fuel burn, which is caused by the inherently smaller sizing thrust and thus dimensions and weight of the wing-installed GTFs. As a conclusion from the investigated sizing strategies it was established that the block fuel saving potential for the given application scenario ranges between 5.4% and 7.8% compared to the advanced reference aircraft. In order to assess the operational performance of the PFC relative to the characteristics of an advanced conventional transport, design cruise Mach number, $M_{cr,ds}$, was investigated as part of the parametric trade studies. It was recognized that independent from the selected level of F_N/w_2, reduced design cruise speeds have a tendency to increase the fuel burn benefit compared to the reference system sized

for identical Mach numbers. As an example, at 65 m/s specific thrust, reducing $M_{cr,ds}$ from 0.82 to 0.78 would enhance the block fuel saving to 8.6%, while choosing $M_{cr,ds}$ to be 0.85 would cause the fuel burn reduction to diminish to 5.2%. One of the major drivers of this effect was identified to be the nonlinear dependency of FF intake total pressure ratio on $M_{cr,ds}$.

The fuel saving potential predicted by the presented methodological framework appears to be slightly diminished compared to previously conducted studies of similar applications. This is attributed to the enhanced level of detail in system modeling, which was considered essential for ensuring a realistic assessment, and the consideration of additional sizing constraints hitherto not fully accounted for. Exemplary aspects included the modeling of the operational impact of the ingested boundary layer flow on the propulsion system performance during off-design conditions, as well as the incorporation of aircraft low-speed performance requirements, which substantially influenced engine sizing characteristics. A sensitivity analysis was considered a useful instrument for inspecting the impact of key sizing and performance parameters connected to the BLI propulsion system installation on important aircraft level metrics. The analysis illustrated the importance of realizing a fuselage and FF nacelle shaping, which seeks to minimize total pressure losses ahead the fuselage propulsor intake since the associated parameter was found to constitute a substantial lever towards increasing the fuel saving benefit of the PFC.

The findings and results obtained as part of the thesis are considered to constitute relevant contributions for more specialized studies in the associated fields. The subsequent section itemizes aspects recommended for further investigations.

7.2 Perspectives for Further Investigations

Due to the large impact of the FF propulsion integration on overall system performance inherently experienced by the investigated configuration, follow-on work should focus on enhanced analysis of the aero-propulsive interaction effects by means of advanced high-fidelity simulation techniques. While the numerical data available for the present work corresponded to a robust aerodynamic design, emphasis should be placed on further optimizing the shaping of the fuselage and FF nacelle contouring with respect to its aerodynamic performance. A three-dimensional numerical setup featuring appropriate coupling with the integrated sizing task could allow for the detailed resolution of additional flow effects. With respect to overall vehicle aerodynamics, this includes aspects such as downwash effects induced by the wing, the effects of operating the aircraft at angle-of-attack and/or sideslip, the implications of extended high-lift devices as well as the impact of crosswind situations. The evaluation should be conducted at all relevant flight conditions within the operating envelope. While a highly automated optimization approach with a large number of design variables was not subject to this work due to the aim of focusing on the global physical relations between major design variables, such an approach might allow for exploiting additional benefits resulting from cross-coupling effects not considered yet. The consideration of three-dimensional fuselage shaping could also allow for increased design freedom at the overall system level. As an example, the introduction of fuselage up-sweep may facilitate a shorter landing gear height, thus giving scope to reducing the penalty in aircraft empty weight exhibited by the PFC.

The fuselage propulsor should be subject to more detailed numerical investigations in order to gain deeper insight on the implications of BLI on attainable fan efficiency levels and stability characteristics for this particular configuration. Once coupled with higher-order numerical analysis of the overall configuration, full-annulus Computational Fluid Dynamics (CFD) simulations would allow for identifying the detailed impact of flow distortion patterns on fan performance. In fact, insightful studies

would be connected to evaluating the operational performance of a FF specifically designed for coping with BLI effects within propulsion system synthesis by means of incorporating corresponding fan performance maps. In this respect, the presence of the flow straightening intake struts should be taken into account. Numerical simulations should be supplemented with experimental investigations in order to validate the results. Most recently, research in this respect has been initiated [123]. Beyond aircraft and propulsor aerodynamics, the detailed analysis of power plant internal flow characteristics (e.g. the s-shaped core engine intake and associated ducting) could allow for minimizing pressure losses while providing a short axial installation space. Apart from the aerodynamic perspective, the FF power plant should in detail be analyzed with regards to the structural integration to the airframe. Aero-structural simulations of the relevant load cases based on advanced numerical methods including the consideration of dynamic loads could increase accuracy and confidence of the weight prediction results, especially when it concerns the FF nacelle structural elements and their attachment to the airframe primary structures. In this respect, topological optimization as well as advanced material options and manufacturing techniques may allow for the reduction of structural weights.

Enhanced variability of the FF propulsion system provided e.g. by means of an adaptive intake may facilitate optimum adaptation of the nacelle geometry to the streamlines entering the engine and hence for minimizing losses. In addition, alternative propulsor architectures such as a FF featuring variable blade pitch may afford improved operational flexibility including potential thrust reversing operation and enhanced robustness against failures. With regards to the performance modeling of the FF propulsion system, future studies may consider sophisticated thrust schedules targeting a flight phase dependent optimization of the power split between the FF and the underwing-podded power plants. Moreover, the transient behavior of the FF power plant should be investigated, especially the implications of the large inertia of the fan during engine acceleration and deceleration maneuvers. This also involves the analysis of the dynamic deformation of the FF nacelle structure and the associated impact on FF aerodynamic and mechanical stability. Follow-on research should also examine the thermal management of the fuselage-buried engine as well as aero-acoustic aspects, vibrations and cabin-induced noise implications. The implemented multi-point sizing approach may be extended by additional facets such as more detailed mapping of turbine cooling air demand taking into account a weighted compilation of relevant mission operating points according to component life targets. The potential of synergistically enhancing the performance of the PFC propulsion system through advanced core engine technologies such as heat exchanging elements, bottoming cycles or cycle-integrated electrification should be examined. In addition, alternative power train concepts such as turbo-electric options may offer benefits with regards to enhanced configurational flexibility and reduced in-flight emissions.

Integrated propulsion and aircraft-level studies should also in-depth investigate the implications of increased commonality in main assemblies and parts including the effects of adopting product family strategies. An analysis of abnormal modes such as FF windmilling or foreign object damage may stipulate requirements for the reliability of critical components and may affect the reserve fuel strategy. The exploration of aircraft-level synergies with other advanced technologies enhancing the benefit of wake filling propulsion integration such as increased laminarity of lifting surfaces may contribute to realizing further fuel efficiency benefits. Beyond the consideration of block fuel, i.e. CO_2 emissions, an enhanced environmental assessment should quantify the emissions associated with additional combustion products such as nitrogen oxides. In addition, the characteristics of the PFC with regards to airframe and propulsion system noise should be analyzed. An evaluation of operating economics should be pursued in order to gauge in what extent supplementary to the derived emission reduction potential cost-related benefits can be expected from the PFC.

Bibliography

[1] N. T. Birch, “2020 Vision: the Prospects for Large Civil Aircraft Propulsion,” in *22nd International Congress of Aeronautical Sciences*, Harrogate, UK, 2000, doi: 10.1017/s0001924000063971.

[2] A. H. Epstein, “Aeropropulsion for Commercial Aviation in the Twenty-First Century and Research Directions Needed,” *AIAA Journal*, vol. 52, no. 5, pp. 901–911, 2014, doi:10.2514/1.j052713.

[3] National Academies of Sciences Engineering and Medicine, *Commercial Aircraft Propulsion and Energy Systems Research*. The National Academies Press, Washington, DC, USA, 2016.

[4] European Commission (EC), “Flightpath 2050: Europe’s Vision for Aviation, Report of the High Level Group on Aviation Research.” Luxembourg, 2011.

[5] Advisory Council for Aviation Research and Innovation in Europe (ACARE), “Realising Europe’s Vision for Aviation: Strategic Research and Innovation Agenda (SRIA), Volume 1.” 2012.

[6] G. J. Follen, R. Del Rosario, R. Wahls, and N. Madavan, “NASA’s Fundamental Aeronautics Subsonic Fixed Wing Project: Generation N+3 Technology Portfolio.” SAE Technical Paper SAE 2011-01-2521, 2011.

[7] International Air Transport Association, *IATA Technology Roadmap*, 4th ed. 2013.

[8] Air Transport Action Group (ATAG), “Flightpath - Which Direction for Market-Based Measures at ICAO’s 38th Assembly?” 38th ICAO Assembly, 2013.

[9] J. Sieber and E. Merkl, “ENOVAL - Low Pressure System Technologies for Ultra High Bypass Ratio Engines,” in *Proceedings of the 23rd International Symposium on Air Breathing Engines*, Manchester, UK, 2017.

[10] A. Bradley, “DREAM - The Alternative Solution for a Cleaner Future,” in *Presentation at the 16th AIAA/CEAS Aeroacoustics Conference*, Stockholm, Sweden, 2010.

[11] G. Wilfert, J. Sieber, A. Rolt, N. Baker, A. Touyeras, and S. Colantuoni, “New Environmental Friendly Aero Engine Core Concepts,” in *Proceedings of the 18th International Symposium on Airbreathing Engines*, Beijing, China, 2007, doi: ISABE-2007-1120.

[12] R. von der Bank, S. Donnerhack, A. Rae, M. Cazalens, A. Lundbladh, and M. Dietz, “LEMCOTEC: Improving the Core-Engine Thermal Efficiency,” in *Proceedings of the International Conference ASME Turbo Expo 2014*, Düsseldorf, Germany, 2014, doi: 10.1115/GT2014-25040.

[13] T. Grönstedt *et al.*, “Ultra Low Emission Technology Innovations for Mid-Century Aircraft Turbine Engines,” in *Proceedings of ASME Turbo Expo 2016*, Seoul, South Korea, 2016, doi: 10.1115/GT2016-56123.

[14] M. Silva, “E-BREAK: Engine Breakthrough Components and Subsystems,” in *Presentation at the 7th European Aeronautics Days*, London, UK, 2015.

[15] M. Hepperle, “Electric Flight – Potential and Limitations,” in *NATO Science and Technology Organization - Energy Efficient Technologies and Concepts of Operation*, Lisbon, Portugal, 2012, doi: 10.14339/STO-MP-AVT-209.

[16] H. Kuhn, A. Seitz, L. Lorenz, A. T. Isikveren, and A. Sizmann, “Progress and Perspectives of Electric Air Transport,” in *28th Congress of the International Council of the Aeronautical Sciences*, Brisbane, Australia, 2012.

[17] L. Lorenz, A. Seitz, H. Kuhn, and A. Sizmann, “Hybrid Power Trains for Future Mobility,” in *Deutscher Luft- und Raumfahrtkongress*, Stuttgart, Germany, 2013.

[18] Clean Sky Joint Undertaking, “Clean Sky at a Glance.” Brussels, Belgium, 2016.

[19] European Commission (EC), “Clean Sky 2: Developing New Generations of Greener Aircraft.” 2014.

[20] M. Hornung, A. T. Isikveren, M. Cole, and A. Sizmann, “Ce-Liner - Case Study for eMobility in Air Transportation,” in *Aviation Technology, Integration and Operations Conference*, Los Angeles, California, USA, 2013, doi: 10.2514/6.2013-4302.

[21] H. D. Kim, “Distributed Propulsion Vehicles,” in *27th International Congress of the Aeronautical Sciences*, Nice, France, 2010.

[22] J. Bijewitz, A. Seitz, and M. Hornung, “A Review of Recent Aircraft Concepts Employing Synergistic Propulsion-Airframe Integration,” in *30th Congress of the International Council of the Aeronautical Sciences*, Daejeon, South Korea, 2016.

[23] J. Bijewitz, A. Seitz, and M. Hornung, “Architectural Comparison of Advanced Ultra-high Bypass Ratio Turbofans for Medium to Long Range Application,” in *Deutscher Luft- und Raumfahrtkongress 2014*, Augsburg, Germany, 2014.

[24] J. Bijewitz, A. Seitz, and M. Hornung, “Power Plant Pre-Design Exploration for a Turbo-Electric Propulsive Fuselage Concept,” in *AIAA Propulsion and Energy Forum*, Cincinnati, Ohio, USA, 2018, doi: 10.2514/6.2018-4402.

[25] J. Bijewitz, A. Seitz, and M. Hornung, “Multi-disciplinary Design Investigation of Propulsive Fuselage Aircraft Concepts,” in *4th EASN Workshop on Flight Physics and Aircraft Design*, Aachen, Germany, 2014.

[26] J. Bijewitz, A. Seitz, A. T. Isikveren, and M. Hornung, “Multi-disciplinary Design Investigation of Propulsive Fuselage Aircraft Concepts,” *Aircraft Engineering and Aerospace Technology*, vol. 88, no. 2, pp. 257–267, 2016, doi:10.1108/AEAT-02-2015-0053.

[27] J. Bijewitz, A. Seitz, A. T. Isikveren, and M. Hornung, “Progress in Optimizing the Propulsive Fuselage Aircraft Concept,” in *AIAA Science and Technology Forum and Exposition*, San Diego, California, USA, doi: 10.2514/6.2016-0767.

[28] J. Bijewitz, A. Seitz, M. Hornung, and A. T. Isikveren, “Progress in Optimizing the Propulsive Fuselage Aircraft Concept,” *Journal of Aircraft*, vol. 54, no. 5, pp. 1979–1989, 2017, doi:10.2514/1.c034002.

[29] J. Bijewitz, A. Seitz, and M. Hornung, “Extended Design Studies for a Mechanically Driven Propulsive Fuselage Aircraft Concept,” in *AIAA Aerospace Sciences Meeting*, Kisseemee, Florida, USA, 2018, doi: 10.2514/6.2018-0408.

[30] V. Rivoire, “Propulsion Integration Challenges - Lecture to DGLR.” Hamburg, Germany, 2007.

[31] T. Pardessus, “Concurrent Engineering Development and Practices for Aircraft Design at Airbus,” in *24th International Congress of the Aeronautical Sciences*, Yokohama, Japan, 2004.

[32] S. Remy, “The Airbus / Engine & Nacelle Manufacturers Relationship: Towards a More Integrated, Environmentally Friendly Engineering Design,” in *24th International Congress of the Aeronautical Sciences*, Yokohama, Japan, 2004.

[33] J. M. Stricker, “The Gas Turbine Engine Conceptual Design Process: An Integrated Approach,” in *Proceedings of the RTO AVT Symposium on “Design Principles and Methods for Aircraft Gas Turbine Engines,”* Toulouse, France, 1998, pp. 11–15.

[34] R. Schaber, “Numerische Auslegung und Simulation von Gasturbinen,” PhD Dissertation, Institut für Luft- und Raumfahrt, Technische Universität München, 2000.

[35] M. H. Sadraey, *Aircraft Design*. Chichester, UK: John Wiley & Sons, 2013.

[36] S. Fricke, V. Ciobaca, A. Kröhnert, J. Wild, and O. Blesbois, “Active Flow Control Applied at the Engine-Wing Junction,” in *5th CEAS Air & Space Conference*, Delft, Netherlands, 2015.

[37] B. K. Kestner, J. S. Schutte, J. C. Gladin, and D. N. Mavris, “Ultra High Bypass Ratio Engine Sizing and Cycle Selection Study for a Subsonic Commercial Aircraft in the N+2 Timeframe,” in *Proceedings of ASME Turbo Expo 2011*, Vancouver, Canada, 2011, doi: 10.1115/GT2011-45370.

[38] R. Becker, M. Schaefer, and S. Reitenbach, “Assessment of the Efficiency Gains Introduced by Novel Aero Engine Concepts,” in *Proceedings of the 21st International Symposium on Air Breathing Engines*, Busan, Korea, 2017.

[39] L. Larsson, R. Avellán, and T. Grönstedt, “Mission Optimization of the Geared Turbofan Engine,” in *Proceedings of the 20th International Symposium on Air Breathing Engines*, Gothenburg, Sweden, 2011, doi: ISABE-2011-1314.

[40] A. Rolt *et al.*, “Scale effects on conventional and intercooled turbofan engine performance,” in *Proceedings of the 23rd International Symposium on Air Breathing Engines*, Manchester, UK, 2017, doi: ISABE 2017-22659.

[41] R. Parker and G. Fedder, “Aircraft Engines: A Proud Heritage and an Exciting Future,” *The Aeronautical Journal*, vol. 120, no. 1223, pp. 131–169, 2016, doi:10.1017/aer.2015.6.

[42] S. M. Jones, W. J. Haller, and M. T. Tong, “An N+3 Technology Level Reference Propulsion System.” NASA Technical Memorandum, NASA TM-2017-219501, Glenn Research Center, Cleveland, Ohio, USA, 2017.

[43] A. Guha, “Optimum Fan Pressure Ratio for Bypass Engines with Separate or Mixed Exhaust Streams,” *Journal of Propulsion and Power*, vol. 17, no. 5, pp. 1117–1122, 2001, doi:10.2514/2.5852.

[44] J. Whurr and P. Beecroft, “Vision 20 - Rolls-Royce’s Long Term Civil Aircraft Propulsion System Concept and Technology Strategy,” in *Proceedings of the 23rd International Symposium on Air Breathing Engines*, Manchester, UK, 2017.

[45] D. Carlson, “GE Aviation: Perspectives on Clean, Efficient Engines.” Presentation, GE Aviation.

[46] W. K. Lord, G. L. Suciu, K. L. Hasel, and J. M. Chandler, “Engine Architecture for High Efficiency at Small Core Size,” in *53rd AIAA Aerospace Sciences Meeting*, Kisseemee, Florida, USA, 2015, doi: 10.1115/1.2015-0071.

[47] A. Turnbull, H. Jouan, P. Giannakakis, and A. T. Isikveren, “Modeling Boundary Layer Ingestion at the Conceptual Level,” in *Proceedings of the 23rd International Symposium on Air Breathing Engines*, 2017, doi: ISABE-2017-22700.

[48] J. Botti, “Airbus Group: A Story of Continuous Innovation,” *The Aeronautical Journal*, vol. 120, no. 1223, pp. 3–12, 2016, doi:10.1017/aer.2015.3.

[49] M. K. Bradley and C. K. Droney, “Subsonic Ultra Green Aircraft Research Phase II: N+4 Advanced Concept Development.” NASA Contractor Report CR-2012-217556, 2012.

[50] S. Bruner *et al.*, “NASA N + 3 Subsonic Fixed Wing Silent Efficient Low-Emissions Commercial Transport (SELECT) Vehicle Study, Revision A.” NASA Contractor Report CR-2010-216798, 2010.

[51] A. T. Wick, J. R. Hooker, C. J. Hardin, and C. H. Zeune, “Integrated Aerodynamic Benefits of Distributed Propulsion,” in *53rd Aerospace Sciences Meeting*, Kisseemee, Florida, USA, 2015, doi: 10.2514/6.2015-1500.

[52] S. Taylor, “Electrical Propulsion for Transport Category Aircraft,” in *Presentation at Aero Engine Round Table Electrification in Propulsion*, 2018.

[53] A. Peters, Z. S. Spakovszky, W. K. Lord, and B. Rose, “Ultrashort Nacelles for Low Fan Pressure Ratio Propulsors,” *Journal of Turbomachinery*, vol. 137, no. 2, 2015, doi:10.1115/1.4028235.

[54] U. Kling *et al.*, “Shape Adaptive Technology for Aircraft Engine Nacelle Inlets,” in *The Royal Aeronautical Society’s 5th Aircraft Structural Design Conference*, Bristol, UK, 2016.

[55] M. K. Bradley and C. K. Droney, “Subsonic Ultra Green Aircraft Research: Phase I Final Report.” Boeing Research & Technology, NASA Contractor Report, NASA CR-2011-216847, Langley Research Center, Hampton, Virginia, USA, 2011.

[56] D. P. Raymer, J. Wilson, H. D. Perkins, A. Rizzi, M. Zhang, and A. R. Puentes, “Advanced Technology Subsonic Transport Study - N+3 Technologies and Design Concepts.” NASA Technical Memorandum, NASA TM-2011-217130, Glenn Research Center, Cleveland, Ohio, USA, 2011.

[57] D. E. Van Zante, “Progress in Open Rotor Research: A U.S. Perspective,” in *Proceedings of ASME Turbo Expo 2015*, Montréal, Quebec, Canada, 2015, doi: GT2015-42203.

[58] J.-F. Brouckaert, “Engine Demonstration Programmes in Clean Sky & Clean Sky 2,” in *Proceedings of the 7th European Aeronautics Days 2015*, London, UK, 2015.

[59] D. J. Campbell, “Revolutionary Propulsion and Power for 21st Century Aviation,” in *AIAA/ICAS International Air and Space Symposium and Exposition*, 2003, no. AIAA 2003-2561.

[60] A. K. Sehra and W. Whitlow, “Propulsion and Power for 21st Century Aviation,” *Progress in Aerospace Sciences*, vol. 40, no. 4–5, pp. 199–235, 2004, doi:10.1016/j.paerosci.2004.06.003.

[61] A. Lundbladh and T. Grönstedt, “Distributed Propulsion and Turbofan Scale Effects,” in *Proceedings of the 17th International Symposium on Air Breathing Engines*, Munich, Germany, 2005.

[62] A. S. Gohardani, G. Doulgeris, and R. Singh, “Challenges of Future Aircraft Propulsion: A Review of Distributed Propulsion Technology and its Potential Application for the All Electric Commercial Aircraft,” *Progress in Aerospace Sciences*, vol. 47, no. 5, pp. 369–391, 2011, doi:10.1016/j.paerosci.2010.09.001.

[63] G. Ameyugo, M. Taylor, and R. Singh, “Distributed Propulsion Feasibility Studies,” in *25th International Congress of the Aeronautical Sciences*, Hamburg, Germany, 2006.

[64] A. H. Epstein, “Distributed Propulsion: New Opportunities for an Old Concept.” Final Technical Report on DARPA Contract #HR0011-07-C-0005, Massachusetts Institute of Technology, Cambridge, Massachussetts, USA, 2007.

[65] E. de la Rosa Blanco, C. A. Hall, and D. Crichton, “Challenges in the Silent Aircraft Engine Design,” in *45th AIAA Aerospace Sciences Meeting and Exhibit*, Reno, Nevada, USA, 2007, no. Special Session-Towards a Silent Aircraft, doi: AIAA-2007-454.

[66] B. R. J. Winborn, “ADAM III V/STOL Concept,” *Journal of Aircraft*, vol. 7, no. 2, pp. 175–181, 1970, doi:10.2514/3.44143.

[67] J. L. Felder, H. D. Kim, and G. V Brown, “Turboelectric Distributed Propulsion Engine Cycle Analysis for Hybrid-Wing-Body Aircraft,” in *47th AIAA Aerospace Sciences Meeting Including The New Horizons Forum and Aerospace Exposition*, Orlando, Florida, USA, 2009, doi: AIAA 2009-1132.

[68] A. Gibson *et al.*, “The Potential and Challenge of TurboElectric Propulsion for Subsonic Transport Aircraft,” in *48th AIAA Aerospace Sciences Meeting Including the New Horizons Forum and Aerospace Exposition*, 2010, doi: 10.2514/6.2010-276.

[69] J. D. Kummer and T. Q. Dang, “High-Lift Propulsive Airfoil with Integrated Crossflow Fan,” *Journal of Aircraft*, vol. 43, no. 4, pp. 1059–1068, 2006, doi:10.2514/1.17610.

[70] T. Q. Dang and P. R. Bushnell, “Aerodynamics of Cross-flow Fans and their Application to Aircraft Propulsion and Flow Control,” *Progress in Aerospace Sciences*, vol. 45, no. 1–3, pp. 1–29, 2009, doi:10.1016/j.paerosci.2008.10.002.

[71] G. F. Wislicenus, “Hydrodynamics and Propulsion of Submerged Bodies,” *ARS Journal*, vol. 30, no. 12, pp. 1140–1148, Dec. 1960, doi:10.2514/8.5351.

[72] W. S. Gearhart and R. E. Henderson, “Selection of a Propulsor for a Submersible System,” *Journal of Aircraft*, vol. 3, no. 1, pp. 84–90, 2008, doi:10.2514/3.59270.

[73] S. Thurston and M. Evenbar, “Efficiency of a Propulsor on a Body of Revolution - Inducting Boundary-Layer Fluid,” *Journal of Aircraft*, vol. 3, no. 3, pp. 270–277, 1966, doi:10.2514/3.43737.

[74] T. T. Huang, H. T. Wang, N. Santelli, and N. C. Groves, “Propeller/Stern/Boundary-Layer Interaction on Axisymmetric Bodies: Theory and Experiment.” Report Number DTNSRDC-76-0113, David W. Taylor Naval Ship R&D Center, Bethesda, Maryland, USA, 1976.

[75] M. Drela, “Power Balance in Aerodynamic Flows,” *AIAA Journal*, vol. 47, no. 7, pp. 1761–1771, 2009.

[76] J. I. Hileman, Z. S. Spakovszky, M. Drela, M. A. Sargeant, and A. Jones, “Airframe Design for Silent

Fuel-Efficient Aircraft," *Journal of Aircraft*, vol. 47, no. 3, pp. 956–969, 2010, doi:10.2514/1.46545.

[77] C. Mehalic, "Effect of Spatial Inlet Temperature and Pressure Distortion on Turbofan Engine Stability." NASA Technical Memorandum, NASA TM 100850, Lewis Research Center, Cleveland, Ohio, USA, 1988.

[78] M. Bakhle, T. S. R. Reddy, G. Herrick, A. Shabbir, and R. V. Florea, "Aeromechanics Analysis of a Boundary Layer Ingesting Fan." NASA Technical Memorandum, NASA TM-2013-217730, Glenn Research Center, Cleveland, Ohio, USA, 2013.

[79] S. Gorton, L. Owens, L. Jenkins, B. G. Allan, and E. Schuster, "Active Flow Control on a Boundary-Layer-Ingesting Inlet," in *42nd AIAA Aerospace Sciences Meeting and Exhibit*, Reno, Nevada, USA, 2004, doi: 10.2514/6.2004-1203.

[80] L. R. Owens, B. G. Allan, and S. A. Gorton, "Boundary-Layer-Ingesting Inlet Flow Control," *Journal of Aircraft*, vol. 45, no. 4, pp. 1431–1440, 2008, doi:10.2514/1.36989.

[81] R. T. Kawai, D. M. Friedman, and L. Serrano, "Blended Wing Body (BWB) Boundary Layer Ingestion (BLI) inlet configuration and system studies." Boeing Phantom Works, NASA Contractor Report NASA CR-2006-214534, Langley Research Center, Hampton, Virginia, USA, 2006.

[82] D. K. Hall, "Analysis of Civil Aircraft Propulsors with Boundary Layer Ingestion," PhD Thesis, Department of Aeronautics and Astronautics, Massachussetts Institute of Technology, 2015.

[83] D. L. Rodriguez, "A Multidisciplinary Optimization Method for Designing Boundary Layer Ingesting Inlets." PhD Dissertation, Massachussetts Institute of Technology, USA, 2001.

[84] E. M. Greitzer *et al.*, "N+3 Aircraft Concept Designs and Trade Studies, Final Report, Vol. 2." NASA Contractor Report CR-2010-216794/VOL2, Glenn Research Center, Cleveland, Ohio, USA, 2010.

[85] F. Heppner, "The General Theory of Boundary Layer Propulsion." T.B. Report No. 18, Armstrong Siddeley Motors Limited, 1944.

[86] A. M. O. Smith and H. E. Roberts, "The Jet Airplane Utilizing Boundary Layer Air for Propulsion," *Journal of the Aeronautical Sciences*, pp. 97–109, 1947.

[87] F. T. Lynch, "A Theoretical Investigation of the Effect of Ingesting Airframe Boundary Layer Air on Turbofan Engine Fuel Consumption." Technical Report SM-23961, Douglas Aircraft Company, 1960.

[88] E. van Dam, "Inlet Distortion Characterization of the Boundary Layer Ingesting D8 Aircraft," Master of Science Thesis, Faculty of Aerospace Engineering, Delft University of Engineering, 2015.

[89] D. Küchemann and J. Weber, *Aerodynamics of Propulsion*. New York, New York, USA: McGraw-Hill Publishing Company Ltd., 1953.

[90] A. Betz, *Introduction to the Theory of Flow Machines*. New York, New York, USA: Pergamon Press, 1966.

[91] W. M. Douglass, "Propulsive Efficiency with Boundary Layer Ingestion." Technical Report MDC J0860, Douglas Aircraft Company, 1970.

[92] F. R. Goldschmied, "Proposal for the Study of Application of Boundary-Layer Control to Lighter-than-Air Craft." Goodyear Aircraft Report GER-5796, 1954.

[93] P. Cerreta, "Wind-tunnel Investigation of the Drag of a Proposed Boundary-Layer-Controlled Airship." David W. Taylor Model Basin Aerodynamics Laboratory, Report 914, Washington, D.C., USA, 1957.

[94] F. R. Goldschmied, "Integrated Hull Design, Boundary-Layer Control, and Propulsion of Submerged Bodies," *Journal of Hydronautics*, vol. 1, no. 1, pp. 2–11, 1967, doi:10.2514/3.62746.

[95] F. R. Goldschmied, "Fuselage Self-Propulsion by Static-Presssure Thrust: Wind-Tunnel Verification," in *AIAA/AHS/ASEE Aircraft Design Systems and Operations Meeting1*, St. Louis, Missouri, USA, 1987, doi: 10.2514/6.1987-2935.

[96] P. N. Peraudo, J. A. Schetz, and C. J. Roy, "Computational Study of the Embedded Engine Static

Pressure Thrust Propulsion System," *Journal of Aircraft*, vol. 49, no. 6, pp. 2033–2045, Nov. 2012, doi:10.2514/1.C031840.

[97] C. A. Seubert, "Analysis of a Goldschmied Propulsor Using Computational Fluid Dynamics Referencing California Polytechnic's Goldschmied Propulsor Testing," Master Thesis, California Polytechnic State University, 2012.

[98] J. Roepke, "An Experimental Investigation of a Goldschmied Propulsor," Master Thesis, California Polytechnic State University, 2012.

[99] L. H. Smith, "Wake Ingestion Propulsion Benefit," *Journal of Propulsion and Power*, vol. 9, no. 1, pp. 74–82, 1993, doi:10.2514/3.11487.

[100] O. Atinault, G. Carrier, R. Grenon, and C. Verbecke, "Numerical and Experimental Aerodynamic Investigations of Boundary Layer Ingestion for Improving Propulsion Efficiency of Future Air Transport," in *31st AIAA Applied Aerodynamics Conference, Fluid Dynamics and Co-located Conferences*, San Diego, California, USA, 2013, doi: 10.2514/6.2013-2406.

[101] O. Atinault, G. Carrier, J.-L. Godard, C. Verbeke, and P. Viscat, "Numerical and Experimental Investigations of the Boundary Layer Ingesting (BLI) and Distributed Propulsion Concepts," in *CEAS-SCAD Conference 2014*, Toulouse, France, 2014.

[102] P. Lv, D. Ragni, L. Veldhuis, A. G. Rao, and T. Hartuc, "Experimental Investigation of the Flow Mechanisms Associated with a Wake-Ingesting Propulsor," *AIAA Journal*, vol. 55, no. 4, pp. 1332–1342, 2017, doi:10.2514/1.j055292.

[103] S. F. Yaros *et al.*, "Synergistic Airframe Propulsion Interactions and Integrations - A White Paper Prepared by the 1996-1997 Langley Aeronautics Technical Committee." NASA Technical Memorandum, NASA TM-1998-207644, Langley Research Center, Hampton, Virginia, USA, 1998.

[104] E. M. Greitzer *et al.*, "N+ 3 Aircraft Concept Designs and Trade Studies, Final Report, Vol. 1." NASA Contractor Report CR-2010-216794/VOL1, Glenn Research Center, Cleveland, Ohio, USA, 2010.

[105] A. Uranga *et al.*, "Preliminary Experimental Assessment of the Boundary Layer Ingestion Benefit for the D8 Aircraft," in *52nd Aerospace Sciences Meeting*, 2014, doi: 10.2514/6.2014-0906.

[106] S. A. Pandya, "External Aerodynamics Simulations for the MIT D8 'Double-Bubble' Aircraft Design," in *Seventh International Conference on Computational Fluid Dynamics (ICCFD7)*, Big Island, Hawaii, USA, 2012.

[107] A. Uranga *et al.*, "Boundary Layer Ingestion Benefit of the D8 Transport Aircraft," *AIAA Journal*, vol. 55, no. 11, pp. 3693–3708, 2017, doi:10.2514/1.j055755.

[108] B. M. Yutko *et al.*, "Conceptual Design of a D8 Commercial Aircraft," in *17th AIAA Aviation Technology, Integration, and Operations Conference*, Denver, Colorado, USA, 2017, doi: 10.2514/6.2017-3590.

[109] L. Wiart, O. Atinault, J.-C. Boniface, and R. Barrier, "Aeropropulsive Performance Analysis of the NOVA Configurations," in *30th Congress of the International Council of the Aeronautical Sciences, ICAS 2016*, Daejeon, South Korea, 2016.

[110] L. Wiart and C. Negulescu, "Exploration of the Airbus 'Nautilius' Engine Integration Concept," in *31st Congress of the International Council of the Aeronautical Sciences*, Belo Horizonte, Brazil, 2018.

[111] Airbus Group, "E-Thrust - Electrical Distributed Propulsion System Concept for Lower Fuel Consumption, Fewer Emissions and Less Noise." Advertising brochure, 2012.

[112] P. Marks, "All-electric Plane Heralds Future of Green Aviation," *New Scientist*, vol. 222, no. 2967, p. 20.

[113] H.-J. Steiner, A. Seitz, K. Wieczorek, K. Plotner, A. T. Isikveren, and M. Hornung, "Multi-disciplinary Design and Feasibility Study of Distributed Propulsion Systems," in *28th Congress of the International Council of the Aeronautical Sciences*, Brisbane, Australia, 2012.

[114] A. T. Isikveren *et al.*, "Distributed Propulsion and Ultra-high By-pass Rotor Study at Aircraft Level,"

The Aeronautical Journal, vol. 119, no. 1221, pp. 1327–1376, 2015.

[115] S. Kaiser, R. Grenon, J. Bijewitz, A. Prendinger, A. T. Isikveren, and M. Hornung, "Quasi-Analytical Aerodynamic Methods for Propulsive Fuselage Concepts," in *29th Congress of the International Council of the Aeronautical Sciences*, St. Petersburg, Russia, 2014.

[116] B. Blumenthal, A. A. Elmiligui, K. Geiselhart, R. L. Campbell, M. D. Maughmer, and S. Schmitz, "Computational Investigation of a Boundary Layer Ingestion Propulsion System for the Common Research Model," in *46th AIAA Fluid Dynamics Conference*, Washington, D.C., USA, 2016, doi: 10.2514/6.2016-3812.

[117] K. R. Antcliff and F. M. Capristan, "Conceptual Design of the Parallel Electric-Gas Architecture with Synergistic Utilization Scheme (PEGASUS) Concept," in *AIAA AVIATION Forum*, Denver, Colorado, USA, 2017, doi: 10.2514/6.2017-4001.

[118] A. Seitz, J. Bijewitz, S. Kaiser, and G. Wortmann, "Conceptual Investigation of a Propulsive Fuselage Aircraft Layout," *Aircraft Engineering and Aerospace Technology*, vol. 86, no. 6, pp. 464–472, 2014, doi:10.1108/AEAT-06-2014-0079.

[119] S. Stückl, J. van Toor, and H. Lobentanzer, "VOLTAIR - The All Electric Propulsion Concept Platform – A Vision For Atmospheric Friendly Flight," in *28th Congress of the International Council of the Aeronautical Sciences*, Brisbane, Australia, 2012.

[120] A. Seitz, "Power Train Options for a Propulsive Fuselage Aircraft Layout," in *More Electric Aircraft USA Conference*, Seattle, Washington, USA, 2016.

[121] J. Welstead and J. L. Felder, "Conceptual Design of a Single-Aisle Turboelectric Commercial Transport with Fuselage Boundary Layer Ingestion," in *54th AIAA Aerospace Sciences Meeting*, San Diego, California, USA, 2016, doi: 10.2514/6.2016-1027.

[122] H. Witte, "Ist die Zukunft des Fliegens elektrisch? Perspektiven und Herausforderungen für eine nachhaltige Luftfahrt." Technisches Seminar Zeuthen.Desy, June 2018, 2018.

[123] A. Seitz *et al.*, "Concept Validation Study for Fuselage Wake-Filling Propulsion Integration," in *31st Congress of the International Council of the Aeronautical Sciences*, Belo Horizonte, Brazil, 2018.

[124] A. Seitz and C. Gologan, "Parametric Design Studies for Propulsive Fuselage Aircraft Concepts," *CEAS Aeronautical Journal*, vol. 6, no. 1, pp. 69–82, 2015, doi:10.1007/s13272-014-0130-3.

[125] J. Welstead *et al.*, "Overview of the NASA STARC-ABL (Rev. B) Advanced Concept," *Boeing NASA Electric Aircraft Workshop, May 30, 2018*. 2018.

[126] A. Bolonkin, "A High Efficiency Fuselage Propeller ('Fusefan') for Subsonic Aircraft," in *Proceedings of the 1999 World Aviation Conference*, San Francisco, California, USA, 1999.

[127] M. C. Schwarze and T. Zold, "Superefficient Quiet Short Range Aircraft," in *Deutscher Luft- und Raumfahrtkongress 2014*, Augsburg, Germany.

[128] C. Combs, "AMPAIRE - High Performance, Zero-Emission Aircraft." Company presentation, 2018.

[129] J. L. Felder, G. V Brown, H. D. Kim, and J. Chu, "Turboelectric Distributed Propulsion in a Hybrid Wing Body Aircraft," in *Proceedings of the 20th International Symposium on Air Breathing Engines*, Gothenburg, Sweden, 2011, doi: ISABE-2011-1340.

[130] Y. Liu, A. Elham, P. Horst, and M. Hepperle, "Exploring Vehicle Level Benefits of Revolutionary Technology Progress via Aircraft Design and Optimization," *Energies*, vol. 11, no. 166, pp. 1–22, 2018, doi:10.3390/en11010166.

[131] A. Harish, J. Gladin, and D. N. Mavris, "Architecture Evaluation of a Single-aisle Turboelectric Aircraft with Single Engine-out Constraint," in *2018 Aviation Technology, Integration, and Operations Conference*, Atlanta, Georgia, USA, 2018, doi: 10.2514/6.2018-3838.

[132] J. Sands, J. Gladin, B. Kestner, and D. Mavris, "Hybrid Wing Body Engine Cycle Design Exploration for Boundary Layer Ingesting (BLI) Propulsion Systems Under Design Uncertainty," in *48th AIAA/ASME/SAE/ASEE Joint Propulsion Conference & Exhibit*, Atlanta, Georgia, USA, 2012, doi:

10.2514/6.2012-3918.

[133] E. A. Valencia, D. Nalianda, P. Laskaridis, and R. Singh, “Methodology to Assess the Performance of an Aircraft Concept with Distributed Propulsion and Boundary Layer Ingestion Using a Parametric Approach,” *Proceedings of the Institution of Mechanical Engineers, Part G: Journal of Aerospace Engineering*, vol. 229, no. 4, pp. 682–693, 2015, doi:10.1177/0954410014539291.

[134] A. Rolt and J. Whurr, “Optimizing Propulsive Efficiency in Aircraft with Boundary Layer Ingesting Distributed Propulsion,” in *Proceedings of the 22nd International Symposium on Air Breathing Engines*, Phoenix, Arizona, USA, 2015, doi: ISABE-2015-20201.

[135] C. Goldberg, D. Nalianda, P. Pilidis, and R. Singh, “Performance Assessment of a Boundary Layer Ingesting Distributed Propulsion System at Off-Design,” in *53rd AIAA/SAE/ASEE Joint Propulsion Conference*, Atlanta, Georgia, USA, 2017, doi: 10.2514/6.2017-5055.

[136] P. F. Pelz, F.-J. Cloos, and J. Sieber, “Analytic Assessment of an Embedded Aircraft Propulsion,” in *Proceedings of ASME Turbo Expo 2016*, Seoul, South Korea, 2016, pp. 1–8, doi: 10.1115/GT2016-57524.

[137] C. Goldberg, D. Nalianda, D. MacManus, and P. Pilidis, “Installed Performance Assessment of a Boundary Layer Ingesting Distributed Propulsion System at Design Point,” in *2nd AIAA/SAE/ASEE Joint Propulsion Conference*, Salt Lake City, Utah, USA, 2016.

[138] C. Goldberg, D. Nalianda, P. Laskaridis, and P. Pilidis, “Installed Performance Assessment of an Array of Distributed Propulsors Ingesting Boundary Layer Flow,” *Journal of Engineering for Gas Turbines and Power*, vol. 140, no. 7, 2017, doi:10.1115/1.4038837.

[139] N. Budziszewski and J. Friedrichs, “Modelling of a Boundary Layer Ingesting Propulsor,” *Energies*, vol. 11, no. 708, pp. 1–15, 2018, doi:10.3390/en11040708.

[140] J. S. Gray, C. A. Mader, G. K. Kenway, and J. R. R. A. Martins, “Approach to Modeling Boundary Layer Ingestion using a Fully Coupled Propulsion-RANS Model,” in *58th AIAA/ASCE/AHS/ASC Structures, Structural Dynamics, and Materials Conference*, Grapevine, Texas, USA, 2017, doi: 10.2514/6.2017-1753.

[141] J. S. Gray and J. R. R. A. Martins, “Coupled Aeropropulsive Design Optimisation of a Boundary-Layer Ingestion Propulsor,” *The Aeronautical Journal*, vol. 123, no. 1259, pp. 121–137, 2018, doi:10.1017/aer.2018.120.

[142] J. S. Gray, G. K. Kenway, C. A. Mader, and J. Martins, “Aero-propulsive Design Optimization of a Turboelectric Boundary Layer Ingestion Propulsion System,” in *2018 Aviation Technology, Integration, and Operations Conference*, Atlanta, Georgia, USA, 2018, doi: 10.2514/6.2018-3976.

[143] M. Elsalamony and L. Teperin, “2D Numerical Investigation of Boundary Layer Ingestion Propulsor on Airfoil,” in *7th European Conference for Aeronautics and Aerospace Sciences (EUCASS)*, Milan, Italy, 2017, doi: 10.13009/EUCASS2017-67.

[144] H. Kim, J. Berton, and S. Jones, “Low Noise Cruise Efficient Short Take-Off and Landing Transport Vehicle Study.” NASA Technical Memorandum, NASA TM 2007-214659, Glenn Research Center, Cleveland, Ohio, USA, 2007.

[145] H. Kim and M.-S. Liou, “Flow Simulation of N3-X Hybrid Wing-Body Configuration,” in *51st AIAA Aerospace Sciences Meeting including the New Horizons Forum and Aerospace Exposition*, Grapevine, Texas, USA, 2013.

[146] A. Arntz, O. Atinault, and A. Merlen, “Exergy-Based Formulation for Aircraft Aeropropulsive Performance Assessment: Theoretical Development,” *AIAA Journal*, vol. 53, no. 6, pp. 1627–1639, 2014, doi:10.2514/1.j053467.

[147] P. Lv, A. G. Rao, D. Ragni, and L. Veldhuis, “Performance Analysis of Wake and Boundary-Layer Ingestion for Aircraft Design,” *Journal of Aircraft*, vol. 53, no. 5, pp. 1517–1526, 2016, doi:10.2514/1.c033395.

[148] G. V. Mikic, A. M. Stoll, J. Bevirt, R. Grah, and M. D. Moore, “Fuselage Boundary Layer Ingestion Propulsion Applied to a Thin Haul Commuter Aircraft for Optimal Efficiency,” in *16th AIAA Aviation*

Technology, Integration, and Operations Conference, Washington, D.C., USA, 2016, doi: 10.2514/6.2016-3764.

[149] S. S. Ochs, G. Tillman, J. Joo, and D. M. Voytovych, "Computational Fluid Dynamics-Based Analysis of Boundary Layer Ingesting Propulsion," *Journal of Propulsion and Power*, vol. 33, no. 2, pp. 522–530, 2016, doi:10.2514/1.b36069.

[150] A. Lundbladh, H. Mårtensson, and A. Petrusson, "Installation Effects for Ultra-high Bypass Engines," in *Proceedings of the 23rd International Symposium on Air Breathing Engines*, Manchester, UK, 2017, doi: ISABE-2017-22592.

[151] A. Plas, "Performance of a Boundary Layer Ingesting Propulsion System," Master Thesis, Massachussetts Institute of Technology, 2006.

[152] J.-L. Godard, "Semi-Buried Engine Installation : The Nacre Project Experience," in *27th International Congress of the Aeronautical Sciences*, Nice, France, 2010.

[153] T. Marien, J. R. Welstead, and S. M. Jones, "Vehicle Level System Impact of Boundary Layer Ingestion for the NASA D8 Concept Aircraft," in *2018 AIAA Aerospace Sciences Meeting*, Kisseemee, Florida, USA, 2018, doi: 10.2514/6.2018-0271.

[154] D. K. Hall, A. C. Huang, A. Uranga, E. M. Greitzer, M. Drela, and S. Sato, "Boundary Layer Ingestion Propulsion Benefit for Transport Aircraft," *Journal of Propulsion and Power*, vol. 33, no. 5, pp. 1118–1129, 2017, doi:10.2514/1.b36321.

[155] D. K. Hall, A. P. Dowdle, J. Gonzalez, Jonas, L. Trollinger, and W. Thalheimer, "Assessment of a Boundary Layer Ingesting Turboelectric Aircraft Configuration using Signomial Programming," in *2018 Aviation Technology, Integration, and Operations Conference*, Atlanta, Georgia, USA, 2018, doi: 10.2514/6.2018-3973.

[156] R. V. Florea *et al.*, "Aerodynamic Analysis of a Boundary-Layer-Ingesting Distortion-Tolerant Fan," in *ASME Turbo Expo 2013*, San Antonio, Texas, USA, 2013, doi: 10.1115/GT2013-94656.

[157] D. K. Hall, E. M. Greitzer, and C. S. Tan, "Analysis of Fan Stage Conceptual Design Attributes for Boundary Layer Ingestion," *Journal of Turbomachinery*, vol. 139, no. 7, 2017, doi:10.1115/1.4035631.

[158] S. Sato, "The Power Balance Method For Aerodynamic Performance Assessment," PhD Thesis, Department of Aeronautics and Astronautics, Massachussetts Institute of Technology, 2012.

[159] J. C. Gladin, "A Sizing and Vehicle Matching Methodology for Boundary Layer Ingesting Propulsion Systems," PhD Dissertation, Daniel Guggenheim School of Aerospace Engineering, Georgia Institute of Technology, 2015.

[160] J. D. Anderson, *Fundamentals of Aerodynamics*, 5th ed. New York, New York, USA: McGraw-Hill.

[161] A. L. Habermann, J. Bijewitz, A. Seitz, and M. Hornung, "Performance Bookkeeping for Aircraft Configurations with Fuselage Wake-Filling Propulsion Integration," in *Deutscher Luft- und Raumfahrtkongress 2018*, Friedrichshafen, Germany, 2018.

[162] L. Hardin, O. Sharma, J. Berton, D. Arend, and G. Tillman, "Aircraft System Study of Boundary Layer Ingesting Propulsion," in *Proceedings of the 48th AIAA/ASME/SAE/ASEE Joint Propulsion Conference & Exhibit*, Atlanta, Georgia, USA, 2012, doi: 10.2514/6.2012-3993.

[163] H. Kim and J. Felder, "Control Volume Analysis of Boundary Layer Ingesting Propulsion Systems With or Without Shock Wave Ahead of the Inlet," in *49th AIAA Aerospace Sciences Meeting including the New Horizons Forum and Aerospace Exposition*, Orlando, Florida, USA, 2011, doi: 10.2514/6.2011-222.

[164] E. S. Hendricks, "A Review of Boundary Layer Ingestion Modeling Approaches for Use in Conceptual Design." NASA Technical Memorandum, NASA TM-2018-219926, Glenn Research Center, Cleveland, Ohio, USA, 2018.

[165] P. Laskaridis, "Application of Distributed Propulsion Concept on Different Aircraft Configurations," in *Proceedings of the 22nd International Symposium on Air Breathing Engines*, Busan, Korea, 2015.

[166] P. Lv and A. G. Rao, “Conceptual Analysis of Boundary Layer Ingestion towards Aircraft Propulsion Integration,” in *Proceedings of the 21st International Symposium on Air Breathing Engines*, Busan, Korea, 2013.

[167] J. Reneaux, V. Brunet, S. Esquieu, M. Meunier, and S. Mouton, “Recent Achievements in Numerical Simulation for Aircraft Power-Plant Configurations,” *The Aeronautical Journal*, vol. 117, no. 1188, pp. 213–231, 2013, doi:10.1017/s0001924000007958.

[168] MIDAP Study Group, “Guide to In-Flight Thrust Measurement of Turbojets and Fan Engines.” NATO AGARDograph No. 237, 1979.

[169] A. Seitz, O. Schmitz, A. T. Isikveren, and M. Hornung, “Electrically Powered Propulsion: Comparison and Contrast To Gas Turbines,” in *Deutscher Luft- und Raumfahrtkongress 2012*, Berlin, Germany, 2012.

[170] J. Kurzke and I. Halliwell, *Propulsion and Power - An Exploration of Gas Turbine Performance Modeling*. Cham, Switzerland: Springer-Verlag, 2018.

[171] E. Torenbeek, *Advanced Aircraft Design*. Chichester, UK: John Wiley & Sons, 2013.

[172] E. Truckenbrodt, *Fluidmechanik, Band 2: Elementare Strömungsvorgänge dichteveränderlicher Fluide sowie Potential- und Grenzschichtströmungen*. Berlin Heidelberg: Springer-Verlag, 1992.

[173] R. Liebeck, M. Page, and B. Rawdon, “Blended-Wing-Body Subsonic Commercial Transport,” in *36th AIAA Aerospace Sciences Meeting and Exhibit*, Reno, Nevada, USA, 1998, doi: 10.2514/6.1998-438.

[174] L. Cambier, S. Heib, and S. Plot, “The Onera elsA CFD Software: Input from Research and Feedback from Industry,” *Mechanics & Industry*, vol. 14, no. 3, pp. 159–174, 2013, doi:10.1051/meca/2013056.

[175] H. Grieb, *Projektierung von Turboflugtriebwerken*. Basel Boston Berlin: Birkhäuser Verlag, 2004.

[176] H. Grieb, *Verdichter für Turbo-Flugtriebwerke*. Berlin Heidelberg: Springer-Verlag, 2009.

[177] H. Rick, *Gasturbinen und Flugantriebe*. Berlin Heidelberg: Springer-Verlag, 2013.

[178] J. Seddon and E. Goldsmith, *Intake Aerodynamics*, 2nd ed. Reston, Virginia, USA: AIAA Education Series, 1999.

[179] W. Chen, A. Sahai, A. Messac, and G. J. Sundararaj, “Exploration of the Effectiveness of Physical Programming in Robust Design,” *ASME Journal of Mechanical Design*, vol. 122, no. 2, pp. 155–163, 2000, doi:10.1115/1.533565.

[180] S. Farokhi, *Aircraft Propulsion*. Chichester, UK: John Wiley & Sons, 2014.

[181] D. P. Raymer, *Aircraft Design: A Conceptual Approach*, 2nd ed. Washington, D.C., USA: AIAA Education Series, 1992.

[182] A. Seitz, “Advanced Methods for Propulsion System Integration in Aircraft Conceptual Design,” PhD Dissertation, Institut für Luft- und Raumfahrt, Technische Universität München, 2012.

[183] J. Roskam, *Airplane Design, Parts I-VII*. Ottawa, Kansas, USA: Roskam Aviation and Engineering Corporation.

[184] The Mathworks Inc., “MATLAB, Version 8.2 (R2013b).” 2013.

[185] P. S. Granville, “The Calculation of the Viscous Drag of Bodies of Revolution.” Navy Department, The David W. Taylor Model Basin, Report 849, Washington, D.C., USA, 1953.

[186] A. Petrusson, “Aerodynamic Evaluation of Nacelles for Engines with Ultra High Bypass Ratio,” Master Thesis, Chalmers University of Technology, Gothenburg, Sweden, 2017.

[187] Airbus, “A330-300 - Powering into the Future,” 2019. [Online]. Available: https://www.airbus.com/aircraft/passenger-aircraft/a330-family/a330-300.html. [Accessed: 01-Mar-2019].

[188] O. Schmitz, “Methodical Assessment of Electric Propulsion Systems for Transport Category Aircraft,”

PhD Dissertation, Institut für Luft- und Raumfahrt, Technische Universität München, 2016.

[189] O. Schmitz and M. Hornung, “Methods for Simulation and Analysis of Hybrid Electric Propulsion Systems,” *CEAS Aeronautical Journal*, vol. 6, no. 2, pp. 245–256, 2015, doi:10.1007/s13272-014-0137-9.

[190] S. Kaiser, A. Seitz, S. Donnerhack, and A. Lundbladh, “Composite Cycle Engine Concept with Hectopressure Ratio,” *Journal of Propulsion and Power*, vol. 32, no. 6, pp. 1413–1421, 2016, doi:10.2514/1.b35976.

[191] J. Kurzke, “GasTurb 11 - Design and Off-Design Performance of Gas Turbines.” 2007.

[192] S. Gordon and B. J. McBride, “Computer Program for Calculation of Complex Chemical Equilibrium Compositions and Applications, I. Analysis.” NASA Reference Publication NASA RP-1311, 1994.

[193] B. J. McBride and S. Gordon, “Computer Program for Calculation of Complex Chemical Equilibrium Compositions and Applications, II. Users Manual and Program Description.” NASA Reference Publication NASA RP-1311, 1996.

[194] J. Kurzke, “GasTurb Details 5 - An Utility for GasTurb 11.” 2007.

[195] H. G. Münzberg and J. Kurzke, *Gasturbinen - Betriebsverhalten und Optimierung*. Berlin Heidelberg New-York: Springer-Verlag, 1977.

[196] P. P. Walsh and P. Fletcher, *Gas Turbine Performance*, 2nd ed. Oxford, UK: Blackwell Science Ltd, 2004.

[197] J. Sieber, “European Technology Programs for Eco-Efficient Ducted Turbofans,” in *Proceedings of the 22nd International Symposium on Air Breathing Engines*, Phoenix, Arizona, USA, 2015.

[198] S. Weber and H.-P. Hackenberg, “GP7000: MTU Aero Engines’ Contribution in a Successful Partnership,” in *Proceedings of the 18th International Symposium on Airbreathing Engines*, Beijing, China, 2007, doi: ISABE-2007-1283.

[199] GE Aviation, “GE Begins GE9X Certification Testing,” 2017. [Online]. Available: https://www.geaviation.com/press-release/ge9x-engine-family/ge-begins-ge9x-certification-testing. [Accessed: 18-May-2017].

[200] CFM, “LEAP - The Power of the Future.” Advertising brochure, 2015.

[201] J. Bosson, “Key Enablers for Power Optimized Aircraft,” in *27th International Congress of the Aeronautical Sciences*, Nice, France, 2010, pp. 1–6.

[202] N. Morioka, M. Takeuchi, and H. Oyori, “Moving to an All-Electric Aircraft System,” *IHI Engineering Review*, vol. 4, no. 1, pp. 33–39, 2014.

[203] P. Thalin, “Overview of Challenges in Active Power Conversion for the More Electric Aircraft,” in *Presentation at the Electrical Technologies for the Aviation of the Future, Europe-Japan Symposium*, Tokyo, Japan, 2015.

[204] D. E. Gray, “Energy Efficient Engine - Preliminary Design and Integration Studies.” United Technologies Corporation, NASA Contractor Report, NASA CR-135396, Lewis Research Center, Cleveland, Ohio, USA, 1978.

[205] A. J. B. Jackson, “Optimisation of Aero and Industrial Gas Turbine Design for the Environment,” PhD Thesis, School of Engineering, Cranfield University, 2009.

[206] N. Gasparovic, “Das Zweistromtriebwerk bei optimaler und nicht-optimaler Auslegung,” *Forsch. Ing.-Wes.*, vol. 42, no. 5, pp. 157–168, 1976.

[207] J. D. Mattingly, W. H. Heiser, and D. T. Pratt, *Aircraft Engine Design*, 2nd ed. Reston, Virginia, USA: AIAA Education Series, 2002.

[208] A. Linke-Diesinger, *Systeme von Turbofan-Triebwerken*. Berlin Heidelberg: Springer-Verlag, 2014.

[209] W. J. G. Bräunling, *Flugzeugtriebwerke*, 4th ed. Berlin Heidelberg: Springer-Verlag, 2015.

[210] N. A. Cumpsty, *Jet Propulsion - A Simple Guide to the Aerodynamic and Thermodynamic Design and Performance of Jet Engines*, 7th ed. Cambridge, UK: Cambridge University Press, 2009.

[211] J. H. Horlock, D. T. Watson, and T. V. Jones, "Limitations on Gas Turbine Performance Imposed by Large Turbine Cooling Flows," *Journal of Engineering for Gas Turbines and Power*, vol. 123, no. 3, p. 487, 2001, doi:10.1115/1.1373398.

[212] J. Kurzke, "Achieving Maximum Thermal Efficiency with the Simple Gas Turbine Cycle," in *Proceedings of the 9th CEAS European Propulsion Forum: "Virtual Engine - A Challenge for Integrated Computer Modelling"*, Rome, Italy, 2003.

[213] F. Donus, "Ermittlung der Genauigkeit und Erarbeitung von Verbesserungsvorschlägen bei der Gewichtsabschätzung mit Gasturb 11," Diploma Thesis, Institut für Luftfahrtantriebe, Universität Stuttgart, 2008.

[214] J. D. Denton, "Loss Mechanisms in Turbomachines," *Journal of Turbomachinery*, vol. 115, no. 4, pp. 621–656, 1993, doi:10.1115/1.2929299.

[215] J. Kurzke, "Calculation of Installation Effects within Performance Computer Programs," in *Steady and Transient Performance Prediction of Gas Turbine Engines, AGARD Lecture Series 183*, NATO Advisory Group for Aerospace Research & Development, 1992.

[216] S. J. Cline, P. H. Halter, J. T. Kutney, and T. J. Sullivan, "Energy Efficient Engine - Fan and Quarter-Stage Component Performance Report." General Electric Company, NASA Contractor Report, NASA CR-168070, Lewis Research Center, Cleveland, Ohio, USA, 1983.

[217] J. E. Halle and C. J. Michael, "Energy Efficient Engine - Fan Component Detailed Design Report." United Technologies Corporation, NASA Contractor Report, NASA CR-16466, 1981.

[218] C. J. Michael and J. E. Halle, "Energy Efficient Engine - Low-Pressure Compressor Component Test Hardware." United Technologies Corporation, NASA Contractor Report, NASA CR-165354, Lewis Research Center, Cleveland, Ohio, USA, 1981.

[219] S. J. Cline, W. Fesler, H. S. Liu, R. C. Lovell, and S. J. Shaffer, "Energy Efficient Engine High Pressure Compressor Component Performance Report." General Electric Company, NASA Contractor Report, NASA CR-168245, Lewis Research Center, Cleveland, Ohio, USA, 1983.

[220] D. C. Howe and R. D. Marchant, "Energy Efficient Engine - High-Pressure Compressor Test Hardware, Detailed Design Report." United Technologies Corporation, NASA Contractor Report, NASA CR-180850, Lewis Research Center, Cleveland, Ohio, USA, 1988.

[221] Timko L. P., "Energy Efficient Engine - High Pressure Turbine Component Test Performance Report." General Electric Company, NASA Contractor Report, NASA CR-168289, Lewis Research Center, Cleveland, Ohio, USA, 1984.

[222] K. Leach, R. Thulin, and D. Howe, "Energy Efficient Engine - Turbine Intermediate Case and Low-Pressure Turbine Component Test Hardware Detailed Design Report." United Technologies Corporation, NASA Contractor Report, NASA CR-167973, Lewis Research Center, Cleveland, Ohio, USA, 1982.

[223] M. J. Bridgeman, D. G. Cherry, and J. Pedersen, "NASA/GE Energy Efficient Engine - Low Pressure Turbine Scaled Test Vehicle Performance Report." General Electric Company, NASA Contractor Report, NASA CR-168290, Lewis Research Center, Cleveland, Ohio, USA, 1983.

[224] R. D. Moore, D. C. Urasek, and G. Kovich, "Performance of a Transonic Fan Stage with Weight Flow Per Unit Annulus Area of 178 Kilograms per Second per Square Meter (36.5 (LB/SEC)/FT^2))." NASA Technical Memorandum, NASA TM X-2904, Lewis Research Center, Cleveland, Ohio, USA, 1973.

[225] K. Kovach and D. M. Sandercock, "Experimental Investigation of a Five-Stage Axial-Flow Research Compressor with Transonic Rotors in All Stages, II-Compressor Overall Performance." NACA Research Memorandum EM E54G01, Washington, D.C., USA, 1954.

[226] F.-O. Methling, H. Stoff, and F. Grauer, “The Pre-Stall Behavior of a 4-Stage Transonic Compressor and Stall Monitoring Based on Artificial Neural Networks,” *International Journal of Rotating Machinery*, vol. 10, no. 5, pp. 387–399, 2004, doi:0.1080/10236210490474548.

[227] S. Kennedy, T. Robinson, S. Spence, and J. Richardson, “Computational Investigation of Inlet Distortion at High Angles of Attack,” *Journal of Aircraft*, vol. 51, no. 2, pp. 361–376, 2014, doi:10.2514/1.c031789.

[228] R. Schnell and J. Corroyer, “Coupled Fan and Intake Design Optimization for Installed UHBR-Engines With Ultra-Short Nacelles,” in *Proceedings of the 22nd International Symposium on Air Breathing Engines*, Phoenix, Arizona, USA, 2015, doi: ISABE-2015-20034.

[229] B. A. Miller, B. J. Dastoli, and H. L. Wesoky, “Effects of Entry-Lip Design on Aerodynamics and Acoustics of High-Throat-Mach-Number Inlets for the Quiet, Clean, Short-Haul Experimental Engine.” NASA Technical Memorandum, NASA TM X-3222, Lewis Research Center, Cleveland, Ohio, USA, 1975.

[230] D. C. Howe and T. A. Wynosky, “Energy Efficient Engine Program - Advanced Turbofan Nacelle Definition Study.” NASA Contractor Report CR-1985-174942, Lewis Research Center, Cleveland, Ohio, USA, 1985.

[231] M. Daly and B. Gunston, *IHS Jane’s Aero-Engines 2013-2014*. Couldsdon, UK: IHS Jane’s, IHS Global Limited, 2013.

[232] Airbus S.A.S, “A320 - Aircraft Characteristics Airport and Maintenance Planning, Revision No. 32, May 01/17.” Airbus Customer Services, Blagnac Cedex, France, 2017.

[233] Airbus S.A.S, “A330 - Aircraft Characteristics Airport and Maintenance Planning, Revision No. 22, Jan 01/14.” Airbus Customer Services, Blagnac Cedex, France, 2014.

[234] Airbus S.A.S, “A340-500/-600 - Aircraft Characteristics Airport and Maintenance Planning, Revision No. 12, Jan 01/14.” Airbus Customer Services, Blagnac Cedex, France, 2014.

[235] Airbus S.A.S, “A380 - Aircraft Characteristics Airport and Maintenance Planning, Revision No. 13, Dec 01/14.” Airbus Customer Services, Blagnac Cedex, France, 2014.

[236] Embraer S.A., “Embraer 190 Airport Planning Manual.” APM-1901, Revision 13, 2015.

[237] Bombardier Inc., “CRJ Regional Jet Series 700 Airport Planning Manual.” Volume 1, CSP B-020, Revision 15, 2015.

[238] Boeing Commercial Airplanes, “717-200 - Airplane Characteristics for Airport Planning, Rev B.” 2014.

[239] E. Kors, “OPENAIR - OPtimisation for low Environmental Noise impact AIRcraft,” in *Proceedings of the 7th European Aeronautics Days 2015*, London, UK, 2015.

[240] D. L. Daggett, S. T. Brown, and R. T. Kawai, “Ultra-Efficient Engine Diameter Study.” Boeing Commercial Airplane Group, NASA Contractor Report CR-2003-212309, Glenn Research Center, Cleveland, Ohio, USA, 2003.

[241] E. Torenbeek, *Synthesis of Subsonic Airplane Design*. Delft University Press, 1976.

[242] H. W. Müller, *Die Umlaufgetriebe*. Berlin: Springer-Verlag, 2001.

[243] N. E. Anderson, S. H. Loewenthal, and J. D. Black, “An Analytical Method to Predict Efficiency of Aircraft Gearboxes.” NASA Technical Memorandum, NASA TM-1984-83716, Lewis Research Center, Cleveland, Ohio, USA, 1984.

[244] D. C. Howe, C. V. Sundt, and A. H. McKibbon, “Advanced Gearbox Technology Detailed Design Report.” United Technologies Corporation, NASA Contractor Report, NASA CR-180883, Lewis Research Center, Cleveland, Ohio, USA, 1988.

[245] A. DeFeo and M. Kulina, “Quiet Clean Short-Haul Experimental Engine (QCSEE) Main Reduction Gears - Detailed Design Report.” Curtiss-Wright Corporation Under Subcontract to General Electric

Co., NASA CR-134872, Lewis Research Center, Cleveland, Ohio, USA, 1975.

[246] B. MacIsaac and R. Langton, *Gas Turbine Propulsion Systems*. Chichester, UK: John Wiley & Sons, 2011.

[247] I. Berlowitz, "Aero-Engine Fan Gearbox Design," in *Presentation at the 16th Israeli Symposium on Jet Engines and Gas Turbines*, 2017.

[248] A. Stroh, G. Wortmann, and A. Seitz, "Conceptual Sizing Methods For Power Gearboxes In Future Gas Turbine Engines," in *Deutscher Luft- und Raumfahrtkongress 2017*, Munich, Germany, 2017.

[249] W. Sheridan, M. McCune, and M. Winter, "Geared Turbofan(TM) Engine: Driven by Innovation," in *Green Aviation*, R. Agarwal, F. Collier, and A. Seabridge, Eds. Chichester, UK: John Wiley & Sons, 2016, pp. 105–111.

[250] P. Coy, "The Little Gear that Could Reshape the Jet Engine," *Bloomberg Businessweek*, Issue: October 19, 2015, 2015.

[251] A. Tovey and S. Jamieson, "Rolls-Royce Boosted by £1.4bn Order for Troubled Trent 700 Engines," *The Telegraph*, 20-Jul-2015.

[252] U.S. Department of Transportation - Federal Aviation Administration, "Type Certificate Data Sheet E39NE." TCDS Number E39NE, Revision 04, March 16, 2007, 2007.

[253] European Aviation Safety Agency, "Type-Certificate Data Sheet for General Electric Company GE90 Series Engines." No. IM.E.002, Issue 03, 2017.

[254] MTU Aero Engines AG, "V2500 Turbofan Engine - The Innovative Power." 2007.

[255] D. Scholz, R. Sereshine, I. Staack, and C. Lawson, "Fuel Consumption due to Shaft Power Off-takes from the Engine," in *4th International Workshop on Aircraft System Technologies (AST 2013)*, Hamburg, Germany, 2013.

[256] W. Lehle, "Konzeption und Entwicklung von Flugzeugklimatisierungsanlagen," in *Praxis-Seminar Luftfahrt: Air Systems*, Hamburg, 2006.

[257] SAE International, "Aircraft Propulsion System Performance Station Designation and Nomenclature." SAE Aerospace Recommended Practice ARP755, 1991.

[258] G. J. Harloff, B. A. Reichert, and S. R. Wellborn, "Navier-Stokes Analysis and Experimental Data Comparison of Compressible Flow in a Diffusing S-Duct." NASA Technical Memorandum, NASA TM-1992-105683, Lewis Researh Center, Cleveland, Ohio, USA, 1992.

[259] C. E. Towne, "Computation of Viscous Flow in Curved Ducts and Comparison with Experimental Data." NASA Technical Memorandum, NASA TM-1984-83548, Lewis Researh Center, Cleveland, Ohio, USA, 1984.

[260] V. J. Fidalgo, C. A. Hall, and Y. Colin, "A Study of Fan-Distortion Interaction Within the NASA Rotor 67 Transonic Stage," *Journal of Turbomachinery*, vol. 134, no. 5, p. 51011, 2012, doi:10.1115/1.4003850.

[261] E. J. Gunn and C. A. Hall, "Aerodynamics of Boundary Layer Ingesting Fans," in *ASME Turbo Expo 2014*, Düsseldorf, Germany, 2014, doi: 10.1115/GT2014-26142.

[262] R. V. Florea, C. Matalanis, L. W. Hardin, M. Stucky, and A. Shabbir, "Parametric Analysis and Design for Embedded Engine Inlets," *Journal of Propulsion and Power*, vol. 31, no. 3, pp. 843–850, 2015, doi:10.2514/1.b34804.

[263] D. J. Arend, G. Tillman, and W. F. O'Brian, "Generation After Next Propulsor Research: Robust Design for Embedded Engine Systems," in *48th AIAA/ASME/SAE/ASEE Joint Propulsion Conference & Exhibit*, Atlanta, Georgia, USA, 2012.

[264] C. Hall, E. Gunn, and D. Perovic, "Fan Systems for Boundary Layer Ingestion," in *Presentation at IMechE Special Conference on Distributed Propulsion*, London, UK, 2014.

[265] E. J. Gunn, S. E. Tooze, C. A. Hall, and Y. Colin, "An Experimental Study of Loss Sources in a Fan Operating With Continuous Inlet Stagnation Pressure Distortion," *Journal of Turbomachinery*, vol. 135, no. 5, 2013, doi:10.1115/1.4007835.

[266] Y. Liu, R. Claus, J. Litt, and T. Guo, "Simulating Effects of High Angle of Attack on Turbofan Engine Performance." NASA Technical Memorandum, NASA TM-2013-217846, Glenn Research Center, Cleveland, Ohio, USA, 2013.

[267] W. Bohl, *Technische Strömungslehre*, 6th ed. Würzburg, Germany: Vogel-Buchverlag, 1984.

[268] I. E. Idelchik, "Handbook of Hydraulic Resistance." The U.S. Atomic Energy Commission, Washington, D.C., USA, 1966.

[269] B. H. Anderson and J. Gibb, "Vortex Generator Installation Studies on Steady State and Dynamic Inlet Distortion." NASA Technical Memorandum, NASA TM 107220, 1996.

[270] S. Mohler, "Wind-US Flow Calculations for the M2129 S-duct Using Structured and Unstructured Grids." NASA Contractor Report CR-2003-212736, Glenn Research Center, Cleveland, Ohio, USA, 2013.

[271] B. L. Berrier, M. B. Carter, and B. G. Allan, "High Reynolds Number Investigation of a Flush-Mounted, S-Duct Inlet With Large Amounts of Boundary Layer Ingestion." NASA Technical Publication, NASA TP-2005-213766, Langley Research Center, Hampton, Virginia, USA, 2005.

[272] H. Khaleghi, G. Doulgeris, M. Boroomand, P. Pilidis, and A. M. Tousi, "A Method for Calculating Inlet Distortion Effects on Stability of Split-flow Fans," *The Aeronautical Journal*, vol. 113, no. 1147, pp. 591–598, 2009, doi:10.1017/s0001924000003250.

[273] J. E. Foley, "Results of a Study of Mach Number and Reynolds Number Effects on the Lee Side Vortex Flow Field Characteristics of an Ogive-Cylinder-Frustum-Cylinder at Angles of Attack to 25 Degrees, Vol. I." Chrysler Corporation Space Division, NASA Contractor Report TN-AP-72-565, New Orleans, Louisiana, USA, 1972.

[274] G. K. Kenway and C. C. Kiris, "Aerodynamic Shape Optimization of the STARC-ABL Concept for Minimal Inlet Distortion," in *2018 AIAA/ASCE/AHS/ASC Structures, Structural Dynamics, and Materials Conference*, 2018, doi: 10.2514/6.2018-1912.

[275] H. Pearson and A. B. McKenzie, "Wakes in Axial Compressors," *Journal of the Royal Aeronautical Society*, vol. 63, 1959.

[276] J. Kurzke, "Effects of Inlet Flow Distortion on the Performance of Aircraft Gas Turbines," in *Proceedings of ASME Turbo Expo 2006*, Barcelona, Spain, 2006, doi: 10.1115/GT2006-90419.

[277] W. Traupel, *Thermische Turbomaschinen, Band II*, 3rd ed. Berlin Heidelberg: Springer-Verlag, 1982.

[278] K. Stegmaier, E. Carpintero, and P. Wackers, "SAGE4 Geared Turbofan Demonstrator," in *Proceedings of the 20th International Symposium on Air Breathing Engines*, Gothenburg, Sweden, 2011, doi: ISABE-2011-1302.

[279] T. Lengyel-Kampmann, T. Otten, T. Schmidt, and E. Nicke, "Optimization of an Engine with Gear Driven Counter Rotating Fan Part I: Fan Performance and Design," in *Proceedings of the 22nd International Symposium on Air Breathing Engines*, Phoenix, Arizona, USA, 2015, doi: ISABE-2015-20091.

[280] M. C.-Y. Niu, *Airframe Structural Design*. Hong Kong: Conmilit Press Ltd., 1989.

[281] J. Roskam, *Airplane Flight Dynamics and Automatic Flight Controls, Part I*, 3rd ed. Lawrence, Kansas, USA: Design, Analysis and Research Corporation (DARcorporation), 2001.

[282] E. Obert, *Aerodynamic Design of Transport Aircraft*. Delft University of Technology, Faculty of Aerospace Engineering, The Netherlands: IOS Press, 2009.

[283] J. Roskam, *Airplane Design, Part V: Component Weight Estimation*. Ottawa, Kansas, USA: Roskam Aviation and Engineering Corporation, 1985.

[284] T. L. Lomax, *Structural Loads Analysis: Theory and Practice for Commercial Aircraft*. Reston, Virginia, USA: AIAA Education Series, 1996.

[285] G. Niemann, H. Winter, and B.-R. Höhn, *Maschinenelemente, Band 1*, 4th ed. Berlin Heidelberg: Springer-Verlag, 2005.

[286] Lehrstuhl für Maschinenelemente - Technische Universität München, "Formelsammlung zur Vorlesung Maschinenelemente." 2008.

[287] Forschungskuratorium Maschinenbau (FKM), *Rechnerischer Festigkeitsnachweis für Maschinenbauteile*. VDMA Verlag, 2003.

[288] NASA Structures and Propulsion Laboratory, "Astronautic Structures Manual, Vol. II." NASA Technical Memorandum, NASA TM X-73306, Marshall Space Flight Center, Huntsville, Alabama, USA, 1975.

[289] G. Ricci, "Mass and Rated Characteristics of Planetary Gear Reduction Units," *Meccanica*, vol. 27, pp. 35–45, 1992, doi:10.1007/BF00453001.

[290] C. N. Reynolds, "Advanced Prop-Fan Engine Technology (APET) Single- and Counter-Rotation Gearbox/Pitch Change Mechanism - Final Report, Vol. II." United Technologies Corporation, NASA Contractor Report, NASA CR-168114, Lewis Research Center, Cleveland, Ohio, USA, 1985.

[291] E. Hendricks and M. T. Tong, "Performance and Weight Estimates for an Advanced Open Rotor Engine." NASA Technical Memorandum, NASA TM-2012-217710, Glenn Research Center, Cleveland, Ohio, USA, 2012.

[292] C. Svoboda, "Turbofan Engine Database as a Preliminary Design Tool," *Aircraft Design*, vol. 3, no. 1, pp. 17–31, 2000, doi:10.1016/S1369-8869(99)00021-X.

[293] F. Donus, R. Schaber, K.-J. Schmidt, and S. Staudacher, "Accuracy of Analytical Engine Weight Estimation During the Conceptual Design Phase," in *Proceedings of ASME Turbo Expo 2010*, Glasgow, UK, 2010, doi: 10.1115/GT2010-23774.

[294] E. Onat and G. W. Klees, "A Method to Estimate Weight and Dimensions of Large and Small Gas Turbine Engines - Final Report." Boeing Military Airplane Development, NASA Contractor Report, NASA CR-199481, Lewis Researh Center, Cleveland, Ohio, USA, 1979.

[295] A. Alexiou, N. Aretakis, I. Roumeliotis, I. Kolias, and K. Mathioudakis, "Performance Modelling of an Ultra-high Bypass Ratio Geared Turbofan," in *Proceedings of the 23rd International Symposium on Air Breathing Engines*, Manchester, UK, 2017, doi: ISABE-2017-22512.

[296] C. Mercer, W. Haller, and M. T. Tong, "Adaptive Engine Technologies for Aviation CO2 Emissions Reduction." NASA Technical Memorandum, NASA TM-2006-214392, Glenn Research Center, Cleveland, Ohio, USA, 2006.

[297] J. P. C. Kleijnen, *Statistical Tool for Simulation Practitioners*. New York, New York, USA: Marcel Dekker, 1987.

[298] W. Simpson, J. Peplinski, P. N. Koch, and J. K. Allen, "Metamodels for Computer-Based Engineering Design: Survey and Recommendations," *Engineering with Computers*, vol. 17, no. 2, pp. 129–150, 2001.

[299] N. V. Queipo, R. T. Haftka, W. Shyy, T. Goel, R. Vaidyanathan, and P. Kevin Tucker, "Surrogate-based Analysis and Optimization," *Progress in Aerospace Sciences*, vol. 41, no. 1, pp. 1–28, Jan. 2005, doi:10.1016/j.paerosci.2005.02.001.

[300] M. D. McKay, R. J. Beckman, and W. J. Conover, "A Comparison of Three Methods for Selecting Input Variables in the Analysis of Output from a Computer Code," *Technometrics*, vol. 42, no. 1, pp. 55–61, 1979, doi:10.1080/00401706.2000.10485979.

[301] The Mathworks Inc., "MATLAB Neural Network Toolbox, Version 8.1." 2013.

[302] L. Papula, *Mathematik für Ingenieure und Naturwissenschaftler, Band 1*, 14th ed. Wiesbaden: Springer Vieweg, 2014.

[303] B. W. McCormick, *Aerodynamics, Aeronautics, and Flight Mechanics*, 2nd ed. New York, New York, USA: John Wiley & Sons, 1995.

[304] D. Howe, *Aircraft Conceptual Design Synthesis*. John Wiley & Sons, Hoboken, New Jersey, USA, 2000.

[305] L. K. J. Loftin, "Subsonic Aircraft: Evolution and the Matching of Size to Performance." NASA Reference Publication NASA RP-1060, Langley Research Center, Hampton, Virginia, USA, 1980.

[306] P. Jackson, *Jane's All The World's Aircraft*. Jane's Information Group, 2005.

[307] International Civil Aviation Organization, *Annex 14 to the Convention on International Civil Aviation - Aerodromes, Volume I*, 6th ed. Montréal, Quebec, Canada: International Civil Aviation Organization, 2013.

[308] V. C. Czitrom, "One-Factor-at-a-Time Versus Designed Experiments," *The American Statistician*, vol. 53, no. 2, pp. 126–131, 1999, doi:10.2307/2685731.

[309] K. G. Kyprianidis, "Multi-disciplinary Conceptual Design of Future Jet Engine Systems," PhD Thesis, School of Engineering, Cranfied University, 2010.

[310] Airbus S.A.S., "A350-900 - Aircraft Characteristics Airport and Maintenance Planning, Issue Jun 01/13, Revision Apr 01/15." Airbus Customer Services, Blagnac Cedex, France, 2015.

[311] J. Scheiderer, *Angewandte Flugleistungen*. Berlin Heidelberg: Springer-Verlag, 2008.

[312] The Mathworks Inc., "MATLAB Optimization Toolbox, Version 6.4." 2013.

[313] J. Sobieszczanski-Sobieski, "Sensitivity Analysis and Multidisciplinary Optimization for Aircraft Design: Recent Advances and Results." NASA Technical Memorandum, NASA TM-100630, Langley Research Center, Hampton, Virginia, USA, 1988.

[314] S. J. Bradbrook, "Common Solutions to Commercial and Military Propulsion Requirements," in *24th International Congress of the Aeronautical Sciences*, Yokohama, Japan, 2004.

[315] R. A. Zimbrick and J. L. Colehour, "Investigation of Very High Bypass Ratio Engines for Subsonic Transports," *Journal of Propulsion and Power*, vol. 6, no. 4, pp. 490–496, 1990, doi:10.2514/3.25461.

[316] D. J. Pannell, "Sensitivity Analysis of Normative Economic Models: Theoretical Framework and Practical Strategies," *Agricultural Economics*, vol. 16, pp. 139–152, 1997.

[317] A. Saltelli, M. Ratto, J. Cariboni, D. Gatelli, M. Saisana, and S. Tarantola, *Global Sensitivity Analysis*. Chichester, UK: John Wiley & Sons, 2008.

[318] A. Hupfer, *Konstruktionsaspekte bei Flugantrieben*, 10.10.2015. Lehrstuhl für Flugantriebe, Technische Universität München, 2015.

[319] L. R. Jenkinson, P. Simpkin, and D. Rhodes, *Civil Jet Aircraft Design. Accompanying Data Set B*. London, UK: Arnold Publishers, 1999.

[320] European Aviation Safety Agency, "Type-Certificate Data Sheet for International Aero Engines AG (IAE) V2500 Series Engines." No.: IM.E.069, Issue: 03, 2017.

[321] H. Arps *et al.*, "Increased Stringency of Noise Limits for Civil Jet Aircraft with Emphasis on the Trade-off between Noise and Pollutant Emissions of Jet Engines." Publikationen des Umweltbundesamtes, UFOPLAN-Ref. No. 202 54 131, 2006.

[322] International Aero Engines, "V2500 - The Engine of Choice." 1996.

[323] S. Kimball and P. Mattis, "GNU Image Manipulation Program (GIMP)." 2013.

[324] LTH-Koordinierungsstelle, "Luftfahrttechnisches Handbuch," 2006. [Online]. Available: www.lth-online.de.

[325] O. Gur, W. H. Mason, and J. A. Schetz, "Full-Configuration Drag Estimation," *Journal of Aircraft*, vol.

47, no. 4, pp. 1356–1367, 2010, doi:10.2514/1.47557.

[326] A. R. Wadia, “Technologies for the Next Engine Generation,” *GE Aviation Company Presentation*. Cincinnati, Ohio, USA, 2014.

[327] Boeing Commercial Airplanes, “787 Airplane Characteristics for Airport Planning.” Document No. D6-58333, Revision REV L, 2015.

[328] U.S. Department of Transportation - Federal Aviation Administration, “Type Certificate Data Sheet E00078NE.” TCDS NumberE00078NE, Revision: original, March 31, 2008, 2008.

[329] A. S. Gohardani, “A Synergistic Glance at the Prospects of Distributed Propulsion Technology and the Electric Aircraft Concept for Future Unmanned Air Vehicles and Commercial/Military Aviation,” *Progress in Aerospace Sciences*, vol. 57, pp. 25–70, 2013, doi:10.1016/j.paerosci.2012.08.001.

[330] A. Seitz, M. Nickl, A. Stroh, and P. C. Vratny, “Conceptual Study of a Mechanically Integrated Parallel Hybrid Electric Turbofan,” *Proceedings of the Institution of Mechanical Engineers, Part G: Journal of Aerospace Engineering*, vol. 232, no. 14, pp. 2688–2712, Jul. 2018, doi:10.1177/0954410018790141.

[331] F. Heppner, “Improvements Relating to Jet-Propelled Aircraft,” GB Patent GB577950, 1941.

[332] NATO Research and Technology Organisation, “Performance Prediction and Simulation of Gas Turbine Engine Operation for Aircraft, Marine, Vehicular, and Power Generation.” RTO Technical Report TR-AVT-036, Final Report of the RTO Applied Vehicle Technology Panel (AVT) Task Group AVT-036, 2007.

[333] M. T. Tong and B. A. Naylor, “An Object-Oriented Computer Code for Aircraft Engine Weight Estimation.” NASA Technical Memorandum, NASA TM-2009-215656, Glenn Research Center, Cleveland, Ohio, USA, 2009.

[334] T. W. Simpson, D. K. J. Lin, and W. Chen, “Sampling Strategies for Computer Experiments: Design and Analysis,” *International Journal of Reliability and Applications*, vol. 2, no. 3, pp. 209–240, 2001.

[335] G. Wrenn, “An Indirect Method for Numerical Optimization Using the Kreisselmeier-Steinhauser Function.” Planning Research Corporation, Aerospace Technologies Division, NASA Contractor Report, NASA CR-4220, Langley Research Center, Hampton, Virginia, USA, 1989.

[336] National Research Council, *Aeronautical Technologies for the Twenty-First Century*. Washington, D.C., USA: The National Academies Press, 1992.

A. Analytical Derivation of Blade Centrifugal Stress

The approach is based on formulating the definition of centrifugal force $\mathrm{d}F_z$ exhibited by an infinitesimal mass element $\mathrm{d}m$ rotating at a radius r with an angular velocity ω [277, Sec. 16.1]:

$$\mathrm{d}F_z = r\omega^2 \mathrm{d}m = r\omega^2 \rho A(r) \mathrm{d}r \tag{A.1}$$

where $A(r)$ denotes the local cross sectional blade area. Assuming constant material density ρ the centrifugal stress acting at an arbitrary radial position $r_h \leq r \leq r_t$ is given by:

$$\sigma_z(r) = \frac{F_z(r)}{A(r)} = \frac{\rho\omega^2}{A(r)} \int_r^{r_t} A(r) \cdot r \mathrm{d}r \tag{A.2}$$

This expression can be analytically integrated only for simple radial distributions of blade cross sections. For demonstration purposes, a linear distribution of chord length between hub and tip radius,

$$c(r) = c_h \left(\frac{1-\tau}{1-1/\nu} \cdot \frac{r - r_h}{r_h} + 1 \right) \tag{A.3}$$

is applied. Here, ν indicates the hub/tip ratio and τ the taper ratio. The cross section area is approximated as the product of thickness and chord length, where a constant relative thickness is assumed. Introducing the abbreviation

$$a = \frac{1-\tau}{1-1/\nu} \tag{A.4}$$

and conducting the integration from a position r up to the tip radius produces a relation indicating the stress level at an arbitrary radial position:

$$\sigma_z(r) = \rho\omega^2 \frac{\frac{a^2}{4}\left(\frac{r_t^4}{r_h^2} - \frac{r^4}{r_h^2}\right) + \frac{2a}{3}(1-a)\left(\frac{r_t^3}{r_h} - \frac{r^3}{h}\right) + \frac{(1-a)^2}{2}(r_t^2 - r^2)}{\left(a\frac{r}{r_h} + 1 - a\right)^2} \tag{A.5}$$

Evaluating equation (A.5) at the hub position and normalizing by the product of ρ and tip speed u_t yields an expression that is solely dependent on ν and τ:

$$\frac{\sigma_z(r_H)}{\rho u_t^2} = \frac{a^2}{4}\left(\frac{1}{\nu^2} - \nu^2\right) + \frac{2a}{3}(1-a)\left(\frac{1}{\nu} - \nu^2\right) + \frac{(1-a)^2}{2}(1-\nu^2) \tag{A.6}$$

Equation (A.6) can be verified by applying a constant cross section, i.e. $\tau = 1$, or $a = 0$, producing the well-known relation [209, p. 733]:

$$\frac{\sigma_z(r_h)}{\rho u_t^2} = \frac{1}{2}(1-\nu^2) \tag{A.7}$$

For more realistic characteristics of $A(r)$, Equation (A.2) can be solved through numerical integration. This is demonstrated for a polynomial area distribution of second degree, which is considered a reasonable approximation of the highly complex distribution of state-of-the-art blade designs (cf. e.g. Reference [277]):

$$A(r) = A_h \cdot \left(\frac{1 - A_t/A_h}{(\nu-1)^2} \cdot \left(\left(\frac{r}{r_t}\right)^2 - 2\frac{r}{r_t} + 1 \right) + \frac{A_t}{A_h} \right) \tag{A.8}$$

Stress due to bending moments resulting from gas forces are considered to be counteracted through appropriate spatial shaping of the stagger line connecting the centers of gravity of the discretized blade cross sections [318].

In Figure A.1, the integration has been conducted for a wide range of ν and τ. Shown are the values of $\sigma_z/(\rho u_t^2)$ evaluated at the root section and normalized by the value obtained for the settings of a typical conventional turbofan, which is indicated using dashed lines. It is visible that for values of ν expected for PFC applications significantly reduced values of normalized blade centrifugal stress are obtained. Furthermore, acknowledging that the annular flow area $\tilde{A}$ is given by $\pi\left(r_t^2 - r_h^2\right)$ and noting that the rotational speed $\widetilde{N}$ is $\omega/(2\pi)$, the classic AN^2 metric can be shown to be solely a function of blade tip speed and hub/tip ratio:

$$AN^2 = \tilde{A} \cdot \widetilde{N}^2 = \pi\left(r_t^2 - r_h^2\right) \cdot \left(\frac{\omega}{2\pi}\right)^2 = (1 - \nu^2)\frac{u_t^2}{4\pi} \tag{A.9}$$

Hence, for a given tip speed, AN^2 exclusively scales with $1 - \nu^2$. Recalling equation (A.7), it can be noted that for $\tau = 1$, the quantities AN^2 and $\sigma_z/(\rho u_t^2)$ are directly proportional.

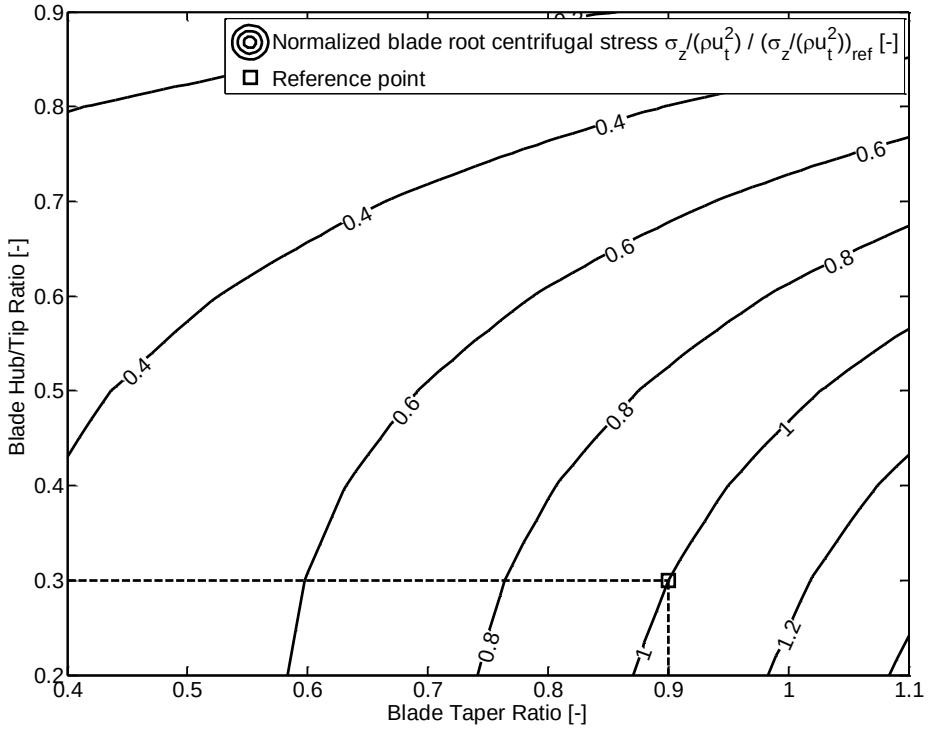

Figure A.1:Normalized blade root centrifugal stress for polynomial cross section area distribution of second degree

B. Supplementary Figures

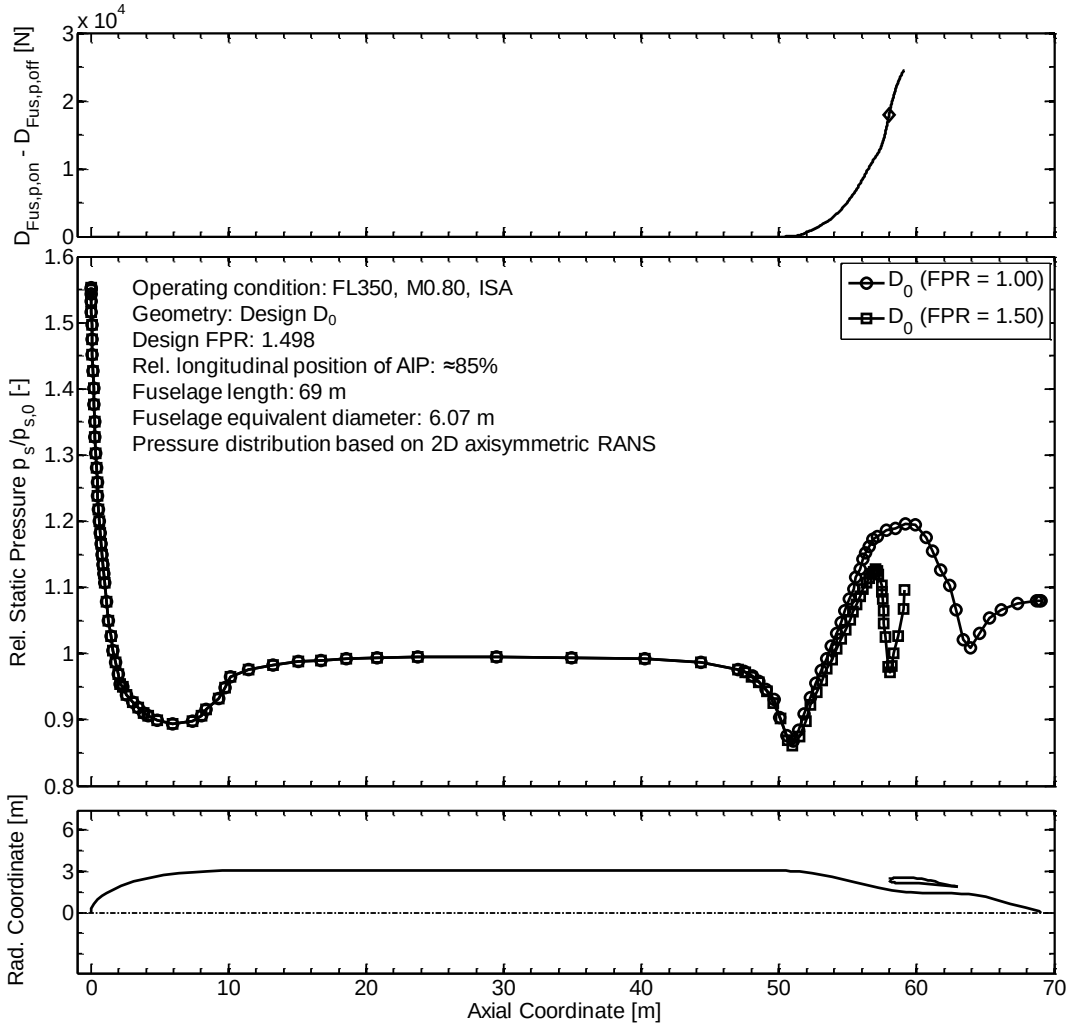

Figure B.1: Half-sectional contour of bare PFC arrangement (bottom), static pressure distribution (middle) and change in fuselage pressure drag between active and inactive fuselage fan operation (top). Note that the pressure values of the active case are only available up to the propulsor disk position.

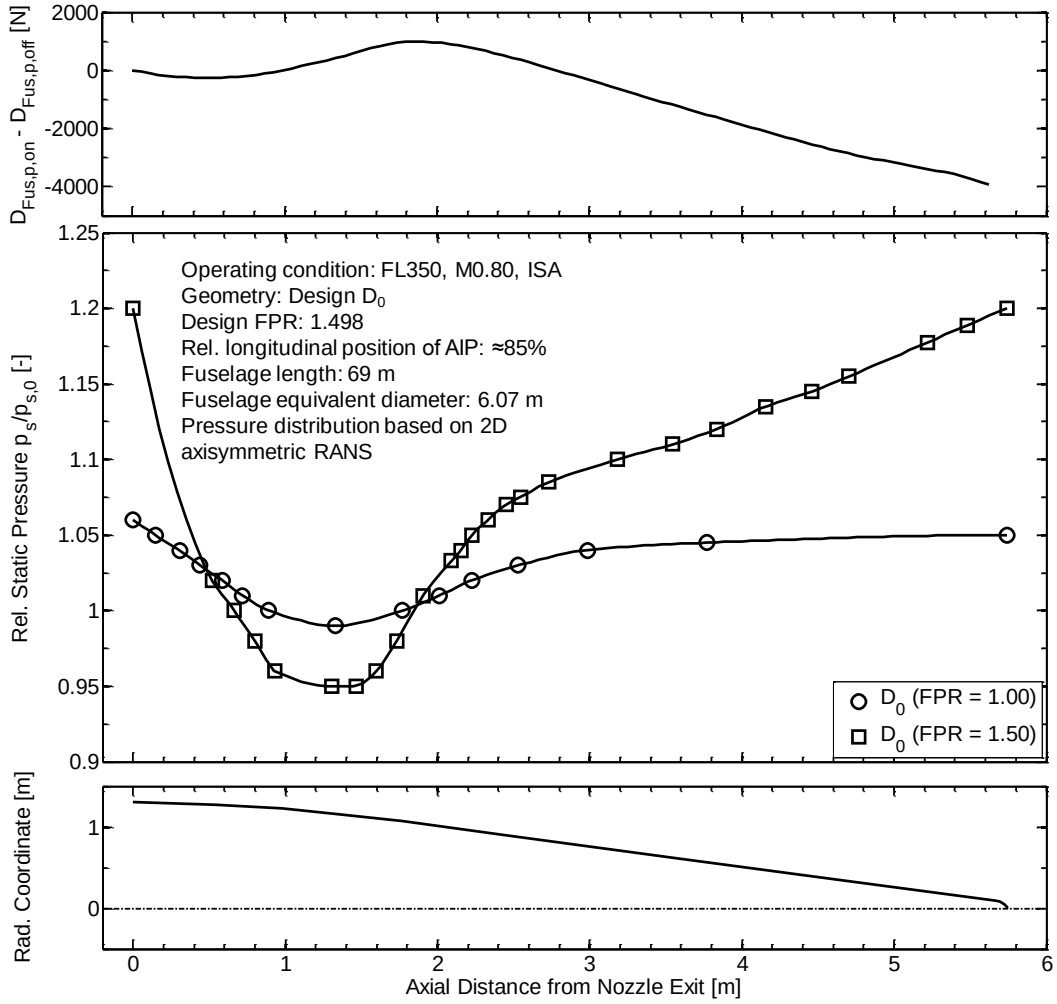

Figure B.2: Half-sectional contour of nozzle cone starting from nozzle exit (bottom), static pressure distribution (middle) and change in pressure drag between active and inactive fuselage fan operation (top)

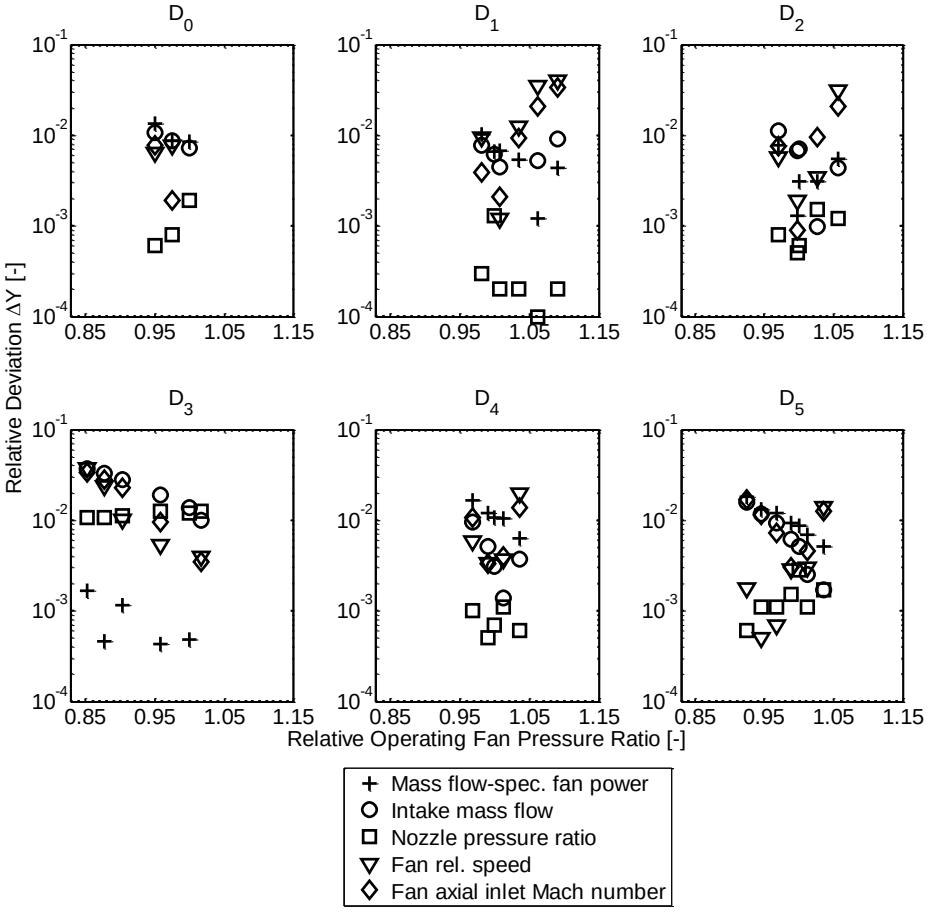

Figure B.3: Validation of CFD and propulsion system model matching procedure at part power conditions

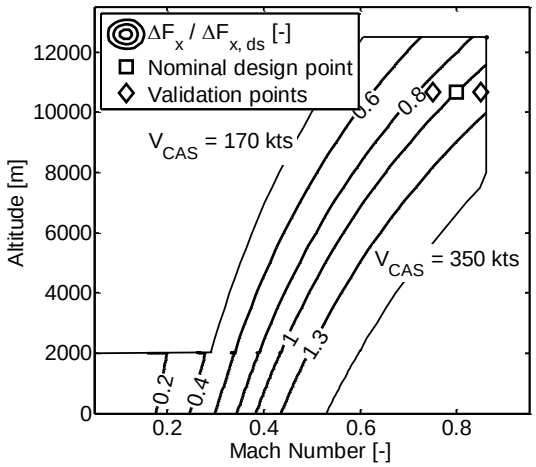

Figure B.4: Estimation of normalized integration impact metric within the typical flight envelope

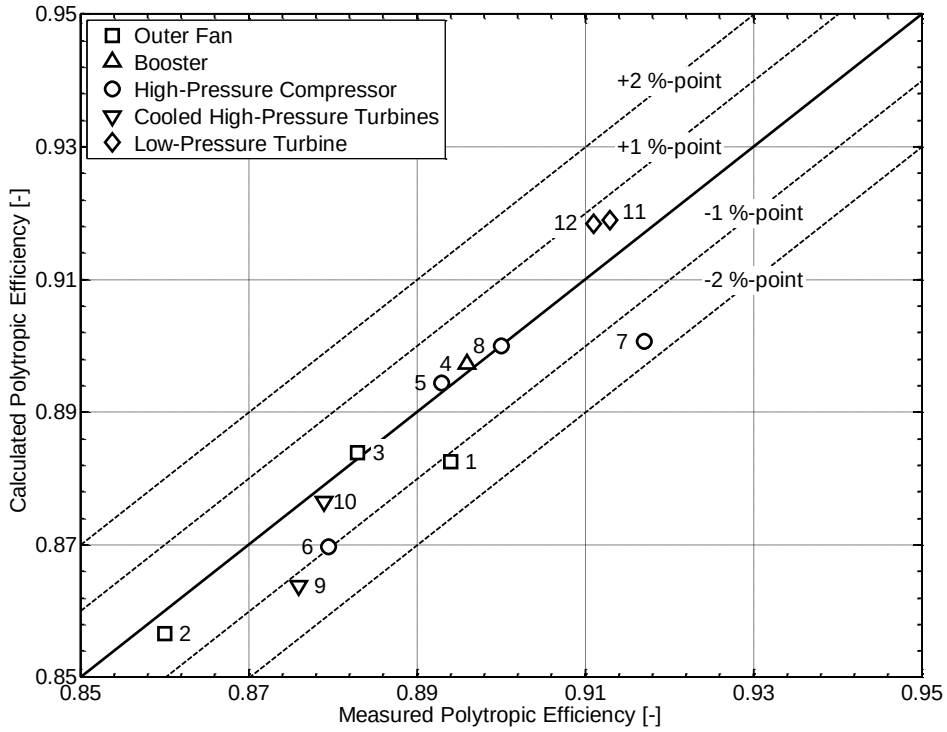

Index	Reference
1	NASA CR-168070, 1983
2	NASA TM X-2904, 1973
3	NASA CR-165466, 1981
4	NASA CR-165354, 1981
5	NASA CR-168245, 1983
6	NACA RM E45G01, 1954
7	NASA CR-180850, 1988
8	*Int. J. of Rot. Machinery*, Vol. 10, No. 5, pp. 387-399, 2004
9	NASA CR-168289, 1984
10	NASA CR-165608, 1982
11	NASA CR-167973, 1982
12	NASA CR-168290, 1983

Figure B.5: Validation of turbo component design efficiency prediction method

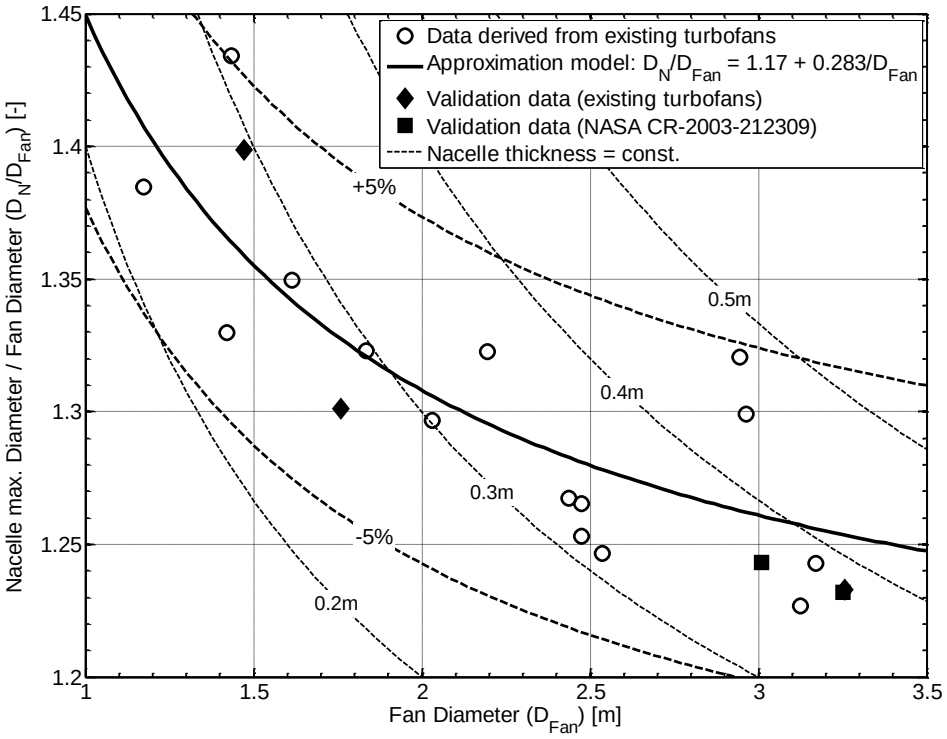

Figure B.6: Implemented model for the mapping of turbofan nacelle maximum diameter, adapted from Reference [23]

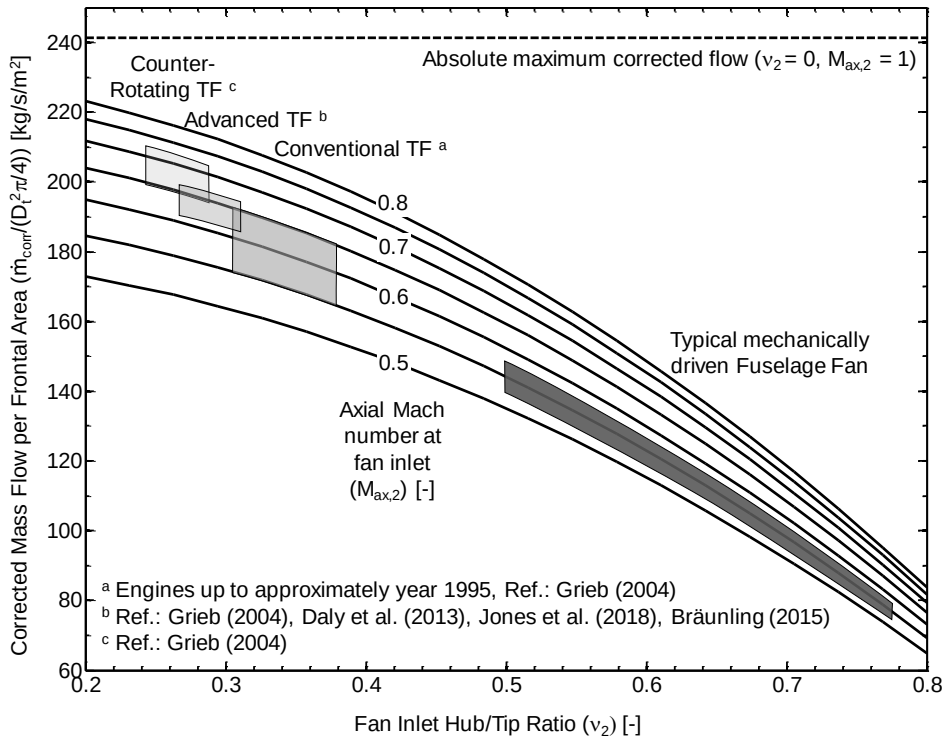

Figure B.7: Impact of fan inlet hub/tip ratio and axial Mach number on corrected flow per fan frontal area (modified from [175, Fig. 5.2.2.11]) including typical ranges for conventional and advanced turbofans (TF), counter-rotating TF studies and the range typically expected for mechanically driven fuselage fan arrangements

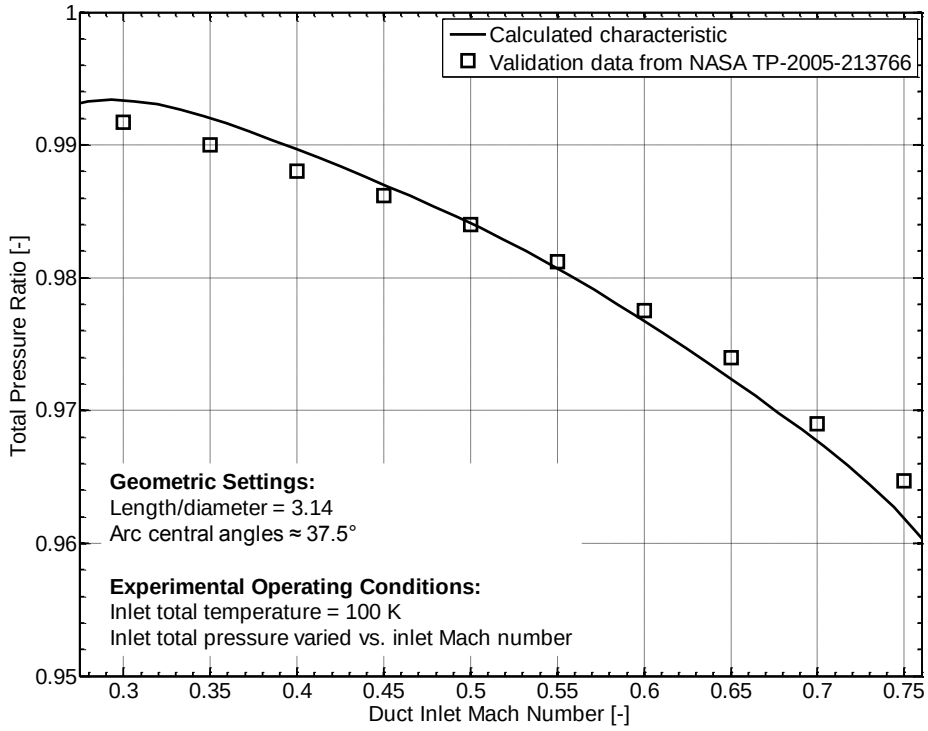

Figure B.8: Validation of core intake pressure loss model. Validation data derived from Reference [271, Fig. 24B]

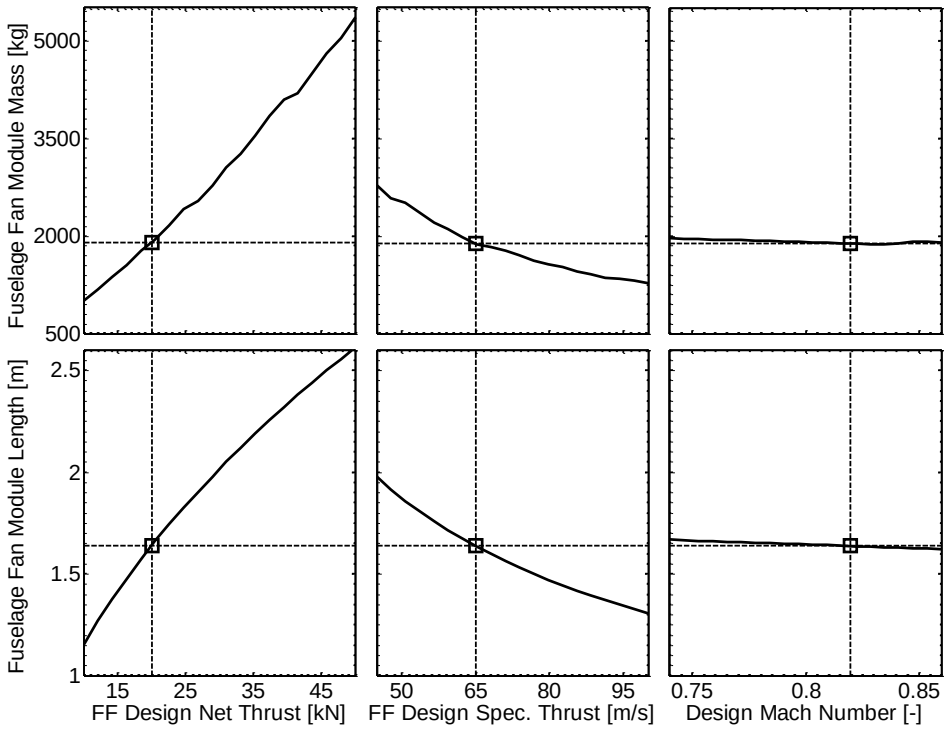

Figure B.9: Evaluation of implemented method for FF module weight and length prediction with respect to important sizing parameters (hub radius at AIP: 1.4 m)

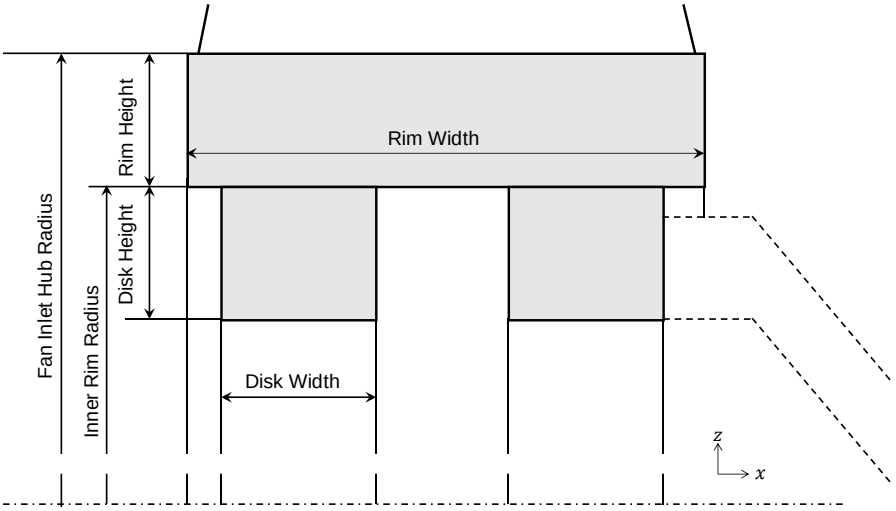

Figure B.10: Simplified parameterization of fuselage fan disk geometry

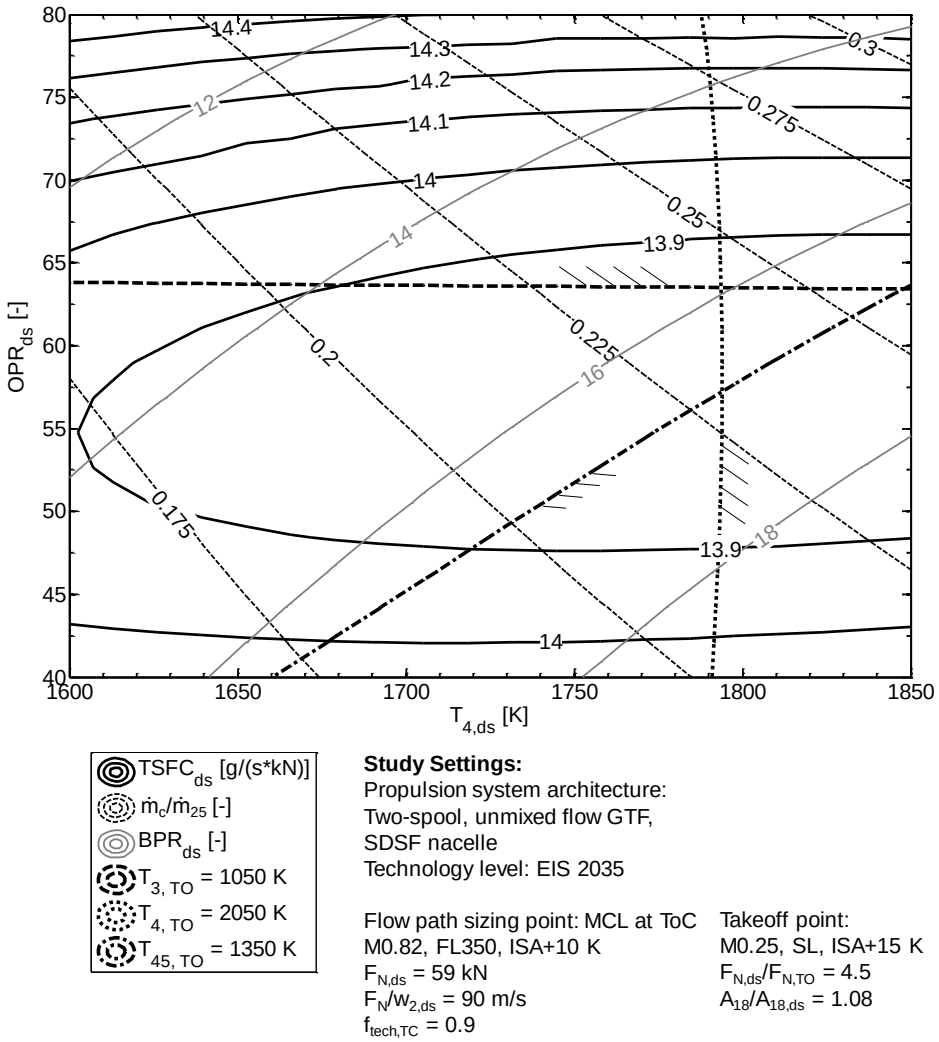

Figure B.11: Cycle design study of conventionally installed, advanced GTF power plant at constant design specific thrust including visualization of maximum permissible temperature levels at takeoff point

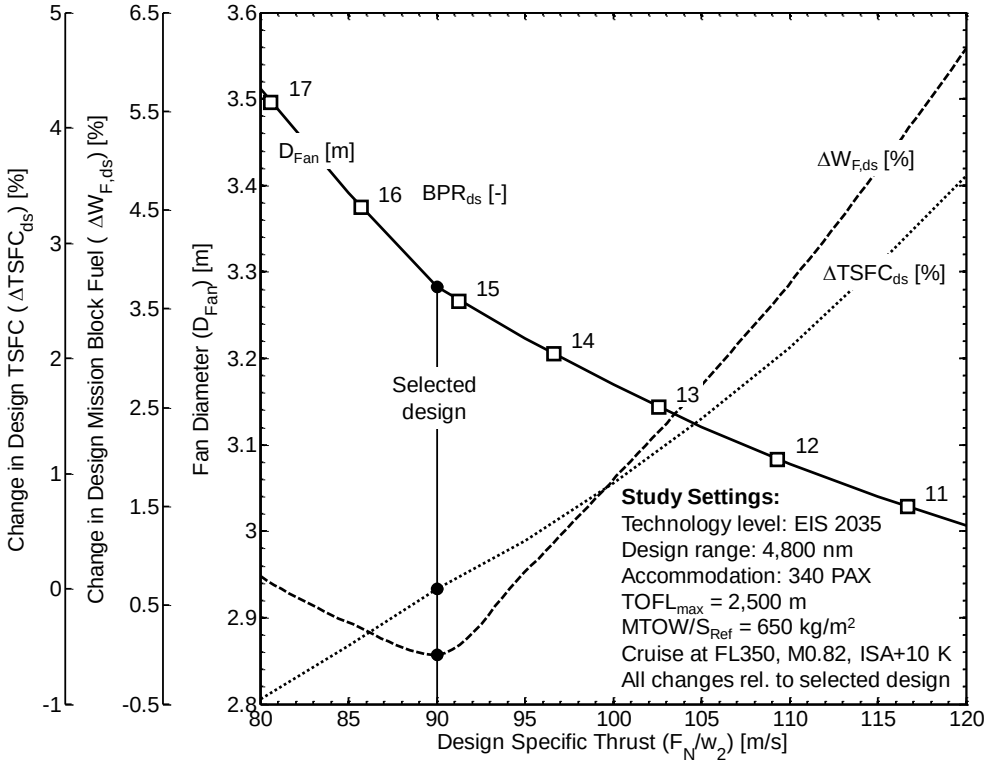

Figure B.12: Aircraft-integrated sizing study of reference aircraft

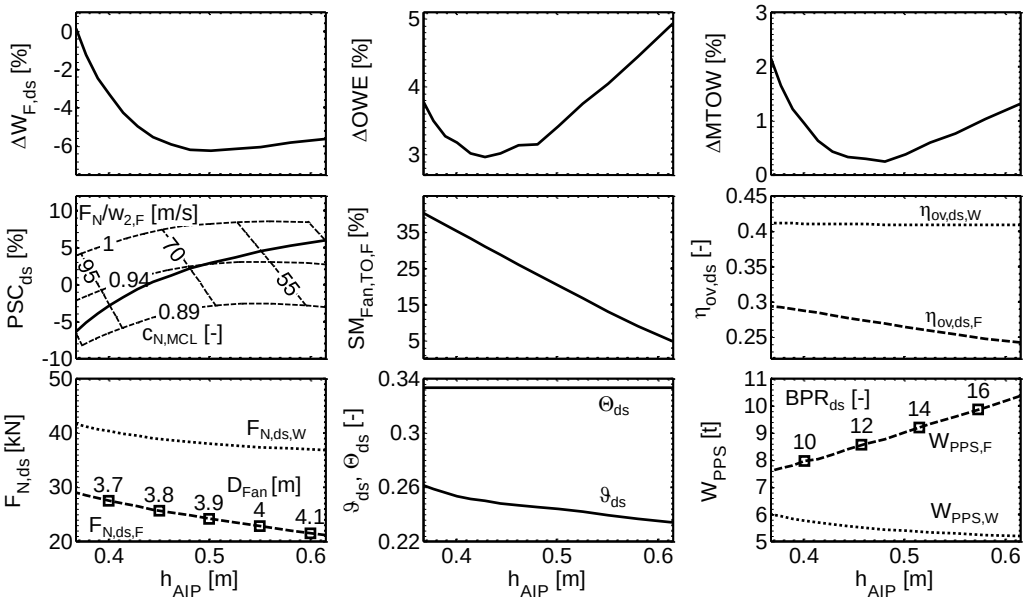

Figure B.13: Characteristics of parametric design study of FF specific thrust. Each design optimized for minimum design mission block fuel

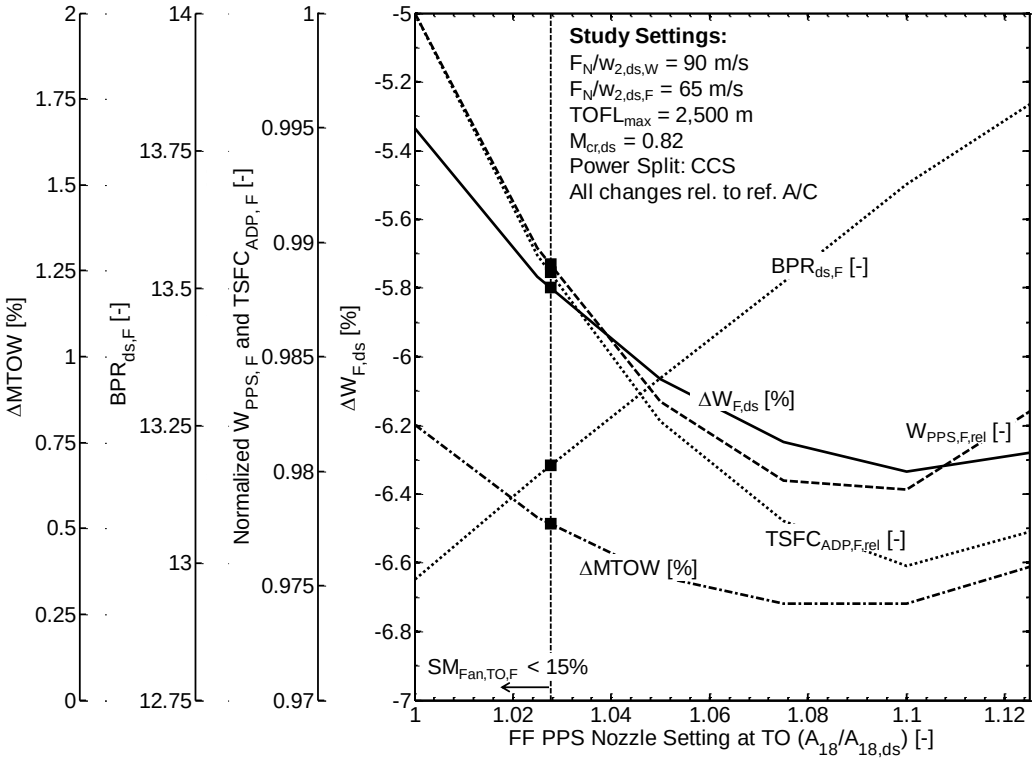

Figure B.14: Aircraft-level implications of FF propulsion system nozzle setting at takeoff conditions for fixed design specific thrusts and application of common core strategy

C. Supplementary Tables

		Design Cases					
	Unit	D_0	D_1	D_2	D_3	D_4	D_5
h_{AIP}	m	0.526	0.65	0.9	0.9	0.5	0.5
FPR	-	1.498	1.369	1.249	1.494	1.490	1.314
$F_{N,GT}$	kN	31.08	28.68	29.62	65.68	14.78	22.14
D_{Fus}	kN	23.24	23.24	23.24	23.24	23.24	23.24
$S_{wet,Nac}$	m^2	69.58	74.2	82.2	81.1	70.0	69.4
$D_{Nac,F}$	kN	5.08	5.48	6.22	6.12	5.10	5.05
F_X	kN	2.76	–0.04	0.16	36.32	–13.56	–6.15
$\hat{F}_X$	kN	23.24	23.46	25.7	63.41	7.56	14.57
ΔF_X	kN	20.48	23.50	25.54	27.09	21.12	20.72

h_{AIP}	Duct height at AIP
FPR	Design Fan Pressure Ratio
$F_{N,GT}$	Net thrust of gas turbine
D_{Fus}	Drag of isolated fuselage
$S_{wet,Nac}$	Fuselage Fan nacelle external wetted area
$D_{Nac,F}$	External drag of Fuselage Fan nacelle
F_X	Net forward force of Setup B (gas turbine performance)
$\hat{F}_X$	Net forward force of Setup A (CFD simulation)
ΔF_X	Integration impact metric

Table C.1: Synopsis of design cases used for matching of CFD setup with gas turbine performance

Parameter	Figure	RMS Error [%]	Max. Abs. Error [%]
Design intake total pressure recovery ratio	Figure 4.7	0.12	0.17
Design integration impact metric	Figure 4.8	0.36	0.69
Design speed sensitivity of intake total pressure recovery ratio	Figure 4.10	$1.91 \cdot 10^{-14}$	$2.22 \cdot 10^{-14}$
Design speed sensitivity of integration impact metric	Figure 4.10	$4.44 \cdot 10^{-8}$	$5.78 \cdot 10^{-8}$
Intake total pressure recovery ratio at part power	Figure 4.11	0.09	0.25
Integration impact metric at part power	Figure 4.12	1.10	2.88

Table C.2: Overview of data fitting quality of regression models presented in Chapter 4

Parameter	Unit	Compressors	Turbines
$\eta_{pol,ref}$	-	0.905	0.945
$\dot{m}_{ref}$	kg/s	70.0	70.0
Re_{ref}	-	105	55
m	-	0.063	0.236
n	-	0.14 [a] 0.12…0.14 [b] 0.10 [c]	0.18

[a] Fans
[b] IPCs and boosters
[c] Axial HPCs and radial compressors

Table C.3: Summary of model parameters of turbo component design efficiency prediction method, adapted from Reference [175, p. 158]

Parameter	Unit	Calculated Value	Value from Reference [228]	Error [%]
Highlight-to-throat diameter ratio	-	1.077	1.110	–2.97
Intake total pressure ratio at flow path sizing point [a]	-	0.9979	-	n / a
Intake total pressure ratio at takeoff point [b]	-	0.9972	≈0.9974	–0.02
Intake total pressure ratio at representative cruise point [c]	-	0.9984	-	n / a

[a] M0.78, FL350 (10,668 m), ISA
[b] M0.20, Sea Level, ISA
[c] M0.78, FL350 (10,668 m), ISA, 80% corrected fan design inlet mass flow

Table C.4: Validation of implemented intake pressure ratio model at zero incidence

Parameter	Unit	Calculated Value	Value from Reference [229]	Error [%]
Highlight-to-throat area ratio	-	1.37	1.37	±0.0[a]
Design throat Mach number	-	0.79	0.79	±0.0[a]
Intake total pressure ratio at flow path sizing point [b]	-	0.9941	-	n / a
Throat Mach number at takeoff point	-	0.71	0.71	±0.0[a]
Intake total pressure ratio at takeoff point, incidence angle of 0° [c]	-	0.9933	0.9923[d]	+0.10
Intake total pressure ratio at takeoff point, incidence angle of 20° [c]	-	0.9789	0.9908[d]	–1.20

[a] Input value
[b] M0.78, FL350 (10,668 m), ISA
[c] M0.18, Sea Level, ISA
[d] graphically approximated from Reference [229, Fig. 16a]

Table C.5: Validation of implemented intake pressure ratio model at incidence

	Unit	Calculated Value	Error [%]	Reference
Stage configuration [a]		1 / 3 / 10 / B / 2 / 6		[231]
Geometry				
Fan inlet tip radius	m	1.562	±0.0[c]	[231]
IPC inlet tip radius [b]	m	1.705	–2.1	[231]
HPC inlet tip radius [b]	m	0.956	–1.6	[231]
HPT exit tip radius [b]	m	1.018	–1.3	[231]
LPT exit tip radius [b]	m	1.995	+0.1	[231]
Bare engine length	m	5.32	+8.5	[253]
Nacelle maximum diameter [d]	m	3.94	+0.7	[253]
Performance at Top-of-Climb (10,668m, M0.85, ISA+10 K)				
Net thrust	kN	80.1	±0.0[c]	[319]
Performance at Cruise (10,668m, M0.85, ISA+10 K)				
Net thrust	kN	69.0	±0.0[c]	[231]
Fan Pressure Ratio	-	1.65	–0.3	[231]
Bypass Ratio	-	8.0	–1.6	[231]
HPT rotor inlet temperature (T_{41})	K	1,446	+4.8	[231]
Engine inlet mass flow	kg/s	572	–0.7	[231]
TSFC [e]	g/(s·kN)	15.78	+1.2	[231]
Performance at Sea Level Static, ISA				
Net thrust	kN	395.3	±0.0[c]	[253]
Fan Pressure Ratio	-	1.63	+3.2	[231]
Bypass Ratio	-	7.9	–4.8	[231]
Overall Pressure Ratio	-	36.0	–2.4	[231]
HPT rotor inlet temperature (T_{41})	K	1,628	+2.3	[231]
Engine inlet mass flow	kg/s	1,385	–2.1	[231]
LP spool speed	RPM	2,315	–6.1	[231]
HP spool speed	RPM	10,918	±0.0[c]	[253]
TSFC [e]	g/(s·kN)	8.06	–2.9	[253]
Masses				
Bare engine [f]	kg	7,994	+1.3	[231]

[a] Nomenclature: stage counts of fan, booster, HPC, HPT and LPT
[b] reference geometries graphically approximated from two-dimensional general arrangement
[c] input value
[d] mean value of nacelle maximum width and height
[e] published value taken as uninstalled
[f] dry mass (excluding operating fluids)

Table C.6: Additional validation results of propulsion system synthesis and weights estimation based on GE90-85B propulsion system

	Unit	Calculated Value	Error [%]	Reference
Stage configuration [a]		1 / 4 / 10 / B / 2 / 5		[231]
Geometry				
Fan inlet tip radius	m	0.807	±0.0[c]	[231]
IPC inlet tip radius [b]	m	0.462	–0.8	[231]
HPC inlet tip radius [b]	m	0.290	–0.4	[231]
HPT exit tip radius [b]	m	0.334	–0.3	[231]
LPT exit tip radius [b]	m	0.476	+0.5	[231]
Bare engine length	m	3.297	+3.0	[320]
Total engine length [b]	m	5.410	+2.9	[321]
Nacelle maximum diameter [b, d]	m	2.170	–0.3	[321]
Performance at Top-of-Climb (10,668m, M0.78, ISA)				
Net thrust	kN	26.7	±0.0[c]	[34]
TSFC	g/(s·kN)	17.23	+0.2	[34]
Performance at Sea Level Static, ISA+15 K				
Net thrust	kN	139.7	±0.0[c]	[34]
Fan Pressure Ratio	-	1.78	+3.2	[322]
Bypass Ratio	-	4.5	–1.7	[322]
Overall Pressure Ratio	-	35.7	+11.3	[322]
Engine inlet mass flow	kg/s	382.5	–1.7	[254]
LP spool speed	RPM	5,619	–0.5	[231]
HP spool speed	RPM	14,950	±0.0[c]	[320]
Masses				
Bare engine [f]	kg	2,223	–5.8	[231]
Propulsion system	kg	3,223	–5.3	[231]

[a] Nomenclature: stage counts of fan, IPC, HPC, HPT and LPT
[b] reference geometries graphically approximated from two-dimensional general arrangement
[c] input value
[d] mean value of nacelle maximum width and height
[e] published value taken as uninstalled
[f] dry mass (excluding operating fluids)

Table C.7: Additional validation results of propulsion system synthesis and weights estimation based on IAE V2530-A5 propulsion system

Flow regime		
Hydraulically smooth, $\mathrm{Re} \cdot \frac{k}{d} < 65$	Hydraulically rough, $\mathrm{Re} \cdot \frac{k}{d} > 1300$	Transition regime $65 \leq \mathrm{Re} \cdot \frac{k}{d} \leq 1300$
Blasius model, applicable for $2320 < \mathrm{Re} < 10^5$: $\lambda_D = 0.3164 \cdot \mathrm{Re}^{-0.25}$		
Nikuradse model, applicable for $10^5 \leq \mathrm{Re} \leq 5 \cdot 10^6$: $\lambda_D = 0.0032 + 0.221 \cdot \mathrm{Re}^{-0.237}$	Nikuradse model: $\frac{1}{\sqrt{\lambda_D}} = 2\log\left(\frac{d}{k}\right) + 1.14$	Prandtl-Colebrook model: [a] $\frac{1}{\sqrt{\lambda_D}} = -2\log\left(\frac{2.51}{\mathrm{Re}\cdot\sqrt{\lambda_D}} + 0.269\frac{k}{d}\right)$
Prandtl / von Kármán model, [a] applicable for $\mathrm{Re} > 5 \cdot 10^6$: $\frac{1}{\sqrt{\lambda_D}} = 2\log\left(\mathrm{Re} \cdot \sqrt{\lambda_D} - 0.8\right)$		

Re [-] Reynolds number
k [mm] Surface roughness height (0.0013…0.0015 for typical technically smooth duct materials [267, p. 259])
d [m] Duct diameter
λ_D [-] Flow coefficient (Darcy friction factor)
[a] application of this model requires iterative solving for λ_D

Table C.8: Summary of implemented formulations for determination of flow coefficient in turbulent duct flow (Re > 2320), adapted from Reference [267, p. 100]

Parameter	Unit	Calculated Value	Reference Value	Error [%]	Reference
Flight Mach number	-	0.25	0.25	±0.0[a]	[274, p. 6]
Altitude	m	0.0	0.0	±0.0[a]	[274, p. 6]
ISA temperature deviation	K	0	0[b]	±0.0[a]	-
Angle-of-attack	°	8.0	8.0	±0.0[a]	[274, p. 6]
Fuselage length	m	38.0	38.0	±0.0[a]	[55, Fig. 5.21]
Relative AIP position	-	0.93	0.93[c]	±0.0[a]	[125, p. 3]
Duct height at AIP	m	0.75	0.75[c]	±0.0[a]	[125, p. 6]
DC_{60}	-	0.0136	0.0145[f]	–5.9%	[274, Fig. 10f]

[a] input value
[b] not given, based on the author's assessment
[c] graphically approximated
[d] total-to-static pressure ratio ($\bar{p}_{60}/p_{s,0}$)
[e] total-to-static pressure ratio ($\bar{p}_{360}/p_{s,0}$)
[f] value derived using graphical image processing [323]

Table C.9: Model settings for the validation of implemented pressure distortion model

Aspect	Method
Component weights	
Empennage	Torenbeek [241]
Propulsion system	
Conventionally installed turbofan	Seitz [182]
Fuselage Fan propulsion system	see Section 5.3
Engine pylon	Seitz [182]
Fuselage	LTH [324], adapted by Seitz [182]
Wing	LTH [324]
Landing gear	Raymer [181]
Systems and cabin	OWE residual (input)
Aerodynamics	
Skin friction, form and interference drag	Raymer [181]
Wave drag	
Lifting surfaces	based on Korn equation [325]
Non-lifting surfaces	Roskam [183]
Induced drag	Oswald factor according to Howe [304]
Trim drag	not explicitly modeled, captured by drag residual
Low-speed aerodynamics	
Lift coefficient and drag increments [a]	Loftin [305]

[a] due to extension of high-lift devices and/or landing gear

Table C.10: Methodological aspects of employed aircraft conceptual design framework, based on Reference [182]

Parameter	Unit	Value	Reference
Flow path sizing point (ToC)			
Engine thrust setting	-	Max. Climb (MCL)	
Flight altitude	m	10,668	
Temperature deviation from ISA	K	+10	
Takeoff point			
Flight altitude	m	Sea Level	
Flight Mach number	-	0.25	
Temperature deviation from ISA	K	+15	
Limiter settings at takeoff			
HPC exit temperature (T_3)	K	1,050	[40], [326]
Combustor exit temperature (T_4)	K	2,050	[309]
LPT inlet temperature (T_{45})	K	1,350	[42]
AN^2 of last HPT rotor	m^2/s^2	9,000	[175, Fig. 5.2.3.22]
AN^2 of last LPT rotor	m^2/s^2	13,500	[175, Fig. 5.2.3.6]
Relative corrected fan speed	%	100.0	
Efficiencies and pressure ratios			
Core inlet pressure ratio [a]	-	0.990	[34]
Combustor pressure ratio	-	0.970	[196, p. 194]
Combustor efficiency	-	0.999	[196, p. 194]
Compressor inter-duct pressure ratio	-	0.990	[196, Fig. 5.37]
Turbine inter-duct pressure ratio	-	0.990	[196, Fig. 5.37]
HP shaft mechanical efficiency	-	0.995	[196, p. 230]
LP shaft mechanical efficiency	-	0.995	[196, p. 230]
FDGS design point efficiency	-	0.994	[248, Fig. 7]
Turbine exit casing pressure ratio	-	0.995	[34]
Turbo component technology factor ($f_{tech,TC}$)	-	0.900	
Miscellaneous settings			
(Lower) Fuel Heating Value	MJ/kg	43.124	[170]
Axial Mach number at fan inlet [a]	-	0.68	[175, Fig. 5.2.2.9]
Hub/tip ratio at fan inlet [a]	-	0.26	[231, p. 300]
Customer bleed [b]	-	0.0	
Power offtake/MTOW [c]	W/kg	2.5	
Cooling air constant [d]	-	0.0246	
Turbine airfoil material temperature	K	1,300	[210, Fig. 5.5]
Relative LPT cooling air	-	0.005	[196, p. 226]

[a] only applicable to conventionally installed turbofans
[b] all-electric subsystems architecture assumed
[c] reference condition derived from Boeing 787 data [327] featuring General Electric GEnx power plants [328]
[d] calibrated (see Section 5.1.3.1)

Table C.11: Synopsis of propulsion system modeling constants and simulation settings for studies presented in Section 6, consideration of advanced technology status (EIS 2035)

Parameter	Estimated from
Boeing "SUGAR Freeze Hybrid BLI" [49]	
Fan power of underwing-podded turbofans, $P_{Fan,W}$ Fan power of reference turbofan, $P_{Fan,ref}$	Cycle calculation using given fan inlet tip diameter, pressure ratio, hub/tip ratio and efficiency [121, p. 6] [a, b]
LPT power of underwing-podded turbofans [c, d]	$P_{LPT} = \frac{P_{Fan,W}}{1 - \frac{P_{Booster}}{P_{LPT}}}$
NASA STARC-ABL [125]	
Aircraft instantaneous gross weight at ToC [e]	$m_{IGW} = 0.95 m_{MTO}$
Aircraft drag at ToC	$D = \frac{m_{IGW} g}{L/D}$
ToC thrust requirement	$F_N = m_{IGW} g \frac{dh}{dt} \frac{1}{V_0} + D$
Ratio of thrust power to LPT power	$\eta = \frac{F_N V_0}{P_{LPT}} = 0.7$
Total LPT power at ToC	$P_{LPT,tot} = \frac{F_{N,W} V_0}{\eta} + P_{Gen}$
Fan power of underwing-podded turbofans [c, d]	$P_{Fan,W} = P_{LPT} \cdot \left(1 - \frac{P_{Booster}}{P_{LPT}}\right) - P_{Gen}$ [b]
Relative fuselage propulsor shaft power at ToC [f]	$P_{rel} = P_{Fan,F} / (P_{Fan,F} + P_{Fan,W})$
Seitz *et al.* (2018) [123]	
Total LPT power at ToC [g]	$P_{LPT,tot} = \frac{F_{N,W} V_0}{\eta} + P_{Gen}$
Ratio of thrust power to LPT power	$\eta = \frac{F_N V_0}{P_{LPT}} = 0.7$
Fan power of underwing-podded turbofans [c, d]	$P_{Fan,W} = P_{LPT} \cdot \left(1 - \frac{P_{Booster}}{P_{LPT}}\right) - P_{Gen}$ [b]

[a] fan axial inlet Mach number assumed 0.68
[b] error bars in Figure 6.3 produced through variation of +/-10%
[c] mechanical shaft efficiency neglected
[d] relative booster power assumed $P_{Booster}/P_{LPT}$ = 0.05
[e] mission segment fuel fraction according to Reference [181]
[f] assuming 2.61 MW [125] to be absorbed at ToC
[g] see Reference [24] for thrust requirements

Table C.12: Assumptions for comparison cases of plausibility analysis